



The
University
Of
Sheffield.

Mechanisms of potato dormancy break: a metabolomics approach

Marion Tout

A thesis submitted for the degree of Doctor of
Philosophy
Faculty of Science
Department of Animal and Plant Sciences

February 2019

Abstract

Potato dormancy break is a commercially important process that leads to losses during crop storage. Dormancy release involves the activation of buds on the tuber surface. Although much is known about hormonal and environmental triggers for dormancy release, there is a lack of knowledge on the metabolic processes stimulated by these factors, enabling bud growth to occur. In this thesis I report on experiments designed to characterise and investigate the earliest metabolic changes occurring as tuber buds exit dormancy and start to sprout.

The majority of previous work focused on changes in the tuber rather than the buds, due to their size limiting analysis. To tackle this problem, I have developed a mass spectrometry approach using individually dissected buds from tubers at different time points in storage, studying cultivars showing a range of genetically determined dormancy characteristics grown under both field and greenhouse conditions.

These investigations identified elements of the citric acid (TCA) cycle as very early markers of bud release from dormancy across a range of storage and growth conditions for a diverse set of tuber cultivars. Moreover, a quantitative analysis indicated that at certain stages the TCA cycle was functioning in a non-cyclic manner, a phenomenon reported in other biological systems. These results provide an insight into the earliest metabolic events in tuber bud sprouting, providing lead markers that may be of interest to the industry as novel approaches to measuring tuber condition during storage.

In the final part of the thesis I report on the development and application of a method to image metabolite distribution around tuber buds as they leave dormancy. An optimisation process is described which allows detection of TCA metabolites in sections of tubers, providing the foundation for future work analysing where and when shifts in TCA metabolites occur within tubers during bud sprouting.

All the data presented in this thesis are available on request from Prof. Andrew Fleming, Department of Animal and Plant Sciences, University of Sheffield (contactable at a.fleming@sheffield.ac.uk).

Acknowledgements

I would like to thank my supervisors; Andy Fleming, Heather Walker, Mike Burrell and Glyn Harper for their guidance and support over the past 4 years. Gemma Newsome and Alice Baillie were also invaluable, particularly at the thesis preparation stage. I would also like to acknowledge the role my research group has played in creating a supportive, welcoming and cake provisioned community for me to work in.

I would like to thank everyone from Wicker Camp Thai Boxing Gym for helping me process my research-related frustrations in a constructive manner. In particular, I need to name Trix, Mick and Roo March-Mullaney, without whom I would never have thought of myself as an athlete, and my various and dedicated sparring partners.

Thanks are also due to my friends and family, who have been unwaveringly generous and kind. I would not have completed this project without their love and encouragement. I must specifically thank Jess Dunn, Laura Saunders, Ellie Healicon, Cat Gibbs, Lindsay Canham, Jess Fairbairn, Anna King, my parents Ann and Paul and my sister Sarah, for putting up with my nonsense.

I gratefully acknowledge the funding provided by a BBSRC industrial CASE award with AHDB Potatoes (previously known as the Potato Council).

Contents

| | |
|--|------------|
| Abstract | i |
| Acknowledgements | ii |
| List of Abbreviations | xii |
| 1 Introduction | 1 |
| 1.1 Meristems, axillary meristems and the cell cycle | 2 |
| 1.1.1 What is known about bud dormancy and sprouting in potato tubers? | 7 |
| 1.2 Metabolism and cell division | 9 |
| 1.3 Mass spectrometry | 12 |
| 1.4 The agronomic relevance of potato sprouting | 14 |
| 1.5 Summary | 19 |
| 1.5.1 Objectives | 19 |
| 1.5.2 Hypotheses | 19 |
| 1.5.3 Approach | 20 |
| 2 Metabolic profiles in tuber buds during the release from dormancy | 21 |
| 2.1 Introduction | 21 |
| 2.1.1 Hypotheses | 23 |
| 2.2 Materials and Methods | 23 |
| 2.2.1 Plant Material | 23 |
| 2.2.2 Potato Growing Conditions | 24 |
| 2.2.3 Assays of sprouting potential | 24 |
| 2.2.4 Histology and microscopy | 25 |
| 2.2.5 Methanol-Chloroform extractions | 26 |
| 2.2.6 ESI-TOF-MS | 28 |
| 2.2.7 Data analysis | 28 |
| 2.3 Results | 29 |

| | | |
|-------|---|----|
| 2.3.1 | Method validation | 29 |
| 2.3.2 | Structure of the dormant tuber bud | 30 |
| 2.3.3 | Synchronising dormancy release | 33 |
| 2.3.4 | Metabolic profiles in response to Gibberellic Acid (GA) treatment . | 37 |
| 2.3.5 | Metabolic profiles along time in storage | 41 |
| 2.3.6 | Field grown tubers | 45 |
| 2.4 | Discussion | 52 |
| 2.4.1 | System and assumptions | 53 |
| 2.4.2 | Development series | 56 |
| 2.4.3 | Apical dominance | 58 |
| 2.4.4 | Storage series | 58 |
| 2.4.5 | Cultivars | 59 |
| 2.4.6 | Conclusions | 61 |

3 The role of TCA cycle activity during early dormancy release in tuber buds 62

| | | |
|-------|---|----|
| 3.1 | Introduction | 62 |
| 3.1.1 | Hypotheses | 65 |
| 3.2 | Material and Methods | 66 |
| 3.2.1 | Marker identification using online databases | 66 |
| 3.2.2 | Tandem Mass Spectrometry | 66 |
| 3.2.3 | Pathway analysis | 66 |
| 3.2.4 | Sugar extraction from potato tissue | 67 |
| 3.2.5 | Enzyme-linked spectrophotometric assay of sugars in potato extracts | 67 |
| 3.3 | Results | 68 |
| 3.3.1 | Identifying ions | 68 |
| 3.3.2 | Enzyme-linked spectrophotometric analysis of sugars | 80 |
| 3.3.3 | The TCA cycle in field grown tubers | 84 |
| 3.4 | Discussion | 90 |
| 3.4.1 | Identification of TCA metabolites as lead markers for early sprouting | 90 |
| 3.4.2 | The role of TCA metabolism in sprouting | 93 |
| 3.4.3 | Comparison of TCA metabolites with other potential metabolic markers for sprouting | 95 |
| 3.4.4 | The TCA cycle in field grown samples | 97 |
| 3.4.5 | Conclusions | 99 |

| | | |
|----------|--|------------|
| 4 | Visualising the spatial distribution of key metabolites during dormancy release in tuber buds | 101 |
| 4.1 | Introduction | 101 |
| 4.1.1 | Hypotheses | 103 |
| 4.2 | Materials and Methods | 103 |
| 4.2.1 | Plant material | 103 |
| 4.2.2 | Samples for phenolics analysis | 103 |
| 4.2.3 | Phenolics detection with DESI | 104 |
| 4.2.4 | Phenolics in tuber sections | 105 |
| 4.2.5 | Data processing | 105 |
| 4.2.6 | Malate detection with DESI | 105 |
| 4.2.7 | TCA cycle metabolites in tuber sections | 106 |
| 4.2.8 | Data processing | 107 |
| 4.3 | Results | 107 |
| 4.3.1 | Phenolics | 107 |
| 4.3.2 | Malate detection | 113 |
| 4.3.3 | The distribution of TCA cycle intermediates in hand sections of tubers | 115 |
| 4.3.4 | The distribution of TCA cycle intermediates in tuber cryosections | 121 |
| 4.3.5 | The distribution of TCA cycle intermediates in GA- and control-treated tubers | 128 |
| 4.3.6 | The distribution of TCA cycle intermediates in stored tubers | 135 |
| 4.4 | Discussion | 144 |
| 4.4.1 | The detection of phenolic compounds by DESI imaging | 144 |
| 4.4.2 | The detection of TCA cycle compounds by DESI imaging | 146 |
| 4.4.3 | Changes in TCA metabolite distribution with GA treatment | 148 |
| 4.4.4 | Changes in DESI images of glasshouse grown cv. King Edward tuber buds during storage | 149 |
| 4.4.5 | Conclusions | 150 |
| 5 | Final discussion | 152 |
| 5.1 | Overview | 152 |
| 5.2 | Approach to potato dormancy research | 153 |
| 5.2.1 | Developmental and metabolic approaches | 153 |
| 5.2.2 | The TCA cycle and tuber sprouting | 156 |
| 5.3 | DESI as a Mass Spectrometry Imaging platform | 157 |
| 5.3.1 | Comparison with MALDI imaging | 158 |

| | | |
|---|-------------------------------|------------|
| 5.3.2 | Future imaging work | 159 |
| 5.4 | Final conclusion | 159 |
| Appendix A Cultivar pedigree | | 167 |
| Appendix B Replicate DESI images | | 169 |

List of Figures

| | | |
|------|---|----|
| 1.1 | Schematic representation of the shoot and root apical meristems | 3 |
| 1.2 | Schematic representation of axillary meristem formation | 4 |
| 1.3 | Schematic representation of the cell cycle | 6 |
| 1.4 | Schematic representation of the classical understanding of potato dormancy, integrated with more recent phytohormone data | 8 |
| 1.5 | Schematic representation of MALDI imaging | 15 |
| 1.6 | Schematic representation of the the DESI ionisation system | 16 |
| 2.1 | Schematic representation of potato dormancy. | 22 |
| 2.2 | Metabolic profiling dilution tests | 30 |
| 2.3 | Inline filter tests | 31 |
| 2.4 | Sections of dormant potato tuber buds. | 32 |
| 2.5 | Scanning electron micrographs of potato buds. | 34 |
| 2.6 | Design of staggered planting experiments under controlled environment. | 35 |
| 2.7 | Sprouting rate of treated buds in the <i>in vitro</i> system. | 35 |
| 2.8 | Multivariate analysis the effect of bud position on metabolic profiles. | 37 |
| 2.9 | Multivariate analysis of field grown cv. Maris Piper metabolic profiles, treated with GA in a development series. | 39 |
| 2.10 | Multivariate analysis of cv. Maris Piper metabolic profiles from the controlled environment, treated with GA in a development series. | 40 |
| 2.11 | PCA of cv. King Edward metabolic profiles from the controlled environment staggered planting system. | 43 |
| 2.12 | OPLS of cv. King Edward metabolic profiles from the controlled environment staggered planting system. | 44 |
| 2.13 | Multivariate analysis of cv. King Edward metabolic profiles from the controlled environment staggered planting system. | 46 |
| 2.14 | An OPLS of field grown King Edward samples, by month. | 47 |
| 2.15 | OPLS of GA-treated, field grown King Edward samples, by time since treatment. | 48 |

| | | |
|------|--|-----|
| 2.16 | An OPLS of field grown Desiree samples, by month. | 49 |
| 2.17 | OPLS of field grown GA-treated Desiree samples, by time since treatment. | 50 |
| 2.18 | An OPLS of field grown Russet Burbank samples, by month. | 51 |
| 2.19 | OPLS and PCA plots of GA-treated field grown Russet Burbank samples, by time since treatment. | 52 |
| 2.20 | An OPLS of field grown Maris Piper samples, by month. | 53 |
| 2.21 | OPLS of GA-treated field grown Maris Piper samples, by time since treat- ment. | 54 |
| | | |
| 3.1 | Malate <i>in silico</i> fragmentation pattern | 69 |
| 3.2 | Organic acid fragmentation patterns | 70 |
| 3.3 | Citrate Isomers | 72 |
| 3.4 | Tandem Mass Spectrometry of samples | 73 |
| 3.5 | TCA cycle | 74 |
| 3.6 | Pathway differences in apical and stolon buds | 75 |
| 3.7 | TCA cycle configuration in response to GA treatment | 77 |
| 3.8 | Changes in metabolite relative levels in response to GA treatment | 78 |
| 3.9 | TCA cycle configuration during storage | 79 |
| 3.10 | Pathway configuration changes with storage | 81 |
| 3.11 | Changes in sugar concentration in tuber tissue | 82 |
| 3.12 | Change in hexose composition with tuber storage | 83 |
| 3.13 | Change in sugar composition in tuber storage | 83 |
| 3.14 | TCA cycle configuration in cv. King Edward | 85 |
| 3.15 | TCA cycle configuration in cv. Desiree | 87 |
| 3.16 | TCA cycle configuration in cv. Russet Burbank | 88 |
| 3.17 | TCA cycle configuration in cv. Maris Piper | 89 |
| | | |
| 4.1 | The standard curve of coumaric acid detection by the DESI. | 108 |
| 4.2 | Metabolite distribution in a fresh tuber section | 109 |
| 4.3 | Metabolite distribution in a tuber piece, sectioned after 24 hours in pH 5.0 buffer | 110 |
| 4.4 | PCA analysis comparing regions of interest from the phenolics method DESI images | 111 |
| 4.5 | The standard curve of malic acid detection by the DESI. | 114 |
| 4.6 | Analysis of a fresh tuber hand section | 116 |
| 4.7 | Metabolite distribution in a fresh tuber hand section | 117 |
| 4.8 | Analysis of a stored tuber hand section | 119 |
| 4.9 | Metabolite distribution in a stored tuber hand section | 120 |

| | | |
|------|---|-----|
| 4.10 | PCA analysis comparing regions of interest from the handsection DESI images | 121 |
| 4.11 | Analysis of a fresh tuber cryosection | 122 |
| 4.12 | Metabolite distribution in a fresh tuber cryosection | 123 |
| 4.13 | Analysis of a stored tuber cryosection | 125 |
| 4.14 | Metabolite distribution in a stored tuber cryosection | 126 |
| 4.15 | PCA analysis comparing regions of interest from the cryosection DESI images | 127 |
| 4.16 | Analysis of a tuber cryosection, treated with GA for 72 hours | 128 |
| 4.17 | Metabolite distribution in a tuber cryosection, treated with GA for 72 hours | 130 |
| 4.18 | Analysis of a tuber cryosection, treated with control (water) for 72 hours | 131 |
| 4.19 | Metabolite distribution in a tuber cryosection, treated with control (water) for 72 hours | 133 |
| 4.20 | Multivariate analyses comparing regions of interest from the GA and control treated tuber DESI images | 134 |
| 4.21 | Analysis of a tuber cryosection, harvested in october, 14 weeks before analysis | 136 |
| 4.22 | Metabolite distribution in a tuber cryosection, harvested in October, 14 weeks before sampling | 137 |
| 4.23 | Analysis of a tuber cryosection, harvested in November, 8 weeks before sampling. | 138 |
| 4.24 | Metabolite distribution in a tuber cryosection, harvested in November, 8 weeks before sampling | 140 |
| 4.25 | Analysis of a tuber cryosection, harvested in January, 2 weeks before analysis | 141 |
| 4.26 | Metabolite distribution in a tuber cryosection, harvested in January, 2 weeks before sampling | 142 |
| 4.27 | Multivariate analyses comparing regions of interest from the glasshouse grown, stored tuber DESI images | 143 |
| A.1 | Partial pedigree of studied cultivars | 168 |
| B.1 | DESI image of a fresh tuber hand section | 169 |
| B.2 | DESI image of a fresh tuber hand section | 170 |
| B.3 | DESI image of a fresh tuber hand section | 171 |
| B.4 | DESI image - aged in buffer | 172 |
| B.5 | DESI image - aged in buffer | 173 |
| B.6 | DESI image of a fresh tuber hand section | 174 |
| B.7 | DESI image of a fresh tuber hand section | 175 |

| | | |
|------|--|-----|
| B.8 | DESI image of a fresh tuber hand section | 176 |
| B.9 | DESI image - tuber stored for 6 weeks | 177 |
| B.10 | DESI image - tuber stored for 6 weeks | 178 |
| B.11 | DESI image of a fresh tuber cryosection | 179 |
| B.12 | DESI image of a fresh tuber cryosection | 180 |
| B.13 | DESI image of a stored tuber cryosection | 181 |

List of Tables

| | | |
|-----|---|-----|
| 2.1 | Methanol-Chloroform extraction solvents | 27 |
| 2.2 | Putative identificaton of metabolic markers | 38 |
| 2.3 | Staggered Planting Design | 42 |
| 4.1 | Coumaric acid standard curve | 104 |
| 4.2 | Malic acid standard curve | 106 |

List of abbreviations

| | |
|---|--|
| ABA | Abscisic acid |
| AHDB | Agriculture and Horticulture Development Board |
| ATP | Adenosine Tri-Phosphate |
| AWEC | Arthur Willis Environment Centre |
| CHCl₃ | Chloroform |
| CIPC | Chlorpropham |
| CK | Cytokinin |
| CKP1 | Cytokinin riboside phosphorylase 1 |
| CTRL | Control |
| cv. | cultivar |
| DESI | Desorption electrospray ionisation |
| DNA | Deoxyribonucleic acid |
| ESI-TOF-MS | Electrospray ionisation time-of-flight mass spectrometry |
| EU | European Union |
| FAO | Food and Agriculture Organization |
| G₁, S and G₂ | Growth 1, Synthesis, Growth 2 phases of the cell cycle |
| G6PDH | Glucose-6-phosphate dehydrogenase |
| GA | Giberellic Acid |
| HDI | Waters High Definition Imaging Software |

| | |
|---------------|--|
| HEPES | 4-(2-hydroxyethyl)-1-piperazineethanesulfonic acid |
| LC-MS | Liquid chromatography–mass spectrometry |
| LOD | Limits of detection |
| m/z | mass to charge ratio |
| MALDI | Matrix Assisted Laser Desorption/Ionisation |
| MeOH | Methanol |
| MES | 2-(N-morpholino)ethanesulfonic acid |
| MS/MS | Tandem mass spectrometry |
| MS | Mass spectrometry |
| MS-I | Mass spectrometry imaging |
| NAD | Nicotinamide adenine dinucleotide |
| OCT | Optimal cutting temperature glycol compound |
| OPLS | Orthogonal Projections to Latent Structures |
| PCA | Principal Component Analysis |
| PGI | Phosphoglucose isomerase |
| RAM | Root apical meristem |
| ROS | Reactive oxygen species |
| SAM | Shoot apical meristem |
| SEM | Scanning Electron Microscopy |
| SEM | Standard Error of the Mean |
| TBO | Toluidine Blue O |
| TCA | Tricarboxylic acid or Krebs cycle |
| TOF-MS | Time of flight mass spectrometry |
| TUoS | The University of Sheffield |

UK United Kingdom

UPLC Ultra Performance Liquid Chromatography

USDA United States Department of Agriculture

WUS-CLV3 WUSCHEL-CLAVATA3

Chapter 1

Introduction

Potato dormancy break is an agronomically important process, so understanding and controlling it has been tackled from various research perspectives. These vary from engineering controlled environments for optimal storage (Heltoft *et al.* 2016), to monitoring changes in physiology, such as respiration rate (Li 1985). In this thesis, a plant development approach is used. Taking this viewpoint, I focus on the fact that potatoes are modified stems with highly reduced, shortened internodes that are radially expanded (Peterson *et al.* 1985). At each stem node, there are axillary buds, which are referred to as eyes in the context of tubers (Teper-Bamnolker *et al.* 2012). Each axillary bud comprises tiny leaf primordia around a meristem. The eyes of a potato are thus developmentally equivalent to the axillary buds typically observed along the aerial stems of most plants (Li 1985). These axillary buds are initially dormant but can become activated (via environmental triggers or an endogenous programme) to form the branches which define the plant architecture. The dormancy habit of a potato is therefore equivalent to the dormancy habit observed in shoots, whereby an overwintering stage of minimal growth is followed by rapid growth once favourable environmental conditions prevail. This new growth occurs at sites formed or determined in the previous season: the axillary buds (Wang *et al.* 2014).

Potato tubers are thus part of an evolutionary ancient vegetative propagation and overwintering strategy, developed to ensure rapid growth of the plant once a temporary harsh environment (winter) has passed. In the wild, this allows the aerial organs to die back in the winter and regenerate at the beginning of the next growing season because the tuber remains protected below the soil. During re-growth, the swollen tuber acts as a source of stored carbon, nutrients and energy, ensuring the new “branches” derived from the tuber can rapidly grow to the surface and establish the new photosynthetic shoot required for plant survival and further growth.

In an agronomic setting, the endogenous dormancy of tubers was exploited in pre-Columbian South America for 4000 years, providing human populations with a ready source of nutrition which could be stored over winter (Burton 1989). Since then, the potato has gained influence in Europe and North America as a major staple crop. However, the tendency, indeed requirement, for the tuber to eventually break dormancy and activate the growth of the axillary buds presents an agronomic challenge, since upon loss of dormancy the storage material (mainly starch) within the tuber is rapidly broken down, making the tuber essentially inedible or, at the very least, of limited nutritional value. The widespread commercial use of potatoes, both directly as a foodstuff or as the raw material for a wealth of high-value processed material, which deliver nutrition to the public all-year round, depends upon the ability to restrain the tendency for tubers to sprout during storage (Lu *et al.* 2012). This tension between the developmental program of the tuber (sprouting of axillary buds) and the agronomic requirement (repression of sprouting of axillary buds) provides the context for the studies reported in this thesis.

1.1 Meristems, axillary meristems and the cell cycle

All plant cells are ultimately derived from meristems, the most important of which are the root and shoot apical meristems (RAM and SAM, Dodsworth 2009). These meristems are represented schematically in Figure 1.1. Apical meristems are niches of stem cells at the growing tips of the roots and shoots, which generate new cells required for organogenesis and growth. Active apical meristems are in a continuous state of proliferation; the future potential for growth is maintained by retaining a subset of daughter cells in the stem cell niche, whilst the other daughter cells leave the meristem and develop into new organs.

In the SAM, the size of the stem cell niche is maintained by means of the WUS-CLAVATA system, an intricate negative feedback loop between transcription factors and locally acting peptide signals (Figure 1.1 A). WUSCHEL (WUS) is expressed in the organising centre, and encodes a homeodomain protein that promotes the maintenance of stem cell properties. WUS also promotes the expression of CLAVATA3 (CLV3) in adjacent tissue layers. CLV3 is expressed in the central zone of the meristem and inhibits WUS at the transcript level. This negative feedback allows the SAM to be maintained at a constant size, even though the cell population is dynamic and proliferating, leading to the regeneration of cells in this organ (Öpik & Rolfe 2003).

Hormones, in particular auxins, also play a role in the maintenance of the stem cell niche. Auxin also provides positional cues for the pattern of organ initiation; for example, the arrangement of leaf primordia around a growing meristem gives rise to phyllotaxy. This patterning process in the differentiating daughter cells is tightly linked

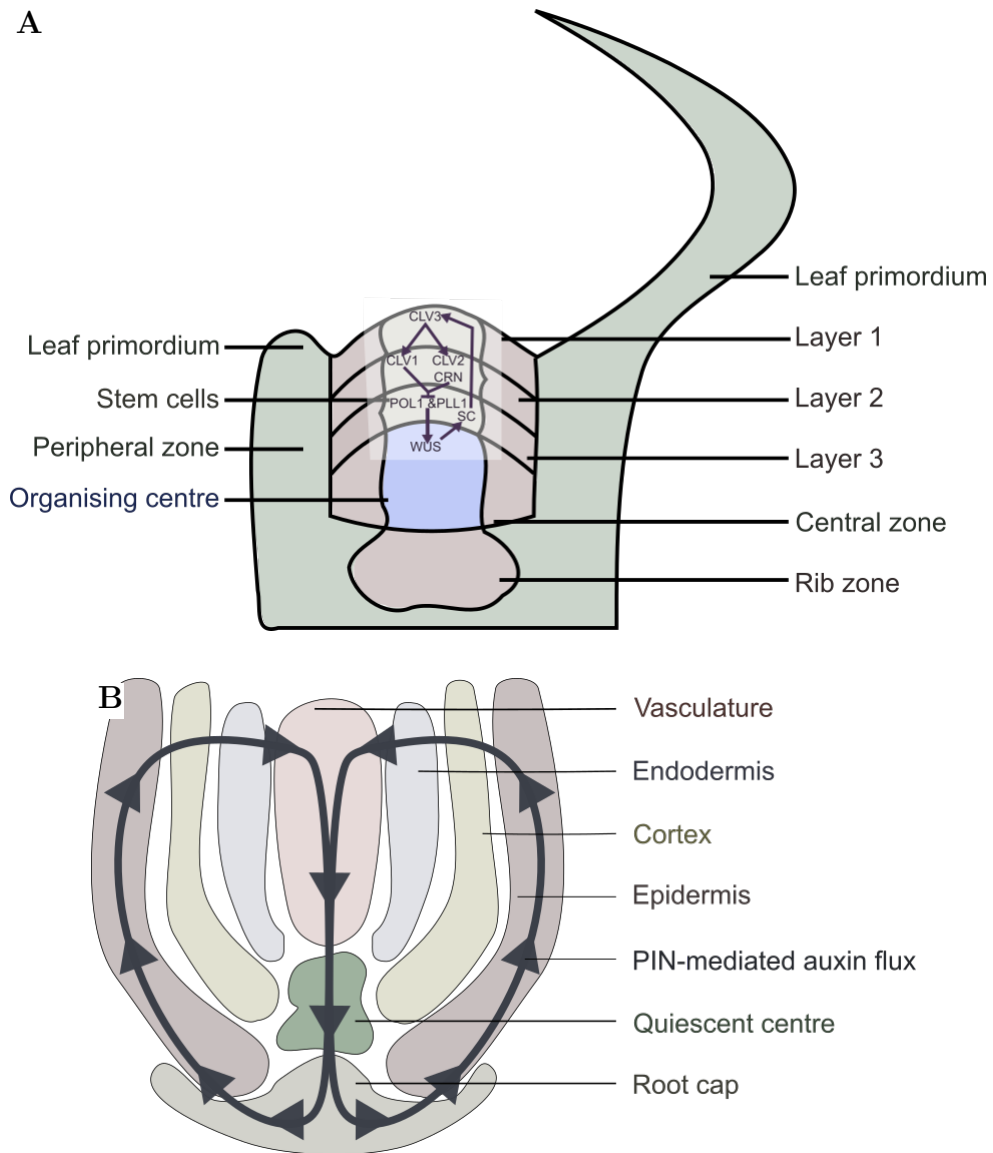


Figure 1.1: Schematic representation of the shoot and root apical meristems
 A: The shoot apical meristem (SAM), including the main zones in the organ, and regulatory proteins involved in meristem control and maintenance in the WUS-CLAVATA feedback loop (superimposed). B: The root apical meristem (RAM) including the main zones in the organ, and the route of PIN-mediated auxin flow (black arrows). Adapted from Öpik & Rolfe (2003)

to the KNOX-ARP transcription factor module, which acts to define the early determination of groups of cells (?). Cell fate is defined by these patterning systems, which lead cells into developmental pathways that ultimately lead to full differentiation and the development of leaves or inflorescences. As such, active SAMs represent tightly controlled stem cell systems: they produce all the cells in a plant in a stable and sustained way and, via the patterning system, dictate the position and fate of organ primordia. Thus, SAMs control the fundamental post embryonic form of the plant.

A similar mechanism operates in the RAM (Friml *et al.* 2002). Figure 1.1B shows the flow of auxin towards the quiescent centre, directed by PIN proteins. In the RAM, the auxin fountain travels through the root cap, epidermis and vasculature, and the auxin maximum maintains the stem cell niche. Although the relative auxin levels have the opposite effect of that seen in the SAM (with an inverted auxin fountain and stem cell maintenance at the auxin maxima), the same molecular toolbox is used to control stem cell niche maintenance in the RAM.

A key aspect of the SAM and RAM's sustained ability to generate new cells is their "stemness" which prevents any overt cell specialisation. In shoots, the development of photosynthesis is a key indicator of differentiation, and cells of the SAM do not show signs of this activity (they are not green and do not contain chloroplasts, Mason *et al.* 2014). This presents a challenge for the plant, since, while being the centre of high metabolic and anabolic activity, meristems lack the ability to generate carbon, energy or reducing power which typifies photosynthetic cells. This means that active meristems must be strong nutrient sinks within the plant; they require a stable external provision of substrate for growth. Simultaneously, by definition the lack of differentiation means they also lack the overt vascular system which the rest of the plant is able to use to redistribute material such as photosynthates (Öpik & Rolfe 2003). This metabolic challenge for an active meristem is one that we will return to later in this thesis.

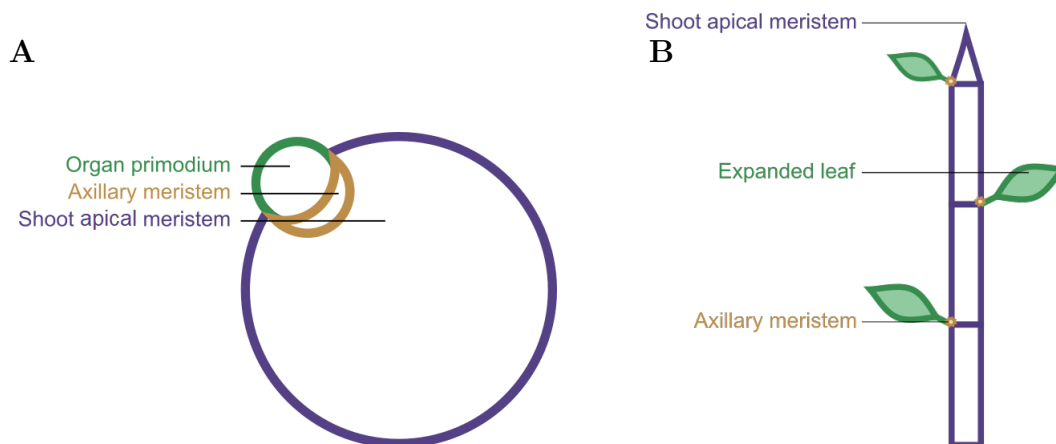


Figure 1.2: Schematic representation of axillary meristem formation

A: an organ primordium developing from the shoot apical meristem. Quiescence is assigned to a pocket of cells adjacent to the meristem. B: the position of axillary meristems once organs have expanded fully. The axillary meristem remains close to the site of organ initiation, whilst the shoot apical meristem grows away. (Öpik & Rolfe 2003)

As well as providing new cells which enter various pathways of differentiation and growth, SAMs also have the ability to lay down new meristems (Janssen *et al.* 2014). These meristems are an important component of the plant's capacity to respond to

environmental conditions (Wang *et al.* 2014). These new meristems are generated at intervals, simultaneously to a new organ primordium. This is shown in Figure 1.2 A. Pockets of stem cells are laid down at the boundary between the apical meristem and the new organ, leading to a meristem in the axil of each fully expanded leaf. This is shown in Figure 1.2 B. On formation these axillary meristems are dormant and it is their coordinated activation and differential growth that generate a mature plant's stereotypical architecture. For example, in plants where the SAM exerts strong apical dominance, the axillary meristems remain suppressed and the plant will develop a columnar, unbranched structure. In contrast, in plants with weaker apical dominance the axillary meristems are activated and start to generate new cells. The growth of these cells (and their progeny) leads to visible branches, thus the plant develops a bushier habit. The suppression-activation status of axillary meristems is to some extent set by the endogenous developmental programme of the plant, but the actual release of axillary meristem potential is often highly influenced by the local environment in which the plant exists (Waldie & Leyser 2018). This fundamental property gives plants their highly plastic response to environmental cues. It is seen above ground (for example in the patterning of branches) and also below ground, where lateral root branch formation and growth is highly influenced by local availability of key nutrients. Roots are often capable of detecting pools of nutrients and proliferating to maximise their exploitation.

At the organ initiation stage, when new axillary meristems form, they tend not to be proliferative. The stem cells are laid down in a quiescent state. Quiescent cells have an arrested cell cycle, yet retain the capacity to initiate proliferation. The cell cycle is a universal phenomenon in eukaryotes, describing the controlled series of events by which DNA is replicated and separated into two new nuclei and, generally, two new daughter cells (Öpik & Rolfe 2003). Variations on this common theme exist, including the capacity for replication of DNA without the formation of new cells (polyploidy) and the ability of cells to exit an active progression through the cell cycle and enter a phase of quiescence. In axillary meristems this quiescent state is thought to be imposed in the G_1 phase prior to DNA replication at S phase (Hartmann *et al.* 2011). This is represented schematically in Figure 1.3. It is thought that these cells only carry out rather basic housekeeping and cell respiration processes, remaining stem-like without dividing. The fact that these groups of quiescent cells are grouped together in relatively accessible and predictable positions in plants (axillary buds) makes them an attractive system to investigate some basic biological processes. As meristem activation can be triggered by cues such as injury or hormonal switches, it is possible to trace the trajectory of processes associated with reactivation *in vivo*. A detailed developmental series can then be investigated following an artificial trigger for quiescence exit. Previous work in this

area has focussed on the activation of axillary meristems along stems of Arabidopsis and tomato, and has led to the characterisation of a complex interaction of hormones (auxin, strigolactones and cytokinins) involved in the release of suppression of axillary buds, as well as various transcription factors (Janssen *et al.* 2014). However the metabolic

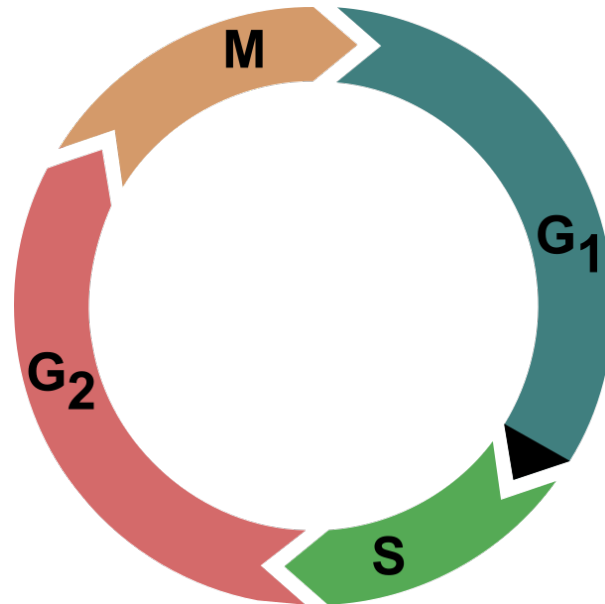


Figure 1.3: Schematic representation of the cell cycle

There are a number of key points in the life of a cell when status is checked (e.g. for DNA damage) before progress can take place. These checkpoints reflect different stages in a cell's life: G_1 and G_2 feature growth, DNA synthesis occurs during S phase, and mitosis takes place during M phase. Quiescent cells usually arrest at the G_1 -S transition, marked in black. Quiescent cells can remain arrested at a checkpoint for prolonged periods of time, yet retain the ability to proceed to cell division. Öpik & Rolfe (2003)

processes that must underpin (and indeed drive) the growth resulting from switching by the established hormonal/transcription factor modules remains under-investigated.

In a study by Liu, *et al.*, proteomic analyses were able to distinguish between dormancy, growth and a transitional state as three separate phases in potato dormancy break, but the metabolic changes linked to these alterations in the proteome are unknown (Liu *et al.* 2014). The ready accessibility of axillary buds (eyes) on potato tubers and the well characterised metabolic events that occur in the tuber during sprouting, such as sweetening, weight loss and increases in respiration, plus its relevance to commercial agriculture, make this an attractive system to investigate this problem.

1.1.1 What is known about bud dormancy and sprouting in potato tubers?

Our basic understanding, gleaned from research in the 1980s posited that potato tuber dormancy has two distinct phases: endodormancy and ecodormancy (sometimes referred to as ecto-dormancy, or simply dormancy where it does not need to be distinguished from endodormancy, Burton 1982). During endodormancy, growth inhibiting compounds are present at high levels and the tuber is unable to respond to any growth promoting environmental cues. Over the course of the storage season, these growth inhibitors are gradually degraded, until the tuber is dormant; by this point it can sprout in response to environmental cues, but only if those cues are present in sufficient strength. Eventually, the levels of growth inhibiting compounds become low enough for dormancy to break and sprouting is guaranteed as long as the potato is viable. Building on this classical understanding, some of the phytohormone dynamics involved in potato dormancy break and sprouting have been identified. These are represented schematically in Figure 1.4 and described below.

It is thought that abscisic acid (ABA) is the main endodormancy promoting hormone; it is observed to decline steadily after harvest (Figure 1.4 A, Campbell *et al.* 2010). In contrast, the plant hormones gibberellic acid (GA) and cytokinin (CK) are associated with dormancy exit and can be thought of as sprouting promoters (Hartmann *et al.* 2011). Specifically, GA appears to contribute to bud growth and elongation, but this is only possible once background CK levels are sufficiently high (Figure 1.4 B, Bromley *et al.* 2014). Free CK availability is modulated by a CK riboside phosphorylase (CKP1). CKP1 interconverts CK from its nucleoside form to the free base form, and hence modulates the plant's ability to perceive it. Other plant hormones, such as brassinosteroids and ethylene are also associated with dormancy, although their role is less clearly elucidated. Both brassinosteroids and ethylene are thought to prolong the period of endodormancy, postponing the time point when tissues become sensitive to dormancy-ending compounds (Figure 1.4 C and D, Aksenova *et al.* 2013). However, the data are somewhat inconsistent, and there is no particularly good evidence of this information being applied successfully to prolonging dormancy in a commercial setting. For example, poor application of ethylene treatment can lead to damaging effects on processing properties (Bethke 2014).

Another way in which potato tubers change during dormancy involves the use of their starch reserves (Davies 1984). As a key part of the potato's overwintering strategy, the tuber contains very large starch deposits to fuel the rapid growth of new shoots once the environment becomes favourable again. This starch undergoes breakdown to release

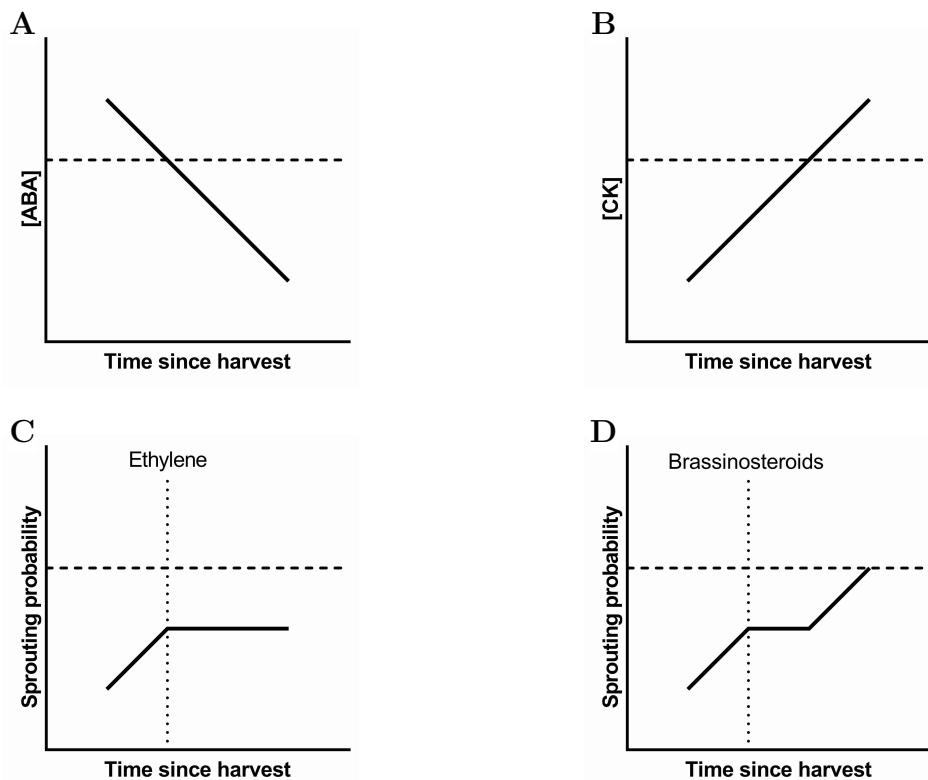


Figure 1.4: Schematic representation of the classical understanding of potato dormancy, integrated with more recent phytohormone data

A: The change in ABA (Abscisic acid) concentration over time since harvest. ABA levels decline steadily, and endodormancy ends once it falls below a critical level. B: The change in cytokinin(CK) concentration over time since harvest. CK levels increase steadily; once they pass a critical threshold, buds become responsive to GA. C: Changes to sprouting probability, over time since harvest, in response to an increase in ethylene. The addition of ethylene is represented by the vertical dotted line. Ethylene can stabilise dormancy, if applied at the correct moment during development. D: Changes to sprouting probability, over time since harvest, in response to increases in brassinosteroids. The addition of brassinosteroids is represented by the vertical dotted line. Brassinosteroids are associated with prolonging dormancy, possibly by promoting quiescence. For all panels, the x axes represent the time since harvest. The dashed horizontal lines represent the threshold for the bud becoming responsive to dormancy ending cues, such as GA (gibberellic acid). Specific references are outlined in the text. The whole system is reviewed in Aksenova *et al.* (2013).

soluble sugars, such as sucrose, as the buds grow to form new plants. In a commercial setting, the relative abundance of sucrose and various reducing sugars has been used as a proxy for tuber activity and depth of dormancy. The main concept underpinning this metric is that the starch reserves in the tuber are mobilised at the point of dormancy break to facilitate sprout growth via the supply of soluble sugars. This has been described as senescent sweetening since the 1960s (Burton 1982). The mobilisation of carbon is associated with amylose activity and it is postulated that this is a key step towards

growth after dormancy break (Huiling *et al.* 2014).

Carbohydrate mobilisation is clearly a key function of the potato tuber. The primary function of this organ is to store reserves for the next growing season. This implies that changes in metabolism are a potentially useful way to understand the stage of dormancy break; the switch from quiescence to growth must involve a change in resource utilisation and transport. However, there are several factors that may cause tuber sugar levels to vary independently of dormancy status, such as cold temperature storage, undermining the generality of reducing sugar concentration as a metric. Whilst sugar mobilisation is certainly necessary for growth, it is not reliably diagnostic of dormancy break. However, a more detailed look at these processes may reveal linked molecular markers that can distinguish between the different sweetening processes. For example, Zhang *et al.* have mined the potato genome for a change in amylase expression in response to cold induced sweetening, and the pattern seems to differ in comparison to sprouting potatoes (Zhang *et al.* 2018). In another study, Herman *et al.* were able to distinguish between low temperature sweetening driven by invertase, and senescent sweetening by phosphorylase (Herman *et al.* 2016). To what extent this metabolic switch is simply a requirement for the process of dormancy break and to what extent it might actually be a driver or key cog in the activation process is discussed below.

1.2 Metabolism and cell division

Most of the work on metabolism potentially being intimately linked to cell division and differentiation has been performed on non-plant systems. A summary of this work is given below, followed by its use as a framework for understanding plant differentiation and the role of metabolism in plant meristems.

Metabolic reconfiguration is an important aspect of cell specialisation, which in turn is an important feature of multicellularity, by which eukaryotic organisms can achieve high levels of complexity and produce sophisticated structures. Cell differentiation allows cells to specialise and act in concert to carry out processes more efficiently than individual cells, allowing organisms to organise cells into tissues that are optimised for a particular function, such as light interception or nutrient uptake. Basic cellular house-keeping processes, such as respiration and DNA repair, are key to all cells, but the process of specialisation involves tailoring metabolism and optimising it for a particular function. This differentiation entails many processes, including gene expression, enzyme activity and nutrient transport changes. In general, it is a unidirectional change, for specialised cells are metabolically constrained and few endogenous conditions will permit the process to be fully reversed. The loss of pluripotency generally involves both a

reduction in the breadth of daughter cell fates and the vigour of cell division.

A moderately well studied system for this is the specialisation of animal embryos, where the switch from proliferating to differentiated status involves an alteration in metabolism (for review, see Shyh-Chang *et al.* 2013). However, substantially more effort has been put into studying the reverse process in mammalian tumours, the development of which involves an aberrant return to a proliferating habit. One recurrent observation from these tumour studies is that these cells differ metabolically from surrounding tissues. In particular, the tricarboxylic acid (TCA) or Krebs cycle and oxidative phosphorylation tend to be replaced by aerobic glycolysis (Vander Heiden *et al.* 2009). There is continuing controversy as to whether this is an emergent property of the switch to proliferation or an integral part of the change.

As early as the 1930s, Warburg proposed that aerobic glycolysis plays a causal role in carcinogenesis. This concept has been revisited recently, in light of progress in our understanding of carcinogenesis (Garber 2004). In particular, it has been observed that proliferating and differentiated cells have different requirements, and it is therefore proposed that they are metabolically optimised differently. Proliferating cells need to replicate their structures rapidly in order to be able to divide. In healthy, differentiated cells, the limiting factor for growth is often energy substrate supply, which is carefully budgeted. In tumour cells, however, this limiting factor is removed due to misregulation of gene expression and metabolism, meaning that it is possible for cells to accumulate matter and extract chemical energy at a fast rate. For these rapidly proliferating cells, it is more advantageous to accumulate monomers for building cell structures as rapidly as possible than to maximise ATP extraction from the substrate. In the absence of a functioning external regulation system, tumours can undertake this rapid turnover of substrates, which is beneficial to individual cells, but has detrimental effects on the energy status of surrounding tissues (Banerjee 2018).

The metabolic status of proliferating tumour cells in eukaryotes has been compared to unicellular systems responding to different environmental conditions (Chen *et al.* 2007). For example, yeast metabolise differently under high stress or high nutrient conditions. Under stressful conditions, respiration is carried out as ATP-efficiently as possible, as the cell's survival is in the balance. On the other hand, under high nutrient conditions, yeast cells become proliferative and carry out fermentation. Glycolysis allows cells to exploit the resources much more rapidly than oxidative phosphorylation, which is advantageous in the short term for multiplication, even though the waste products have a higher energetic value than those of the TCA cycle. Yeast cells are capable of switching between these metabolic modes. Cells that are capable of detecting a pool of nutrients and adjusting their metabolism accordingly have a substantial competitive,

and hence selective advantage in a patchy habitat.

The switch in metabolism seen in such unicellular systems can be used as a simple conceptual model for the conflicting interests of proliferating cells and the multicellular organisms of which they form a part. In more general terms, individual interests are served by rapidly metabolising nutrient sources at the expense of ATP efficiency. This is particularly true when nutrient sources are available; it is advantageous for cells to act as strong sinks and outcompete other cells. In multicellular organisms, regulation usually prevents this, forcing cells into a slower, more ATP-efficient regime. This is of benefit to the entire organism.

Alternative interpretations to the Warburg effect playing a causal role in the development of proliferative capacity have also been proposed. When discussing embryo systems, it has been suggested that mitochondrial number and development status are also involved in the change in metabolism associated with proliferation (Shyh-Chang *et al.* 2013). During early mammalian embryogenesis, there are a number of cell divisions without any net embryo growth before implantation. This means that the cell contents are repeatedly divided without being replenished, leading to cells with small volume and a small number of immature mitochondria (Rahman *et al.* 2013). A preference for aerobic glycolysis under these conditions could be explained by the fact that it takes less time and resource investment to establish a functional glycolysis pathway in the cytoplasm than to produce enough mitochondria with full TCA capacity. However, in oncological studies, there does not seem to be clear evidence of mitochondrial defects being involved in early carcinogenesis. Whilst mitochondrial defects do appear in tumours, they tend to arise much later than detectable changes in metabolism (Vander Heiden *et al.* 2009). Greater clarity is required on the sequence of metabolic events associated with a switch to a proliferative habit to identify the drivers in the process. A better understanding of the order in which metabolic changes appear could be used to understand whether altered mitochondrial properties are causally involved in the switch, or an emergent property. A competing interpretation of these observations could hinge on the fact that mitochondrial processes operating at a lower level lead to a reduction in their rate of development, by means of interrupted positive feedbacks, as opposed to *vice versa*.

Another putative advantage of cytoplasm-based respiratory pathways is that aerobic glycolysis bypasses oxidative phosphorylation. This process is involved in ATP synthesis, using the products of the TCA cycle in an electron transport chain, leading to ATP synthase. Oxidative phosphorylation can produce Reactive oxygen species (ROS), which are particularly deleterious in the context of DNA replication before cell division. The exclusion of the mitochondrial steps of cell respiration may thus protect proliferating cell

lineages from accumulating excessive DNA damage. Limiting ROS exposure could be part of the DNA protection mechanism in stem cells (Rahman *et al.* 2013).

From the above summary, it is clear that in mammalian and microbial research there has been extensive interest in exploring the concept that rapidly dividing cells may benefit from or require an altered oxidative metabolism compared to non-dividing cells (which have generally formed the “norm” for classical biochemical analysis). The transfer of these oncological concepts into plant biology has been extremely limited so far, despite the availability of the relatively accessible and well characterised meristem systems described above (see section 1.1). However, there is emerging evidence that the TCA cycle varies, in terms of dominance over nutrient flows in the cell, in response to changes in cell status (Zhang *et al.* 2018). For example, heterotrophic plant cells are much more likely to carry out the full, conventional TCA cycle for efficient ATP synthesis, compared to photosynthesising tissues (for review, see Sweetlove *et al.* 2010).

The identification of some TCA changes in different plant tissues bodes well for the application of some of the animal approaches and metabolic ideas to the study of axillary meristems. From a technical point of view, a major challenge is that meristems are relatively small, so the use of conventional biochemical techniques is very difficult. However, continued advances in mass spectrometry have opened the door to comparing the metabolic profiles of quiescent, proliferative and transitioning tissue samples. These advances are described in the next section.

1.3 Mass spectrometry

There have been recent technological innovations that make it tractable to apply a metabolomics approach to the question of meristem quiescence (for review see Heyman & Dubery 2015). For a long time, studying the biochemistry of meristems was extremely laborious. For example, cytohistology studies of shoot apical meristem development in plants relied on histochemistry, which tended to be highly targeted for particular substrates with known colour development protocols, meaning analysis proceeded on a metabolite-by-metabolite basis. Often these involved complex enzyme series, at a time when purified enzymes were not readily available. Another major limitation of these approaches is that they are too specific to permit a non-targeted scan, capturing a wide range of molecules. For example, Fosket and Miksche visualised three metabolites by staining them individually on separate tissue sections (acid phosphatase, protein-bound sulfhydryl and succinic dehydrogenase - Fosket & Miksche 1966). In spite of the labour involved, these classical approaches have continued to be applied; with Kerk and Feldman using immunolocalisation to study the formation of the quiescent centre in the root apical

meristem in response to ascorbate oxidase (Kerk & Feldman 1995). A major limitation here is that immunolocalisation involves raising antibodies against desired antigens in a mammal, then producing them by cell culture, limiting the scale of different molecules that can be analysed. Whilst this study was informative, potentially linking ascorbate oxidase to cell cycle arrest at the G_1 to S transition, this information could not be integrated into the context of a larger metabolic network at the time.

Recent technological innovations, particularly advances in mass spectrometry, could help to vastly improve our understanding of axillary meristems and their metabolism (Lee *et al.* 2012). Mass spectrometry is a technique used to analyse the relative abundance of ions in a sample. Analysis involves ionising sample molecules and accelerating these ions across an electromagnetic field. Differences in time of flight assort ions by their mass/charge ratio, producing a profile of the relative abundance of different moieties in a sample. This spectrum can be used to identify and discriminate between molecules to a very high mass resolution and capture related ions that differ because of post-translational modifications. Current mass spectrometers are highly sensitive, making them suitable for detecting differences in concentration on a biologically relevant scale. These innovations lend mass spectrometry the power to accurately analyse samples as small as dormant meristems.

In later chapters, mass spectrometry is used to track changes in the abundance of organic acids at intervals along a developmental series, responding to a quiescence-ending trigger. The sensitivity is great enough to detect changes in the pools of intermediates associated with enzyme-catalysed cycles, which fluctuate at the very low concentrations associated with biological systems. This allows the progress of *in vivo* reactions to be monitored at intervals. This developmental metabolomics approach is used in this thesis to elucidate metabolic changes linked to growth responses.

One of the most exciting innovations in the field of biological mass spectrometry has been the development of mass spectrometry imaging (MS-I, Horn *et al.* 2012). The most established method uses the MALDI platform (Matrix Assisted Laser Desorption/Ionization, illustrated schematically in Figure 1.5), but other ionisation systems operate on similar principles. MALDI imaging involves taking readings from a tissue sample mounted on a moving stage (Figure 1.5 A). Metabolic profiles are generated for each point on a grid (Figure 1.5 B); individual masses can be extracted from the dataset and plotted at their coordinates on a colour intensity scale (Figure 1.5 C). These metabolite heat maps provide information on the spatial distribution of a metabolite and co-occurring moieties. This imaging can achieve a spatial accuracy of $10\mu\text{m}$ and be used to visualise differences in the composition of individual cells *in situ*. Another, related MS-I system is Desorption Electro-Spray Ionization (DESI, Figure 1.6, Tata *et al.* 2014).

DESI uses some of the same principles as MALDI, including a moving stage, but uses a solvent spray to ionise molecules. Whilst less established than MALDI imaging, DESI seems promising for the highly soluble molecules discussed in chapters 3 and 4. Both of these ionising heads can be coupled to extremely sensitive spectrometers, maintaining the extraordinarily robust mass identification discussed above.

However, there are caveats associated with a metabolomics approach to be considered. One limitation of mass spectrometry is that it tends to be a descriptive technology. Whilst it is possible to generate very large datasets and identify discriminant data points, this does not provide much biological insight on its own. The data need to be integrated into a biological understanding of the processes taking place in the tissue and the role the key masses are thought to play in these. The challenge of mass spectrometry is deriving meaning from the technique's substantial output. Integrating the data generated into the context of the literature reviewed here is essential for this technology to be informative.

In summary, advanced mass spectrometry provides a tool to begin to investigate the metabolic processes linked to the exit from quiescence to active growth in axillary buds following exit from dormancy, yet its application in this context has been limited. A previous study utilised these mass spectrometry innovations to examine metabolic processes in tomato axillary meristems (Steels 2012), thus providing the foundation for the analysis of potato tuber buds. The relevance of this experimental system in agronomy is described in the following section.

1.4 The agronomic relevance of potato sprouting

The control of axillary meristem activity is of particular agricultural importance in the case of the potato. As indicated earlier, tubers form as swollen underground stems, with shortened internodes and radial expansion, and each tuber possesses several meristems within small buds (often referred to as eyes), which are developmentally defined as axillary meristems. When formed, these axillary meristems are quiescent and cannot be activated. However, these meristems gradually become capable of reactivation after a period of time, at which point they become responsive to several environmental cues (see Aksenova *et al.* 2013 for review). Activation of the axillary meristems is key to sprouting, which leads to loss of tuber integrity and, essentially, wastage from a commercial point of view.

The potato industry is hugely important to the United Kingdom. According to the FAO the UK produced over 5.4 million tonnes of potatoes in 2016, including 270 thousand tonnes for the export market, mainly in the form of seed potatoes. It is the UK's most important non-cereal crop. The country is reliably over 80% self-sufficient

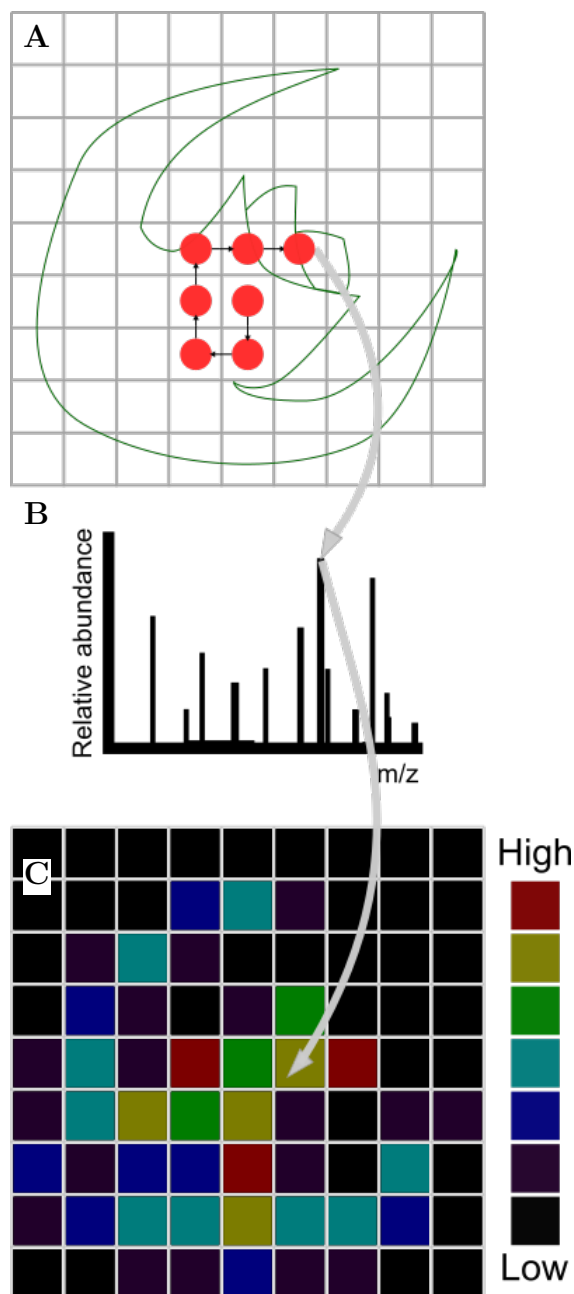


Figure 1.5: Schematic representation of MALDI imaging

A: A schematic illustration of the MALDI laser firing pattern on a tissue section, represented by red circles. B: Each time the MALDI laser fires on a point on the tissue, shown in A, a full mass spectrum is collected by TOF-MS. C: An individual m/z bin, representing a moiety, can be extracted from all the mass spectra like B and mapped on a colour intensity scale, linked to the positional information from A. This creates a heat map for ion distribution in a sample.

in this crop (2016 imports represented 3.5% of consumed potatoes) and it is one of the staple components of the national diet (FAO 2017). In addition to contributing to fresh and processed food, it can be used in industrial products such as adhesives and

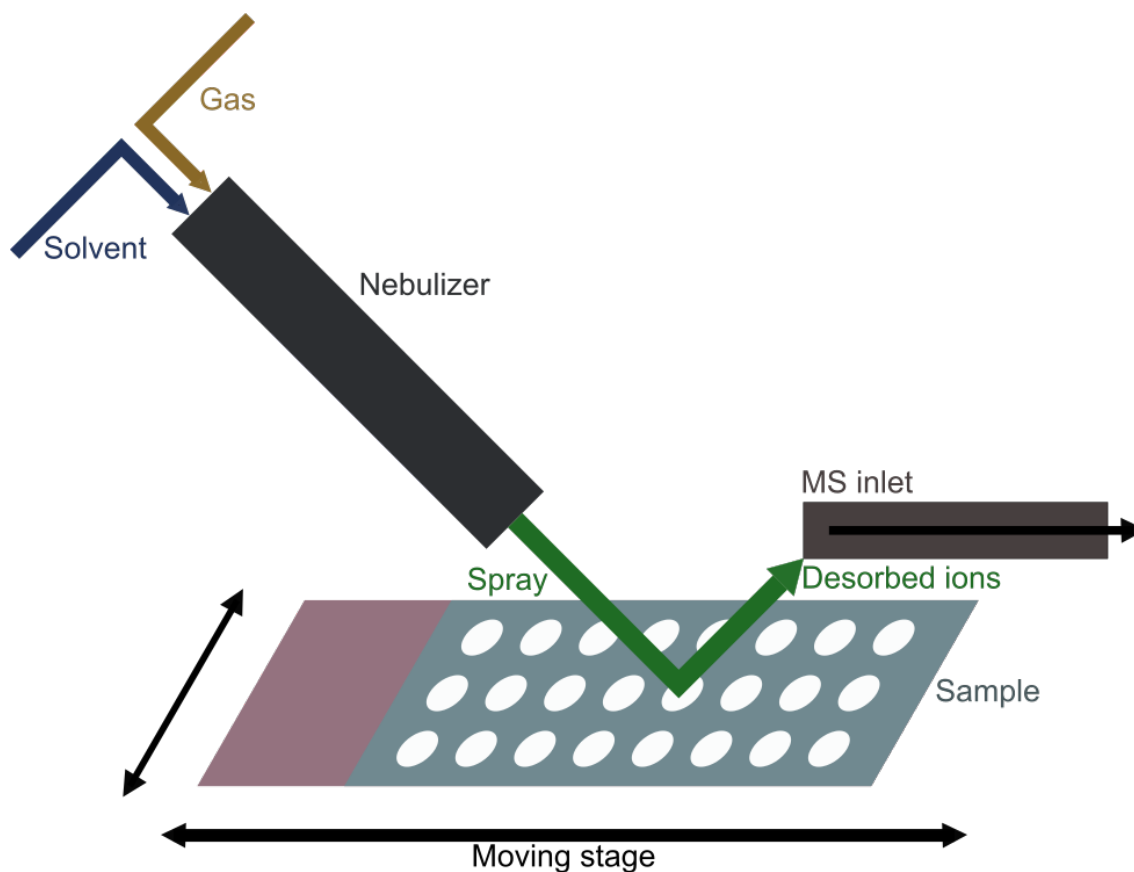


Figure 1.6: Schematic representation of the the DESI ionisation system

Our Desorption Electro-Spray Ionization (DESI) platform mixes a solvent flow with N_2 gas to create a spray. This desorbs ions for analysis. The moving stage allows mass spectra to be linked to positional information, making it possible to visualise the distribution of moieties in a tissue section.

biodegradable plastic replacements. This latter example is not currently a particularly large use of potato in the UK, but interest is growing.

The storage of this important food crop can be problematic. If potatoes sprout in storage, they are no longer fit for human consumption or for processing. This sprouting is associated with sugar mobilisation, softening and rapid respiration, all of which negatively affect nutritional and processing properties. The probability of sprouting depends on length of time in storage, chemical treatment and variety. However, perturbations in the field and in storage, such as drought or disease outbreaks, can also promote premature dormancy break. Cold storage (approximately 3°C) promotes potato sweetening, which has negative effects on processing properties, meaning it is not a practical solution (Herman *et al.* 2016). From a broader perspective, the environmental penalties associated with potato production are substantially higher if waste at the end of the production chain is extensive.

Potato storage is more challenging than that of cereals, because the nature of tubers makes them fundamentally different from seeds (Matsuura-Endo *et al.* 2006). The tuber tissue is of uniform ploidy (tetraploid), entirely maternal and never desiccated. The control of tubers and dormancy maintenance is therefore very different from that of seeds. Tubers continue to contain relatively high levels of water and metabolise moderately throughout dormancy, meaning that different cues are involved in release. There are also fewer pressures for multi-season dormancy, as potato tubers do not generate a seed bank.

Prolonging potato dormancy is highly desirable, because of the problems associated with late dormancy and dormancy break and their impact on processing quality. One of the ways in which potato quality can be compromised is with an increase in acrylamide risk (Mottram & Dodson 2002). Acrylamide formation potential is a function of sugar availability for a given background level of suitable amino acids, in particular asparagine, and available water (Muttucumaru *et al.* 2016). Acrylamide forms via the Maillard reaction between reducing sugars and asparagine, with the reaction occurring at cooking temperatures in the presence of water. It is believed that acrylamide is potentially a high risk carcinogen in humans, in part due to high levels of dietary exposure (Tareke *et al.* 2002). Potato is particularly vulnerable to acrylamide formation, due to its amino acid composition, tissue water status and the scale of consumption. Acrylamide risk is potentially promoted by several storage factors, including cold, hormonal activity, irradiation and sprouting, further limiting the use of otherwise obvious refrigeration-based storage mechanisms.

Recently, there have been efforts to reduce the acrylamide risk in potatoes by genetically modifying them so that less asparagine is synthesised. In 2014, J. R. Simplot company achieved USDA approval for the cultivation of the Innate low asparagine tubers, and are now in the process of bringing the second generation to market (Simplot 2018). However, the European Union (EU) maintains a low level of cultural acceptance of this kind of technology, meaning that uptake in the UK is unlikely. Furthermore, there are other negative processing effects of potato sweetening that would not be resolved by low asparagine levels, so studies into improving storage and understanding of dormancy remain pertinent. Potato processors currently use sugar levels as the basis of consumer rejection of potato batches, with associated waste and cost. By generating better predictive markers, sprouting-vulnerable tubers could be identified earlier or more reliably, leading to a prioritisation of their use to reduce potential waste and cost to the industry.

Currently, most potato tubers are treated with Chlorpropham (CIPC) in storage to delay bud break (Kleinkopf *et al.* 2003). CIPC does not target dormancy directly, rather it is a mitotic inhibitor, leading to incorrect chromosome sorting during cell division

(Vaughn & Lehen 1991). This loss of cell division capacity means that the sprouting process cannot occur. This mechanism of CIPC action has led to some concerns pertaining to its large scale use, since it is thought to have carcinogenic potential and there is some evidence of endocrine disruptive activity in mammals (Orton *et al.* 2011 and Nakagawa *et al.* 2004). It is also considered to be a potential threat to aquatic ecosystems and occupationally exposed users (Passananti *et al.* 2014).

This evidence of CIPC toxicity is particularly problematic for the potato industry, as the EU is displaying a shift in the policies underpinning its regulatory framework. The use of a threat based regulatory principle is increasingly common, as opposed to hazard-based frameworks. This makes increased regulation of CIPC likely, leading to the effectiveness of application procedures being compromised. In the case of potato sprouting, the safety margin for successful inhibition has already been eroded substantially by regulation (Paul *et al.* 2016). Therefore, more severe regulation could eliminate CIPC as an effective future treatment for sprouting. Although CIPC alternatives are beginning to be commercialised, none of these strategies replicates the original efficacy of CIPC. In many cases the new tools need to operate together to prevent sprouting (Huang *et al.* 2014). Improving fundamental knowledge of the metabolic events in buds during sprouting could inform new approaches or identify targets for the development of new suppressors.

In view of these regulatory hurdles, it would be highly beneficial to understand the endogenous process of dormancy break and sprouting better. Much of the sophisticated previous work has focussed on hormones and aspects of whole tuber biochemistry. In the near future, these studies are likely to harness the publicly available genome (Potato Genome Sequencing Consortium 2011). Much less attention has been paid to the role of the axillary bud containing the quiescent meristem. However, from a developmental point of view the activity or signalling from these small pieces of tissue is likely to play a key role in regulating the process of sprouting, from initial dormancy release to the overall regulation of storage material breakdown as metabolites are mobilised from the tuber to the activated bud. The new ideas and evidence from the fields of oncology and microbial metabolomics, coupled with the technological advances occurring in metabolite analysis and metabolite imaging, make the potato tuber an intriguing system to provide a deeper understanding of fundamental biology (meristem activity) and to address a key agronomic challenge (potato sprouting).

1.5 Summary

Recent technological innovations coupled with advances in our understanding of the potential role of metabolism in cell and developmental biology provide a novel approach to understanding potato dormancy and sprouting. The aim of this study is to use axillary meristems on the surface of potato tubers as a model system to characterise the metabolic changes that occur as quiescent cell populations re-enter proliferation after a phase of dormancy. This will provide both a new insight into a fundamental aspect of plant biology and a potential route to improving post-harvest crop storage.

1.5.1 Objectives

- Core science: Elucidate the metabolic changes associated with the switch from quiescence to a proliferation and growth in potato tuber axillary meristems. By identifying the pathways represented by these metabolite patterns, gain a functional understanding of the metabolic events involved in dormancy release and sprouting.
- Industry: As a result of the above, identify metabolic pathways that could be used to diagnose dormancy break before tuber quality is compromised, decreasing waste. The identification of particular pathways may also reveal novel targets for new sprouting suppressor development for commercial application.

1.5.2 Hypotheses

- Meristems undergoing release from dormancy to sprouting display a stereotypical trajectory of metabolic change.
- Different metabolic profiles can be used to distinguish meristems at different stages of dormancy release. Once the trajectory associated with the metabolic change has been elucidated, it will be possible to identify where a sample representing a snapshot in the dormancy break process fits into the sequence of metabolic changes.
- Analysis of the trajectory of metabolic change will inform on the underlying molecular basis of dormancy release.
- Dormancy release and sprouting involve altered spatial patterns of metabolites around and within the axillary meristem, linked to the metabolic pathways underpinning the process.

1.5.3 Approach

- Set up in vitro system for analysing release of potato tuber meristems from dormancy, based on Hartmann *et al.* 2011.
- Use the in vitro system to characterise metabolic profiles by carrying out mass spectrometry of meristems and their surrounding tissue in a series representing different stages of dormancy release.
- Compare the responses of molecular markers to dormancy release in different cultivars in order to test the universality of findings. A partial pedigree of the cultivars studied can be found in Figure A.1 on page 168.
- Interrogate the data to identify potential metabolic pathways involved in the release or maintenance of quiescent cell status, relating individual metabolites to the literature.
- Use MS imaging to characterise local changes in metabolism occurring during dormancy release. This will make it possible to link metabolism to stem cell status and highlight any spatial organisation and local transport.

Chapter 2

Metabolic profiles in tuber buds during the release from dormancy

2.1 Introduction

This chapter reports changes in metabolic profiles associated with potato dormancy break, in particular, examining dormancy release at the bud level. A key innovation is the application of mass spectrometry techniques to these extremely small (less than 1mm) features on the potato tuber. Innovations in instrument versatility and sensitivity mean that developmental metabolomics is now sophisticated enough to examine these features (for review, see Heyman & Dubery 2015). A single 3 minute analysis of a 10mg sample can detect 2'500 masses in a 750Da window. The power of these instruments lends itself to the untargeted analysis of very small plant organs.

The metabolomics approach used in this chapter is predicated on the idea that these structures contain quiescent meristem complexes, similar to those found in leaf axils. It is postulated that the switch from meristem quiescence to actively proliferating involves metabolic configuration, and metabolic changes are key to these buds' capacity to change their function. In many ways, these potato tuber buds are comparable to axillary meristems in the aerial parts of related plants, such as those examined by Steels (2012).

A crucial additional element in potatoes is endodormancy. The process of dormancy break is not fully understood but involves a concerted interaction of genetic and environmental factors, mediated by hormonal signalling (for review, see Aksenova *et al.* 2013). It is a core part of the plant's overwintering strategy. In the wild, the aerial parts of the plant die back and do not regrow until winter has passed and conditions are favourable. In an agricultural context, tubers are deeply dormant at harvest (endodormancy) and not responsive to external growth promoting stimuli and sprouting probability is low.

During endodormancy, changes required for sprouting proceed gradually. After endodormancy is complete, buds become primed and are responsive to a narrow range of stimuli, including the phytohormone GA and factors such as light and temperature (Peterson *et al.* 1985). At later points in dormancy, sprouting is effectively guaranteed; buds are very responsive to environmental changes. This is illustrated schematically in Figure 2.1 on page 22. The exact length of dormancy is influenced by genetic factors, varying substantially by cultivar. Perturbations, both in the field and in storage, may radically reduce the expected dormancy length. Dormancy can be artificially prolonged using the sprouting inhibitor CIPC, but this mechanism is independent of meristem reactivation; it perturbs cell division, blocking continued growth (Vaughn & Lehen 1991).

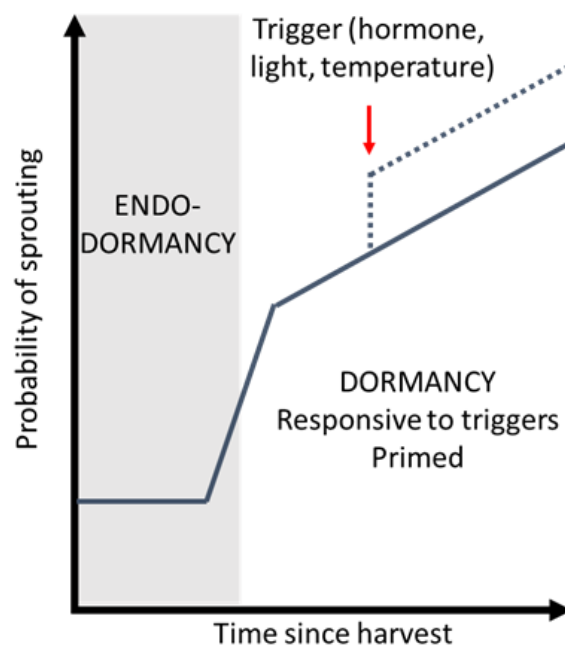


Figure 2.1: Schematic representation of potato dormancy.

At harvest, sprouting probability is low. It increases gradually during endodormancy. Sprouting probability increases rapidly once tubers are primed and responsive to external stimuli. After endodormancy is complete, buds become responsive to a narrow range of stimuli, including the phytohormone GA. The sprouting probability continues to increase, until the tuber is highly susceptible to a wide range of factors, such as light and temperature. The length of endodormancy and sprouting probability absolute values are cultivar- and season-dependent.

Current understanding of endodormancy points towards two contrasting hormonal signals. ABA inhibits sprouting and is abundant in freshly harvested tubers, declining during storage. CK, on the other hand, is found at low levels after harvest, increasing steadily during storage. Once the relative levels of these hormones pass a threshold, the tuber becomes responsive to growth promoters such as GA (Hartmann *et al.* 2011).

However, these whole tuber dynamics do not capture the changes at the meristem level. Quiescent axillary meristems are typically arrested at the G₁-S phase transition of the cell cycle (Öpik & Rolfe 2003). As the quiescent cells in the tuber buds regain the competence to proliferate, their metabolism changes. The change in cell function has huge implications for their energetic status. The meristems use tuber nutrient reserves to generate new aerial plant tissue. Rapid cell division and contents replication requires a very different kind of metabolic strategy, compared to quiescence. This implies that there should be changes to the meristem leading up to a visible change in bud size.

Throughout this chapter the concept of a metabolic switch being core to sprouting is corroborated by examining the internal anatomy of tuber buds, then characterising their metabolic responses to growth promoters in a detailed development series. Markers from these experiments are compared to samples at various points in storage and across a range of cultivars. I predict that this metabolic switch involves a stereotypical set of changes, yielding markers for staging tubers and predicting sprouting behaviour. The identity of these markers and their associated biochemistry are explored in later chapters.

2.1.1 Hypotheses

- Tubers undergoing dormancy release display a set of stereotypical changes to their metabolic profiles.
- Different metabolic profiles can be used to distinguish tuber buds at different stages of dormancy release.
- The markers in the metabolic profiles are independent of cultivar and the type of dormancy ending signal.

2.2 Materials and Methods

2.2.1 Plant Material

Solanum tuberosum tubers of cv. King Edward, Desiree, Maris Piper and Russet Burbank were grown in the field under commercial conditions (Yorkshire, United Kingdom) during the seasons 2014-2017 and supplied by Glynn Harper (Agriculture and Horticulture Development Board, Sutton Bridge). *Solanum tuberosum* tubers of cv. King Edward were grown at the Arthur Willis Environment Centre (AWEC). Original seed potatoes were purchased from Suttons Consumer Products Limited. After the first season, potatoes were propagated from spare samples. Seed potatoes were planted in 15L

pots in M3 compost. They were irrigated by hand and grown under a 12hr light regime at 20°C during the day and 12°C during the night. Illumination was ambient light and supplementary light (200flux at bench level) if the ambient fell below 1000flux. Tubers were collected once the plants senesced.

2.2.2 Potato Growing Conditions

Solanum tuberosum tubers of cv. King Edward, Desiree, Maris Piper and Russet Burbank were grown in the field (Yorkshire, UK) during the seasons 2014-2017. After harvest they were stored at Sutton Bridge Crop Storage Research in their controlled environments. After cooling, they were kept in 1 tonne boxes in the dark at 4°C before transport to TUoS at regular intervals (as indicated in the relevant Results sections).

Solanum tuberosum tubers of cv. King Edward were grown at AWEC. Tubers were planted in 15L pots with M3 compost and grown in the greenhouse. The photoperiod was 12 hours of ambient light with supplementary light (200flux at bench level) if the ambient falls below 1000flux. Daytime temperature was 20°C and nighttime temperature 12°C. The plants were hand irrigated and harvested after 12 weeks (once the canopy started to die back). After harvest, tubers were stored in the dark at 7°C, in paper bags.

2.2.3 Assays of sprouting potential

A GA treatment based on Hartmann *et al.* (2011) was used to characterise the dormancy status of stored tubers and produce staged samples for metabolic analysis. Samples were prepared by removing the apical primordium from a tuber with a #4 Korkborer (8mm diameter), slicing it to a height of 5mm with a razor blade and placing it in a 48-well plate (Thermo Scientific, 11mm diameter). The primordium-containing potato discs were surface sterilised by submerging them in excess 50% bleach for 15 minutes. After surface sterilisation, tuber discs are transferred to wells containing sterile filtered buffer in the lamina flow hood (buffer contains 20mM MES, 300mM D-mannitol, 5mM ascorbic acid, pH 6.5). The buffer was filtered using a 0.45µm pore syringe filter. The tuber discs were washed by transferring them into a new well of buffer every 15 minutes, 3 times. Samples were treated by submersion in excess 0.45µm-filtered 50µM GA or control (filtered water) for 5 minutes. Treated potato discs were placed on moist filter paper in 12-well plates (Thermo Scientific, 25mm diameter), sealed, and wrapped in aluminium foil. The multiwell plates were kept in a growth cabinet at 22°C. Potato discs were observed daily and their sprouting phenotype scored as follows: no change, swollen bud, some growth (≤ 1 mm) and growth (> 1 mm). Preliminary analysis compared control and treated discs for 7 days. Early data suggested that during the first 4 days

after treatment there was no visible effect. Primordia were dissected out of the potato discs at 0, 1, 2 and 3 days after treatment and frozen for metabolite analysis. Concentric cores (16mm diameter) of the apical primordium were taken at the same time as the GA treatment and frozen. These were stored at -80°C for later sugar analysis. A limitation of my preliminary use of the Hartmann *in vitro* was contamination and rotting in the multiwell plates. All the solutions used were filtered and used inside the flow hood, so the issue was ascribed to the tubers themselves. In order to reduce the frequency of sample decay, a surface sterilisation step was introduced to the process.

Surface sterilisation involves immersion in a bleach solution. A range of bleach concentrations were trialled to identify optimal cleaning effects without damaging the meristems. This involved 15 minute surface sterilisation with bleach before buffer wash and treatment. Three bleach concentrations were used: 10, 25 and 50% v/v in water. After 7 days, GA-treated samples had an average sprouting level of 0.75 at 50% bleach, compared to 0.15 at 10% bleach. 50% bleach was also the only concentration that yielded enough sample survival to differentiate between GA and control samples. 50% bleach was used in all subsequent experiments (Data not shown). All reagents were purchased from Sigma Aldrich, unless otherwise specified.

2.2.4 Histology and microscopy

Tuber buds at various stages of sprouting were embedded in Technovit 7100 resin (TAAB Laboratories Equipment Ltd), sectioned, stained and visualised using light microscopy, as described below.

Small (less than 5x5 mm) samples containing the apical bud were collected in Eppendorf and dehydrated in an ethanol series by vacuum infiltrating them in excess 10%, 30% and 50% ethanol (v/v) for 20 minutes at each concentration at room temperature. The samples were vacuum infiltrated in formalin fixative (50:5:10:35 ethanol:glacial acetic acid:37% formaldehyde:water v/v/v/v) for 30 minutes, then sealed and kept at room temperature for at least 16 hours.

The formalin fixative was replaced with 100% ethanol and vacuum infiltrated for 30 minutes, then sealed and kept at room temperature for at least 16 hours. The ethanol was replaced with 1:1 Technovit liquid 1:ethanol (100%) v/v and vacuum infiltrated for 30 minutes, then sealed and refrigerated (4°C) for at least 16 hours. The Technovit 1-ethanol was replaced with 100% Technovit liquid 1 and vacuum infiltrated for 30 minutes, then sealed and refrigerated (4°C) for at least 16 hours. The Technovit liquid 1 was replaced with Technovit liquid 1 with hardener powder (1 g per 100ml) and vacuum infiltrated for 30 minutes, then sealed and refrigerated

(4°C) for at least 72 hours.

Samples were embedded in histoform moulds (volume 1ml) or Eppendorf caps (volume circa 300 μ l). The embedding resin was produced by mixing Technovit liquid 1 (with hardener powder - 1g per 100ml) and Technovit hardener liquid 2 (15:1 v/v). Samples could be adjusted with forceps for 7-10 minutes after mixing, followed by incubation at 37°C for 1 hour.

Samples were mounted on blocks using Technovit 3040 resin. The mounting blocks were given a smooth surface by placing them face down on aluminium foil and filling them with Technovit 3040 resin (1.5ml yellow powder:0.5ml Technovit 3040 liquid v/v) and allowing them to set for 30 minutes. Embedded samples were attached to the mounting blocks using the same Technovit 3040 resin and allowed to set for 1 hour. Samples in histoform moulds were attached to the blocks before removal, then levered out once the resin dried.

Embedded samples were sectioned using Leica RM 2245 microtome to a thickness of 12 μ m. Sections were transferred with forceps and floated on a drop of water on a slide. Slides were dried on a hot plate at 65°C. Sections were stained with Toluidine Blue O (0.1% w/v in 100mM pH7.0 phosphate buffer - K₂HPO₄, KH₂PO₄). Toluidine Blue O (TBO) was incubated for 1 minute at 65°C, rinsed twice with water at room temperature and dried on the 65°C hotplate. Slides were imaged using an Olympus BX51 microscope at 4x magnification and captured using an Olympus DP71 camera and Cell-A software.

Potato tuber buds were also imaged using the Hitachi Tabletop Scanning Electron Microscope TM3030 and TM3030Plus software. Small (<5mm) pieces of fresh tuber were excised and mounted using OCT (Optimal cutting temperature compound, Sigma Aldrich). The sample was placed in the imaging vacuum and cooled to -20°C. The images were collected in standard mode with a voltage of 15kV and a magnification of 80-100x. Analysed samples came from the in house tuber growing and storage system described in 2.2.2. Tubers were either sampled directly or after *in vitro* treatment according to 2.2.3. All solvents were HPLC grade purchased from ThermoFisher, unless otherwise specified.

2.2.5 Methanol-Chloroform extractions

Potato buds' metabolites were extracted using the methanol-chloroform method (Walker 2013). LC-MS grade solvents and distilled, deionised water were used throughout. Samples were kept on ice and a refrigerated centrifuge at 4°C was used throughout. Two mixes of solvents were used: Solvent A (MeOH:CHCl₃:H₂O - 2.5:1:1 - v/v/v) and solvent

Table 2.1: Methanol-Chloroform extraction solvents

| Solvent Name | Composition (solvents) | Ratios (v, v/v or v/v/v) | μl solvent per mg tissue |
|--------------|--|--------------------------|-------------------------------------|
| A | MeOH:CHCl ₃ :H ₂ O | 2.5:1:1 | 10 |
| B | MeOH:CHCl ₃ | 1:1 | 5 |
| C | H ₂ O | 1 | 3.5 |
| D | CHCl ₃ | 1 | 2 |

B (MeOH:CHCl₃ - 1:1 - v/v) and these were scaled to match the sample fresh weight. This is summarised in Table 2.1 on page 27. The quantities quoted refer to 1mg of tissue.

10 μl of pre-chilled solvent mixture A was added to the potato bud sample, excised using a scalpel from the apical region of a tuber, and collected in a 1.5ml Eppendorf tube. A 3mm steel ball bearing (Ital Ball) was added to each tube. These were shaken in the fastprep (MP Biomedicals) for 40 seconds at 4.0m.s⁻¹ to grind the tissue. The ground samples were vortexed for 10 seconds and left on ice for 5 minutes.

Samples were then vortexed for 10 seconds and centrifuged at 14'000rpm and 4°C for 2 minutes. The supernatant was transferred into a pre-chilled storage tube. The pellet was re-extracted with 5 μl of pre-chilled solvent mixture B, then vortexed for 10 seconds and kept on ice for 10 minutes. Samples were vortexed for 10 seconds and centrifuged at 14'000rpm and 4°C for 2 minutes. The supernatant was transferred into the same pre-chilled storage tube and supernatant A.

The aqueous and organic phases of the supernatant mix were separated by adding 3.5 μl chilled, distilled, deionised water and 2 μl chloroform per mg of tissue in the sample. Supernatant mixes were vortexed for 10 seconds and centrifuged at 14'000rpm and 4°C for 15 minutes. The aqueous phase was pipetted into a separate tube, vortexed for 10 seconds and centrifuged at 14'000rpm and 4°C for 2 minutes. 2 μl of the aqueous phase was added to 198 μl of Methanol to produce diluted samples for analysis. Extracts were stored at -20°C before analysis, or -80°C for long term (more than 2 weeks) storage. Thawed extracts were vortexed for 10 seconds and centrifuged at 14'000rpm and 4°C for 2 minutes before pipetting them into the autosampler analysis vials.

The repeated centrifugation steps were particularly important in this process, because starch does not precipitate and form a good pellet in this solvent combination. The samples from the methanol-chloroform extraction process are analysed by mass

spectrometry, and early experiments had problems with blocked tubes hampering analysis. By repeatedly cleaning the sample through centrifugation, the risk of starch granules blocking the capillary tubes is reduced.

All solvents were LC grade purchased from Sigma Aldrich, unless otherwise specified. The Chloroform was from ThermoFisher.

2.2.6 ESI-TOF-MS

Metabolite extracts were analysed using a QSTAR - an electrospray ionisation - time of flight - mass spectrometer. 75 μ l samples were injected using a 1090 UPLC autosampler with an in-line 0.5 μ m pore KrudKatcher Classic filter (Phenomenex), and flow rate of 10 μ l.min⁻¹. The autosampler ran 90% methanol (v/v) between samples, including a 15 minute backwash to waste programme.

Spectral data were collected in negative ionisation mode with a mass window of 50-850Da and scan rate of 1 per second. A malate standard solution (10 μ g.ml⁻¹ w/v) was analysed before, after every tenth sample and at the end of every batch run, to corroborate calibration and sensitivity. Technical replicates were obtained by treating the long sample runs as 3 separate sets of 60 scans.

2.2.7 Data analysis

For each biological replicate, centroided scans were summed over 1-minute segments, producing 3 technical replicates. Data were simplified through binning, using an in-house macro first described by Overy *et al.* (2005), combining recorded mass measurements to an accuracy of ± 0.1 Da. Noise reduction was achieved by only including masses that appeared in all 3 technical replicates in subsequent analysis. Subsequent analysis used average percentage ion intensities to normalise differences between samples.

Percentage ion counts and binned m/z values were imported into Simca-P+ (14.1) for multivariate analysis, in accordance with Eriksson *et al.* (2006). Analysis usually took the form of a principal component analysis (PCA). Data could also be subsetted to explore a narrower question, such as treatment differences at a particular time point. The loading plots of these were used to select masses for use in supervised analyses (orthogonal partial least squares: OPLS) and marker selection.

2.3 Results

In this chapter a system for generating metabolic profiles linked to dormancy status in tubers is established, with the overarching goal of identifying markers that can predict tuber dormancy status and the subsequent sprouting phenotype.

Having established an optimised set of reliable protocols, the question was explored in detail in the short dormancy cultivar King Edward's and the medium dormancy cultivar Maris Piper. These categories were designated on the basis of advice from Dr Harper from Sutton Bridge and reflected the patterns I observed in subsequent analysis and when I handled commercially stored material (Harper, G. priv. comm). Subsequent experiments looked at a wider set of varieties, to examine the reproducibility of candidate markers. As a result of this work, a set of markers (defined as masses (m/z) detected by the mass spectrometry) are described which can be used to define the dormancy status in extracts of tuber buds from a range of potato varieties.

2.3.1 Method validation

The main focus of this chapter was to identify and characterise metabolic markers associated with dormancy break. One important precursor to this is establishing a robust analysis technique that captures differences between samples reliably. This includes optimal sample extraction for analysis. Very concentrated samples run the risk of ion suppression, whereas very dilute samples may present detection challenges.

Figure 2.2, Panel A shows a principal component analysis (PCA) score plot of a dilution test. Three samples were run at two different levels of dilution. Methanol-chloroform extracted tuber buds were diluted 10- or 100-fold in methanol before running in negative mode on the mass spectrometer. The concentrated (10-fold) samples are less clustered than the dilute samples. This clustering is based on very large quantities of a small subset of ions in the concentrated samples. A number of less abundant ions are not detected at all in these concentrated samples. This is illustrated by Figure 2.2, Panel B, showing differences in m/z 380 detection in the dilution test.

Preliminary work revealed an issue with starchy samples blocking the capillary tubing in the mass spectrometers. 0.5 μm pore Krudkatcher inline filters were introduced. Before applying them the putative issue of carryover between samples was examined. Figure 2.3, Panel A shows a PCA score plot of a filter test. Krudkatcher filters were tested by injecting malic standards or samples, followed by a methanol blank. There does not seem to be an issue with carryover between samples, as there is clean separation between the groups. Based on Figure 2.3, Panel B, malate levels are high in the standard

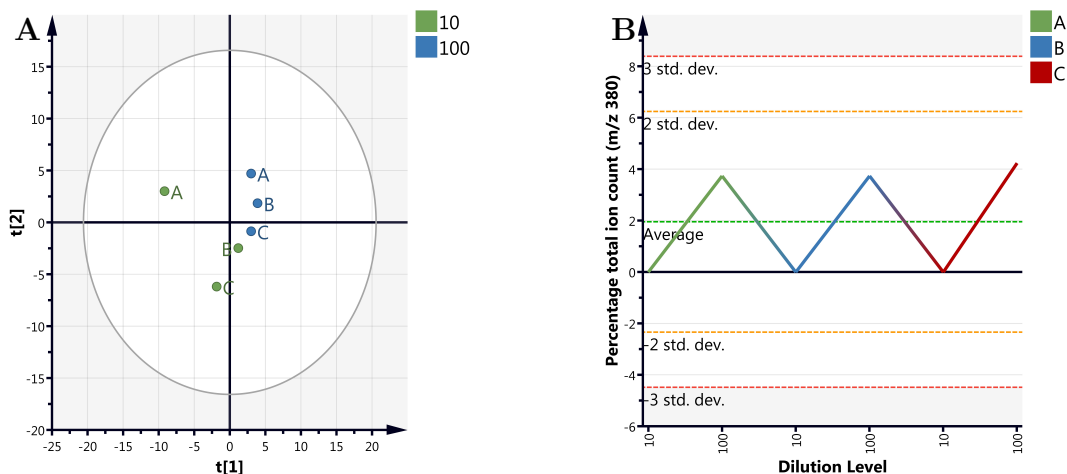


Figure 2.2: Metabolic profiling dilution tests

Three samples were run at two different levels of dilution. Data were simplified by binning to a mass accuracy of $\pm 0.1\text{Da}$ and using the in-house noise reduction macro. Methanol-chloroform extracts from tuber buds were diluted 10- or 100-fold in methanol before running in negative mode on the mass spectrometer. A: PCA score plot of a dilution test. Point colour refers to dilution level. Point labels refer to sample identity. Axes are components 1 and 2 of the PCA model. Ellipse = 95% confidence (Hotelling T₂). Total n = 6. B: Differences in m/z 380 detection in a dilution test. The Y axis shows the percentage of the total ion count for m/z 380. X axis labels refer to dilution level. Line colour refers to sample identity.

and low in the blanks. The other mass is only detected in the potato samples (Figure 2.3, Panel C). There does not seem to be an issue with carryover, based on the blanks injected after samples.

2.3.2 Structure of the dormant tuber bud

As outlined in the introduction, the process of dormancy break is not fully understood and involves a concerted interaction of genetic and environmental factors, mediated by hormonal signalling. At harvest, tubers are deeply dormant (endodormancy); they are not responsive to external stimuli and sprouting probability is low. During endodormancy, processes required for sprouting proceed gradually. After endodormancy is complete, buds become primed and are responsive to a narrow range of stimuli, including the phytohormone GA and factors such as light and temperature (Peterson, et al. 1985). At this point, sprouting is effectively guaranteed. This is illustrated schematically in Figure 2.1 on page 22.

In this chapter, dormancy break is investigated at the tuber bud level. Tuber buds are quiescent axillary meristems. Sections of embedded samples reveal the internal structure. Images from this process are shown in Figure 2.4 on page 32. Figure 2.4 A shows a

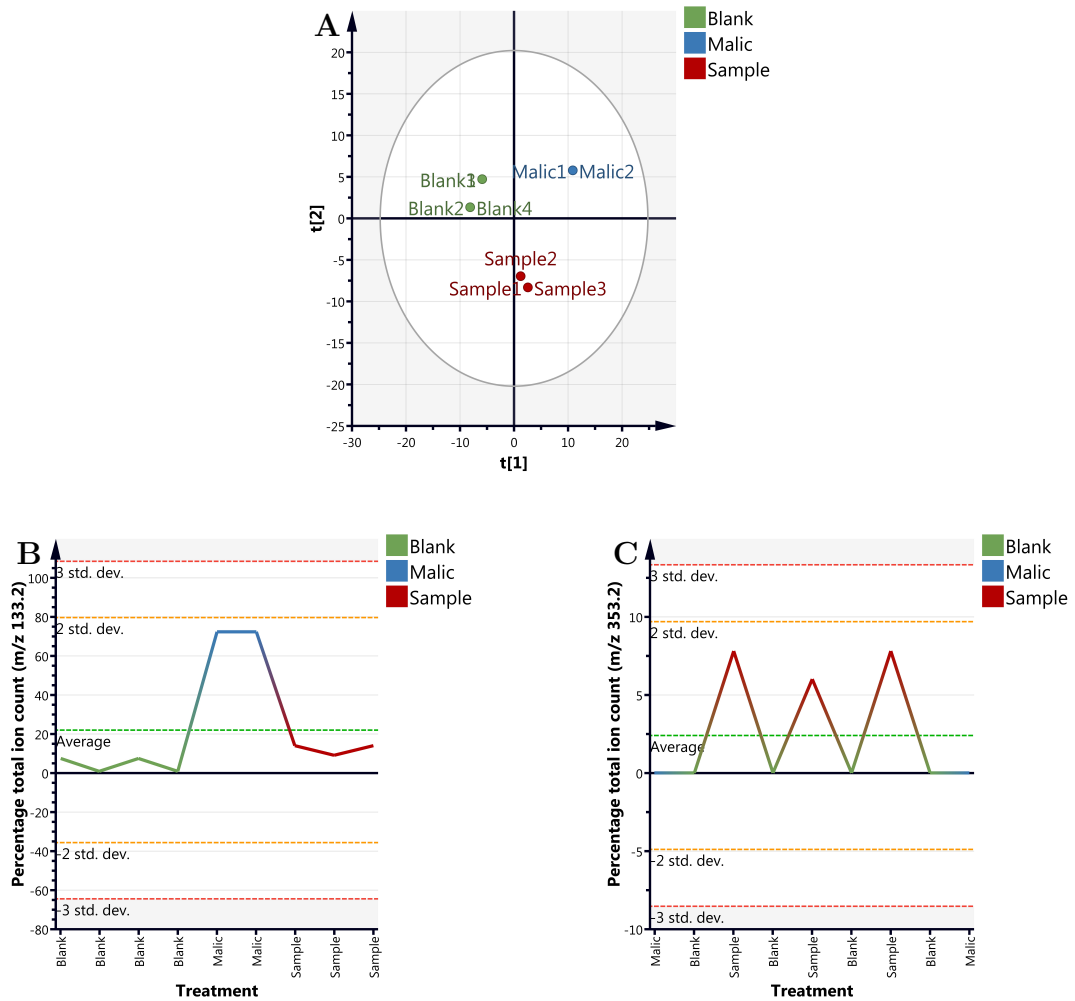


Figure 2.3: Inline filter tests

0.5 μm pore Krudkatcher filters were tested by injecting Malic standards or samples, followed by a methanol blank. Data were simplified by binning to a mass accuracy of $\pm 0.1\text{Da}$ and using the in-house noise reduction macro. A: PCA score plot of a filter test. There does not seem to be an issue with carryover between samples, as there is clean separation between the groups. Point labels and point colour refers to sample identity. Axes are components 1 and 2 of the PCA model. Ellipse = 95% confidence (Hotelling T2). Total n = 9. B: Differences in m/z 133.2 detection. Malate levels are high in the standard and low in the blanks. The Y axis shows the percentage of the total ion count for a m/z 133.2 (Putative malate). X axis labels and line colour refer to sample identity. C: Differences in m/z 353.2 detection. Most masses are only detected in the potato samples. The Y axis shows the percentage of the total ion count for a m/z 353.2. X axis labels and line colour refer to sample identity. Samples are displayed in order of injection. There does not seem to be an issue with carryover.

longitudinal section of a dormant bud containing the apical meristem (arrow) and two dormant surrounding leaf primordia. A cross-section of a dormant bud (Figure 2.4 B) reveals the central meristem sheathed by several primordia (arrows), indicating that during tuber growth the meristem generates a number of leaf primordia which then,

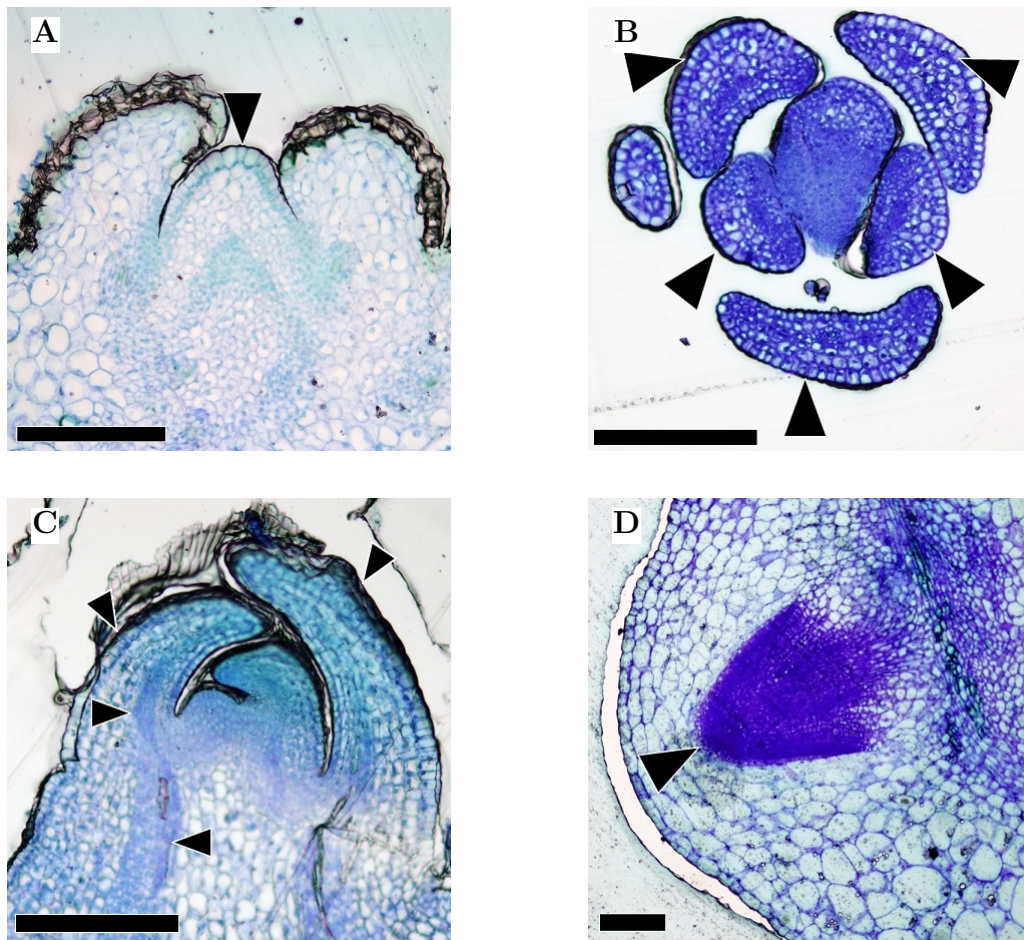


Figure 2.4: Sections of dormant potato tuber buds.

Buds were fixed in formalin and embedded in Technovit plastic resin. $12\mu\text{m}$ sections were stained with TBO and imaged using an Olympus BX51 microscope. Scale bars are $200\mu\text{m}$. A: a longitudinal section of a bud. The arrowhead indicates the meristem, sheathed by leaf bases. B: a transverse section of a bud. The central meristem is surrounded by a spiral of leaf primordia and leaf bases, highlighted by the arrows. C: a longitudinal section of a bud. Meristem, primordium and leaf bases are visible. Arrowheads indicate specialised tissues: the epidermis and connections to the vascular bundle. D: longitudinal section of tissue adjacent to a bud. The arrowhead indicates the area of the cortex with large numbers of small cells, ready to expand and grow the plant.

along with the meristem from which they were generated, enter a phase of dormancy. These leaf primordia are associated with differentiated vascular and epidermal tissue (Figure 2.4 C) and subtending the bud a dense region of cortex is visible (Figure 2.4 D). The entire bud is dormant while the meristem is quiescent, with no obvious cell division or cell expansion occurring.

A detailed examination of the effects of GA, compared to naturally occurring dormancy break, is illustrated in Figure 2.5 on page 34. Figure 2.5 shows four scanning electron micrographs of tuber buds at various stages of storage. Figure 2.5 A and B are

untreated and differ in the length of their storage; Figure 2.5 A was imaged 1 week after harvest, whereas Figure 2.5 B was imaged 12 weeks after harvest. Figure 2.5 C and D are water- and GA-treated outputs of the *in vitro* assay described in 2.2.3 after 96 hours respectively. This material had been stored for 8 weeks before treatment.

Figure 2.5 A is at 80x magnification. It shows a deeply dormant bud, with at least 2 leaf bases, largely covered by 2 fairly old leaflike structures. A fully developed stoma is clearly visible on the older leaf to the left. Figure 2.5 B, at 100x magnification, shows a rosette of leaf primordia. At least 11 of these are present and at least 9 display stomata or trichomes on the leaf surface. Figure 2.5 C, at 100x magnification, shows a small pair of leaf primordia in a recess, covered by a shrivelled leaf scale coming down from the top right corner. The leaf primordium on the left shows several stomata, although the central part of the bud structure is obscured by the protective leaf. Figure 2.5 D, at 100x magnification, shows a compact bud with 7 leaf primordia. To the left of the image is a shrivelled sheathing leaf, out of focus because it is at a different plane compared to the top of the bud. The outer 5 leaf primordia have stomata and 3 of them show substantial damage and shrivelling. The bud is raised, relative to the surrounding tissue.

As indicated in the Introduction, following formation, tubers undergo a period of endodormancy after which sprouting initiation increases in response to exogenous factors. We exploited the observation that exogenous supply of GA can be used to trigger sprouting to set up a standardised system whereby we could isolate tubers buds at precise, reproducible stages of dormancy release/sprouting. A robust system for staging buds facilitates comparison between buds at different stages of sprouting, thus allowing the identification of metabolic changes that might be occurring at these stages.

2.3.3 Synchronising dormancy release

In order to generate a standardised system, tubers (cv. King Edward's) were grown under glass with a photoperiod of 12 hours and staggered planting dates. This makes it possible to simultaneously sample material that has been stored for a range of time periods. Resampling stored material at intervals can also corroborate development-linked patterns, as batch effects are controlled. As sampling is destructive, this is the only way to track the fate of tubers, whilst collecting metabolic data. The design of these staggered planting experiments is illustrated in Figure 2.6 on page 35.

In addition to the staggered planting, dormancy break was artificially initiated using an *in vitro* system of controlled bud dormancy release, based on that described by Hartmann *et al.* (2011). This uses treatment with GA as a sprout initiator, allowing differences in response to be calculated. In initial experiments, buds from field-grown

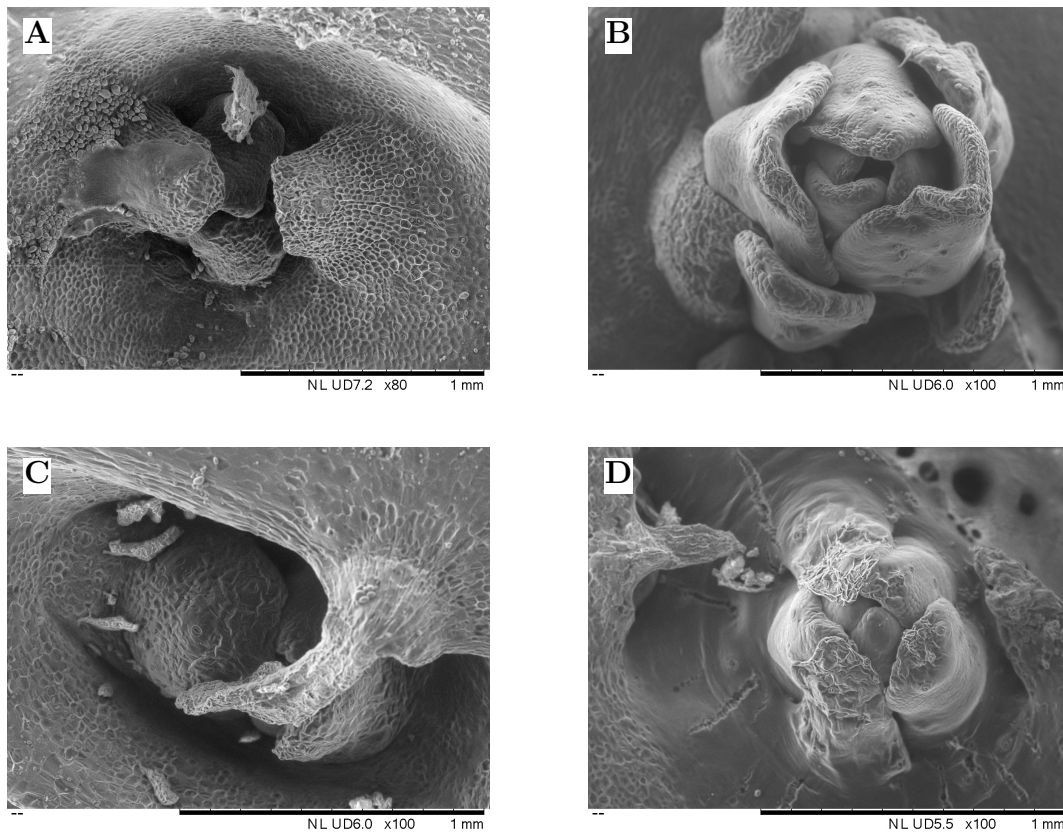


Figure 2.5: Scanning electron micrographs of potato buds.

3mm pieces of potato tuber containing buds were imaged using a scanning electron microscope. Tuber tissue was stuck to stubs with OCT and cooled to -20°C . Scale bars are 1 mm. A: bud 1 week after harvest at 80x magnification; B: bud 12 weeks after harvest at 100x magnification; C: bud 8 weeks after harvest, treated with water *in vitro* for 96 hours prior to imaging at 100x magnification; D: bud 8 weeks after harvest, treated with GA *in vitro* for 96 hours prior to imaging at 100x magnification.

King Edward tubers were used. As shown in Figure 2.7 on page 35, after 168 hours the GA and control-treated apices could be distinguished from controls, with GA treatment leading to larger visible buds (Figure 2.7A). However, the SAM is large, so subsequent values were quoted as proportion $>1\text{mm}$. At $t=168$ hours, 66% of GA-treated apices were greater than 1mm, whereas only 30% controls were this size (Figure 2.7B). The *in vitro* system thus produces two populations of buds with a predictable sprouting fate.

The pattern observed in experiments such as that in Figure 2.7 changed during tuber storage. During endodormancy, none of the buds sprouted, regardless of treatment. By the time tubers had exited endodormancy and were in a primed and responsive state (see schematic in Figure 2.1), samples were responsive to the GA trigger (Figure 2.7). Tubers that had been stored for a long time sprouted at a high rate, regardless of treatment. In the short dormancy cultivar King Edward, I found this plant material was unresponsive

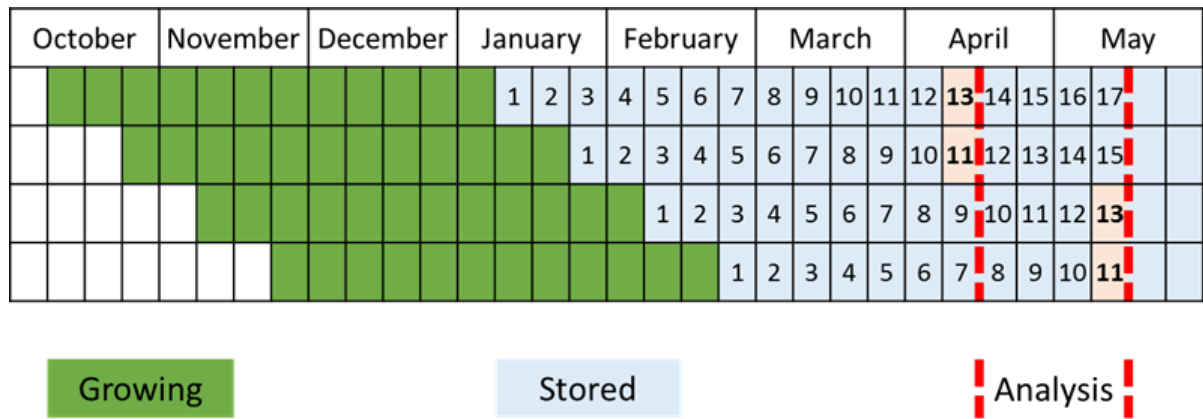


Figure 2.6: Design of staggered planting experiments under controlled environment. Seed tubers are planted every 2 weeks and harvested after 12 weeks of growth (Green). Harvested tubers are stored at 7°C in the dark (Blue). Analysis is carried out for several batches simultaneously (Red dashed line). These have been in storage for a range of time periods. This design controls for batch effect and allows resampling of material to take place.

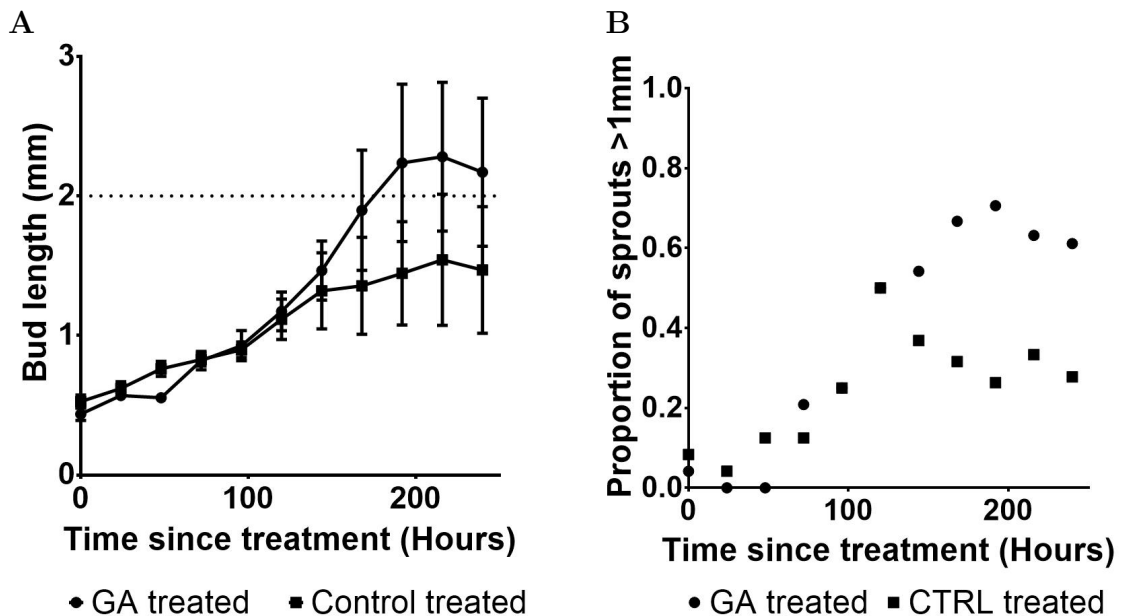


Figure 2.7: Sprouting rate of treated buds in the *in vitro* system. Explanted buds were treated with either GA (50 μ M) or with water and measured at daily intervals (values in hours). There is negligible visible response during the first 72 hours after treatment. This process lends the ability to predict meristem fate before the emergence of a visible phenotype. Cultivar: King Edward, Glasshouse grown. n=48. A: Changes in bud length (mm), comparing GA- and control-treatment over time (hours). The dotted line represents the industry standard of 2mm buds. Error bars represent Standard error of the mean. B: The proportion of sprouts >1mm, comparing GA- and control-treatment over time (hours).

to GA for the first 4-6 weeks after harvest. After a GA sensitive window of a further 6-8 weeks, sprouting could be expected, irrespective of treatment, 12-14 weeks after harvest.

In addition to the whole tuber aspect of dormancy progress, there was a discernible developmental gradient within the tuber of bud sprouting. Each tuber contains a group of buds, generally arranged in a spiral in which the bud opposite the stolon can be termed the apical bud. Visual inspection of tubers during sprouting suggested that the apical meristem exerted dominance over the rest of the tuber, with a much lower level of sprouting in the meristems at the stolon end, compared to the apical bud. In preliminary experiments, analysis of explanted stolon and apical buds substantiated these observations, with a much lower level of sprouting observed in the stolon meristems compared to the apex. Initial experiments in which metabolic profiles were obtained from the apical bud and the surrounding stolon buds also indicated that buds are metabolically distinct based on their developmental ranking. Methanol-chloroform extracts from ranked tuber buds (1 to 6, with “1” specifying the apical bud) were analysed in negative and positive mode (Figure 2.8). In the PCA plot of data obtained in negative mode (Figure 2.8 A) there is a clear distribution of tuber rank, apart from the apical bud of sample “R”. The other apices generally cluster well depending on rank. This distribution is matched by the highlighted m/z in the respective loadings plot (Figure 2.8 B), with notably m/z 191.0, 133.0, 115.0 potentially having a large influence in discriminating the apical buds from the stolon buds.

When the samples were analysed in positive mode (Figure 2.8 C) although there was some clustering of the apical buds at the origin, the pattern was less clear than that observed in negative mode analysis. Similarly, the loading plots analysis (Figure 2.8 D) was less informative. Some of the influential masses in this plot, such as 398.4 (putative solanidine) are linked to glycoalkaloids which potato tubers use as an anti-herbivory defence mechanism.

Overall, the analysis presented in Figure 2.8 substantiated the visual impression that dormancy release/sprouting behaviour was influenced by relative developmental rank of a bud on the tuber. In all subsequent analyses care was taken to use the apical bud of each tuber (unless otherwise specified) to minimise the influence of initial developmental stage of the bud on the results obtained analysing the progression from dormancy to sprouting (Teper-Bamnolker *et al.* 2012).

A number of markers are highlighted as interesting in Figure 2.8B. These are highlighted at many stages in this chapter. The identity, abundance and consistent influence over a range of analyses make them particularly interesting. A detailed discussion of how these m/z markers are identified is presented in Chapter 3. However, at this early stage, these m/z markers were putatively identified on the basis of mass as key components of the Krebs cycle, as shown in Table 2.2 on page 38. A comprehensive description of this methodology and subsequent experimental steps are explored in 3.3.1, on page 68.

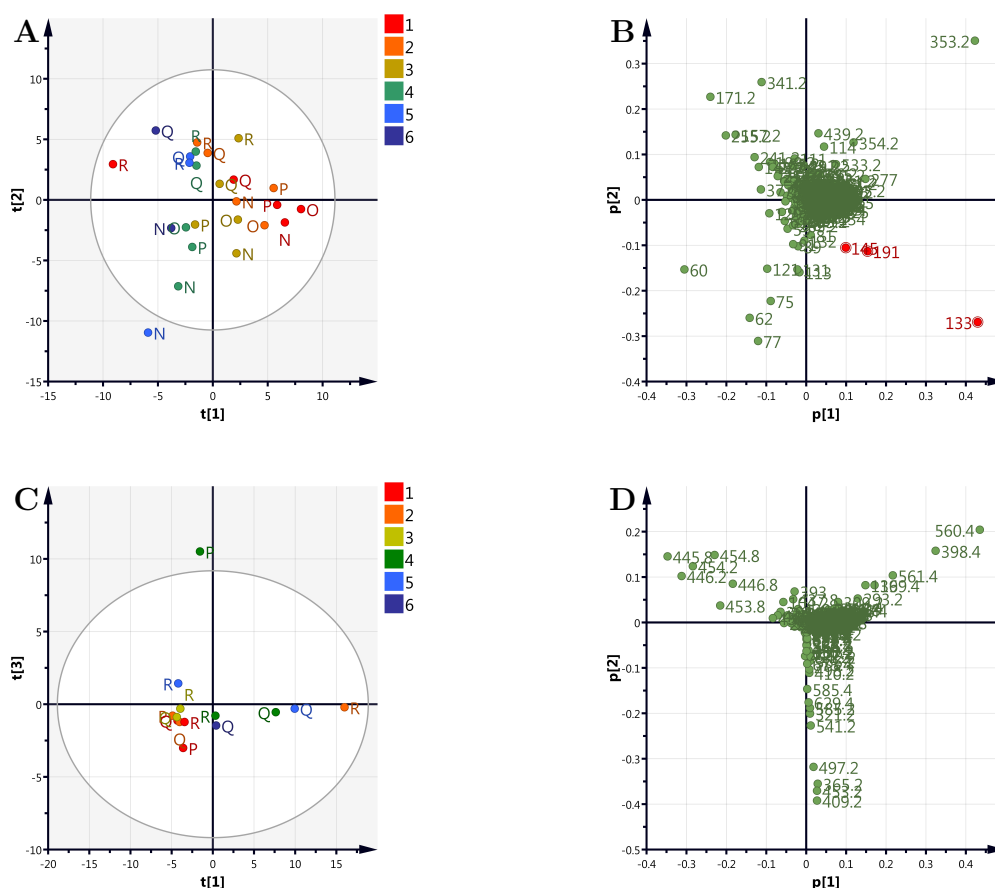


Figure 2.8: Multivariate analysis the effect of bud position on metabolic profiles. Extracts from ranked tuber buds (1 to 6, if available) were analysed in negative and positive mode. Data were simplified by binning to a mass accuracy of $\pm 0.1\text{Da}$. On PCA score plot: Ellipse = 95% confidence (Hotelling T2). On Loadings plot: Each point refers to an individual m/z bin, labeled accordingly. A: PCA score plot of a negative apical dominance test. Point labels (N-R) refer to tuber identity. Point colour refers to bud rank. Axes are components 1 and 2 of the PCA model. Total $n = 24$. B: PCA loadings plot of an apical dominance test (Negative ionisation). Axes are loadings for components 1 and 2 of the PCA model. The highlighted m/z ; 145, 191 and 133 are influential. C: PCA score plot of an apical dominance test (Positive ionisation). Point labels (N-R) refer to bud identity. Point colour refers to bud rank. Axes are components 1 and 2 of the PCA model. Total $n = 15$. D: PCA loadings plot of a negative apical dominance test. Axes are loadings for components 1 and 2 of the PCA model.

2.3.4 Metabolic profiles in response to GA treatment

Having established a robust system for sprouting initiation and identification of which bud to use for analysis, I performed a time-course metabolomic analysis of isolated apical buds from field grown Maris Piper tubers. These were treated with GA in January, approximately 3 months after harvest, using a similar system to that in section 2.2.3. In the context of the schematic representation of dormancy in Figure 2.1 on page 22, these

Table 2.2: Putative identification of metabolic markers

Markers are putatively identified, based on their m/z (Da), based on database search of KEGG and Solcyc. Masses of interest were selected from loadings plots in chapter 2. Masses for associated ions were identified in the dataset.

| Detected negative ion m/z (± 0.1 Da) | Putative metabolite | Molecule exact mass (Da) |
|--|------------------------|-----------------------------|
| 191.0 | Citrate | 192.027 |
| 133.0 | Malate | 134.022 |
| 115.0 | Fumarate | 116.011 |
| 173.0 | Aconitate | 174.016 |
| 145.0 | Ketoglutarate | 146.022 |
| 131.0 | Oxaloacetate | 132.006 |

samples were towards the right of the graph, and were responsive to growth promoters. The results of this analysis are presented in Figures 2.9 and 2.10.

Figure 2.9A,B on page 39 show the results of an Orthogonal Partial Least Squares (OPLS) analysis of buds either treated with GA or mock inoculated with water, with time since treatment with GA used as a Y-variable. The points are colour-coded with time since GA treatment used as a continuous variable. A supervised analysis produces the clear time-based distribution in the score plot (Figure 2.9A), with samples at time points 0h, 24h, 48h and 72h separating from each other, irrespective of treatment. Based on this, the loadings plot in Figure 2.9B can be used to infer that m/z 191 and 133 are most influential in dictating this temporal distribution, although they do not explain the distribution perfectly.

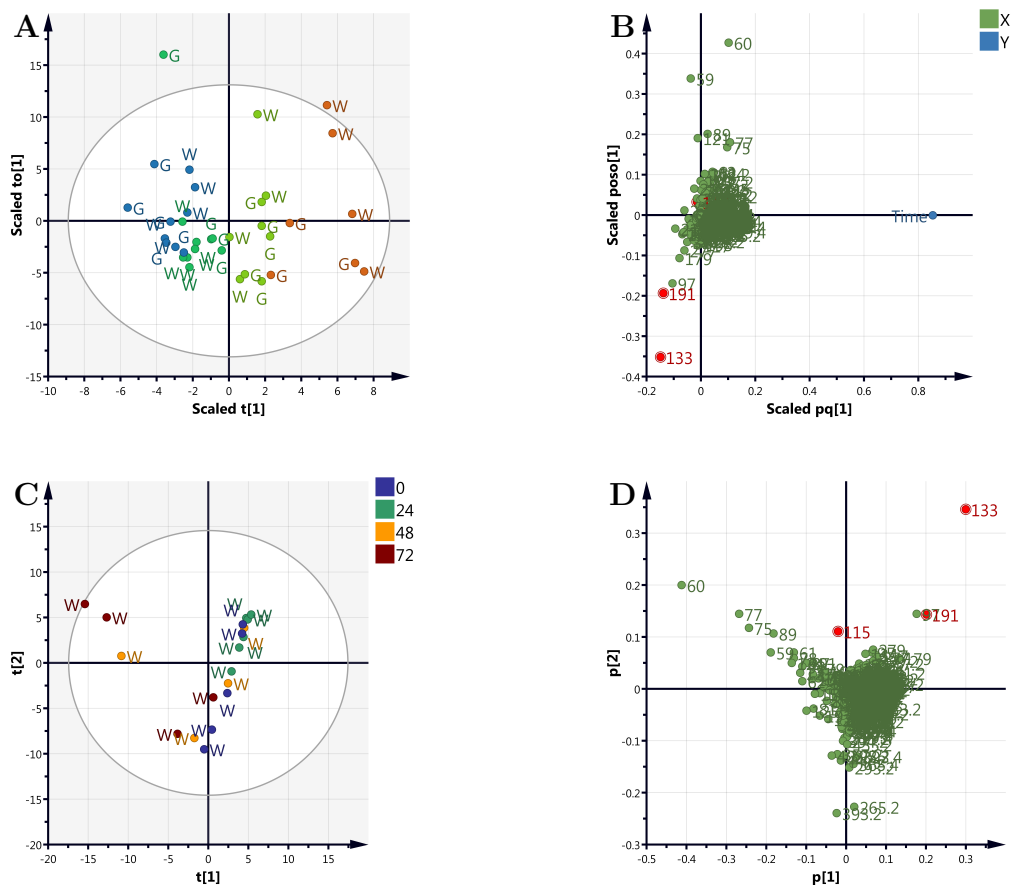


Figure 2.9: Multivariate analysis of field grown cv. Maris Piper metabolic profiles, treated with GA in a development series.

Extracts from cv. Maris Piper tubers, analysed on the QSTAR in negative ionisation mode. Samples from stored tubers were treated with GA or a control (water), and flash frozen at 24 hour intervals. Data were simplified by binning to a mass accuracy of $\pm 0.1\text{Da}$. OPLS and PCA Ellipse = 95% confidence (Hotelling T2). On loadings plots, each point refers to an individual m/z bin, labeled accordingly. A: OPLS score plot of the development series. Point labels refer to treatment (G or W) and point colour refers to time since treatment (in hours). Axes are scaled components 1 and 2 of the OPLS model, based on the time since treatment. Total $n = 36$. B: OPLS loadings plot of the development series. Axes are loadings for the predictive component and orthogonal component of the OPLS model. Time since treatment is in blue. C: PCA score plot of untreated samples from the development series. Point labels refer to treatment (W) and point colour refers to time since treatment (in hours). Axes are components 1 and 2 of the PCA model. Total $n = 19$. D: PCA loadings plot of untreated samples in the development series. Axes are loadings for components 1 and 2 of the PCA model.

This may be caused by the spread of control samples being poorly explained by time since treatment, as seen in Figure 2.9C,D. These figure parts refer to a PC analysis of the mock-inoculated (water-treated) samples. This score plot shows poor discrimination based on time since treatment, i.e. there is no clear response to time since treatment.

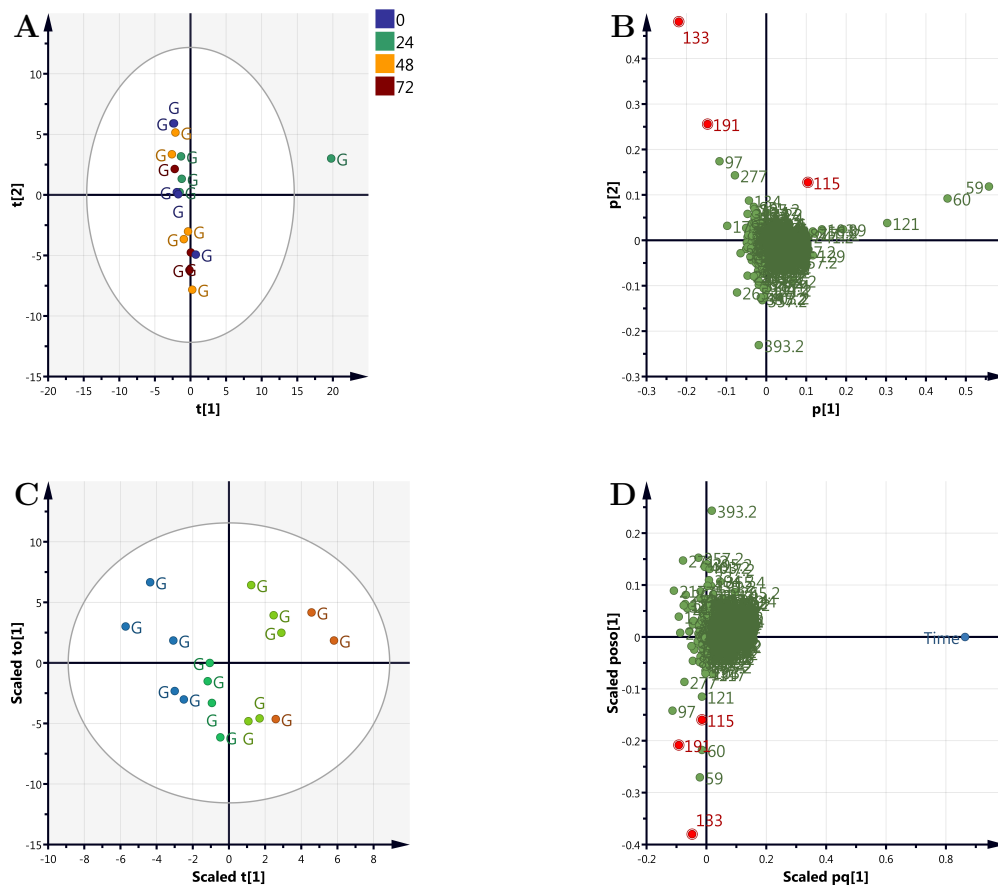


Figure 2.10: Multivariate analysis of cv. Maris Piper metabolic profiles from the controlled environment, treated with GA in a development series.

Extracts from GA treated cv. Maris Piper tubers, analysed on the QSTAR in negative ionisation mode. Samples from stored tubers were treated with GA, and flash frozen at 24 hour intervals. Data were simplified by binning to a mass accuracy of ± 0.1 Da. OPLS and PCA Ellipse = 95% confidence (Hotelling T₂). On loadings plots, each point refers to an individual m/z bin, labeled accordingly. Total n = 17. A: PCA score plot of GA treated samples from the development series. Point labels refer to treatment (GA) and point colour refers to time since treatment (in hours). Axes are components 1 and 2 of the PCA model. B: PCA loadings plot of GA treated samples in the development series. Axes are loadings for components 1 and 2 of the PCA model. C: OPLS score plot of the development series. Point labels refer to treatment (G) and point colour refers to time since treatment (in hours, blue=0, green=24, lime=48, red=72). Axes are scaled components 1 and 2 of the OPLS model, based on the time since treatment. D: OPLS loadings plot of the development series. Axes are loadings for the predictive component and orthogonal component of the OPLS model. Time since treatment is in blue.

The PCA loadings plot (Figure 2.9D), highlights the same m/z (191, 133 and 115) as having the major influence on the distribution observed as highlighted in Figure 2.9B.

Focussing on the GA-treated samples in this analysis, an unsupervised PCA and an OPLS analysis were carried out (Figure 2.10 on page 40), with Panels A and B referring

to PCA plots. The score plot Figure 2.10 A indicates a better grouping of samples by time since treatment, compared to the analysis of the water-treated data set shown in Figure 2.9 C. Figure 2.10 B shows a loadings plot for the data shown in Figure 2.10 A, and reveals that the key metabolites in this process remain m/z 191 and 133. These markers correspond to those identified in Figure 2.9 B (above).

To explore this pattern in more detail, a supervised analysis of the GA-treated dataset was carried out. The output of this OPLS is illustrated in Figure 2.10, C and D. Figure 2.10 C shows an OPLS score plot, arranging samples by time since GA treatment, i.e. the OPLS forces the data to distribute according to time since treatment. The points are colour-coded with time since GA treatment used as a continuous variable. Figure 2.10 D illustrates the loadings plot for this OPLS. When time since treatment is used as an explanatory variable, the key markers from Figure 2.10 B remain influential, but do not covary unequivocally with the Y variable (time since GA treatment). The repeated appearance of these markers suggests involvement in GA-activated potato bud sprouting.

2.3.5 Metabolic profiles along time in storage

The data in the previous section indicated that excised buds from field grown tubers (Maris Piper) stored for a set time could be distinguished by metabolic profiling in response to a GA-treatment which triggered sprouting. Since it is known that tendency for sprouting increases with time in storage, I proceeded to perform a series of experiments in which apical buds from tubers of the short dormancy variety King Edward's (grown in controlled environment) were analysed by a similar metabolic profiling approach but after different times in storage. The staggered planting system shown in Figure 2.6 (on page 35) provides a useful way to study this process, since by growing samples in a controlled environment, developmental comparisons can be made without the complications of seasonality. This approach also allows any impacts caused by unusual, outlier batches to be identified, since multiple sets of tubers are eventually sampled for the same time point, which is not possible for field grown samples. Thus in the following figures (Figures 2.11 and 2.12), tuber samples were harvested at different calendar times to cover time in storage at weekly intervals from 2 to 8 weeks (see Table 2.3 on 42). The relationship between the samples in Figures 2.11 and 2.12 are summarised in Table 2.3. The same population of tubers was resampled at a later date to capture any metabolic changes occurring during storage.

At each time point (weeks in storage) apical buds were excised and treated with either GA ($50\mu\text{M}$) or water control (section 2.2.3). Buds were then flash-frozen after 72h and Methanol-chloroform extracts (section 2.2.5) analysed by mass spectrometry in

negative ionisation mode. The results are shown in Figure 2.11 on page 43. A PCA score plot for all data (GA and water-treated) (Figure 2.11 A) shows a moderate separation (by time in storage) along component 2. This distribution is matched by the highlighted m/z in the PCA loadings plot shown in Figure 2.11 B, with m/z 191 being particularly influential. m/z 133 is associated with a small cluster of GA-treated samples.

When the water-treated controls alone are analysed in an unsupervised PCA score plot (Figure 2.11 C), there is separation according to storage time along component 1. The samples that were harvested 2-4 weeks before analysis are on the negative half of the component 1 axis, whereas those stored for 6-8 weeks are almost all on the other half. All the highlighted m/z on the PCA loadings plot (shown in Figure 2.11 D) co-vary with this gradient. Yet again, the markers, m/z 191, 133 and 115 are the key ions, as also highlighted in Figures 2.9 and 2.10.

The tuber batches used for the analysis shown in Figure 2.11 were re-sampled and analysed in a similar way but at later time points (as shown in Table 2.3) to obtain further information on the shift in metabolic profiles in apical buds during storage. The results are shown in Figure 2.12 on page 44 and provide data on tubers sampled 3-7 weeks after harvest. Due to poor clustering in the initial PCA, a supervised OPLS was used to analyse these data, with time since harvest as a predictive variable.

Figure 2.12 A shows an OPLS score plot for all samples (GA-treated and water-treated controls). The nature of the supervised analysis means that there is good clustering of samples by time since harvest along component 1. This distribution makes it possible to identify influential markers from the OPLS loadings of these data, shown in Figure 2.12 B, with m/z 133.2 and 115.2 being most influential. The discrepancy of 0.2Da between these m/z and the ions identified previously (e.g. Figure 2.11 on 43) can be attributed to minor changes in instrument calibration, leading to issues when binning masses to ± 0.1 Da.

Table 2.3: Staggered Planting Design

| Correspondence between samples in Figures 2.11 and 2.12 | | |
|---|---------------------|---------------------|
| Time since harvest (weeks) | | |
| Planting date | Data in Figure 2.11 | Data in Figure 2.12 |
| 02/07/2015 | 8 | N/A |
| 17/07/2015 | 6 | 7 |
| 31/07/2015 | 4 | 5 |
| 13/08/2015 | 2 | 3 |

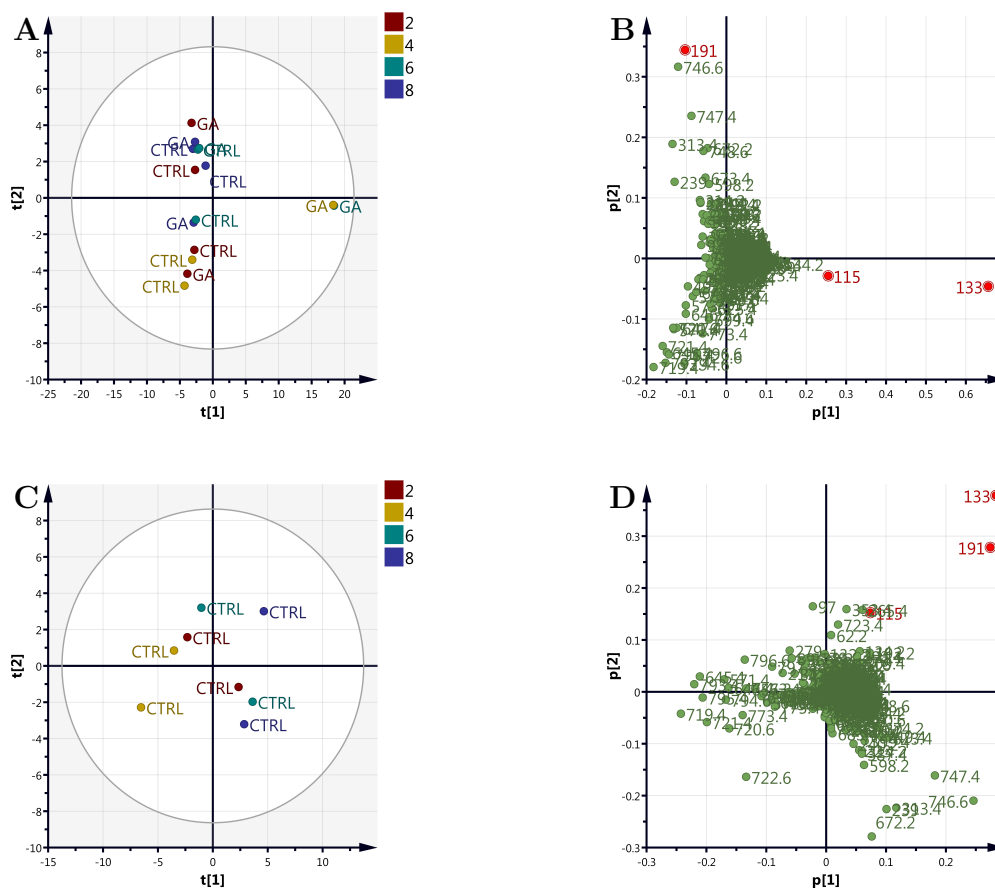


Figure 2.11: PCA of cv. King Edward metabolic profiles from the controlled environment staggered planting system.

Extracts from the staggered planting system, analysed on the QSTAR in negative ionisation mode. Samples from stored tubers were treated with GA or a water control, and flash frozen after 72 hours. Data were simplified by binning to a mass accuracy of ± 0.2 Da. PCA Ellipse = 95% confidence (Hotelling T₂). On loadings plots, each point refers to an individual m/z bin, labeled accordingly. A: PCA score plot of the harvest series. Point labels refer to treatment (GA or CTRL) and point colour refers to time since harvest (in weeks). Axes are components 1 and 2 of the PCA model. Total n = 15. B: PCA loadings plot of the harvest series. Axes are loadings for components 1 and 2 of the PCA model. C: PCA score plot of untreated samples from the harvest series. Point labels refer to treatment (CTRL) and point colour refers to time since harvest (in weeks). Axes are components 1 and 2 of the PCA model. Total n = 8. D: PCA loadings plot of untreated samples in the harvest series. Axes are loadings for components 1 and 2 of the PCA model.

Figure 2.12 C and D focus on the water-treated (control) samples from this experiment. Figure 2.12 C shows an OPLS score plot with a clear distribution along component 1, which is associated with m/z 133.2 in the loadings plot in shown in Figure 2.12 D. There is a small cluster of outliers with a strong association with m/z 133.2, but all the other relatively freshly harvested samples (3 weeks after harvest) seem to co-vary along

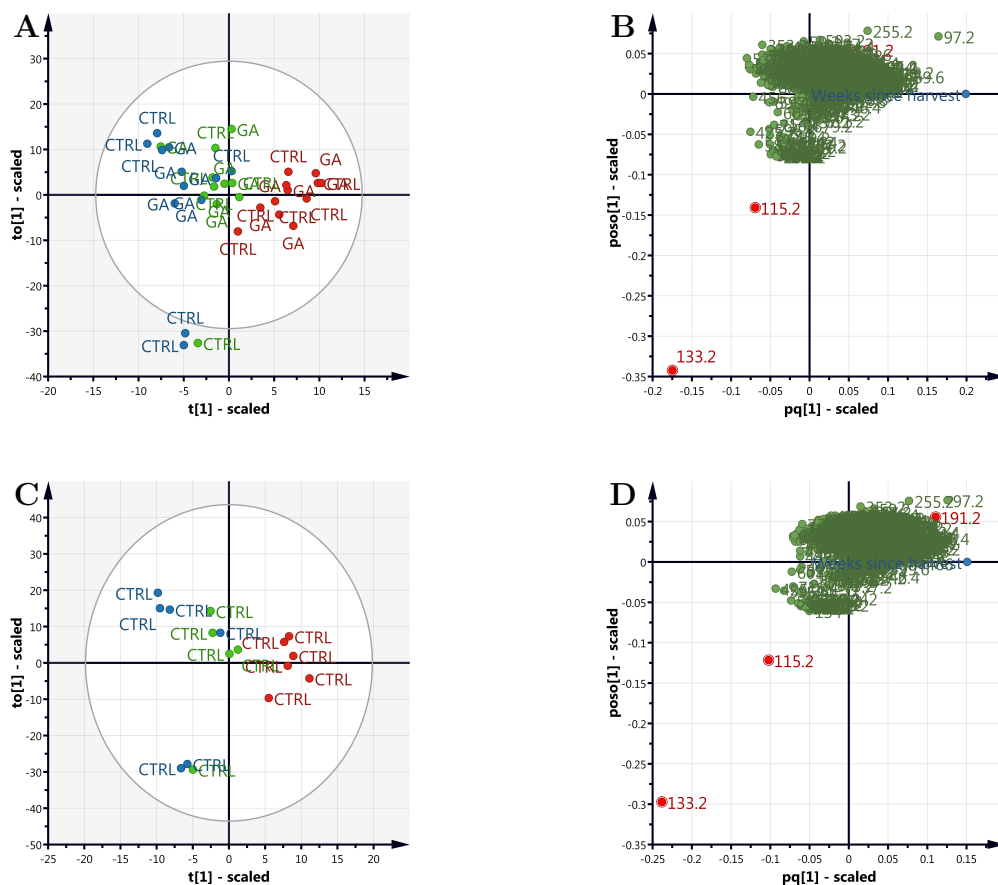


Figure 2.12: OPLS of cv. King Edward metabolic profiles from the controlled environment staggered planting system.

Extracts from the staggered planting system, analysed on the QSTAR in negative ionisation mode. Samples from stored tubers were treated with GA or a water control, and then flash frozen. Data were simplified by binning to a mass accuracy of $\pm 0.2\text{Da}$. OPLS Ellipse = 95% confidence (Hotelling T²). On loadings plots: Each point is labeled as its m/z bin. Weeks since harvest, is in blue. A: OPLS score plot of the harvest series. Point labels refer to treatment (GA or CTRL) and point colour refers to time since harvest (in weeks, red=7, green=5, blue=3). Axes are components 1 and 2 of the OPLS model, based on the number of weeks since harvest. Total $n = 35$. B: OPLS loadings plot of samples from the harvest series. Axes are loadings for the predictive component and orthogonal component of the OPLS model. C: OPLS score plot of untreated samples in the harvest series. Point colour refers to time since harvest (in weeks, green=5, blue=3). Axes are components 1 and 2 of the OPLS model, based on the number of weeks since harvest. Total $n = 17$. D: OPLS loadings plot of untreated samples from the harvest series. Axes are loadings for the predictive component and orthogonal component of the OPLS model.

the horizontal axis. m/z 115.2 and 191.2 are also influential.

In order to extend the analysis of bud metabolite profiles during storage, an experiment was performed in which apical buds were harvested at time point 4, 8, 12 and 14 weeks after harvest, i.e. beyond the 8 storage weeks analysed in the previous datasets.

In this experiment buds were flash frozen immediately after washing with buffer (i.e. not treated with GA), then analysed in negative ion mode as previously described. These data are shown in Figure 2.13 on page 46.

Figure 2.13 A shows a PCA score plot for these data, labelled according to time since harvest (in weeks). The data for week 12 cluster unusually along component 2, perturbing any other effects. To circumvent this issue, a supervised OPLS was performed, with time since harvest as the predictive variable. The score plot for this analysis is shown in Figure 2.13 B. In this analysis the buds taken and analysed from tubers at different time points in storage are clearly discriminated.

According to the OPLS loadings plot, shown in Figure 2.13 C, some key markers explain a lot of the variation observed in these samples, but are orthogonal to the time since harvest. m/z 133.2, 115.2 and 191.2 are all influential, but the unusual characteristics of the 12 week samples in this analysis obfuscates any storage-time linked pattern.

2.3.6 Field grown tubers

To follow on from the work in glasshouse-grown tubers, and test the generality of the observations made, tests were performed on field grown tubers. Tubers were from 4 established commercial cultivars with different dormancy habits: cv. King Edward, Maris Piper, Desiree and Russet Burbank. These were grown in Yorkshire in 2016 and transported to Sutton Bridge Crop Storage Research, where they were cooled and stored under commercial conditions. Samples were sent to the University of Sheffield at 4 week intervals for processing and analysis during the 2016-2017 storage season. At each sampling date I performed a time-course metabolomic analysis of isolated apical buds, capturing metabolic profiles and responses to GA treatment.

Cv. King Edward

A key question to investigate was the reproducibility of my results from glasshouse-grown tubers. Field grown cv. King Edward tubers were analysed in October, November and December 2016. The results of these analyses are presented in Figures 2.14 and 2.15. Figure 2.14 on page 47 shows the score and loadings plots of an OPLS analysis of control buds, with the sampling month used as a Y-variable. By using Month as a Y-variable, the samples are separated along the horizontal axis in Figure 2.14A, as clearly denoted by the colours. The supervised analysis means that co-varying bins can be identified from the loadings plot in Figure 2.14B. Based on this loadings plot, m/z 191.2 (in red) is influential along the seasonal axis. There are other influential markers, several of which are also influential on these axes.

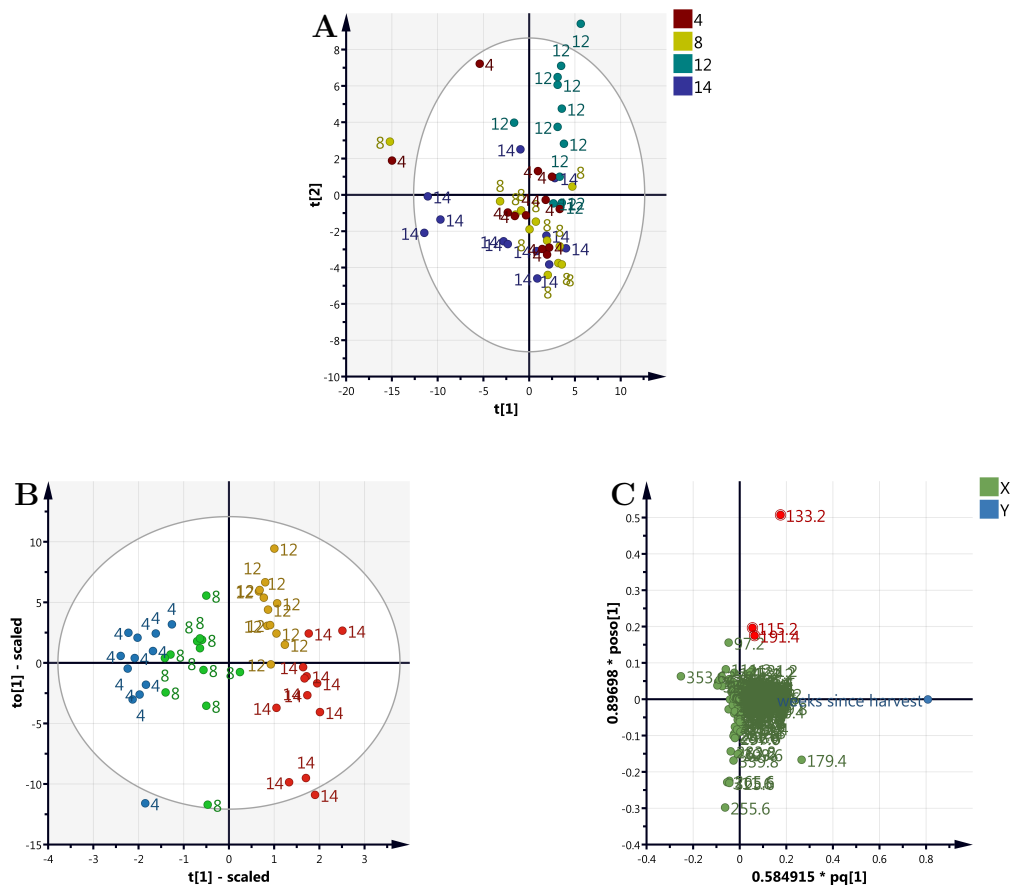


Figure 2.13: Multivariate analysis of cv. King Edward metabolic profiles from the controlled environment staggered planting system.

Extracts from the staggered planting system. Samples from stored tubers were not treated with GA and were analysed on the QSTAR in negative ionisation mode. Data were binned to a mass accuracy of $\pm 0.1\text{Da}$. Ellipse = 95% confidence (Hotelling T₂). A: PCA score plot of the harvest series. Point colour refers to time since harvest (in weeks). Axes are components 1 and 2 of the PCA model. Total n = 48. B: OPLS score plot of samples in the harvest series. Point colour refers to time since harvest (in weeks, red=14, yellow=12, green=8, blue=4). Axes are components 1 and 2 of the OPLS model, based on the number of weeks since harvest. Total n = 48. C: OPLS loadings plot of untreated samples from the harvest series. Axes are loadings for the predictive component and orthogonal component of the OPLS model. Each point is labeled as its m/z bin. Weeks since harvest is in blue.

Figure 2.15 on page 48 displays data for the GA-treated samples, prepared in the same experiment as Figure 2.14. Figure 2.15A and B show the data for samples treated with GA in October. They are the score and loadings plot of an OPLS that uses time since GA-treatment as a Y-variable. This yields the familiar well-separated pattern in Figure 2.15A. Based on Figure 2.15B, none of the previously discussed m/z markers dominate the loadings. In contrast, Figure 2.15C and D show an OPLS analysis of samples treated with GA in December. Whilst the score plot, Figure 2.15C, resembles

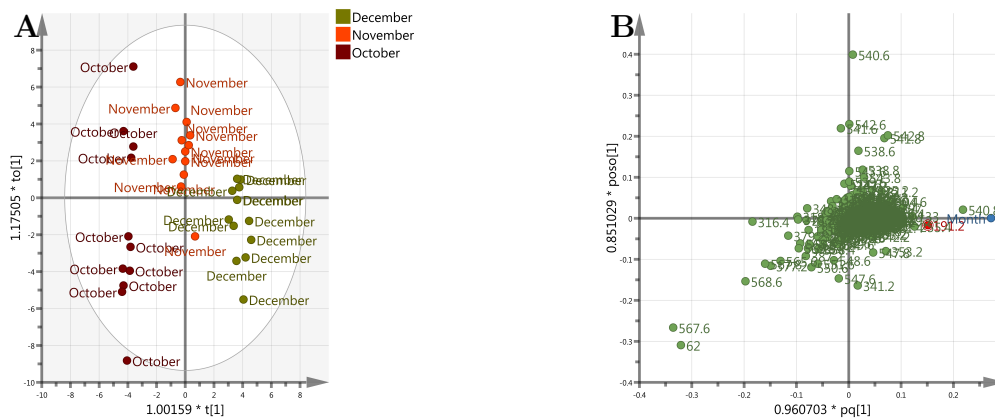


Figure 2.14: An OPLS of field grown King Edward samples, by month.

A: An OPLS score plot of field grown King Edward samples, at $t=0$ in the *in vitro*. Samples are coloured and labelled by month of analysis. The supervised analysis arranges samples along the horizontal axis, based on month of analysis. B: an OPLS loadings plot of field grown King Edward's samples. Each point refers to a m/z bin. The Y-variable, Month, is on the far right side of the horizontal axis. Bins that co-vary with the month lie close to the pq axis. $n=36$, months = October, November, December 2016.

Figure 2.15A quite closely, there is a key difference in the loadings: m/z 133 and 191.2 are clearly key metabolites in the distribution of samples in December.

Cv. Desiree

Data for another relatively short dormancy cultivar, Desiree, are presented in Figures 2.16 and 2.17. Field grown cv. Desiree samples were analysed in October, November and December 2016 and January 2017. Figure 2.16 on page 49 shows PCA plots from control samples. Figure 2.16A is a score plot for components 2 and 3, which show good separation along the (horizontal) component 2 axis. Figure 2.16B is the loadings plot for the PCA. As in Figure 2.16A, the axes refer to components 2 and 3. m/z 191 and 133, important markers throughout this chapter, align closely to the horizontal axis, implying influence.

Figure 2.17 on page 50 shows PCA score and loadings plots for GA-treated Desiree bud profiles. Figure 2.17A and B show the data for samples treated with GA in October, coloured and labelled according to time since treatment. Figure 2.17A, the score plot, shows separation into 2 quadrants, with $t=0$ and 24 on the left and $t=48$ and 72 on the right. The corresponding loadings plot, in Figure 2.17 B, shows 191 and 133 in influential positions on the far right of the axis. In contrast, the January GA-treated samples, Figure 2.17C and D, lose this pattern. The loadings plot, Figure 2.17D, looks deceptively similar to Figure 2.17B. However, upon examination of the score plot in

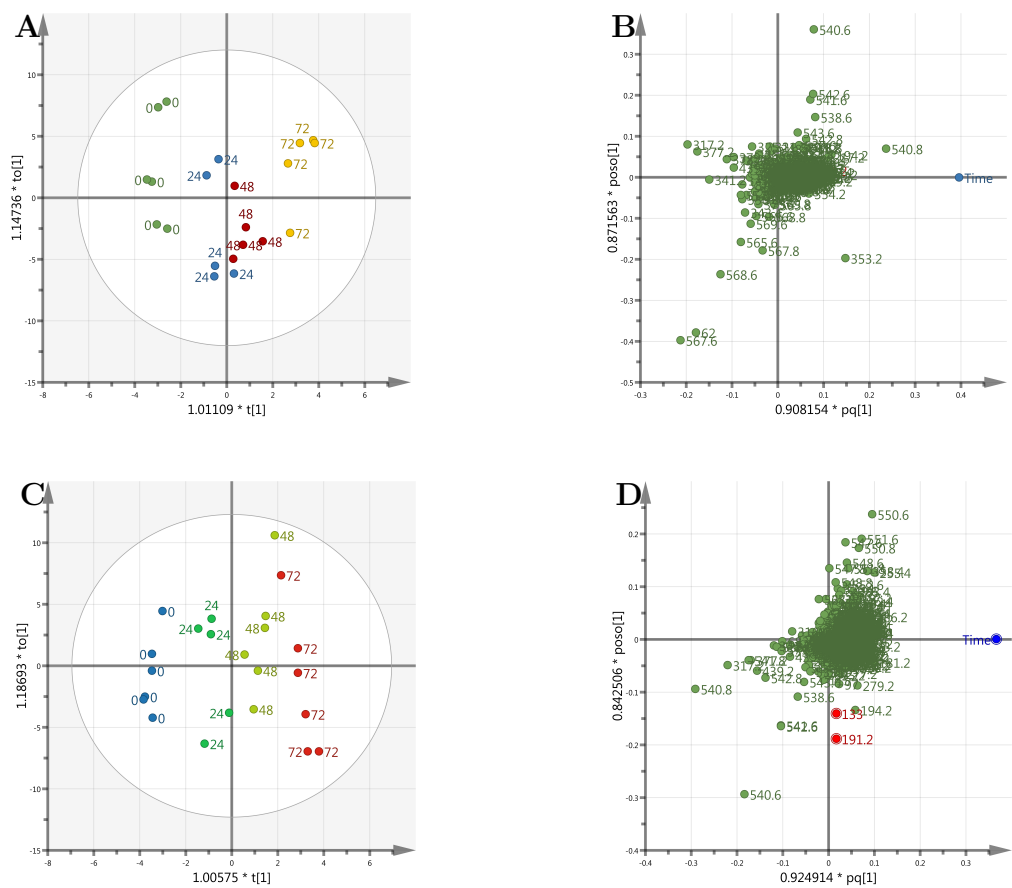


Figure 2.15: OPLS of GA-treated, field grown King Edward samples, by time since treatment.

Samples were treated *in vitro* with GA and collected at $t=0, 24, 48$ and 72 . Panels A and B: Samples prepared in October 2016. Panels C and D: Samples prepared in December 2016. A: An OPLS score plot of field grown King Edward samples, in October. Samples are coloured and labelled time since treatment (in hours). The supervised analysis arranges samples along the horizontal axis, based on time since treatment. B: an OPLS loadings plot of field grown King Edward's samples, treated with GA in October. Each point refers to a m/z bin. The Y-variable, Time (since treatment, in hours), is on the far right side of the horizontal axis. Bins that co-vary with the time since treatment lie close to the pq axis. $n=24$. C: An OPLS score plot of field grown King Edward samples, in December. Samples are coloured and labelled time since treatment (in hours). The supervised analysis arranges samples along the horizontal axis, based on time since treatment. B: an OPLS loadings plot of field grown King Edward's samples, treated with GA in December. Each point refers to a m/z bin. The Y-variable, Time (since treatment, in hours), is on the far right side of the horizontal axis. Bins that co-vary with the time since treatment lie close to the pq axis. $n=24$.

Figure 2.17C, it is clear that the temporal pattern has been lost in this PCA.

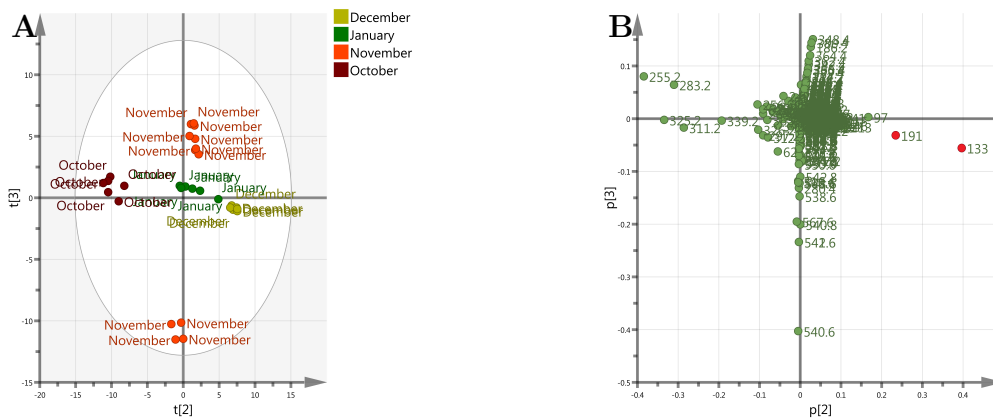


Figure 2.16: An OPLS of field grown Desiree samples, by month.

A: PCA score plot of field grown Desiree samples, at $t=0$ in the *in vitro*. Samples are coloured and labelled by month of analysis. The axes are components 2 and 3 of the PCA model. B: a PCA loadings plot of field grown Desiree samples. Each point refers to a m/z bin. A and B axes are linked: samples that cluster on the PCA score plot are influenced by masses in the same region of the loadings plot. $n=48$, months = October, November, December 2016, January 2017.

Cv. Russet Burbank

The long dormancy cultivar, Russet Burbank, was used to generate the data in Figures 2.18 and 2.19. Due to a later harvest time compared to the cultivars discussed above, Russet Burbank samples were analysed in December 2016, and January, February, March 2017. Figure 2.18 on page 51 shows results of an OPLS analysis of control samples, using sampling month as a Y-variable. This produces the separation observed in the score plot, Figure 2.18A, with a spectrum of samples corresponding to storage month. In the loadings plot, Figure 2.18B, the Month is at the far right of the plot. The highlighted m/z correspond to the markers observed in earlier analyses. m/z 133 appears to be orthogonal to the Y-variable, whereas m/z 191 lies on the same axis, if not particularly far from the origin.

Figure 2.19 on page 52 shows plots from OPLS analysis and PCAs of GA-treated Russet Burbank samples. The OPLS plots in Figure 2.19 A and B refer to the earliest sampling month, December. In the score plot, Figure 2.19A, the samples are coloured and labeled by time since GA-treatment. The separation observed is generated by setting the time since treatment as a Y-variable. This can be seen on the far right of the loadings plot in Figure 2.19B. According to these loadings, m/z 133 is highly influential, though not completely in line with time since treatment, m/z 191 is also at the edge of the metabolite cluster, suggesting it co-varies with the Y-variable. Samples for Figure 2.19C and D were analysed in March. Figure 2.19C is a PCA score plot, with samples labelled

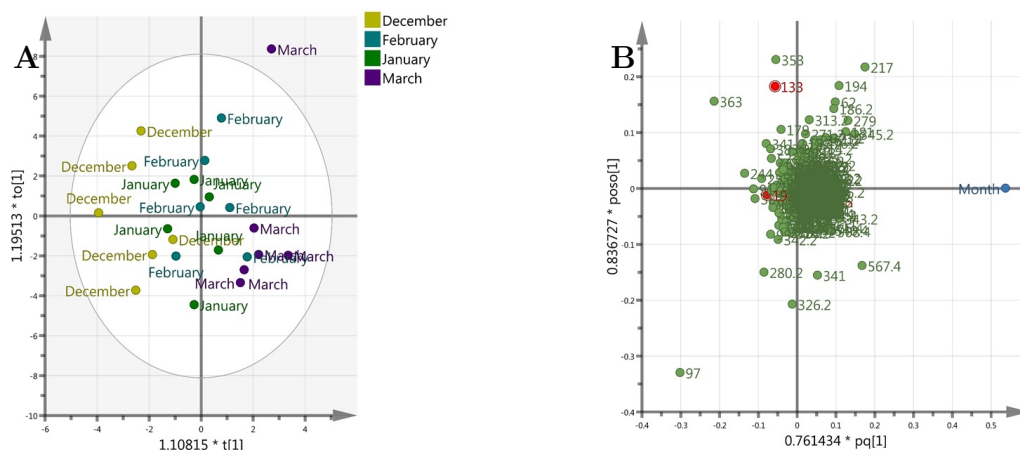


Figure 2.18: An OPLS of field grown Russet Burbank samples, by month.

A: An OPLS score plot of field grown Russet Burbank samples, at $t=0$ in the *in vitro*. Samples are coloured and labelled by month of analysis. The supervised analysis arranges samples along the horizontal axis, based on month of analysis. B: an OPLS loadings plot of field grown Russet Burbank samples. Each point refers to a m/z bin. The Y-variable, Month, is on the far right side of the horizontal axis. Bins that co-vary with the month lie close to the pq axis. $n=48$, months = December 2016, January, February, March 2017.

Burbank tubers discussed above, but had shorter dormancy, leading to sampling in December 2016, January and February 2017. Figure 2.20 on page 53 shows an OPLS analysis of control samples from the sampling period. The storage month is used as a Y-variable, leading to the separation seen in the score plot in Figure 2.20A. The loadings are displayed in Figure 2.20B. The Y-value, harvest month, is displayed to the far right of the horizontal axis. m/z 133 and 191 are both clearly influential, although only m/z 133 varies along the horizontal component as much as the orthogonal component. Data for GA-treated December and February (freshly harvested and starting to sprout respectively) are displayed in Figure 2.21 on page 54. Figure 2.21A and B display OPLS data for December samples. The time since treatment with GA is used as a Y-variable, leading to the separation of data points on the bases of these scores in Figure 2.21A. The loadings plot in Figure 2.21B shows strong influence from m/z 133, whereas most of m/z 191's influence is orthogonal to the time since treatment. The February OPLS loadings plot, Figure 2.21D shows the opposite pattern. m/z 191 co-varies strongly with time since GA-treatment, whereas m/z 133 is orthogonal. The pattern in the February score plot, Figure 2.21C is similar to that in Figure 2.21A, suggesting that this is a fair comparison.

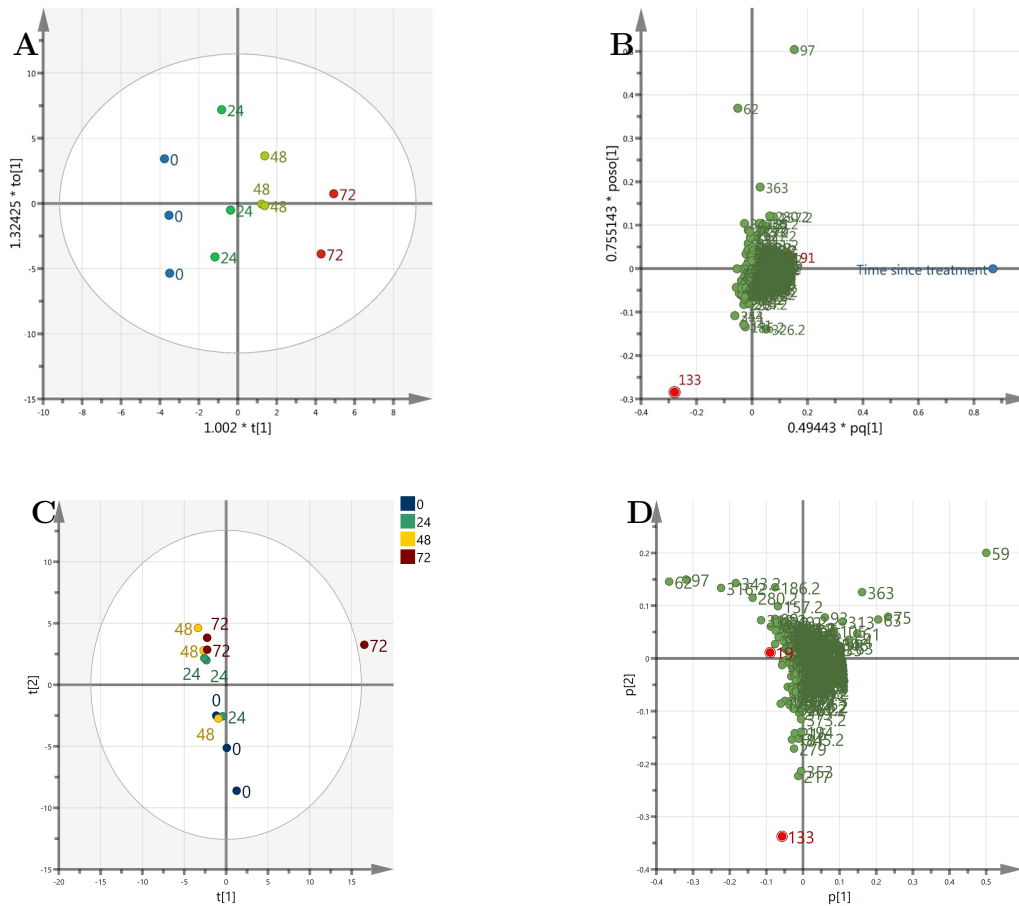


Figure 2.19: OPLS and PCA plots of GA-treated field grown Russet Burbank samples, by time since treatment.

Samples were treated *in vitro* with GA and collected at $t=0$, 24, 48 and 72. Panels A and B: Samples prepared in December 2016. Panels C and D: Samples prepared in March 2017. A: An OPLS score plot of field grown Russet Burbank samples, in December. Samples are coloured and labelled time since treatment (in hours). The supervised analysis arranges samples along the horizontal axis, based on time since treatment. B: an OPLS loadings plot of field grown Russet Burbank samples, treated with GA in December. Each point refers to a m/z bin. The Y-variable, Time (since treatment, in hours), is on the far right side of the horizontal axis. Bins that co-vary with the time since treatment lie close to the pq axis. $n=12$. Panel C: A PCA score plot of field grown Russet Burbank samples, in March. Samples are coloured and labelled time since treatment (in hours). D: a PCA loadings plot of field grown Russet Burbank samples, treated with GA in March. Each point refers to a m/z bin. $n=12$.

2.4 Discussion

Potato tuber dormancy break is a commercially important biological process. This trait is an artefact of wild potatoes' overwintering strategy, which has important implications for industry. Tuber sprouting has important consequences for shelf life and processing properties, therefore optimising storage and utilisation practices are important to

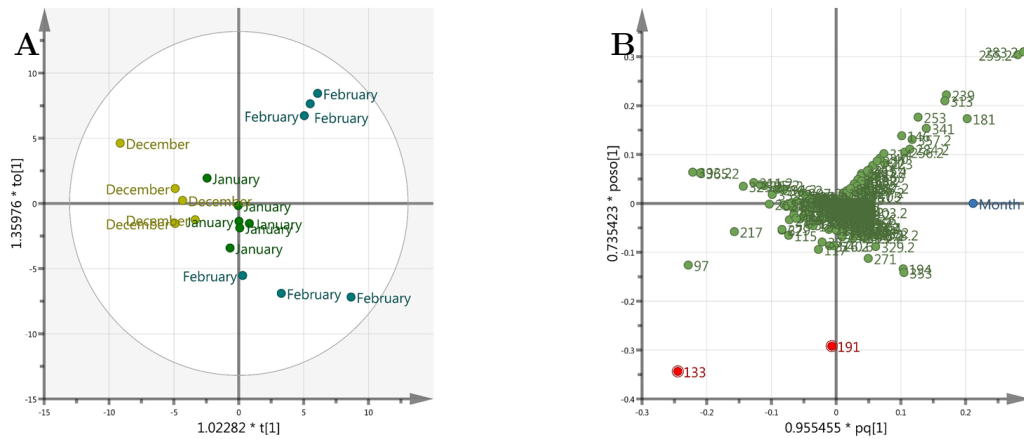


Figure 2.20: An OPLS of field grown Maris Piper samples, by month.

A: An OPLS score plot of field grown MarisPiper samples, at $t=0$ in the *in vitro*. Samples are coloured and labelled by month of analysis. The supervised analysis arranges samples along the horizontal axis, based on month of analysis. B: an OPLS loadings plot of field grown Maris Piper samples. Each point refers to a m/z bin. The Y-variable, Month, is on the far right side of the horizontal axis. Bins that co-vary with the month lie close to the pq axis. $n=36$, months = December 2016, January, February 2017.

minimise waste-related losses.

The biological mechanisms underpinning the process have been studied from a number of perspectives, but usually focus on whole tuber dynamics. This chapter frames the question of dormancy break at the bud level and examines the associated metabolic profile changes. This approach links a very practical agronomic question to ideas about meristem quiescence found in plant developmental biology.

2.4.1 System and assumptions

The buds analysed in this chapter are quiescent axillary meristems. Our current understanding of axillary meristem quiescence suggests that these entire structures are arrested at the transition between G_1 and S cell cycle phases. Upon reactivation, they regain competence and proliferate rapidly. This reversible cell cycle exit does not involve cell specialisation; function is limited to housekeeping and cell respiration processes. Quiescent meristems remain stem-like, without dividing. The release of quiescence is an essential part of tuber sprouting; as dormancy breaks, meristems become proliferative. Here, I suggest this process is closely linked to changes in their metabolism. This chapter uses a mass spectrometry approach to capture metabolic profiles changing with sprouting and discover markers linked to different stages of sprouting.

Samples in this chapter build on Hartmann's GA work by using their *in vitro* system to generate experimental material. A closer examination of the internal structures is a

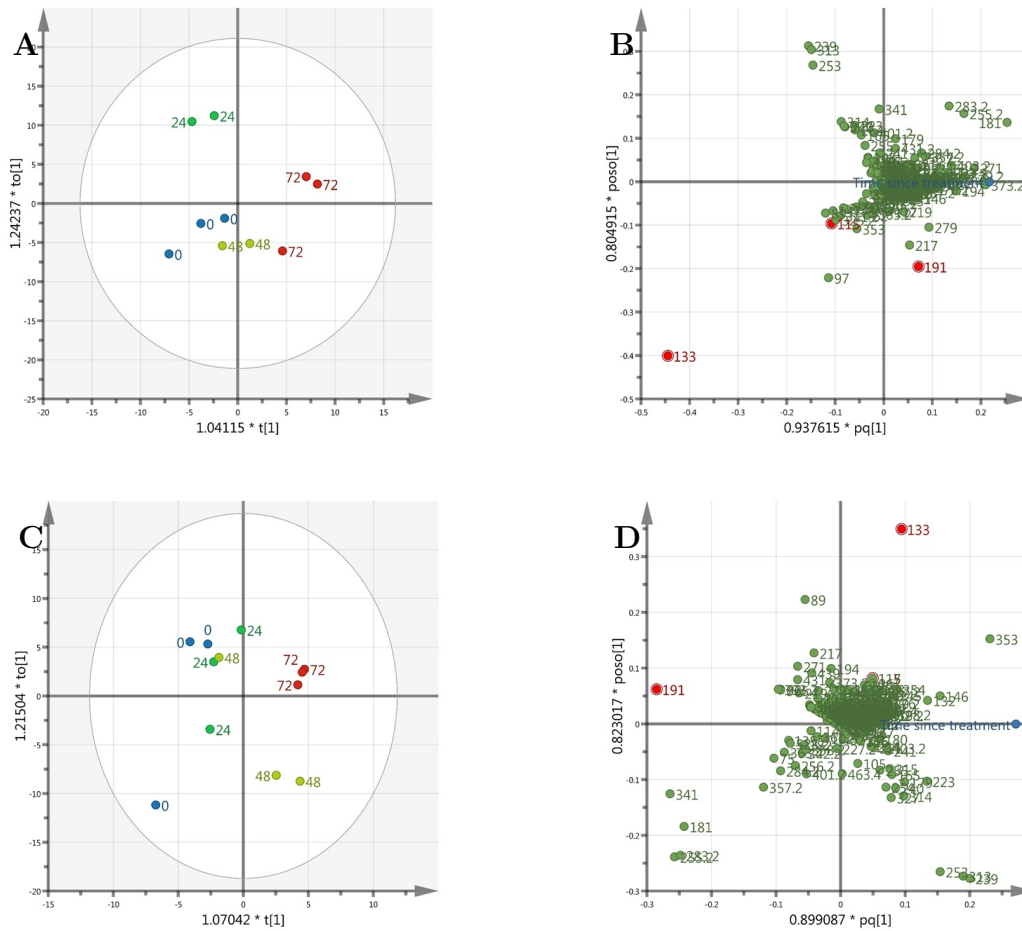


Figure 2.21: OPLS of GA-treated field grown Maris Piper samples, by time since treatment.

Samples were treated *in vitro* with GA and collected at $t=0, 24, 48$ and 72 . Panels A and B: Samples prepared in December 2016. Panels C and D: Samples prepared in February 2017. A: An OPLS score plot of field grown Maris Piper samples, in December. Samples are coloured and labelled time since treatment (in hours). The supervised analysis arranges samples along the horizontal axis, based on time since treatment. B: an OPLS loadings plot of field grown Maris Piper samples, treated with GA in December. Each point refers to a m/z bin. The Y-variable, Time (since treatment, in hours), is on the far right side of the horizontal axis. Bins that co-vary with the time since treatment lie close to the pq axis. $n=12$. C: An OPLS score plot of field grown Maris Piper samples, in February. Samples are coloured and labelled time since treatment (in hours). The supervised analysis arranges samples along the horizontal axis, based on time since treatment. D: an OPLS loadings plot of field grown Maris Piper samples, treated with GA in February. Each point refers to a m/z bin. The Y-variable, Time (since treatment, in hours), is on the far right side of the horizontal axis. Bins that co-vary with the time since treatment lie close to the pq axis. $n=12$.

useful way to corroborate some assumptions about the system. Material was fixed and sectioned to confirm the idea that GA-treatment elicits proliferation (Hartmann *et al.* 2011). The internal anatomy of the sampled buds is illustrated in Figure 2.4 on page

32. These images reveal the typical shape of these structures, in many ways resembling a classical shoot apical meristem. These buds include a central meristem, surrounded by leaf primordia and sheathed in leaf bases. There is further evidence that these structures are operating like activated meristems; they are linked to the cortex, which contain the tuber's stored reserves. This ties into the tuber's function as an overwintering structure with a large nutrient store. Meristems are heterotrophic and require the import of nutrients to sustain their activity (Janssen *et al.* 2014). The buds use tuber reserves to rapidly regenerate the aerial structures during the subsequent growing season.

As illustrated in Figure 2.4 on page 32, these entire tuber buds contain a number of tissue types, including leaf primordia, epidermis and the meristem. Liquid extracts lose this spatial resolution, but capture the whole structure associated with sprouting. This entire feature is in a state of arrested development during dormancy, and undergoes reactivation during sprouting.

Figure 2.5 on page 34 presents high resolution images of buds exiting dormancy. Figure 2.5 A and B capture the endogenous process: over the course of storage, the buds grows from the small, recessed structure seen in Figure 2.5 A to the larger and more elaborate rosette in Figure 2.5 B. It is not possible to attribute the difference in the texture of the outer leaves to senescence, as it could be an artefact of the imaging process, leading to damage. However, there is a clear difference in the arrangement of leaf primordia. The youngest leaf bases emerge from the bud in Figure 2.5 B and have a more clearly flattened shape. In Figure 2.5 A the leaf bases are still contained within the depression and the primordia are rounder in shape. Figure 2.5 C and D compared the responses to water- and GA-treatment after 96 hours. The control in Figure 2.5 C clearly shows that after 8 weeks in storage the bud largely resembles the freshly harvested one in Figure 2.5 A. there are only a small number of visible leaf primordia and they are all contained within the cavity and covered by the protective older leaf. In contrast, Figure 2.5 D is much more protuberant. It is not at the same stage as Figure 2.5 B, with fewer leaf bases visible, but a substantial change has occurred in the 96 hours since it resembled Figure 2.5 C. Crucially, individual cells are visible and there doesn't appear to be any inappropriate elongation. This suggests that the observed growth and emergence is driven by cell division, rather than changes in turgidity and cell wall dynamics, leading to cell enlargement. There is no evidence that the cells are elongating in response to treatment; the meristem is genuinely proliferative. This supports the subsequent use of GA as a sprouting initiator to examine the metabolic dimensions of potato sprouting; it seems to be a reasonably good mimic for the process, rather than an elongation driver.

Even though the data in this chapter mask some of the smaller features in the bud complex, sampling was carried out on a much finer scale compared to much of the existing

literature. Previous studies have framed their questions on the whole tuber scale, for example examining hormone signalling (for review, see Aksenova *et al.* 2013). This is a substantially more mature area of research. The maintenance of dormancy during early storage is thought to involve insensitivity to growth promoters such as GA. As endodormancy progresses, ABA levels fall and CK levels increase; once threshold levels of these are reached, the meristem becomes primed to respond to cues. At this point GA perception is possible and it can elicit growth. This model underpins the schematic in Figure 2.1 on page 22.

The Hartmann *et al.* (2011) *in vitro* system of controlled dormancy release is used throughout this chapter to assess the endodormancy status of stored material and produce staged samples for metabolic profiling. Figure 2.7 on page 35 supports the idea that GA promotes sprouting in primed, weakly dormant tuber buds - a week after treatment, control samples show significantly lower levels of sprouting compared to the GA treated ones. This is in spite of the potential growth stimulating effects of manipulating the buds and transferring them from storage at 7°C to a growth cabinet at 22°C.

The pattern observed in experiments such as that in Figure 2.7 changes during tuber storage. During endodormancy, none of the buds sprout, regardless of treatment. After endodormancy, samples are primed and responsive to the GA trigger (as shown). Tubers that have been stored for a long time sprout at a high rate, regardless of treatment; the change in temperature associated with the *in vitro* is enough to trigger dormancy break. The length of time associated with these stages is variable and depends on genetic and environmental factors. Some influential forces are stochastic, such as conditions encountered in the field or perturbation in storage. However, cultivars and genetic backgrounds also have a substantial impact.

2.4.2 Development series

In this chapter, the GA-treatment *in vitro* system was an important tool for improving the consistency of the dormancy status of biological material when examining potato sprouting. As such, the system could be used to answer a range of interesting and valuable questions. For example, identifying the switch from endodormant to primed could be a commercially useful study target. Here it was used as the basis of a development series and to identify the window of interest for analysis. The metabolomics approach used here is better suited to questions pertaining to the switch from quiescence to proliferation, rather than GA-sensitivity. Data presented here are associated with metabolic changes occurring before a visible sprouting response would be observed. Based on the sprouting time observed in primed, weakly dormant tuber buds treated with GA, 0-72

hours after treatment is the key window for observation.

The *in vitro* system was used to generate samples for metabolic profiling. A key innovation in this study was the application of mass spectrometry to these very small samples. The mass spectrometry captured the rapid metabolic reconfiguration associated with sprout initiation. A key aspect of the mass spectrometry platform used in this chapter was the ability to perform non-targeted mass scans. The non targeted platform yields a global look at changes in the metabolome. In addition to a non targeted platform, an unsupervised analysis (using multivariate techniques such as principal component analysis) can be used to explore the data. This allows patterns to be found without assumptions about the system biasing the outcome. In this analysis, the PCA loadings plots were useful decision tools for marker selection for subsequent study (Overy *et al.* 2005). Influential variables in these plots were considered candidate markers. From these markers, key metabolic changes in response to meristem reactivation were examined. Marker identity and associated biochemistry are discussed in later chapters.

Based on Figure 2.9A on page 39, it is possible to discriminate metabolically between treated and control samples after 24 hours. This suggest that there are rapid changes as the buds prepare to sprout. In GA-treated samples, there is a time-linked distribution of these profiles, as seen in Figure 2.10 A and C. Lead m/z markers can be identified from the loadings plots (Figure 2.10 B and D). This allows metabolic changes that co-occur with sprout initiation and have been captured in these datasets to be identified. A detailed discussion of how these m/z markers are identified is presented in Chapter 3. However, at this early stage, these m/z markers were putatively identified on the basis of mass as key components of the Krebs cycle, as shown in Table 2.2 on page 38. A comprehensive description of this methodology and subsequent experimental steps are explored in 3.3.1, on page 68.

The development series design offered a system with a robust control system. The changes in metabolism in response to a growth promoter could be separated from manipulation effects, such as responses elicited by temperature changes, physical damage or microbial activity. This allowed a time series in association with the treatment to be analysed and any potential metabolic switches to be captured.

When this experimental design used primed, but dormant material, it was ideal for dissecting responses directly involved in the switch to growth (“primed” material as discussed in Figure 2.1 on page 22). Competent cells reacted to the growth promoter by switching their metabolic strategy, meaning a well controlled time lapse could be produced. This is in contrast to subsequent experiments, such as the storage series. The experiments involving a storage series may have been a better reflection of the endogenous process, but needed to infer the sprouting initiation time point, so the process could not

be captured in such fine detail.

2.4.3 Apical dominance

A contrasting approach exploited the developmental gradient present in tubers, produced by apical dominance. The apical bud produces a zone of inhibition, restricting the growth of adjacent buds (Teper-Bamnolker *et al.* 2012). When treated with GA, apical buds displayed a much greater sprouting response than those at the stolon end (60% compared to 10% at stolon end, preliminary data). This represents a naturally occurring sprouting gradient system. Using this naturally occurring apical dominance meant that the tuber identity can be used as an alternative prediction for clustering. If the buds were metabolically equivalent, it would follow that minor differences between tubers would explain most of the variation. Figure 2.8 on page 37, particularly Figure 2.8 A, demonstrates that sampled apices were more similar to each other than to lateral buds from the same tuber, in terms of metabolic profiles. Key markers identified from this separation could be linked to the differences in endodormancy status. It is interesting that several of the same markers appear to be influential on the loadings plots for Figure 2.8 and Figure 2.10. This suggests that the differences in apical and stolon buds are linked to the response to GA discussed above. The apical buds are more metabolically active than stolon buds, and this appears to involve the same processes as the growth promotion seen in response to GA-treatment.

2.4.4 Storage series

Interesting as the effects of apical dominance are, they do not tackle the main commercial question. Once the apical meristem has sprouted, the tuber loses processing properties rapidly (Burton 1982). The design that produced the data for Figures 2.11 to 2.13 on page Pages 43, 44 and 46 represents the closest experimental system to the agricultural question underpinning this chapter. Stored material from the staggered planting regime was sampled repeatedly to track metabolic changes taking place as dormancy progressed. Different batches were examined simultaneously to capture changes in response to storage time, but resampling at intervals meant that outlier batches could be identified and consistent patterns were independent of events in the growth season. This is illustrated in Table 2.3.

Figures 2.11 and 2.12 link the same m/z markers found in the development series and apical dominance analyses to the distribution of profiles along the storage gradient. This is a promising corroboration of the *in vitro* system. It suggests the long term release of dormancy in storage is associated with the same metabolic changes driven by the growth

promoter GA. This implies it is a useful model system in which to conduct experiments to examine the question of potato dormancy break.

Figure 2.13 on page 46 is more equivocal, suggesting that there are larger-scale changes to the bud metabolic profile during storage. This could mean that the GA-challenge system is a key tool for examining changes in metabolic ability as sprouting ability increases. Sprouting-linked changes are of most interest, as opposed to any other processes co-occurring during storage. This dataset contains useful information about other changes associated with storage, but it is somewhat limited given the difficulties in inferring the exact timing of sprouting initiation in the absence of GA.

2.4.5 Cultivars

The final section of this chapter examines metabolic profiles from a range of cultivars. So far, most of the data presented have been from glasshouse grown cv. King Edward tubers. The following figures aim to test the generality of those observations and use genetic background as a variable. The markers identified in King Edward support the hypothesis that metabolic profiles can be used to stage tubers with relation to dormancy status. The fact that the same markers (m/z 133, 191, 115) appeared in response to artificial dormancy ending cues, apical dominance and different storage timings bodes well for their generality as useful tools for monitoring dormancy break. By expanding into a range of cultivars, I aimed to ascertain whether the changes I observed were stereotypical in a range of potato cultivars that differed in dormancy length.

Figure 2.14 and 2.15 on pages 47 and 48 examine cv. King Edward tubers that were grown in the field in Yorkshire 2016. Once harvested, these were transported to Sutton Bridge Crop Storage Research, cooled by 1°C per day to a temperature of 4°C . Once cooled, they were kept at 4°C in 1t boxes until it was couriered to the University of Sheffield for analysis. As such, these data aim to bridge the gap between observations from glasshouse grown tubers and standard industry practice.

On the basis of the OPLS analysis in Figure 2.14 on page 47, I conclude that m/z 191.2 is a key marker for the metabolic changes occurring in tubers during storage. This is corroborated by the patterns observed in Figure 2.15 on page 48 - m/z 191.2 shows different levels of influence in samples treated with GA in October (Figure 2.15A and B) and December (Figure 2.15C and D). This may reflect differences in tubers' capacity to perceive and respond to GA, triggering the same set of metabolic changes observed in previous experiments.

Figures 2.16 and 2.17 on pages 49 and 50 present PCA data for the medium-length dormancy cultivar, Désirée. The unsupervised analysis in Figures 2.16A produces a good

level of separation along component 2, closely linked to m/z 133 and 191 in Figures 2.16B. This evidence, from a distantly related tuber lineage, strongly supports the generality of the observations made using the in-house system.

The GA-response PCAs, in Figure 2.17 on page 50, show that in October (Figure 2.17A and B), m/z 191 and 133 are clearly influential in separating $t=0/24$ from $t=48/72$ along component 1. This suggests that GA is successfully triggering a response in October, and that m/z 133 and 191 are diagnostic of this response. By January, the temporal pattern in response to GA is lost: m/z 133 and 191 remain key variables, but they do not lead to time-based separation. This may mean that, by January, all buds are committed to sprouting, therefore there is a limited GA-response. The fact that m/z 191 and 133 vary may reflect that the sampled buds were all at slightly different points along the reactivation process.

The longest dormancy cultivar studied is Russet Burbank. Sampling these tubers was possible until March 2017, which represents the limit of non-treated potato tuber storage. Russet Burbank is also a well studied cultivar, as it is the most important in the USA. Data for this cultivar are presented in Figure 2.18 and Figure 2.19 on pages 51 and 52.

Figure 2.18 on page 51 is an OPLS plot of bud metabolic profiles, separated by month of analysis. In the OPLS loadings plot (Figure 2.18 on page 51B) m/z 133 is clearly separated from the central cluster, but orthogonal to the sampling month. On the other hand, m/z 191, on the edge of the central cluster is very close to the y -variable axis and may be more informative as a covarying marker.

A similar pattern can be observed in Figure 2.19 on page 52B; m/z 191 covaries well with the time since GA-treatment, whereas m/z 133's influence is more equivocal. By March, as illustrated in Figure 2.19 on page 52C and D, there is a really good separation by time since treatment along component 2, which is well explained by m/z 133. This shows a change in the relative influence of m/z 191, in favour of 133 over the storage period.

Data for the final cultivar, Maris Piper, are shown in Figure 2.20 and Figure 2.21 on pages 53 and 54. Maris Piper has an intermediate dormancy length, similar to Désirée. The OPLS loadings plot in Figure 2.20B on page 53 shows that the key markers, m/z 191 and 133 are both separate from the central cluster of metabolite bins, although they are both orthogonal to the sampling month. As m/z 133 is in the bottom left quadrant, it does co-vary with the y -variable, although it is as important as m/z 191 on the orthogonal component.

Figure 2.21 on page 54A and B refer to an OPLS analysis of GA-treated bud metabolic profiles in December. Figure 2.21B is the loadings plot. Much like the Loadings plot

in Figure 2.20B, m/z 133 is in the bottom-left quadrant, meaning it does co-vary with the Y-variable (time since treatment with GA), but is also influences the orthogonal component. m/z 191 is mostly orthogonal to the time since treatment, suggesting it is not a discriminant marker at this stage in storage.

Figure 2.21C and D are OPLS plots for buds treated with GA in February. In contrast to Figure 2.21B, this loadings plot (Figure 2.21D) shows m/z 191 close to the same component axis as time since treatment, showing it as an influential variable. m/z 133, on the other hand, is largely orthogonal to the Y-variable, suggesting it does not explain the observed GA-response.

In conclusion, the key m/z markers from the detailed glasshouse King Edward study are influential on the seasonal plots (Figures 2.14, 2.16, 2.18 and 2.20). In many cases the same ones appear in the GA-response plots at the earliest sampling point (Figures 2.15, 2.17, 2.19 and 2.21B). By the latest time point (GA+72hours), these GA treatment temporal patterns have often dissipated (Figures 2.15 and 2.17D) or even flipped (Figures 2.19 and 2.21D) so that m/z 191 and 133 swap axis of influence. All this suggests that the changes observed in cv. King Edward are stereotypical of potato dormancy break and cultivar independent.

2.4.6 Conclusions

The data discussed in this chapter produce some highly promising m/z markers for the diagnosis of dormancy status. Metabolic profiles have characteristic patterns, linked to the dormancy status of sampled material. All four of the the contrasting experimental designs seem to corroborate each other (GA treatment, staggered planting, field grown cultivars and bud apex-stolon rank), as the same ions shape the loadings plots independently. The main markers in the metabolic profiles are generally independent of cultivar and the type of dormancy ending signal used. This suggests the experiments were successful in capturing endogenous dormancy release process; tuber buds sprouting display a set of stereotypical changes to their metabolic profiles. The next chapter will take these markers forward for more specific and detailed biochemical analysis. This information will be linked to the underlying mechanisms involved in the process of dormancy break.

Chapter 3

The role of TCA cycle activity during early dormancy release in tuber buds

3.1 Introduction

The results described in Chapter 2 led to the putative identification of a number of metabolites linked to the TCA cycle as early markers of the exit from dormancy/entry to sprouting in potato tubers. In this chapter techniques will be used to definitively identify these metabolites, followed by a series of experiments to investigate the potential role of altered TCA metabolism during sprouting. Before describing the results of these experiments, let us first consider the biological context of sprouting and published ideas on how metabolism might be linked to the observed growth phenomenon.

At first sight, the link between metabolism and growth appears trivial. Clearly growth requires energy and the synthesis of macromolecules to provide the structures for growth. In plant cells there is the added element that maintenance of turgor is needed via uptake of water into the vacuole to physically drive growth, but nevertheless it seems obvious that a general increase in metabolism will accompany an increase in growth (Öpik & Rolfe 2003). However, especially when considering the initiation of cell division-associated growth, the mechanistic role of metabolism may become more complicated. A key (and still puzzling) observation in this area stems from research performed in the 1930s which led to the identification of the Warburg effect in oncology. It has been revisited many times, due to the recurrent observation that metabolism changes in an unexpected way during the development of aberrantly proliferating cells associated with mammalian tumours (for review, see Garber 2004). Essentially, despite the requirement

for a high growth rate, tumours often display a preference for an aerobic glycolytic pathway rather than an oxidative pathway. These cells appear to favour an apparently less efficient mechanism for energy production, despite there being an apparent need for high energy supply. The fundamental proposition (which remains contentious) is that the observed metabolic reconfiguration associated with the Warburg effect plays a causal role in the development of rapidly expanding cancerous tissues (Vander Heiden *et al.* 2009).

In biology, cell specialisation tends to be a unidirectional process. As gene expression changes during cell specialisation, a lineage becomes committed to an increasingly narrow range of fates. A consequence of this differentiation is an eventual loss of the ability to carry out cell division. Thus, starting from embryogenesis, and continuing during post-embryonic development, stem-like properties become increasingly rare so that, eventually, only relatively small numbers of adult stem cells are present to perform damage repair functions.

A key property of oncogenesis is the inappropriate resumption of rapid cell division in somatic cells, which lose these constraints on cell division. Concurrently cells gain the ability to rapidly utilize nutrients from surrounding tissues. Acting as a strong sink is a key component of tumour evolution: in order to proliferate at the distinctively high rate, cells need to replicate their contents rapidly, performing anabolism. To accomplish this, tumours demand the rapid catabolism of any available resources, and this fuels the anabolic processes required for their growth. During carcinogenesis, the normal controls preventing runaway metabolism are lost, so the developing tumour can divert and appropriate vast quantities of substrate, which eventually leads to the detrimental symptoms associated with it in a medical context (Banerjee 2018).

On a metabolic level, this fast breakdown of substrate has been linked to aerobic glycolysis. Although the necrotic centre of tumours can develop anoxic conditions, a reduction in the intensity of the canonical TCA cycle and oxidative phosphorylation in favour of the reactions usually associated with fermentation is observable before this characteristic develops. There are a range of explanations for this phenomenon, including mitochondrial immaturity in newly divided cells (glycolysis takes place in the cytoplasm and does not depend on mitochondria), decrease in the DNA damage risk by ROS associated with oxidative phosphorylation, or the Warburg effect (Rahman *et al.* 2013). According to the Warburg effect, aerobic fermentation could be taking place because cancer cells are not ATP starved; chemical energy is not the rate limiting factor for them to thrive. By bypassing the TCA cycle and oxidative phosphorylation, tumour cells can perform the initial breakdown of macromolecules, required to repurpose them, without investing time and substrate into the production of a functional system of oxidative

phosphorylation. Warburg proposed that the ability to implement this change had a causal role in the development of cancerous traits.

A non pathological system that demonstrates a similar change in function has been observed in a unicellular context (Chen *et al.* 2007). These authors observed that yeast metabolise differently under stress or high nutrient conditions. Stress promotes a highly ATP efficient metabolic strategy in order to maximise the probability of survival. However, yeast is capable of detecting pools of nutrients and switching to a system of fermentation and proliferation in order to exploit new resources and use them more rapidly than competitors. In the yeast model, the features described in mammalian carcinogenesis provide a simple conceptual model for metabolic changes in association with proliferation; this system demands speed and simplicity to allow the rapid exploitation of carbon resources, which might be better served by non-oxidative catabolism provided ATP generation is not limiting.

Plant multicellularity evolved independently of the animal equivalent, so many of the controls in place to prevent aberrant cell division are unrelated to those observed in an oncology setting. However, plants possess cells that have an interesting parallel; meristems are pools of stem cells that remain proliferative and avoid specialisation (Öpik & Rolfe 2003). In the case of quiescent meristems, there can be a long hiatus in the active cell division process. followed by a relatively rapid activation of cell division, fueled by catabolism of carbon stores which, with respect to the size of the meristem, provide a massive excess of resource. However, in plants the reactivation of cell division in the quiescent meristem is not maladaptive for the organism (in contrast to mammalian cancer), rather an important tool in plant plasticity, mediating responses to environmental cues through development (Dodsworth 2009).

Such metabolic comparisons between plant and animal cell proliferation events have been little explored and the results described in Chapter 2 provide an entry point for the exploration of such ideas, which will be investigated further in this chapter.

Sugar measurements have retained value in an agricultural setting because sugar levels covary with other potato quality factors. For example, high levels of reducing sugars are suboptimal in processing because they lead to browning during cooking and high risk of acrylamide formation. Acrylamide is a toxic product of the Maillard reaction, where the amino acid asparagine reacts with reducing sugars under cooking temperatures. Acrylamide is a carcinogen and it is now thought that dietary exposure is a genuine health risk (Mottram & Dodson 2002).

However, sucrose and reducing sugar levels are not the most dependable marker, as they can be perturbed by a range of factors. For example, there are substantial differences between cultivars in sugar composition, and many environmental factors can

also influence sugar dynamics, such as cold induced sweetening, associated with low temperature phosphorolysis of starch (Herman *et al.* 2016). Clearly, most of the changes in starch-related metabolism are occurring at the tuber level, so it is difficult to relate changes in reducing sugar levels measured in tuber tissue to what is taking place at the meristem level. As alluded to in previous chapters, a key innovation in this thesis is to consider the question of potato dormancy break at the bud level, and the examination of the question from a plant development perspective. A comparison of the findings at bud level to bulk changes at tuber level would provide an insight into just how metabolically different these two tissues are, and potentially provide an insight into how the two tissues are coordinated at a metabolic level.

As indicated at the beginning of the introduction, the results described in Chapter 2 provide putative identities of a number of metabolites linked to the TCA cycle. Although profiling is a powerful technique to provide leads on interesting metabolites, the confirmation of metabolite identity requires the application of further analytical techniques, and this chapter uses tandem mass spectrometry to identify moieties of interest discussed in chapter 2. The premise of tandem mass spectrometry, or MS/MS, is that different isobaric molecules will have different labile groups. A narrow mass window of interest is selected and these moieties are bombarded with neutral gas, leading to the production of many fragment ions, which are detected during the second mass spectrometry phase. Differences in structural properties mean that isobaric molecules lose different labile side groups, yielding different fragment fingerprints. Comparisons between samples can confirm that the same molecule is observed at a given mass, and standard solutions can be used to generate an expected fingerprint for identification.

The overarching objective of this chapter is to examine the identity of the markers discussed in Chapter 2 and put them into a plant metabolism context. The concepts from animal and yeast systems, discussed above, point to other proliferative cell types and the ways in which they modify metabolism to facilitate growth. When these questions are applied in a plant development context, they also have agronomic importance. Current potato storage best practice is examined to produce a baseline level of understanding of the current process.

3.1.1 Hypotheses

- The metabolic changes associated with dormancy break in (described in Chapter 2) correspond to altered aspects of primary metabolism; specifically the TCA cycle.
- The TCA-linked metabolism of deeply dormant tissues shows a different pattern to samples approaching sprouting

- The changes in TCA-metabolite pattern that occur in buds during sprouting provide a more consistent assay of tuber growth status than the traditional analysis of sugar levels in tubers, particularly across when comparing different cultivars.

3.2 Material and Methods

3.2.1 Marker identification using online databases

Mass/charge markers from chapter 2 were putatively identified using the online databases Kanehisa *et al.* (2018), SolCyc (2018), CHEMnetBASE (2015) by means of their exact mass search function. Outputs from the search were eliminated to leave plausible candidates, based on their monoisotopic exact mass, association with plant biochemical pathways and structural suitability for ionisation. SolCyc (2018) was particularly useful, in that candidate mass identities were all found in related species, as opposed to animal or pharmaceutical contexts.

3.2.2 Tandem Mass Spectrometry

Marker identification was confirmed using tandem mass spectrometry. *In silico* fragmentation patterns were predicted using ChemDraw. These were corroborated using standard solutions of the predicted TCA cycle intermediates.

Concentrated standard solutions (0.1 g/ml w/v in) 100% methanol were analysed on the QSTAR in negative ionisation mode. A product ion (to the nearest Dalton) was selected, then analysed to produce a fragmentation pattern for the ion of interest. Sample extracts, produced as in 2.2.5 were analysed using the parameters established for each m/z of interest. Sample extracts from buds treated with GA and control, for t=0-48 were examined and their fragmentation pattern was compared to the predicted pattern and the standard solution. In this way, marker identification was confirmed across sample types.

3.2.3 Pathway analysis

Once m/z markers were identified, the data were reexamined to extract m/z of linked metabolites. The relative intensity of these m/z in GA-treated samples, compared to controls (% total ion count, GA value/control value), were mapped on metabolic network diagrams on a color intensity scale.

Solcyc had an automated version of this process. Full datasets with automated putative identities could be uploaded to solcyc using an equivalent formula. This mapped

putative mass identities to a global *Solanum* metabolic network. Solcyc allowed any responsive pathways to be identified. However, it lacked an export function, so identified metabolites from pathways of interest were examined manually (as above) when looking for consistent patterns between datasets.

3.2.4 Sugar extraction from potato tissue

Sugars were extracted from tuber tissue using an ethanol series. Samples were concentric cores of material used in the *in vitro* assay from Chapter 2. 80% ethanol (v/v, adjusted to pH 4.0 with glacial acetic acid) was heated to 80°C. 50 μ l of hot ethanol was added to 100mg of tissue, then vortexed. An additional 250 μ l of hot ethanol was added to the sample, which was incubated on a heating block at 80°C for 10 minutes. The sample was centrifuged at 14000rpm for 5 minutes and the supernatant was decanted.

The pellet was resuspended in 50 μ l of hot 80% (v/v) pH4.0 ethanol by vortexing. An additional 250 μ l of hot ethanol was added to the sample, which was incubated on a heating block at 80°C for 10 minutes. The sample was centrifuged at 14000rpm for 5 minutes and the supernatant was decanted into the same tube as above.

The pellet was resuspended in 50 μ l of hot 50% ethanol (v/v) by vortexing. An additional 250 μ l of hot ethanol was added to the sample, which was incubated on a heating block at 80°C for 10 minutes. The sample was centrifuged at 14000rpm for 5 minutes and the supernatant was decanted into the same tube as above.

The pellet was resuspended in 50 μ l of hot 18 Ω ultrapure distilled deionised water by vortexing. An additional 250 μ l of hot water was added to the sample, which was incubated on a heating block at 80°C for 10 minutes. The sample was centrifuged at 14000rpm for 5 minutes and the supernatant was decanted into the same tube as above.

The combined supernatants were flash frozen in liquid nitrogen and freeze dried at -40°C. The residue was resuspended in 500 μ l of 18 Ω ultrapure distilled deionised water for sugar analysis.

3.2.5 Enzyme-linked spectrophotometric assay of sugars in potato extracts

Sugar extracts from tuber tissue were analysed using an enzyme-linked spectrophotometric assay. This used a pH8.0 100mM HEPES, 5mM MgCl₂, 4mM NAD and 1mM ATP (w/v in water) assay cocktail. 20 μ l of extract was added to 980 μ l of the assay cocktail and mixed. Absorbance was calibrated at 340nm.

1 μ l of hexokinase (5 enzyme activity units) was added to the solution and mixed.

The change in absorbance at 340nm was measured until it stabilised. 1 μ l of G6PDH (5 enzyme activity units) was added to the solution and mixed. The change in absorbance at 340nm was measured until it stabilised. 1 μ l of PGI (5 enzyme activity units) was added to the solution and mixed. The change in absorbance at 340nm was measured until it stabilised. 2 μ l of invertase (2mg/ml w/v, 5 enzyme activity units) was added to the solution and mixed. The change in absorbance at 340nm was measured until it stabilised.

Glucose concentration is proportional to the change in absorbance due to the addition of G6PDH. Fructose concentration is proportional to the change in absorbance due to the addition of PGI. Sucrose concentration is proportional to the change in absorbance due to the addition of Invertase.

3.3 Results

3.3.1 Identifying ions

The results presented in Chapter 2 identified a number of key m/z moieties that reproducibly and under different conditions acted as robust markers of the tuber bud sprouting process. In particular, m/z 191.0, 133.0 and 115.0 were consistently highlighted as potential markers for sprouting. Table 2.2 on page 38 lists these markers and putatively identifies them, based on an exact mass search of Kanehisa *et al.* (2018), as citrate (m/z 191.0), malate (m/z 133.0), and fumarate (m/z 115.0). A knowledge of basic biochemistry leads to a clear association of these metabolites with the Krebs cycle, the core and universal biochemical pathway of oxidative metabolism. Using this as lead, other metabolites associated with the Krebs cycle were analysed in a targeted fashion within datasets reported in Chapter 2, leading to the identification of peaks for aconitate (m/z 173.0), ketoglutarate (m/z 145.0) and oxaloacetate (m/z 131.0).

Initial characterisation of m/z by comparison with available databases is a powerful method for the putative identification of metabolites. However, further analysis is generally required for full confirmation of metabolite identity. To do this, putative mass identities were confirmed using tandem mass spectrometry. In this process, ions in a mass window are fragmented, yielding a MS/MS fingerprint of product ions, created by the loss of labile side groups. These MS/MS spectra can be compared to predicted fragment patterns or experimental data from standard solutions. For example, Figure 3.1 on page 69 shows malate and three of its predicted fragments. Figure 3.1 A shows the molecular structure of malate. Figure 3.1 B-D show malate product ions, their exact masses, and the bonds broken to produce these fragments. This process was repeated for

all metabolites listed in Table 2.2 is first presented in Chapter 2 on page 38, but will be discussed in more detail here. Figure 3.2 on page 70 shows the observed MS/MS spectra for these eight organic acids.

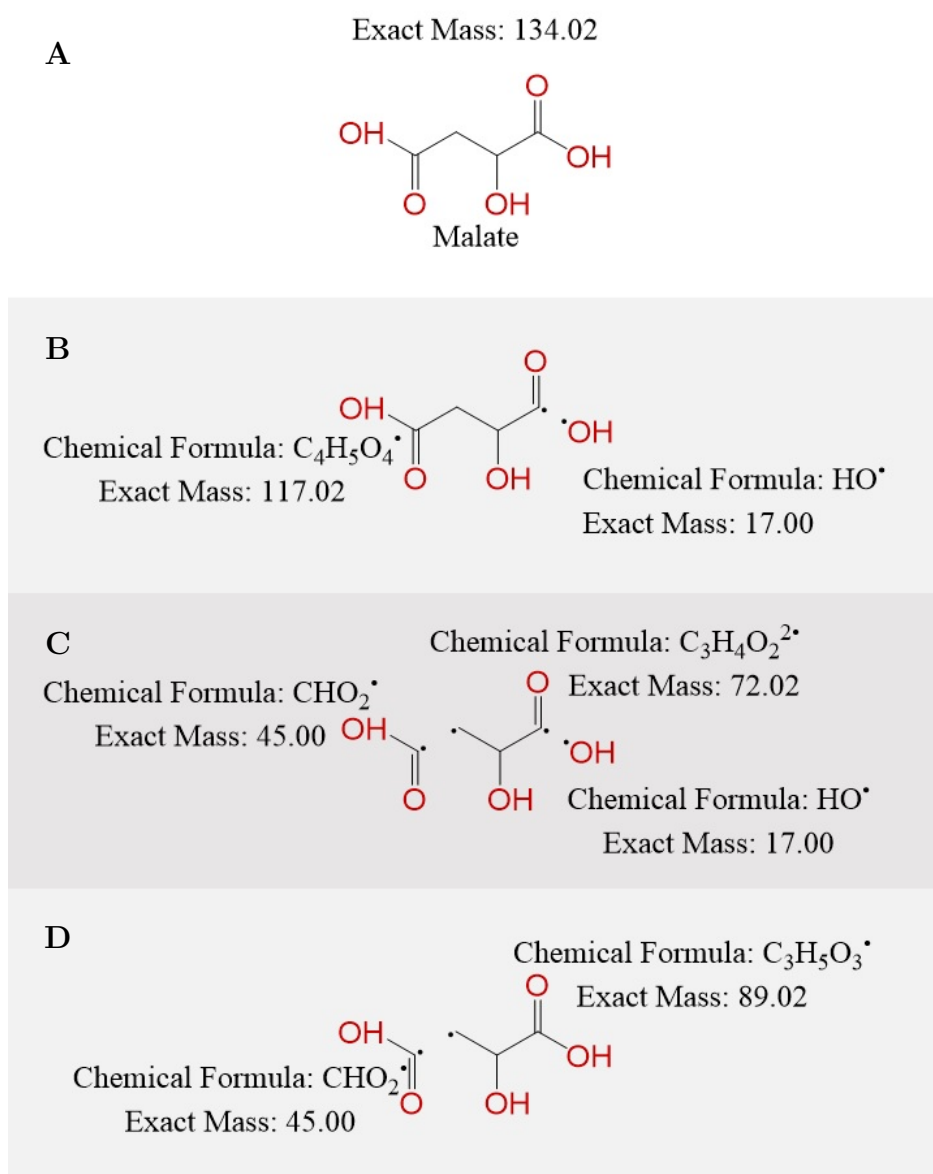


Figure 3.1: Malate *in silico* fragmentation pattern

The software Chemdraw was used to generate predicted fragmentation patterns for metabolites of interest. Malate is illustrated as an exemplar. Chemdraw predicts the mass of product ions when a particular bond is broken. A: The structure of malate, including the exact mass. Panels B, C and D: 3 sets of malate product ions, depending on the fragmentation. Masses and formulae of predicted fragments are displayed.

Figure 3.2 G shows the product ions for malate, discussed above in Figure 3.1 on page 69. The parent ion, m/z 133, (corresponding to Figure 3.1 A) was successfully detected. In addition there are peaks for product ions at m/z 115 (corresponding to Figure 3.1 B),

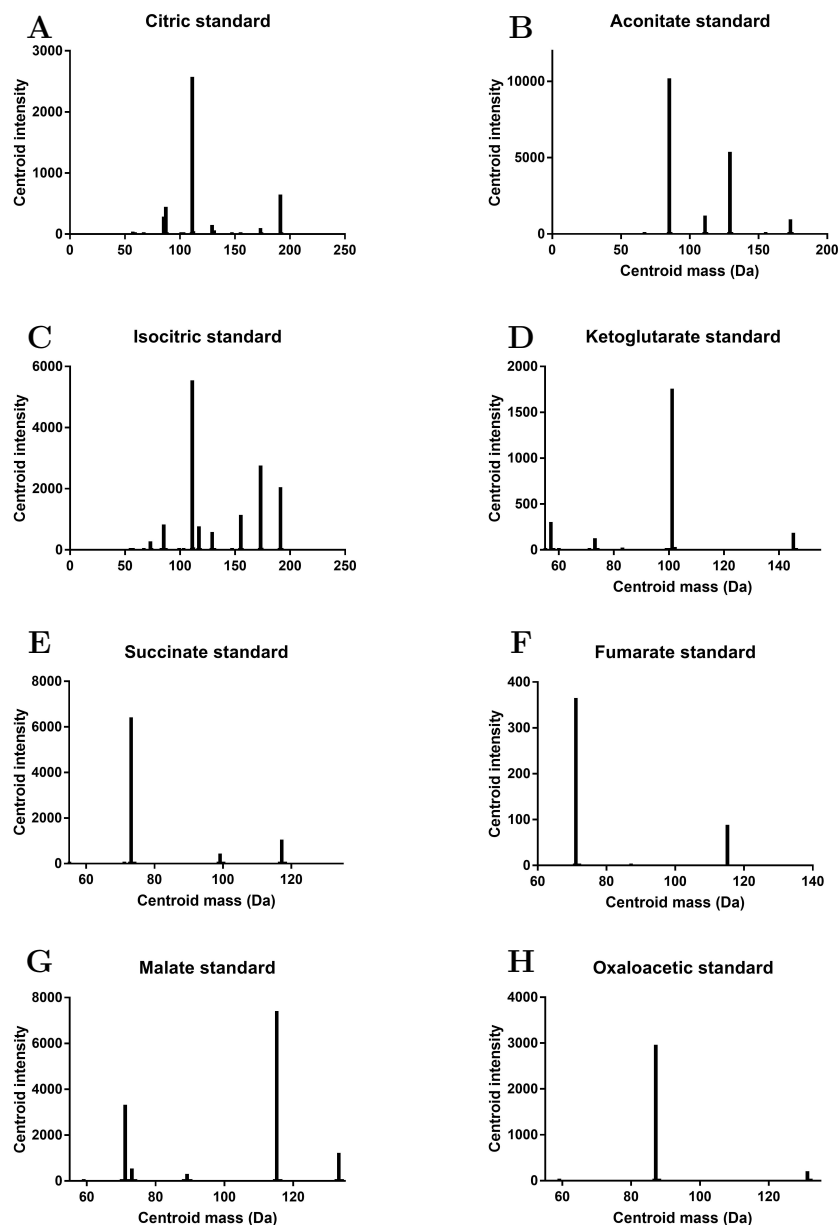


Figure 3.2: Organic acid fragmentation patterns

Standard samples of TCA cycle intermediates were fragmented using tandem MS to yield a fragmentation pattern. These MS/MS fingerprints were the basis for corroboration of putatively identified m/z . A: Citric acid (m/z 191.0); B: Aconitate (m/z 173.0); C: Isocitric acid (m/z 191.0), D: Ketoglutarate (m/z 145.0); E: Succinate (m/z 117.0); F: Fumarate (m/z 115.0); G: Malate (m/z 133.0); H: Oxaloacetic acid (m/z 131.0)

m/z 89 (corresponding to Figure 3.1 D) and m/z 71 (corresponding to Figure 3.1 C).

Figure 3.2 A and C should be considered in conjunction with Figure 3.3 on page 72. These data relate to the fragment pattern of the isomers citrate and isocitrate, overlain in Figure 3.3 C. The original datasets are unable to discriminate between citrate and

isocitrate, because they have the same exact mass (this includes Table2.2). However, as seen in Figure 3.3 A and B, there is a key structural difference, due to the location of the hydroxyl group. This is possibly best illustrated by the key differences in their IUPAC name: citrate (Figure 3.3 A) is **2**-Hydroxypropane-1,2,3-tricarboxylic acid, whereas isocitrate (Figure 3.3 A) is **1**-Hydroxypropane-1,2,3-tricarboxylic acid. As the position of the hydroxyl group in citrate makes the molecule symmetrical, breaking $C_1 - C_2$ and $C_2 - C_3$ yields the same product ions: m/z 85 and 111. By having the hydroxyl group on C_1 , isocitrate is more likely to lose the hydroxyl and a carboxyl group independently. This yields the additional, larger fragments at m/z 155 and 173, highlighted with the red dashed line in Figure 3.3 C.

Figure 3.2 C shows the fragment pattern of aconitic acid. In addition to the parent ion (m/z 173) there are peaks at m/z 85, 111 and 129. For Ketoglutarate (Figure 3.2 D) the key fragment ions correspond to m/z 57, 73 and 101. The succinate MS/MS spectrum (Figure 3.2 E) shows peaks at the parent ion (m/z 117) and at m/z 99 and 73. Fumarate and Oxaloacetate (Figure 3.2 F and H respectively) only have one detected product ion each; m/z 71 and m/z 87 respectively.

Each organic acid's MS/MS detection protocol was applied to a set of six contrasting samples. Their preparation was equivalent to that in Figure 2.9 in chapter 2 on page 39. Tuber buds were GA-treated or mock-inoculated with water. These buds were dissected and flash frozen at $t=0$, 24 and 48 hours from treatment, Then extracted in MeOH/CHCl₃. Figure 3.4 on page 73 shows the MS/MS spectra for fumarate as an example. Figure 3.4 A is the standard solution, also reported in Figure 3.2 F (above). Figure 3.4 B, D and F are water-treated controls, Figure 3.4 C, E and G are GA-treated. Figure 3.4 B and C were frozen immediately after treatment. Figure 3.4 D and E were dissected 24 hours after treatment. Figure 3.4 F and G were sampled at $t=48$ hours. All seven spectra display a peak at m/z 115 (parent ion) and/or m/z 71. This confirms that the previously detected ion at m/z 115 is a match for fumarate.

As indicated at the beginning of this section, all of the metabolites listed in Table2.2 on page 38 and corroborated by MS/MS in Figures 3.1 to 3.4 correspond to components of the Tricarboxylic (Krebs) cycle, shown schematically in Figure 3.5 on page 74. The masses of ions of interest are displayed below the name of each organic acid. In subsequent figures, where possible, components are arranged in the order the metabolites occur in the pathway (for example Figure 3.2). This makes it easier to group components visually and infer any pattern changes. Where the TCA cycle is discussed as a whole, Figure 3.5 will be used as a basic framework for reference.

Having established that the lead m/z markers identified in Chapter 2 were linked with the TCA cycle, I revisited the data sets to provide an overview of the entire pathway

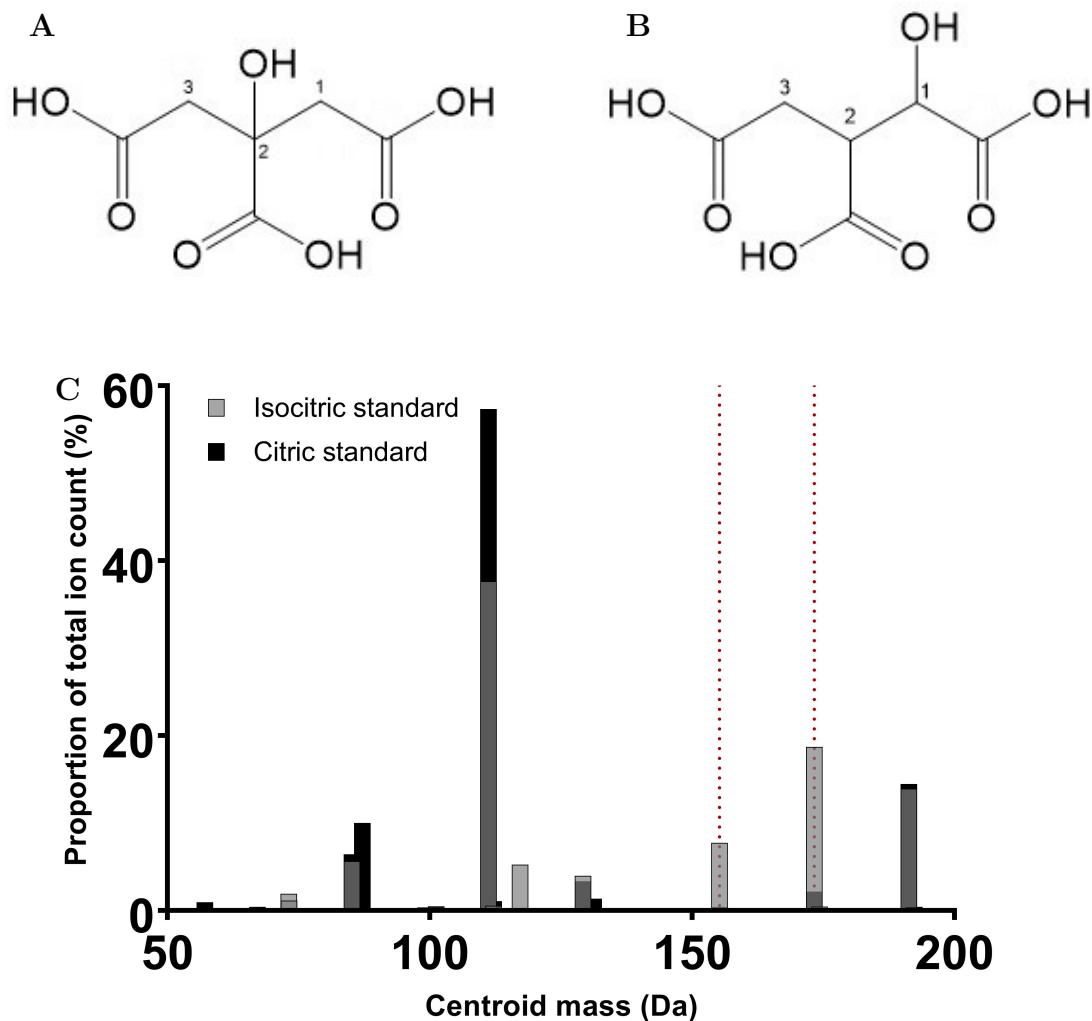


Figure 3.3: Citrate Isomers

Differences in the molecular structure of citrate and isocitrate means they can be discriminated by MS/MS. A: Molecular structure of citric acid. It is symmetrical, with a hydroxyl group and carboxyl group on C_3 . Breaking $C_2 - C_3$ and $C_3 - C_4$ yields the same product ions. B: Molecular structure of isocitric acid. The carboxyl group is on C_3 , whereas the hydroxyl group is on C_4 . The position of the hydroxyl group means that breaking $C_2 - C_3$ and $C_3 - C_4$ yield different product ions. C: MS/MS fragmentation pattern of citric and isocitric acid. The red dashed line indicates two product ions that are predominantly linked to isocitrate.

under different conditions and at different time points in the sprouting process.

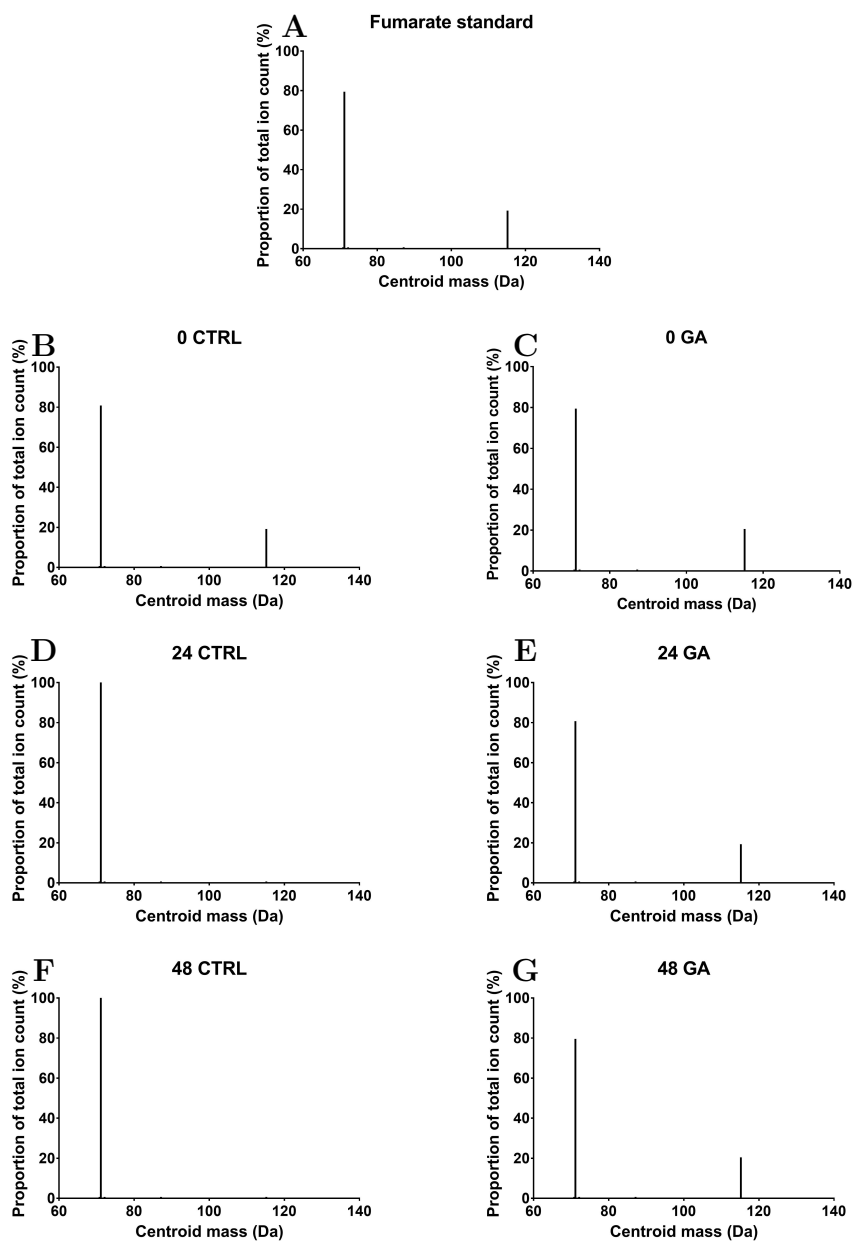


Figure 3.4: Tandem Mass Spectrometry of samples

MS/MS protocols, established for each metabolite, were applied to contrasting samples from 2.9 in chapter 2 to corroborate metabolite identification. Here, Fumarate is illustrated as an exemplar. The diagnostic product ion m/z 71.1 is detected in all samples. A: Fumarate standard solution. B: Water-treated, $t=0$ hours. C: GA-treated, $t=0$ hours. D: Water-treated, $t=24$ hours. E: GA-treated, $t=24$ hours. F: Water-treated, $t=48$ hours. G: GA-treated, $t=48$ hours.

Figure 3.6 on page 75 displays summary data for the relative intensity of TCA cycle intermediates in apical buds, normalised against the stolon bud. These data correspond to those presented in Chapter 2 in Figure 2.8 A and B (glasshouse grown cv. King Ed-

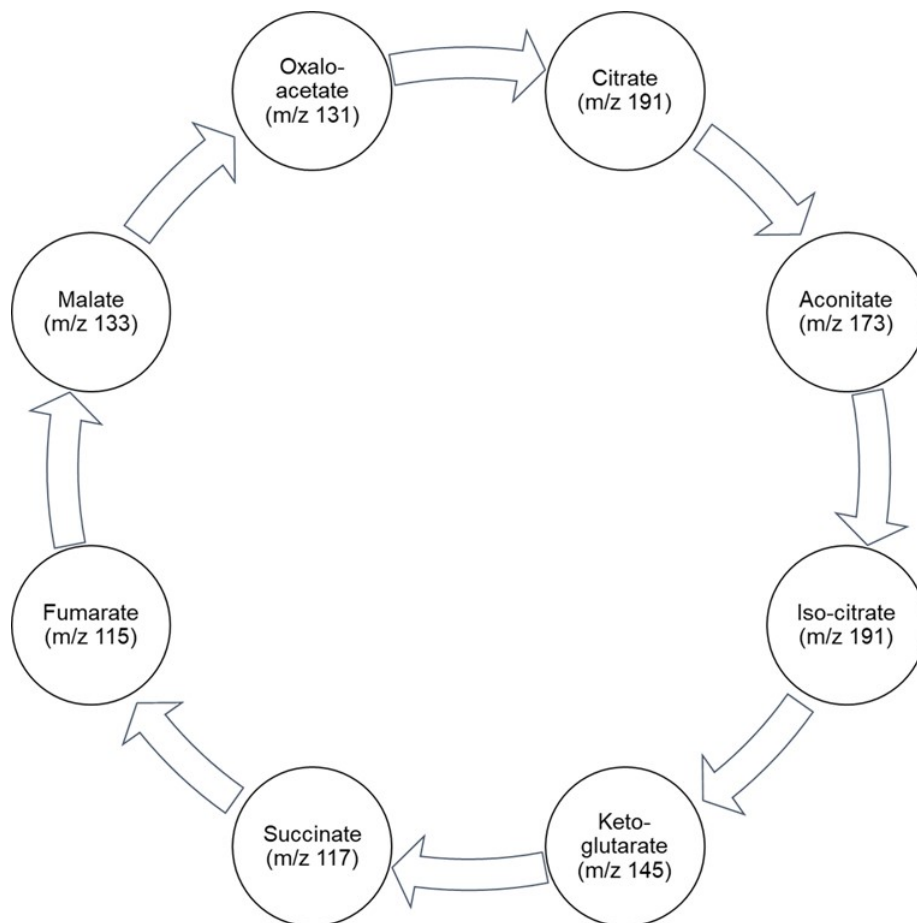


Figure 3.5: TCA cycle

The putatively identified markers correspond to components of primary metabolism. These metabolites are key to the TCA cycle. Detected m/z for each metabolite are displayed below their names.

ward tubers). The tubers were sampled directly, without GA treatment, while they were dormant, but plausibly susceptible to dormancy-ending cues. The red dashed line indicates a 1:1 ratio, i.e. equal intensity in the apex and stolon buds. Apart from succinate and ketoglutarate, all the metabolites clearly show a different level in the apical bud, compared to the stolon bud. Malate and fumarate are detected at substantially higher relative intensities in the apical buds (marginally significant, $p < 0.1$, 2-tailed 1-sample t-test). Citrate and aconitate were marginally lower in the apical buds (marginally significant, $p < 0.1$, 2-tailed 1-sample t-test). The only metabolite to be tested as having a significantly different relative level from 1 was Oxaloacetate. It is present at much lower levels in the apical bud, which has been previously described as less dormant than other meristems on the same tuber (highly significant, $p = 0.0092$, 2-tailed 1-sample t-test). These data are undermined by low levels of replication, although the paired nature of the data adds to the power of the analysis.

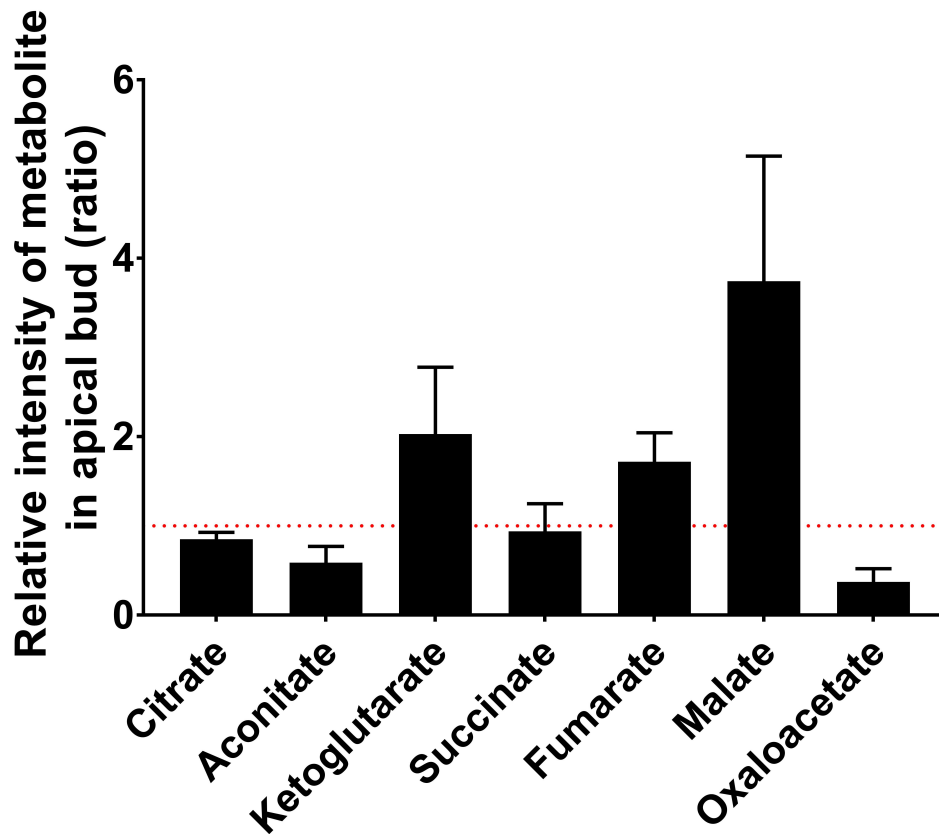


Figure 3.6: Pathway differences in apical and stolon buds

The relative abundance of TCA cycle intermediates in apical bud (ratio with stolon bud). Red dashed line indicates a 1:1 ratio. Ratios were performed on proportion of ion count (%). Error bars are SEM. n=5

Figure 3.7 on page 77 schematically represents changes in the levels of TCA pathway metabolites in apical buds at different times after GA-treatment. Each of the panels in Figure 3.7 uses the framework in Figure 3.5, with a colour intensity scale to indicate metabolite levels in GA treated samples, normalised against controls. Hot colours indicate that a metabolite was detected at higher levels in the GA-treated samples, compared to the controls and cold colours reflect lower detected levels after GA treatment. Samples that are coloured green had roughly similar levels in treated and control samples. Figure 3.7 A represents timepoint t=0, immediately after treatment. Most of the pathway is green and yellow, indicating a moderate increase in detected levels of metabolites, notably citrate, fumarate and malate. The only metabolite to show decreased levels is oxaloacetate. Figure 3.7 B (at 24 hours after GA treatment) shows a contrasting pattern. Although fumarate is more abundant in comparison to the control samples, all the other metabolites show decreased levels. By 48 hours after treatment (Figure 3.7 C) higher levels for most metabolites in the pathway are present, compared to the pattern shown

in Figure 3.7 C, returning to a scenario not dissimilar from that observed at $t=0$. Figure 3.7 D shows the pattern of accumulation at 72 hours after GA treatment. Very high levels of malate and citrates are observed, and aconitate and ketoglutarate levels are also relatively high. Succinate and oxaloacetate levels remain similar to those observed at $t=48$, but the level of fumarate is strongly decrease relative to earlier time points.

The changes in relative metabolite level over time after treatment with GA are summarised in Figure 3.8 on page 78. In all the panels the red dotted line indicates a 1:1 ratio between GA-treated samples and the controls. Figure 3.8 A displays the change in citrate levels with time since treatment. The level remains fairly close to the red line over the first 48 hours, then increases dramatically at 72 hours. Similarly, both aconitate and ketoglutarate show a rise in relative level by 72 hours (Figure 3.8 B and C), and malate shows a dramatic increase in level at this time point (Figure 3.8 F), whereas succinate (Figure 3.8 D) and oxaloacetate do not show an increase at 72hrs. It is noteworthy that six of the seven metabolites analysed show a reproducible drop in relative level at 24 hours after treatment, with the exception of fumarate (Figure 3.8 E) which shows a rise, followed by a continual decrease over the subsequent 48 hours, which is a distinct pattern from those observed for the other TCA metabolites.

Figure 3.9 on page 79 schematically represents changes in the TCA pathway in buds excised from tubers after a time in storage (3, 5 or 7 weeks) and incubated for 72 hours after treatment with GA, as in Chapter 2 Figure 2.12. Each of the panels in Figure 3.9, like those in Figure 3.7 uses the framework in Figure 3.5, with a colour intensity scale to indicate metabolite levels in response to GA treatment. Hot colours indicate that a metabolite was detected at higher levels in the GA-treated samples, compared to the controls, with cold colours reflecting lower levels with GA. Figure 3.9A shows the data for samples after 3 weeks in storage. The citrate and aconitate levels have increased compared to controls, whereas ketoglutarate and oxaloacetate levels are relatively unchanged. Succinate, fumarate and malate are all detected at lower levels compared to the water-treated control samples.

At 5 weeks after harvest (Figure 3.9 B), succinate, fumarate, malate and oxaloacetate are all detected at lower levels, compared to the water-treated samples, with the rest of the pathway being relatively unchanged, apart from an increase in ketoglutarate levels. Finally, Figure 3.9 C shows the TCA metabolite pattern for buds treated with GA after storage for 7 weeks. Unlike the previous time points, the majority of samples display similar levels of metabolites in control and GA-treated samples, apart from ketoglutarate and oxaloacetate, which are detected at lower levels compared to controls.

A deeper insight into the altered responsiveness to sprouting triggers during tuber storage is shown in Figure 3.10 on page 81. Samples in this figure are extracts of buds

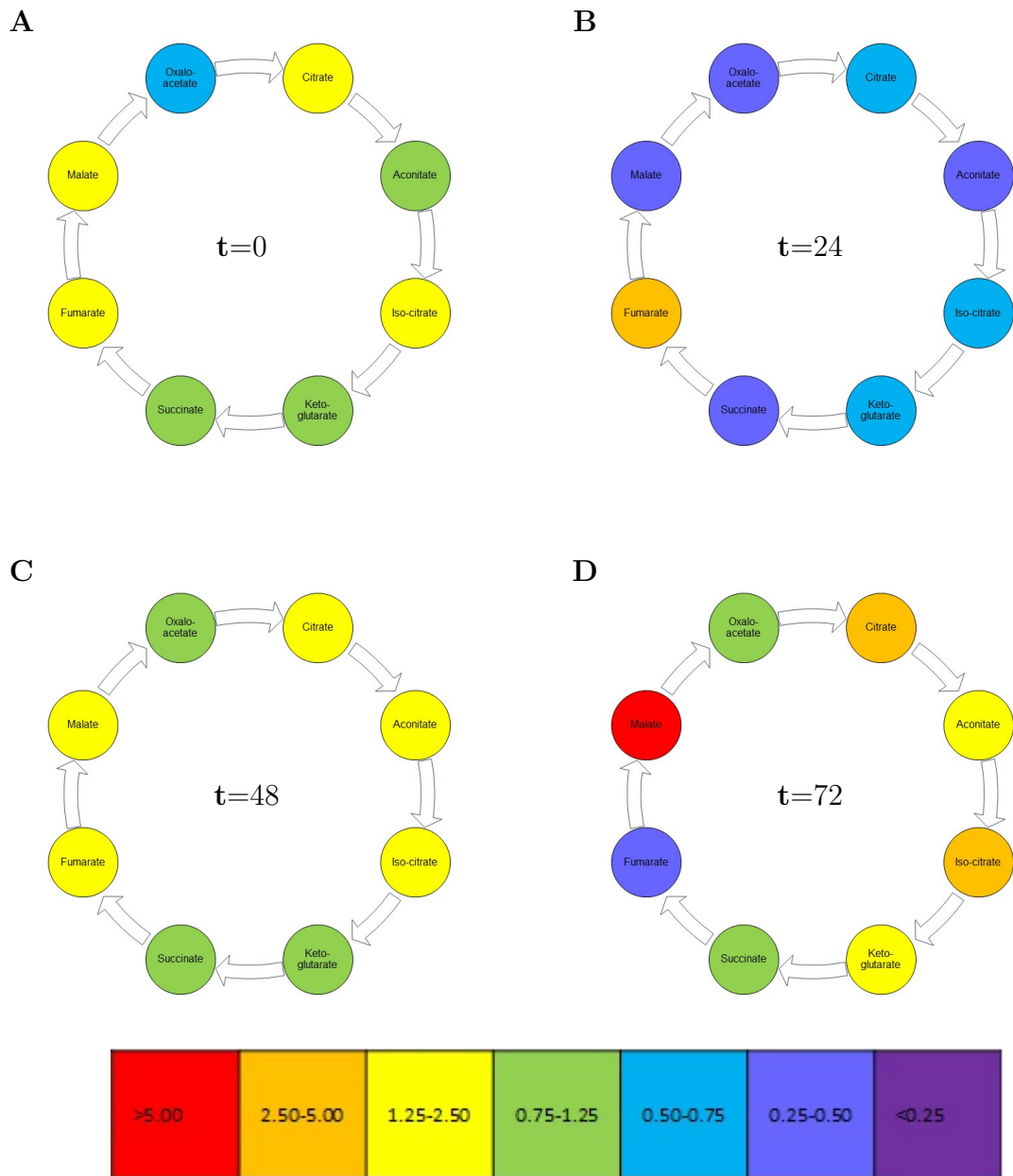


Figure 3.7: TCA cycle configuration in response to GA treatment

The relative abundance of TCA cycle intermediates in GA-treated buds (ratio with water-treated buds). Data relate to samples in 2.9 in chapter 2. Ratios were performed on proportion of ion count (%). Hot colours indicate an ion was more abundant in GA-treated samples than controls. Cold colours indicate an ion was less abundant in GA-treated samples than controls. The colour scale is displayed below the 4 panels. n=38. A: t=0 hours from treatment. B: t=24 hours from treatment. C: t=48 hours from treatment. D: t=72 hours from treatment.

excised from tubers after a time in storage (2, 4, 6 and 8 weeks) and incubated for 72 hours after treatment with GA. Note this is using a \log_2 scale to ensure that scaling factors have the same visual impact regardless of whether they represent increases or

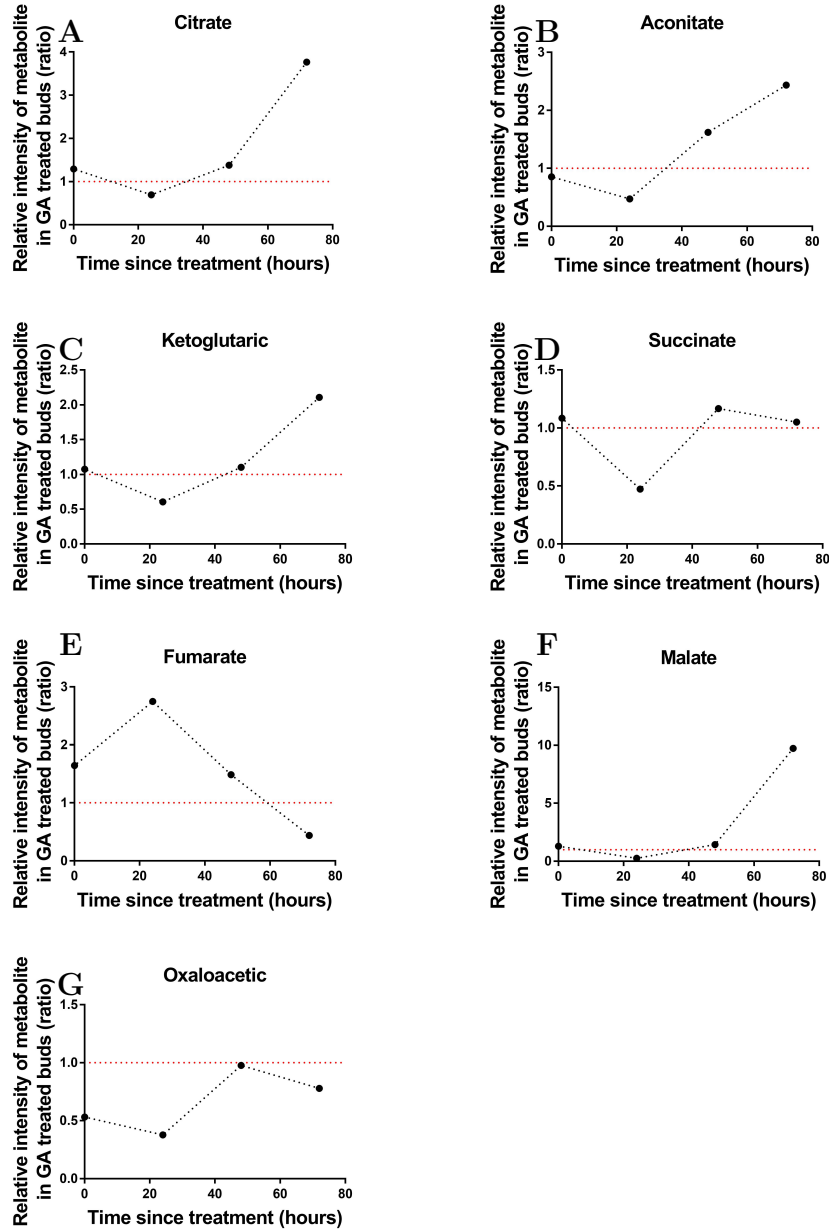


Figure 3.8: Changes in metabolite relative levels in response to GA treatment

The relative abundance of TCA cycle intermediates in GA-treated buds (ratio with water-treated buds) against time since treatment (hours). Data relate to samples in 2.9 in chapter 2. Red dashed line indicates a 1:1 ratio. Ratios were performed on proportion of ion count (%). $n=38$. A: Citrate; B: Aconitate; C: Ketoglutaric; D: Succinate; E: Fumarate; F: Malate; G: Oxaloacetic.

reductions in metabolite levels, with the red dotted line representing the 1:1 ratio between GA-treated and water-treated control samples. Metabolites on the x axis are arranged in the order they appear in the TCA cycle. These data were also presented in chapter 2 in Figure 2.11 on page 43. For treatments at 2 weeks after harvest, all the metabolites

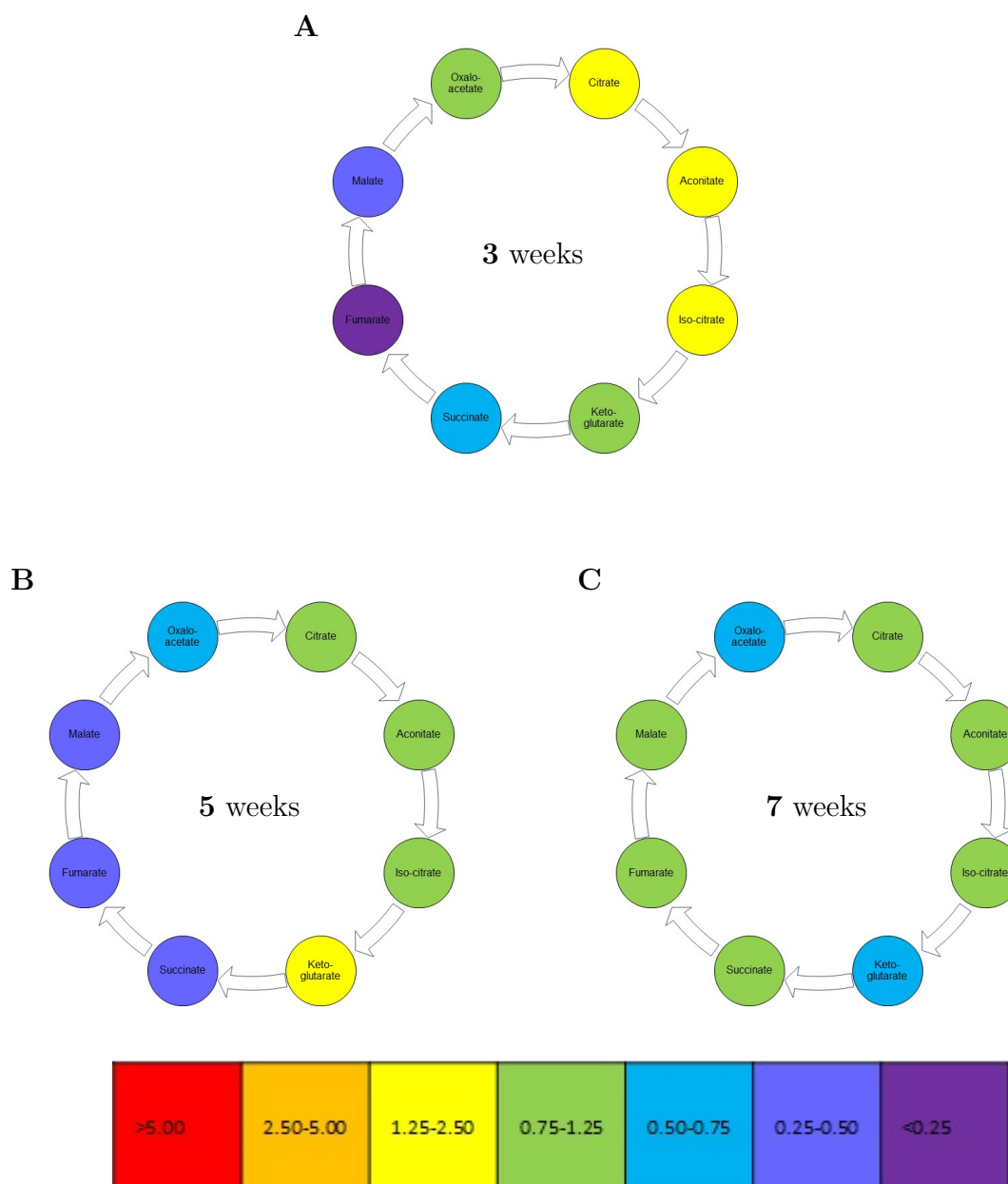


Figure 3.9: TCA cycle configuration during storage

The relative abundance of TCA cycle intermediates in GA-treated buds (ratio with water-treated buds) at various points in storage. Data relate to samples in 2.12 in chapter 2, 72 hours after GA-treatment. Ratios were performed on proportion of ion count (%). Hot colours indicate an ion was more abundant in GA-treated samples than controls. Cold colours indicate an ion was less abundant in GA-treated samples than controls. The colour scale is displayed below the 4 panels. n=36 A: 3 weeks in storage; B: 5 weeks in storage; C: 7 weeks in storage.

were detected at lower levels in the GA-treated samples than in the controls. Citrate and malate showed the lowest relative levels, leading to a non-uniform response around the pathway. By week 4 in storage, there was a marked change in metabolite response, with

aconitate, ketoglutarate and succinate accumulating to high levels after GA treatment, malate and oxaloacetate falling to low levels, and citrate and succinate being essentially non-detectable. Overall, at 4 weeks in storage the TCA response to GA with respect to metabolite level was highly asymmetric. At 6 weeks in storage the response to GA treatment was similar for to that observed at 4 weeks for aconitate, ketoglutarate and succinate, but there were markedly higher levels of malate, oxaloacetate and citrate. By 8 weeks in storage the response of metabolite levels to GA treatment was more similar across all steps of the TCA cycle, the main exception being fumarate which showed a marked relative increase in level compared with control treated samples.

3.3.2 Enzyme-linked spectrophotometric analysis of sugars

In contrast to the focus in this thesis on the molecular events occurring in buds during sprouting, most investigations on tuber growth have analysed tuber tissue, with a specific emphasis on the gross changes in carbohydrate metabolism that occur (since these have direct consequences on processing and product quality). To provide a link between these classical studies and the work reported here on buds, we performed an analysis of sugar levels during sprouting. These data were produced, in part, by Tom Grand during his M. Res. project.

Using an enzyme-linked spectrophotometric assay, sugar levels (glucose, fructose and sucrose) were analysed in four tuber varieties (King Edward, Desiree, Maris Piper, Russet Burbank) at different time points after storage in a commercial storage unit (Sutton Bridge Crop Storage Research Centre). Each of the varieties displays a different dormancy trait, with King Edwards showing the shortest period of dormancy and Russet Burbank the longest. As a consequence, for some varieties (e.g., King Edward) samples do not extend beyond December, whereas others (Russet Burbank) extend into March. Due to differences in the timing of harvest and transport, not all varieties have data for the early time points (October, November) and this should be borne in mind when comparing the datasets.

The results of the analysis are shown in Figure 3.11 on page 82. These tuber samples were excised at the same time as buds discussed in chapter 2 (2.4.5, on page 59). Three of the four cultivars showed an increase in glucose and fructose level during storage, but this was not apparent in Maris Piper (Figure 3.11 C). At the end of the storage period analysed for each cultivar, the level of sucrose was lower than at preceding time points, though the pattern was different for each cultivar. Again Maris Piper (Figure 3.11 C) showed a very minor decrease in sucrose level during storage, whereas in the other three cultivars the changes in level were more dramatic. It is noticeable that in the two varieties

Harvest series

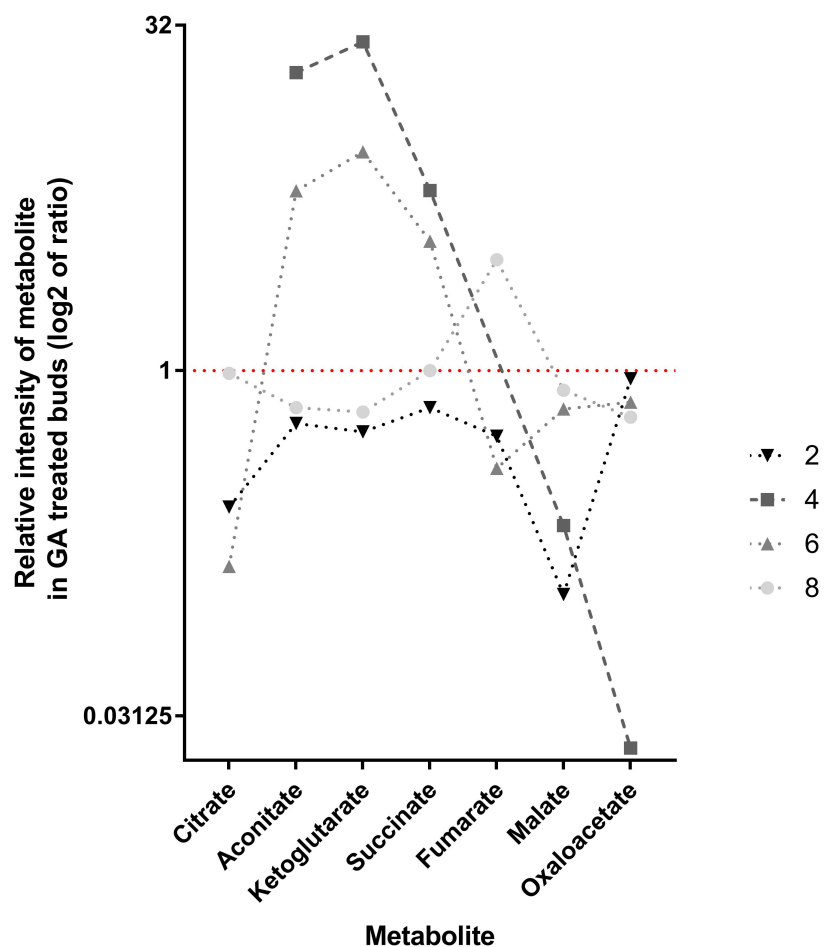


Figure 3.10: Pathway configuration changes with storage

The relative abundance of metabolites in GA-treated buds (ratio with water-treated buds) in the order they appear in the TCA cycle. Data relate to samples in 2.11 in chapter 2, 72 hours after GA-treatment. These were stored for 2-8 weeks after harvest. Ratios were performed on proportion of ion count (%). Data are displayed on a log2 scale. Red dashed line indicates a 1:1 ratio. Note: Values equating to 0 have been excluded (4 weeks in storage: citrate and fumarate). n=15

with data for the earliest sampling point (October) (King Edward and Desiree, Figure 3.11 A and B), sucrose levels were initially very low, rose during storage, then fell to lower values at a late stage in storage. Thus, although there was a general tendency for lower sucrose during storage, there was a more complicated temporal dynamics.

When the ratio of the two hexose sugars glucose and fructose were compared, both over time within a cultivar and between different cultivars (Figure 3.12 on page 83) a complicated pattern emerged. Overall, apart from post-October Desiree samples, glucose

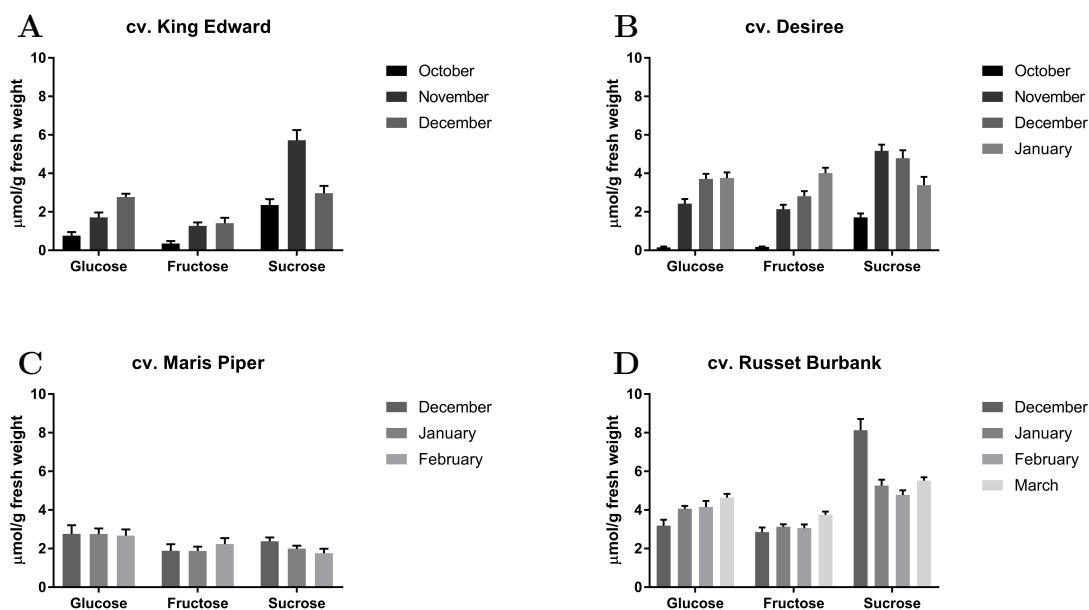


Figure 3.11: Changes in sugar concentration in tuber tissue

Changes in glucose, fructose and sucrose concentration in potato tuber tissue during storage across a range of cultivars ($\mu\text{mol/g}$ fresh weight). Samples were collected from the apical end of tubers at the same time as buds were prepared for GA-treatment. Data are based on enzyme-linked spectrophotometry. Error bars are SEM. Bars are grouped by sugar and coloured by month of analysis. Biological replicates: A: cv. King Edward, $n=90$; B: cv. Desiree, $n=42$; C: Maris Piper, $n=36$; D: cv. Russet Burbank, $n=144$.

was consistently detected at higher levels than fructose. In King Edward the ratio fell and rose during storage, in Desiree it fell dramatically during early storage, and in Maris Piper and Russet Burbank the changes in glucose - fructose ratio were more minor. Similarly, when the ratio of sucrose to total hexose level was analysed (Figure 3.13 on page 83) a complex picture emerged. For three varieties (Russet Burbank, King Edward and Desiree) the final sucrose - hexose ratio measured in storage was lower than preceding values, but the overall temporal pattern was complicated. Russet Burbank showed a dramatic fall in ratio in January, whereas King Edward and Desiree showed a more nuanced fall in sucrose/hexose ratio in December. In contrast, Maris Piper showed a slight increase in sucrose - hexose ratio during storage. Unfortunately for this variety the data points for November/December are not available, since it would be interesting to gauge whether the low level was preceded by a higher sucrose - hexose ratio (as observed in the other varieties).

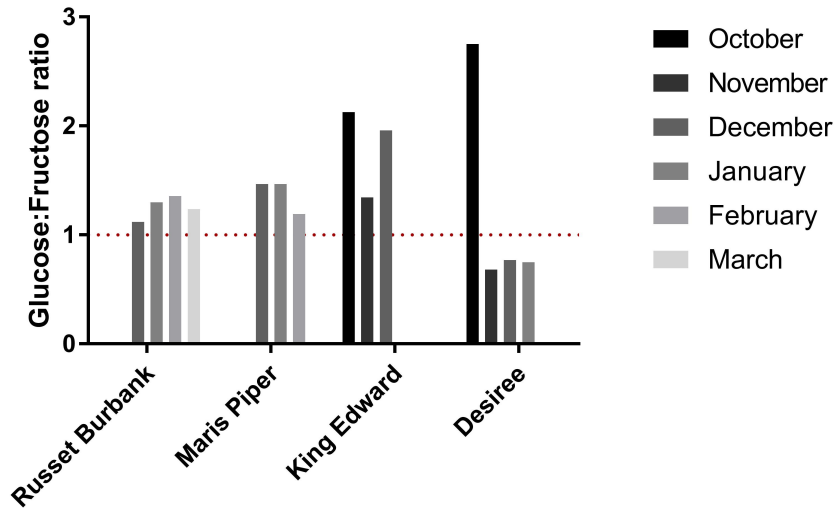


Figure 3.12: Change in hexose composition with tuber storage

Changes in hexose composition in potato tuber tissue during storage across a range of cultivars (Glucose-Fructose concentrations' ratio). Samples were collected from the apical end of tubers at the same time as buds were prepared for GA-treatment. Data are based on enzyme-linked spectrophotometry. Bars are grouped by cultivar and coloured by month of analysis. n=312 biological replicates. Red dashed line indicates a 1:1 ratio.

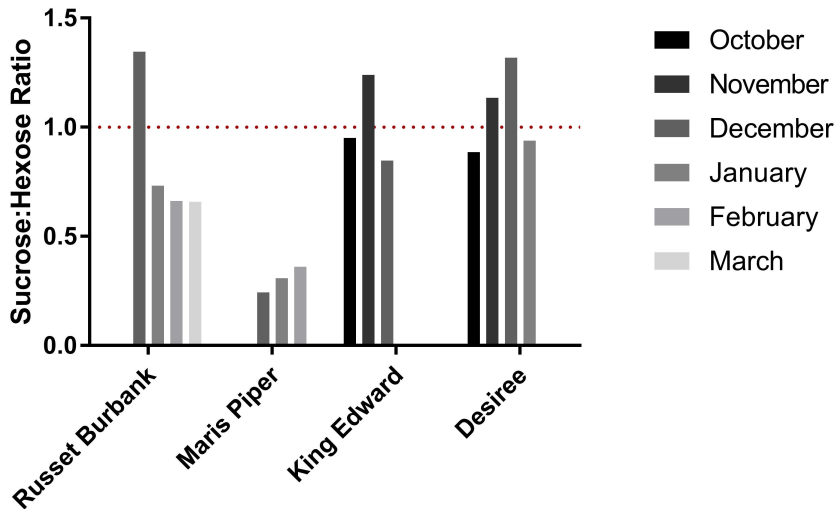


Figure 3.13: Change in sugar composition in tuber storage

Changes in sugar composition in potato tuber tissue during storage across a range of cultivars (Sucrose-Hexose concentrations' ratio). Samples were collected from the apical end of tubers at the same time as buds were prepared for GA-treatment. Data are based on enzyme-linked spectrophotometry. Bars are grouped by cultivar and coloured by month of analysis. n=312. Red dashed line indicates a 1:1 ratio.

3.3.3 The TCA cycle in field grown tubers

Figure 3.14 on page 85 schematically represents the levels of TCA pathway metabolites in field-grown King Edward apical buds at 72 hours after GA-treatment relative to water treated controls also at 72 hours after treatment. The patterns of TCA metabolites are shown for tubers harvested and treated at different time points after harvest (October, November, December), with dormancy status of the tubers decreasing from October (endodormant) through to December (starting to sprout). Each of the panels in Figure 3.14 uses the framework in Figure 3.5, with a colour intensity scale to indicate metabolite levels in GA treated samples, normalised against controls. Hot colours indicate that a metabolite was detected at higher levels in the GA-treated samples, compared to the controls and cold colours reflect relatively lower detected levels after GA treatment. Samples that are coloured green had roughly similar levels in treated and control samples. Figure 3.14 A (October), most of the pathway is green and yellow, indicating a moderate increase in detected levels of metabolites in response to GA, notably citrate, ketoglutarate and oxaloacetate. The only metabolite to show substantially decreased levels is fumarate. Figure 3.14 B (samples from tubers in November, 4 weeks after coming into storage) shows a contrasting pattern. Although ketoglutarate remains as abundant in the GA-treated samples as the controls, the other metabolites show decreased levels, with fumarate and malate particularly depleted. Oxaloacetate was not successfully detected in the control samples, meaning it could not be plotted on this colour intensity scale. By December (by which time buds were beginning to sprout), the associated metabolite pattern (in Figure 3.14 C) is in some ways similar to the pattern observed in October (Figure 3.14 A), as yellow and green dominate. This is the first time-point where fumarate is detected at the same level in the GA-treated samples as the controls.

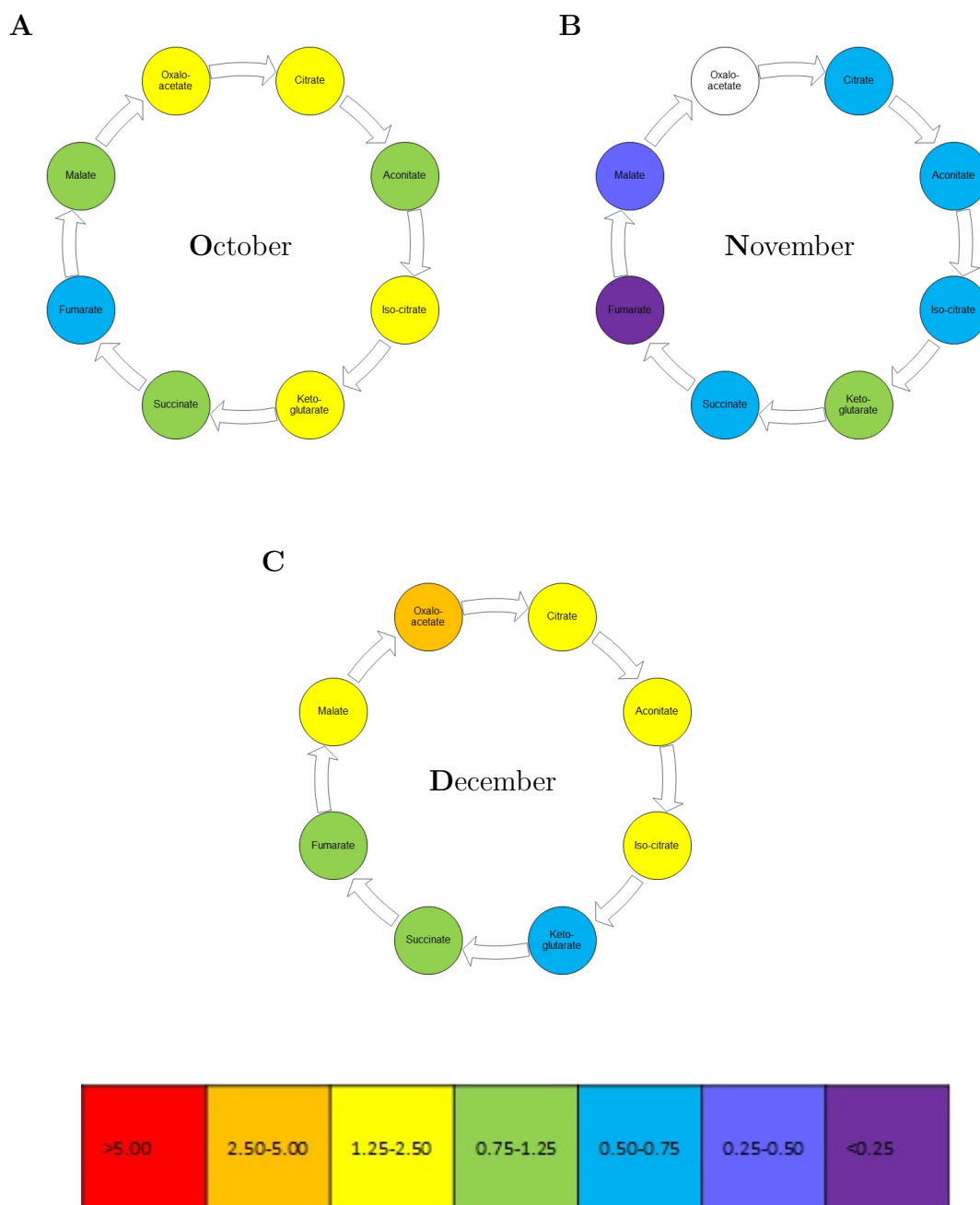


Figure 3.14: TCA cycle configuration in cv. King Edward

The relative abundance of TCA cycle intermediates in King Edward GA-treated buds (ratio with water-treated buds) at $t=72$ hours after treatment. Data relate to samples in 2.15 in chapter 2. Ratios were performed on proportion of ion count (%). Hot colours indicate an ion was more abundant in GA-treated samples than controls. Cold colours indicate an ion was less abundant in GA-treated samples than controls. The colour scale is displayed below the 3 panels. $n=36$. A: GA treatment in October. B: GA treatment in November. (Oxaloacetate = 0% total ion count in the controls) C: GA treatment in December.

The only metabolite detected at lower levels in the December GA-treated buds (rel-

tive to controls) is ketoglutarate. At this time point, oxaloacetate is the metabolite that shows the greatest increase in level, compared to the controls.

Figure 3.15 on page 87 schematically represents the levels of TCA pathway metabolites in field-grown Desiree apical buds at 72 hours after GA-treatment, relative to control-treated tubers. Again, these were analysed at various time points after harvest (October through to January), as indicated, with the colour intensity scale being similar to that described for Figure 3.14. Figure 3.15 A represents samples analysed in October, immediately after harvest. Most of the pathway is yellow, indicating a moderate relative increase in detected levels of metabolites after GA-treatment, notably aconitate, ketoglutarate, succinate and fumarate. The only metabolites to show substantially decreased relative levels at this early dormancy stage were citrate and isocitrate (which were not distinguishable in this analysis). Oxaloacetate was more abundant in the GA-treated samples than the controls. By November (Figure 3.15 B, 4 weeks after coming into storage) a contrasting pattern is observed. By this dormancy stage, all the TCA cycle intermediates were detected at similar levels in control and GA-treated samples, apart from oxaloacetate, which was depleted in the treated samples. Figure 3.15 C (December), shows a similar pattern to Figure 3.15 B, but with values generally shifted slightly. By January, buds were beginning to sprout. The associated metabolite pattern (Figure 3.15 D) shows that all the GA-treated samples had a relatively high concentration of TCA cycle intermediates, with malate and fumarate being particularly enhanced.

Figure 3.16 on page 88 schematically shows the levels of TCA pathway metabolites in field-grown Russet Burbank apical buds at 72 hours after GA-treatment relative to water-treated controls. Again, tubers were analysed at various time points after harvest (December through to March), as indicated, with the colour intensity scale being similar to that described for Figure 3.14. Figure 3.16 A represents samples analysed in December, shortly after harvest. Most of the pathway is green or yellow, indicating a moderate increase in detected levels of metabolites, in GA-treated samples, relative to controls, notably citrate, ketoglutarate, succinate, fumarate and malate. The only metabolites to show substantially decreased relative levels were aconitate and oxaloacetate. By 4 weeks after coming into storage (Figure 3.16 B, January), all the TCA cycle intermediates were detected at similar levels in control and GA-treated samples, apart from oxaloacetate, which was depleted in the GA-treated samples, and malate, which was relatively more abundant. Figure 3.16 C (February), shows a slight general shift upwards in metabolite levels in response to GA-treatment, notably in fumarate and oxaloacetate, with lower relative levels of aconitate. By March buds were beginning to sprout and the associated metabolite pattern (Figure 3.16 D) shows that aconitate is now the most abundant metabolite, compared to controls. At the same time there is a general depletion of

fumarate, malate and oxaloacetate.

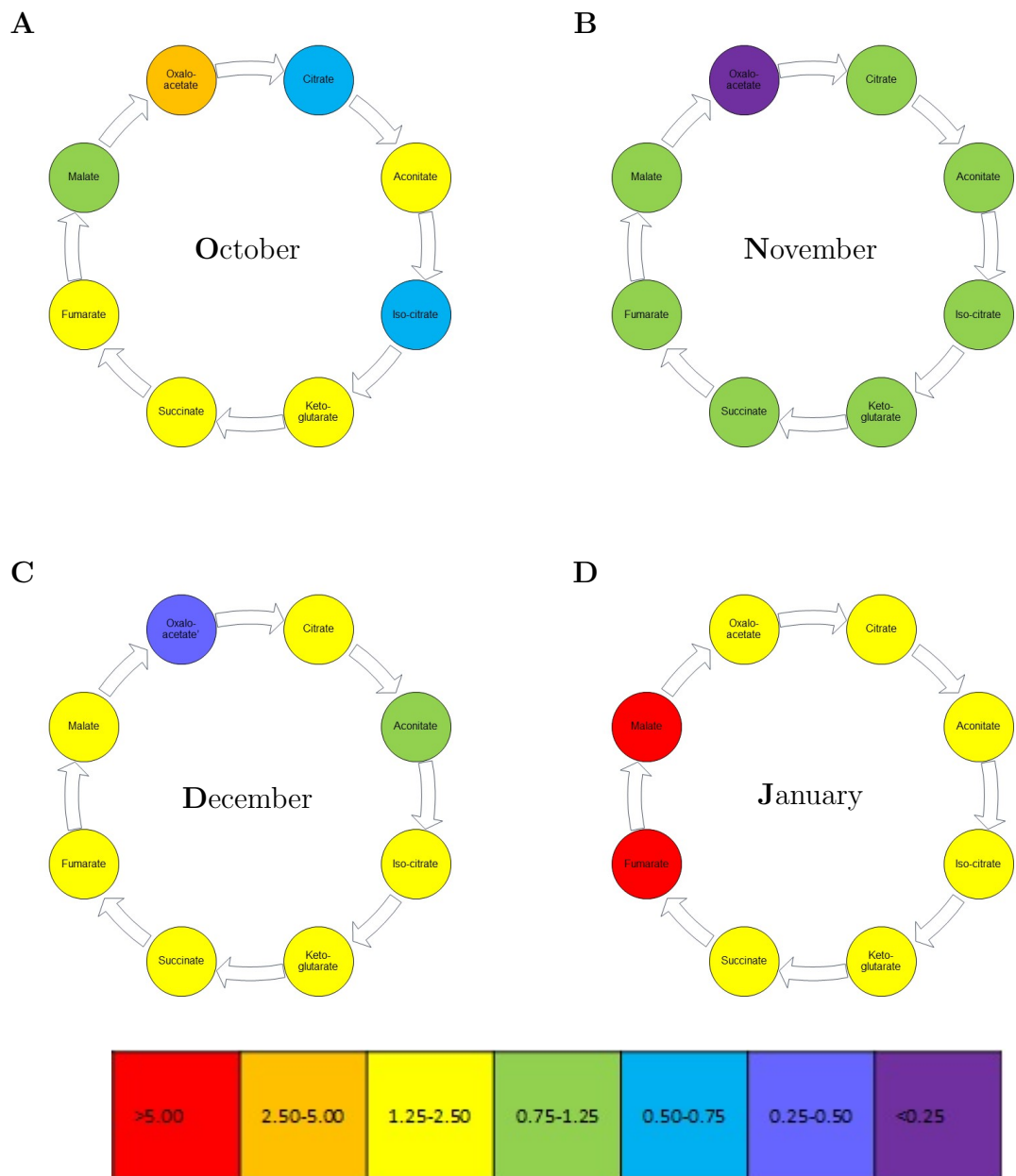


Figure 3.15: TCA cycle configuration in cv. Desiree

The relative abundance of TCA cycle intermediates in Desiree GA-treated buds (ratio with water-treated buds) at $t=72$ hours after treatment. Data relate to samples in 2.17 in chapter 2. Ratios were performed on proportion of ion count (%). Hot colours indicate an ion was more abundant in GA-treated samples than controls. Cold colours indicate an ion was less abundant in GA-treated samples than controls. The colour scale is displayed below the 4 panels. $n=48$. A: GA treatment in October. B: GA treatment in November. C: GA treatment in December. D: GA treatment in January.

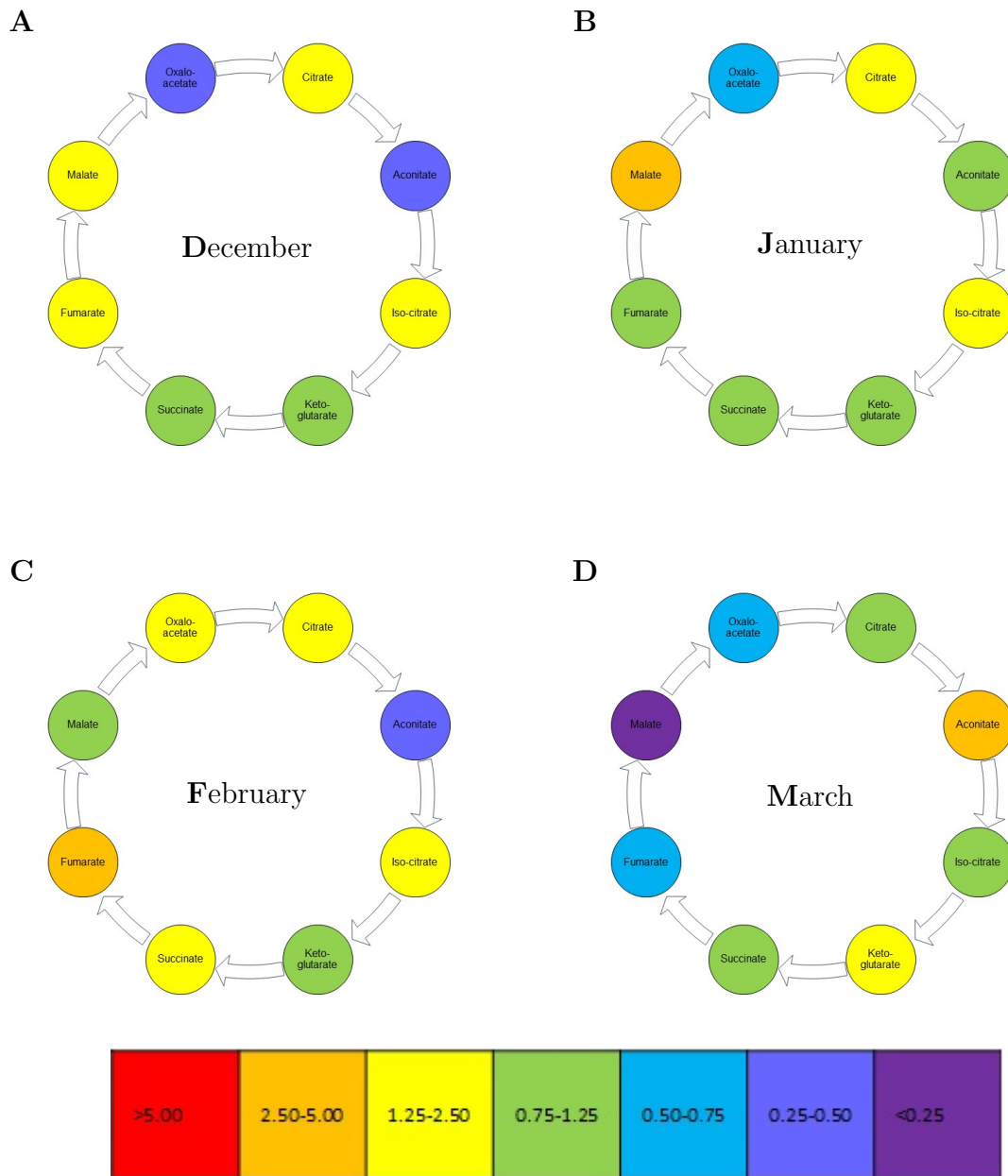


Figure 3.16: TCA cycle configuration in cv. Russet Burbank

The relative abundance of TCA cycle intermediates in Russet Burbank GA-treated buds (ratio with water-treated buds) at t=72 hours after treatment. Data relate to samples in 2.19 in chapter 2. Ratios were performed on proportion of ion count (%). Hot colours indicate an ion was more abundant in GA-treated samples than controls. Cold colours indicate an ion was less abundant in GA-treated samples than controls. The colour scale is displayed below the 4 panels. n=48. A: GA treatment in December. B: GA treatment in January. C: GA treatment in February. D: GA treatment in March.

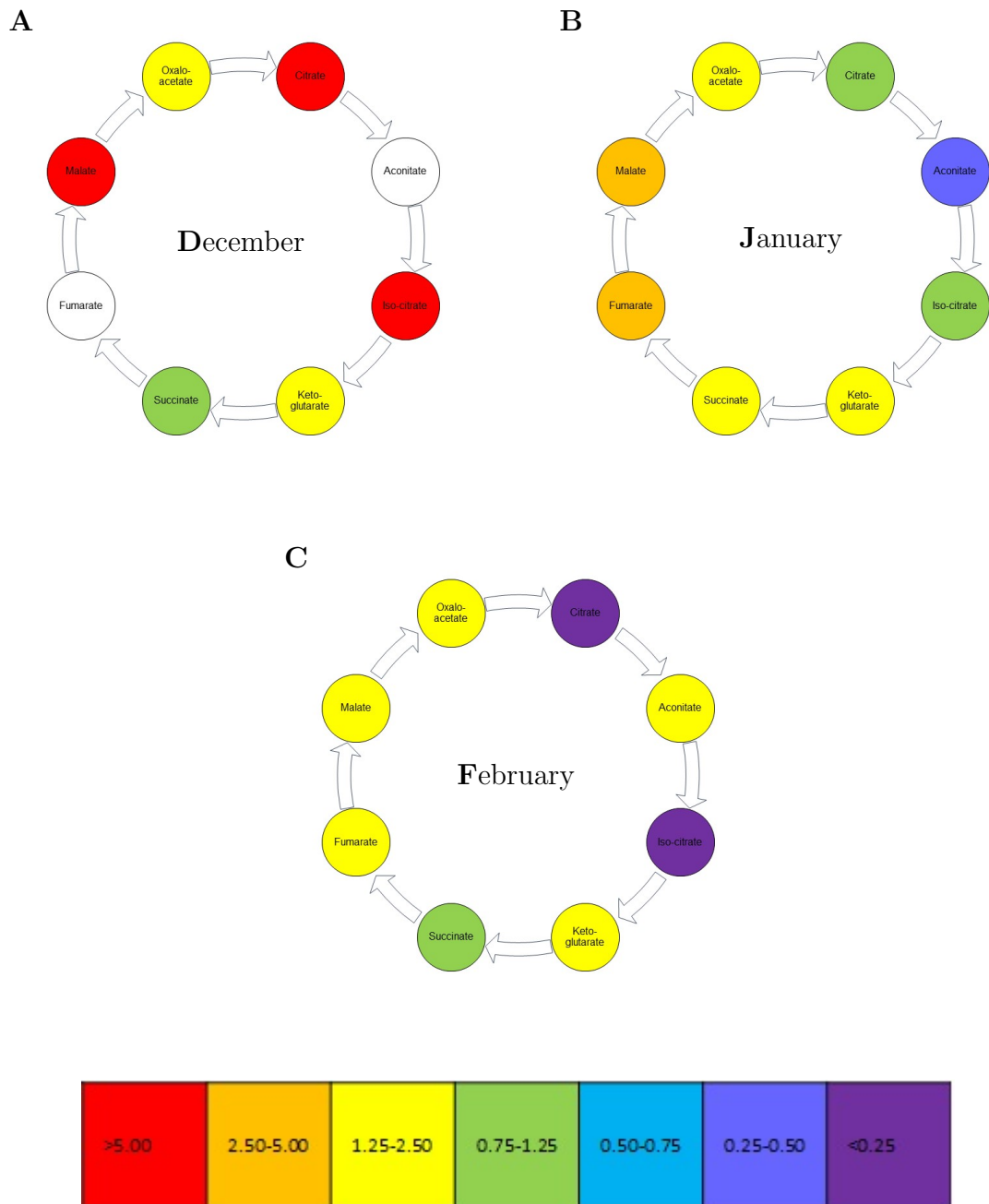


Figure 3.17: TCA cycle configuration in cv. Maris Piper

The relative abundance of TCA cycle intermediates in Maris Piper GA-treated buds (ratio with water-treated buds) at $t=72$ hours after treatment. Data relate to samples in 2.21 in chapter 2. Ratios were performed on proportion of ion count (%). Hot colours indicate an ion was more abundant in GA-treated samples than controls. Cold colours indicate an ion was less abundant in GA-treated samples than controls. The colour scale is displayed below the 3 panels. $n=36$. A: GA treatment in December (Aconitate and fumarate = 0% total ion count in the controls). B: GA treatment in January. C: GA treatment in February.

Finally, Figure 3.17 on page 89 schematically portrays the levels of TCA pathway metabolites in field-grown Maris Piper apical buds at 72 hours after GA-treatment relative to control treated samples, with data shown for tubers at various times after harvest (December, January, February). Each of the panels in Figure 3.17 uses the colour intensity framework in Figure 3.14. Figure 3.17 A represents samples analysed in December, shortly after harvest. Aconitate and fumarate were not successfully detected in the controls, meaning they could not be plotted on this colour intensity scale. Apart from succinate, all the successfully detected TCA cycle intermediates were relatively more abundant in the GA-treated samples. Citrate and isocitrate (which were not distinguishable in this analysis) and malate showed the highest relative levels. Figure 3.17 B (samples produced in January, 4 weeks after coming into storage) shows a contrasting pattern. By this time, citrate and isocitrate were detected at similar levels in control and GA-treated samples, and aconitate levels were very low. By February, when buds were beginning to sprout (Figure 3.17C), most of the pathway is green or yellow, indicating a moderately higher level in the detected levels of metabolites in GA-treated samples, relative to controls. The most noticeable exceptions are citrate and isocitrate, which is substantially less abundant in GA-treated samples relative to controls at this stage of storage.

3.4 Discussion

This chapter examines the biochemical implications of the changes associated with dormancy break in Chapter 2. It aims to link these markers to the functional changes associated with potato sprouting. During dormancy break, quiescent meristems reactivate and re-enter proliferation. This has major implications for the energetic budget of the cells involved. Here, m/z markers from Chapter 2 are identified as metabolites and put into the context of the change in metabolism associated with sprouting.

3.4.1 Identification of TCA metabolites as lead markers for early sprouting

The moieties identified from loadings plots in chapter 2 were used as the basis of metabolic database searches to characterise putative identities for the various m/z markers. Although such databases are obviously invaluable for this process, one must be aware that, depending on database source, there may be a bias in the outputs. For example, for studies on plant metabolomics the SolCyc (2018) database is particularly useful, since it only includes metabolites from Solanaceae plants. This can be contrasted with other

databases (e.g. Kanehisa *et al.* 2018) which are almost exclusively based on animal and pharmacological datasets. Bearing in mind the extraordinary wealth and distinctiveness of much of plant metabolism, screening an inappropriate database can easily lead to problems in accurate identification of metabolites. A good strategy (as implemented here) is to use a variety of databases in a structured way to first provide plant-plausible putative identities then, using, e.g., Kanehisa *et al.* (2018) to provide metabolic context for candidate moiety identities. This makes it easier to exclude isobaric molecules that are highly unlikely to occur in our research context and identify metabolic pathways which can be associated with the biological process being studied, thus providing potential insight.

Our analysis identified the top three m/z markers as m/z 191, 133 and 115 (highly influential in chapter 2 loadings plots - e.g. Figure 2.12 C). In Table 2.2 on page 38 and the associated section in this Chapter (3.3.1 on page 68) these are putatively identified as citrate, malate and fumarate. These metabolites are all core to primary metabolism since they are key components of the Tricarboxylic acid or Krebs cycle (TCA) cycle. The other three rows in Table 2.2 correspond to other TCA cycle components; aconitate, ketoglutarate and oxaloacetate. These were not identified as highly influential in the loadings plots shown in Chapter 2, but a re-examination of the relevant raw datasets revealed that these moieties were all detected at the relevant m/z .

The initial identification of metabolites and relevant metabolic pathways discussed above is a very useful first step in the process of linking a metabolomic approach to a biological problem. However, unequivocal identification of the metabolite identities requires further analytical steps. In this investigation this was performed by Tandem Mass Spectrometry.

These mass-based putative identifications have been corroborated using tandem MS. The basic principle underpinning tandem MS (or MS/MS) is that ions break in a stereotypical pattern, through the loss of labile groups. After the ion of interest is selected, it is fragmented using collision gas, and these product ions generate a spectrum. This spectrum has characteristic peaks that are linked to the structure of the precursor ion, so isobaric ions can be distinguished and identification confirmed.

A metabolite's MS/MS spectrum pattern can be predicted using *in silico* fragmentation (Figure 3.1 on page 69). In software such as ChemDraw, it is possible to calculate the masses of product ions obtained by breaking a particular bond in a candidate molecule. In Figure 3.1 A, the precursor ion malate is shown. The subsequent panels reveal the product ions expected from the removal of hydroxyl and carboxyl groups in various combinations, and the masses of these product ions. These *in silico* fragment patterns are used to interpret sample MS/MS spectra. m/z identity can be corroborated by linking

fragments to the loss of known labile groups.

Where available, a better approach than the *in silico* fragmentation in Figure 3.1 is to compare a standard solution of a metabolite to sample from the experiment. These spectra are shown in Figure 3.2 on page 70 for eight organic acids associated with the TCA cycle. Each of these solutions yields a spectrum with a small number of peaks, corresponding to the product ions produced by the collision gas between MS runs. If Figure 3.2 G is compared to Figure 3.1, it is possible to see that the peaks correspond to hydroxyl and carboxyl group loss. m/z 115 could be the product ion shown in Figure malchemdraw B, where a hydroxyl group is lost. Figure 3.1 D has a mass of m/z 89; this peak corresponds to the loss of a carboxyl group. The peak at m/z 71 appears to coincide with the ion produced by the loss of a hydroxyl and a carboxyl group.

Each of the organic acids examined in Figure 3.2 yield a fragmentation spectrum that is suitable to corroborate the putative identification in Table 2.2. A particularly interesting pattern is seen in Figure 3.2 A and C; the isomers citrate and isocitrate. There is a difference in the fragmentation pattern of citrate and isocitrate; this is explored in more detail in Figure 3.3 on page 72. The structural differences between citrate and isocitrate (Figure 3.3 A and B respectively) mean that only isocitrate can produce the fragment 2-Hydroxyethanoic acid, producing extra product ions, compared to citrate. Citrate can only lose carboxyl groups or an ethanoic fragment. This isomer example also illustrates how MS/MS can be used to identify metabolites; isobaric molecules will fragment in different patterns, even when they share molecular domains. In the case of citrate/isocitrate, it makes it possible to confirm that a mixed sample contains isocitrate.

The standard spectra in Figure 3.2 are used as the basis to corroborate the identification of metabolites in sample extracts. Figure 3.4 on page 73 shows the MS/MS spectra for a fumarate standard and six contrasting tuber extracts, run using the same method. Data in Figure 3.4 A are the same as those in Figure 3.2 F. Fumarate was successfully detected in all these samples; the product ion (m/z 71) is visible in all spectra and the precursor ion is visible in Figure 3.4 B, C, E and G. The precursor ion may be absent from Figure 3.4 D and E because it was present at low levels, meaning all target ions were fragmented. This process was repeated for all the metabolites illustrated in Figure 3.2; this corroborates that the metabolites corresponding to the moieties of interest in chapter 2 are correctly identified in Table 2.2, for a range of studied treatment combinations.

3.4.2 The role of TCA metabolism in sprouting

The metabolites discussed so far in this chapter all correspond to components of the TCA cycle, illustrated schematically in Figure 3.5 on page 74. As discussed in the introduction, it has been suggested that this conventional depiction of the TCA cycle, with a focus on ATP generation, is a simplification, and it may function in a variety of configurations and fluxes. The configuration depends on factors such as resource availability and the balance of demands on the system. It is proposed that in a heterotrophic system, like a proliferating meristem, particularly one with large nutrient reserves like a tuber, ATP is not the limiting factor. Under these conditions, ATP efficiency may be sacrificed in favour of faster metabolism and more productive, so the cell division necessary for growth and establishment can occur (Sweetlove *et al.* 2010). The subsequent section of the Discussion examines whether potato buds exhibit a noncanonical TCA cycle configuration during the early stages of sprouting and, if so, what the biological relevance of such a configuration might be.

Starting with the analysis of the developmental series of buds on a tuber (as described in Chapter 2, Figure 2.8), the apical bud sprouts much earlier than the others, and bud metabolic profiles differ on the basis of their rank. Figure 3.6 on page 75 illustrates the differences between the TCA cycles of apical and stolon buds. If their TCA cycles were identical, the ratios would cluster on the 1:1 red dotted line shown in this Figure. In addition, if the TCA cycle were operating in its conventional configuration, but at different intensities, a uniform scaling of all metabolites would be expected. However, the data in Figure 3.6 show a nonuniform distribution of the relative level of TCA metabolites in the apical and stolon buds. Malate, fumarate and ketoglutarate all showed higher levels in the apical buds relative to the stolon buds, whereas aconitate and oxaloacetate were all less abundant in the apical buds relative to the stolon buds. It should be noted that these data refer to paired samples; each value corresponds to the ratio between an individual apical bud and its furthest bud, thus controlling for tuber and storage conditions. Although all the buds are dormant and non-growing, their TCA metabolite patterns show different distributions around the canonical cycle. We know that the apical bud is closer to breaking dormancy than the stolon bud, so the data are consistent with the hypothesis that TCA metabolite pattern changes as dormancy status changes, with an increase in malate and a fall in oxaloacetate potentially being linked to an exit from dormancy and concurrent increased propensity for sprouting. These changes can be interpreted in the context of the ideas discussed in Sweetlove *et al.* (2010); changes in cell function and energy demands as buds gain sprouting competence lead to reconfigurations of the primary metabolism strategy adopted.

Our analysis of bud response to GA-induced sprouting also supported a role for a non-canonical TCA metabolism acting during the first 72h of bud growth. As can be seen in the data presented in Figure 3.7 on page 77, the relative change in TCA metabolites in response to GA is not uniform across the timepoints. During the first 24 hours there is a general decrease in all metabolite around the cycle but with the marked exception of fumarate (Figure 3.7 B (t=24)). By 72 hours after GA-treatment (Figure 3.7 D), the citrate-ketoglutarate half of the cycle is stimulated, but fumarate troughs and malate peaks. This could suggest that succinate and fumarate are being bypassed in the sprouting tissue, i.e. the process is not acting as a cycle. These data are presented as time courses for each metabolite in Figure 3.8. There is an increase in the relative abundance of each metabolite as time since treatment progresses, apart from fumarate (Figure 3.8 E), i.e. a non-uniform process. Succinate and oxaloacetate levels (Figure 3.8 D and G) stabilize between t=48 and t=72, whereas citrate and malate levels (Figure 3.8 A and F) increase the most at this time point. The increase in aconitate and ketoglutarate relative levels (Figure 3.8 B and C) is pretty uniform over t=24-72. Presented in this form, it is clear that the pattern of metabolite accumulation in the TCA pathway is not a simple stimulation of all metabolite levels. One must be careful in inferring fluxes from measurements of pool size, so actual measurements of flux would need to be done to absolutely confirm interpretation of these data. Although such flux measurements have been done, they generally involve much larger tissues where a steady state can be achieved (e.g. Bethke 2014). Performing such experiments in small buds which are in a highly dynamic state would be technically extremely challenging. Nevertheless, even with these caveats, it is difficult to reconcile our data with a uniform change in TCA metabolism occurring either across the developmental series or in response to sprouting triggers. The alternative, more plausible interpretation is that in these instances a sizeable proportion of the tissue contains a TCA pathway which is not configured in the conventional pattern linked with oxidative metabolism for the generation of ATP. It seems most likely that a non-canonical TCA pathway is active during the exit from dormancy and the entry to sprouting.

To investigate whether the TCA markers identified in the work discussed above might have relevance to tubers maintained under storage for different lengths of time, I performed this analysis on the data for the harvest series discussed in Chapter 2 Figures 2.11 and 2.12. These samples were stored for between 3-7 and 2-8 weeks (as discussed in Table 2.3) respectively, prior to undergoing the GA-sprouting/metabolomic test assay.

Figures 3.9 and 3.10 on Pages 79 to 81 present the data for stored tubers in a similar format to Figures 3.7 and 3.8. Figure 3.9 on page 79 presents the TCA cycle data also found in chapter 2 Figure 2.12; extracts were produced 3, 5 and 7 weeks after

harvest. These data refer to buds sampled 72 hours after treatment; in terms of dormancy status Figure 3.9 B is probably the closest to Figure 3.7 D. The pattern observed across Figure 3.9 is like that in Figure 3.7 D, apart from the absence of a malate peak. The pathway appears to contain 3 groups, showing coordinated responses. This suggests the pathway is not operating in a cycle configuration, but contain more closely linked units of activity. Metabolites appear grouped into 3 functional groups: citrate-aconitate, succinate-fumarate-malate and ketoglutarate-oxaloacetate.

Figure 3.10 on page 81 presents the TCA cycle for data from a second, independent harvest series test, previously discussed in chapter 2 Figure 2.11; tuber buds were sampled 2, 4, 6 and 8 weeks after harvest. For 4 and 6 weeks after harvest, the data roughly mirror the pattern observed in Figure 3.9; the relative intensity of the metabolites is high for part of the cycle (aconitate, ketoglutarate and succinate) and falls dramatically for the other half. The freshest sample, 2 weeks after harvest, shows a uniform, if moderately repressed TCA cycle, with lows for malate and citrate in the GA-treated sample. The pattern is also quite uniform in week 8 after harvest; apart from the fumarate value, most relative metabolite intensities fall just below the 1:1 line.

Figure 3.10 presents a wider sampling window than Figure 3.9, but the data for weeks 3-6 after harvest seem to suggest the same non-canonical form of the TCA pathway, in which different parts of the pathway operate independently, as opposed to cycling. In the more extreme parts of the sampling window (2, 7 and 8 weeks after harvest), GA-treated buds do not seem to differ substantially from the controls. In the case of samples from 2 weeks after harvest, this lack of discrimination may reflect the buds' inability to perceive and respond to GA-treatment. By 7-8 weeks after harvest, the water-treated controls may be sprouting autonomously, reducing the measured differences.

The analyses discussed above were all performed using the King Edward cultivar. To investigate whether the TCA metabolites identified as potential sprouting markers in this cultivar held true in other cultivars (with different dormancy phenotypes), I performed a similar analysis on the cultivars Maris Piper, Desiree and Russet Burbank. This analysis is discussed on section 3.4.3.

3.4.3 Comparison of TCA metabolites with other potential metabolic markers for sprouting

Tuber sprouting has long been known to be linked with major changes in carbohydrate metabolism in the tubers, with starch breakdown leading to the accumulation of hexoses, with major knock-on outcomes on the commercial use of the tubers (Burrell, M. priv. comm.). To investigate how the novel TCA markers described above linked with the

timing and extent of changes in carbohydrate metabolism during sprouting, I performed a series of enzyme-linked spectrophotometric assay to quantify sugar levels in tuber tissue.

The efficacy of these markers in predicting dormancy status needs to be looked at in the context of more conventional markers. Figures 3.11 to 3.13 on Pages 82 to 83 present data from an enzyme-linked spectrophotometric assay to quantify sugar levels in tuber tissue. These data are associated with the samples presented in chapter 2 Figures 2.14 to 2.21, so there is information on the metabolome associated with these sugar patterns.

The data presented are in Figure 3.11 on page 82. A key observation is that the quantity of sugars in tuber tissue varies by cultivar. Cv. Maris Piper (Figure 3.11 C) has lower and more consistent sugar levels than cv. Russet Burbank (Figure 3.11 D), thus cultivar type influences the study window and the absolute levels of sugars. However, some patterns are fairly consistent; glucose and fructose increase during the storage period and sucrose decreases, possibly after an initial spike (most evident in Figure 3.11 A and B, which have data for October). The patterns observed reflect the release of reducing sugars from starch reserves as dormancy progresses and the metabolism of sucrose pools.

A caveat that is worthy of note is that storage conditions may alter tuber sugar levels independently of dormancy status. In particular, stresses such as cold storage are associated with tuber sweetening (Bethke 2014), thus, even if sugar levels were normalised against normal cultivar levels, they could be a misleading indication of dormancy status. Bearing this caveat in mind, the composition of sugars was examined in more detail to relate the gross pattern to the possible endogenous processes generating the sugars measured.

Data shown in Figure 12 3.12 on page 83 are the glucose - fructose ratio for the data presented in Figure 3.11. This ratio is informative for the following reasons. Firstly, starch is a polymer of glucose, so using starch as a resource pool for hexoses will yield higher levels of glucose than fructose. When sucrose is hydrolysed by invertase it produces a glucose and a fructose molecule, so the expected ratio is 1:1. If sucrose breakdown is by sucrose synthase, then UDP-Glc and fructose is generated, thus generating more fructose than glucose, meaning the glucose - fructose ratio from sucrose is below 1:1. The value of this ratio yields information about the nutrient pools being used and the enzymes involved. Apart from cv. Desiree, all the values in Figure 3.12 are above the 1:1 ratio line, suggesting that the reducing sugars come from a range of sources, but not predominantly sucrose. In general, the glucose - fructose ratio falls over the course of the storage period; consistent with a switch from using starch as a nutrient source to metabolising sucrose.

Another important analysis of these data is the sucrose - hexose ratio, presented in Figure 3.13 on page 83. The sucrose - hexose ratio provides information on the sink strength of a sample, as the capacity to metabolise sucrose into free hexoses is often linked to sink strength. It also demonstrates that pools of sucrose are being consumed. The data for cv. Russet Burbank show a clear decrease in the sucrose - hexose ratio as storage proceeds. This is the expected pattern: as the bud becomes more metabolically active during sprouting, it regains the ability to use sucrose from the surrounding tissues. However, the pattern is not observed across all cultivars. For the cv. King Edward and Desiree, there is an initial increase in the sucrose - hexose ratio, but this is followed by a decline in the ratio. In cv. Maris Piper, there is no observed reduction over storage time, and the value of the sucrose - hexose ratio is always very low, compared to the other cultivars.

Based on the data presented here, the metabolic markers identified as influential in chapter 2 are TCA cycle intermediates. Not only are these moieties identified consistently and in tandem, fragmentation patterns confirm this identification. Previously discussed datasets reveal interesting TCA cycle patterns. There are very few examples of a uniform change to the entire cycle, suggesting that the process of dormancy break involves a reconfiguration of metabolism, not merely a stimulation of the process. In contrast, the sugar data show strong cultivar-based differences in the pattern detected during storage. This corroborates one of the basic assumptions underlying this thesis: whilst sugar level does vary in relation to dormancy break, it is a highly variable property and not the most reliable marker.

3.4.4 The TCA cycle in field grown samples

The analyses discussed above were all performed using the King Edward cultivar, grown in a glasshouse. As discussed, during the early part of dormancy (endodormancy), GA is associated with a limited response in the TCA cycle metabolites, including suppression of the succinate-fumarate-malate part of the loop (see Figure 3.9 on page 79). By 7 weeks after harvest (Figure 3.9C), there is a relative increase in these metabolites in the presence of GA, whilst ketoglutarate and oxaloacetate levels are relatively low. To investigate whether the TCA metabolites identified as potential sprouting markers in the King Edward cultivar held true in other cultivars (with different dormancy phenotypes), I performed a similar analysis on the cultivars Maris Piper, Desiree and Russet Burbank, as well as investigating the metabolite patterns in field grown tubers of cv. King Edward.

Figure 3.14 on page 85 is roughly equivalent to Figure 3.9 on page 79. Both show data for the TCA cycle in King Edward buds at various points in storage. They key

difference between these datasets is that the data in Figure 3.14 refer to potatoes grown and stored under commercial conditions in 2016. These data are not on exactly the same timescale, but the similarities in the metabolite pattern are striking. Figure 3.14A and B show data for potatoes treated with GA in October and November respectively. In both of these, the most depleted metabolite (compared to control samples) is fumarate. In endodormant samples 3 and 5 weeks after harvest (Figure 3.9A and B), fumarate is also the key depleted metabolite. This may reflect a general suppression of metabolic responsiveness to GA during endodormancy. This pattern is completely altered at the December sampling point (Figure 3.14C), when tubers were starting to sprout. During ecodormancy, the samples appear more responsive to GA, but display a depletion in the relative levels of ketoglutarate. This pattern is partially mirrored in Figure 3.9 (storage for 3, 5 and 7 weeks), which displays a depletion in ketoglutarate and oxaloacetate. As ketoglutarate is a key exit point from the TCA cycle, linked to arginine biosynthesis, this asymmetry may reflect resources being redirected towards protein synthesis.

Having examined the change in metabolic response to GA trigger during storage with both glasshouse and field grown King Edward, the same question was examined during storage of cultivars with different dormancy characteristics: Desiree (short dormancy), Maris Piper (medium dormancy) and Russet Burbank (long dormancy).

The data for Desiree, presented in Figure 3.15 on page 87, are dominated by relative changes in oxaloacetate levels. There were the highest of all the TCA cycle metabolites in October (Figure 3.15A), but fell dramatically in November and December, where it is the only TCA cycle intermediate that doesn't conform to a uniform, whole cycle pattern at these timepoints (Figure 3.15B and C). The final sampling time point, January, features a major change in the relative abundance of malate and fumarate (Figure 3.15D). All the other metabolites increase moderately, including oxaloacetate for the first time in this cultivar's analysis.

Figure 3.16 on page 88 shows that changes in oxaloacetate also dominate the changes in the TCA configuration for cv. Russet Burbank. As with Desiree, Figure 3.16A and B, representing December and January, show a depleted oxaloacetate concentration, compared to controls. In January, there is also a higher level of malate in response to GA, compared to the other metabolites. By February (Figure 3.16C), malate levels have fallen, and fumarate is the most enhanced metabolite. In the final sampling month, March (Figure 3.16D), fumarate and malate are strongly depleted, resembling the pattern seen in King Edward in November (Figure 3.14B).

Figure 3.17 on page 89 shows that citrate is key to the TCA cycle differences in cv. Maris Piper buds. Figure 3.17A shows the data for December, the first available sampling month. Citrate, isocitrate and malate are detected at much higher levels in

GA-treated samples, compared to the controls. Aconitate and fumarate were not successfully detected in the controls. If these values are below the limits of detection, the relative abundance of these moieties would fall in a hot colour category, as they are more abundant in treated samples. By January (Figure 3.17B), the citrate levels are similar in GA-treated and control samples, whereas aconitate is depleted in the presence of GA. Malate and fumarate are still more abundant with treatment, but the difference is less striking than in Figure 3.17A. During the final sampling month, February (Figure 3.17C), the citrate and isocitrate are severely depleted in GA treated samples, compared to controls, suggesting a reconfiguration in the pathway over the storage period.

In synthesis, whilst there are mixed patterns in the cultivar data at the point of harvest, for the mid storage samples, the TCA pathway response to GA is uniform (Figures 3.14A, 3.15B and C, 3.16B and C, 3.17B). This potentially indicates the use of starch breakdown products in a conventional TCA cycle, with varying levels of intensity. Then, as endodormancy ends, there is a gradual shift towards asymmetry in the relative levels of metabolites in response to GA. The “cycle” appears to break down, polarising different parts of the pathway: in the final sampling month, 3 of the cultivars show depletion in the most responsive metabolite (Ketoglutarate: Figure 3.14C, Oxaloacetate and malate: Figure 3.16D, and Citrate: Figure 3.17C). The succinate-fumarate-malate part of the loop seems to respond separately to the citrate-aconitate-isocitrate. This may link to the fact that ketoglutarate (via glutamate) and oxaloacetate (via acetyl CoA and aspartate) are key entry and exit points for the TCA cycle, interacting with amino acid synthesis, so these patterns may underlie changes in the fluxes of carbon in these samples. As proliferating cells demand proteins required for basic cellular housekeeping and continuing division, the TCA cycle may adapt to drive amino acid biosynthesis, rather than maximum ATP yield.

3.4.5 Conclusions

The data in this chapter confirm the identification of the metabolic markers from Chapter 2 as organic acids from the TCA cycle, leading to the analysis of the pathway as a whole. The subsequent data show that the TCA pathway has a stereotypical set of asymmetrical responses to the various dormancy ending cues examined. These are potentially linked to the synthesis of amino acids from ketoglutarate and oxaloacetate.

An additional step that was beyond the scope of this chapter would be metabolite quantification with liquid chromatography (LC-MS). By running samples through a column, there is an additional separation step, meaning moieties are separated on the basis of their interaction with the column before they reach the spectrometer. This can be

particularly useful to separate isomers, as they may have the same labile groups but interact differently with the column (although the key isomers in this chapter fragmented differently). LC also helps clean samples up and remove any large molecules that potentially cause ion suppression by absorbing most of the ionising energy. By reducing these matrix effect, a clearer picture of the quantities of different moieties can be inferred. It is possible to apply tandem MS after the LC step, identifying a metabolite with a high degree of confidence.

The sugar data suggest that there is an increase in reducing sugar availability during storage. The glucose - fructose ratio implies that resource utilisation changes during storage, supporting the other metabolic conclusions about the process. However, cultivar differences mean this is not as reliable a marker as the m/z markers discussed in Chapter 2 and identified in this chapter.

Chapter 4

Visualising the spatial distribution of key metabolites during dormancy release in tuber buds

4.1 Introduction

Chapters 2 and 3 contain intriguing results about the Krebs cycle and its role in the reactivation of dormant potato buds. However, these data refer to liquid samples, extracted from dissected apices. Therefore, the resolution of tissue specificity is limited by my ability to dissect the primordia and distinguish unsprouted meristems from adjacent leaf bases. This constrains any inferences that can be made about the markers' role in quiescent meristem reactivation. The meristem only represents a fraction of the analysed tissue. One way to resolve the issue of heterogeneous samples containing several cell types is to perform mass spectrometry imaging. By performing analysis of tissue sections, rather than liquid extracts, spatial patterns are preserved, meaning that metabolic fingerprints can be linked to anatomical features. This approach also permits *in silico* dissection: mass spectra associated with particular regions of interest can be selected and examined in more detail.

So far, the majority of mass spectrometry imaging in plants has used a MALDI (Matrix-assisted laser desorption ionization) platform (for a recent review, see Heyman & Dubery 2015). MALDI uses a laser beam to ionise metabolites from freeze dried tissue sections that have been sprayed with a chemical matrix and analysed in a vacuum. This has proved itself to be a useful approach for improving the sophistication of analyses by adding a spatial element. For example, Yoshimura *et al.* 2012 were able to use MALDI-MSI to demonstrate anthocyanin accumulation in the pericarp of black rice. It was

already known that these compounds were abundant, but tissue specific accumulation had important implications for understanding the underlying processes and assessing the potential importance for human nutrition.

More recently another method for visualising metabolite distribution in tissues has been developed: DESI (Desorption electrospray ionization). DESI uses a fine solvent spray to ionise tissue samples. Unlike MALDI, it does not require matrix application to the sample surface, and analysis can take place at ambient pressure. These factors make the experimental procedure simpler than MALDI. It has also been reported that DESI shows good ionisation efficiency for small molecules. DESI has been used most widely in the context of human disease. A range of examples are discussed in the review by Banerjee 2018. Intriguingly, this review reports on Banerjee and Mazumdar's earlier findings imaging Krebs cycle intermediates in prostate cancer biopsies, in particular citrate (Banerjee & Mazumdar 2012). In another example of DESI-MSI in oncology, Margulis *et al.* (2018) identified fumarate as a key marker for detecting malignant microlesions associated with skin cancer. These animal examples are deeply encouraging since they both corroborate some of the ideas from Chapter 3 about the Warburg effect and cell division, and they show that Krebs cycle intermediate detection ought to be possible using this technique. Furthermore, the similarities to the electrospray ionisation (ESI) techniques used in Chapter 2 mean that it should ionise a similar subset of metabolites as the molecular species discussed earlier in this thesis, again suggesting that DESI could be a good approach for the visualisation of these TCA metabolites.

The application of DESI to plant systems has been limited so far. There are several examples of tissue printing being used in conjunction with DESI (e.g. Tata *et al.* 2014), but I have found only one published example of direct DESI imaging of a cryosection, as part of a technical advance paper by Li *et al.* 2013. In this paper, the authors report good detection of tissue-specific metabolite patterns in cross sections of cassava tubers, a tissue not dissimilar to potato tubers. This article also presents data for tissue imprints. The imprints approach benefits from reduced risk of metabolome degradation by intracellular enzymes, as the imprint does not contain a full suite of cellular material. However, the process of imprinting is associated with risks of contamination and disruption of tissue patterns. These limitations are deemed acceptable on low spatial resolution images, such as those in Tata *et al.* (2014), who imaged prints of tubers responding to various levels of *Pythium ultimum* infection, but do not lend themselves to high spatial resolution analysis.

Since the DESI platform is not well established in plant systems, I decided to validate the approach before addressing my main question. I used a training system based on phenolics accumulation after injury. Wounding potato tubers leads to the rapid ac-

cumulation of phenolic compounds which should be relatively easy to detect by mass spectrometry (Burrell 1984). I therefore first optimised and tested the DESI approach using this simple experimental system, before then attempting to characterise the distribution of the TCA metabolites identified in Chapter 2 and 3 as being early markers of sprouting.

4.1.1 Hypotheses

- DESI mass spectrometry imaging can be used to detect masses in fresh tuber sections.
- TCA markers identified from liquid extracts show a non-uniform distribution on a tissue section.
- Tubers at different stages of dormancy release have differing spatial patterns of TCA metabolism.

4.2 Materials and Methods

4.2.1 Plant material

Solanum tuberosum tubers of cv. King Edward were grown at AWEC. Tubers were planted in 15L pots with M3 compost and grown in the greenhouse. The photoperiod was 12 hours of ambient light with supplementary light ($200\mu\text{M}$ at bench level) if the ambient falls below $1000\mu\text{M}$. Daytime temperature was 20°C and nighttime temperature 15°C . The plants were hand irrigated and harvested after 12 weeks (once the canopy started to die back). After harvest, tubers were stored in the dark at 7°C , in paper bags.

4.2.2 Samples for phenolics analysis

Glass house grown tubers were analysed for differences in phenolics accumulation in association with injury. Tuber apices were excised and either hand sectioned and flash frozen, or aged in potassium phosphate buffer for 24 hours. The fresh samples prepared by hand sectioning excised pieces of tuber to $<1\text{mm}$ thickness; these were attached to slides with OCT, then flash frozen. To ensure minimal contamination of the surface of sections, or loss of samples, slides were placed in 50ml falcon tubes during the flash freezing step. Sections were freeze dried overnight, then stored in petri dishes at -20°C until analysis. Buffer aged samples were excised as 8mm diameter discs with a cork borer (depth 5mm) and placed on buffer-soaked filter paper in a conical flask. The potassium

phosphate buffer was 0.2M KH_2PO_4 , adjusted to pH 5.0 with 0.2M K_2HPO_4 , prepared in distilled water. The flask was stoppered with a sponge bung and placed in a growth chamber at 22°C and long day lighting for 24 hours. After this time had elapsed, the tuber discs were hand sectioned, flash frozen and freeze dried as above.

4.2.3 Phenolics detection with DESI

A coumaric acid detection assay was developed using a 1mg.ml⁻¹ (equivalent to 6mM) standard solution. Coumaric acid was dissolved in MeOH to the desired concentration and spotted on a polysine slide in 2μl aliquots. Once the optimal parameters had been identified, the limits of detection for this method were estimated using a dilution series. Six concentrations were investigated, as detailed in the table below.

Table 4.1: Coumaric acid standard curve

| Quantities of coumaric acid used in the standard curve in Figure 4.4 | | | |
|--|----------------------|--|---|
| Quantity (w/v) | Concentration (M) | Quantity per mm ⁻² (mol.mm ⁻²) | Quantity per pixel (mol.px ⁻¹) |
| 1mg.ml ⁻¹ | 6mM | 1.7nmol | 426pmol |
| 10μg.ml ⁻¹ | 60μM | 17pmol | 4.26pmol |
| 100ng.ml ⁻¹ | 600nM | 170fmol | 42.6fmol |
| 1ng.ml ⁻¹ | 6nM | 1.7fmol | 426amol |
| 10pg.ml ⁻¹ | 60pM | 17amol | 4.26amol |
| Methanol | 0 | 0 | 0 |

This dilution series was used to estimate the limits of detection (LOD) of the current setup. Spotted slides were imaged in negative ionisation mode, using a 95% MeOH:5%H₂O (v/v) spray, operating at a 1μl.min⁻¹ flow rate. The pixel size used was 50x50μm. The imaging pattern file used the same area selection in the imaging software (Waters High Definition Imaging software - HDI), offset appropriately to correspond to the correct spot, in order to ensure the sampled areas were comparable. 6 technical replicates were generated from each spot analysis by summing 300 scans (5 minutes of data) to generate each data point. The mean values and standard error of the mean are discussed in the results section below.

4.2.4 Phenolics in tuber sections

The samples prepared in section 4.2.2 were analysed using the same method developed in section 4.2.3: in negative ionisation mode, using a 95% MeOH:5% H_2O (v/v) spray, operating at a $1\mu\text{l}\cdot\text{min}^{-1}$ flow rate. Freeze dried sections were mounted on PolySine slides using UHU solvent free liquid paper glue (UHU). The slides were photographed using a dissecting microscope at 10x magnification, in order to generate an accurate pattern file to set the sampling area in HDI. With a pixel size of $50\times 50\mu\text{m}$, the total imaging time was approximately 3-4 hours and the file size around 300MB. Spots of standard solution (as in Table 4.1) were added to some sections to estimate the quality of metabolite recovery on the tissue, which is a more complex matrix than the slides in section 4.2.3.

4.2.5 Data processing

Data were processed in HDI, which automatically sets the 100 most abundant peaks and prepares them for display on heat maps, although this value can be adjusted easily. The m/z bins were linked to x-y data, and was plotted on a colour intensity scale at these coordinates. The image of the section (from the pattern file step) was superimposed on this heat map to assist in linking patterns with sample topography. To assist with data and image alignment, the most abundant ion (m/z 255.2) was selected. This showed clear boundaries between the sample and the slide. Using a ubiquitous m/z for alignment meant that any patterns displayed by other m/z could be attributed to features in the sample. Regions of interest were drawn onto heat maps and full spectra for these regions exported for detailed analysis in other software. This allows *in silico* dissection of the images, so different regions of the tissue sample can be examined for contrasting metabolic profiles, as seen in chapter 2.

4.2.6 Malate detection with DESI

A malic acid detection assay was developed using a $1\text{mg}\cdot\text{ml}^{-1}$ (equivalent to 7.5mM) standard solution. Malic acid was dissolved in MeOH to the desired concentration and spotted on a polysine slide in $2\mu\text{l}$ aliquots. Spots of standard solution corresponded to the concentrations in Table 4.2. Once the optimal parameters had been identified, the limits of detection for this method were estimated using a dilution series. Six concentrations were investigated, as detailed in the table below.

This dilution series was used to estimate the limits of detection (LOD) of the current setup. Spotted slides were imaged in negative ionisation mode, using a 95% MeOH:5% H_2O

(v/v) spray, operating at a $1\mu\text{l}\cdot\text{min}^{-1}$ flow rate. The pixel size used was $50\times 50\mu\text{m}$. The imaging pattern file used the same area selection in HDI, offset appropriately to correspond to the correct spot, in order to ensure the sampled areas were comparable. 5 technical replicates were generated from each spot analysis by summing 600 scans (10 minutes of data) to generate each data point. The mean values and standard error of the mean are discussed in the results section below.

4.2.7 TCA cycle metabolites in tuber sections

Glasshouse grown tubers were analysed 0 and 6 weeks after harvest, using the same method developed for the serial dilution of malate. Samples were ionised in negative ionisation mode, using a 95% MeOH:5% H_2O (v/v) spray, operating at a $1\mu\text{l}\cdot\text{min}^{-1}$ flow rate. Freeze dried hand sections, containing meristems, were mounted on PolySine slides using UHU solvent free liquid paper glue (UHU). The slides were photographed using a dissecting microscope at 10x magnification, in order to generate an accurate pattern file to set the sampling area in HDI. With a pixel size of $50\times 50\mu\text{mm}$, the total imaging time was approximately 3-4 hours and the file size around 300MB.

The glasshouse tubers were analysed again using cryosections, 2 and 8 weeks after harvest. Flash frozen tuber meristems were mounted in OCT and thaw mounted (blade at -15°C , cabinet at -20°C) onto polysine slides. The sections were $50\mu\text{m}$ thick. A Leica cryomicrotome was used. In the final experiments, samples were freeze dried overnight at -50°C before analysis. The slides were photographed using a dissecting microscope at 10x magnification, in order to generate an accurate pattern file to set the sampling area in HDI. With a pixel size of $50\times 50\mu\text{mm}$, the total imaging time was approximately 3-4

Table 4.2: Malic acid standard curve

| Quantities of malic acid used in the standard curve in Figure 4.5 | | | |
|---|----------------------|--|---|
| Quantity (w/v) | Concentration (M) | Quantity per mm^{-2} ($\text{mol}\cdot\text{mm}^{-2}$) | Quantity per pixel ($\text{mol}\cdot\text{px}^{-1}$) |
| $1\text{mg}\cdot\text{ml}^{-1}$ | 7.5mM | 2.09nmol | 522pmol |
| $10\mu\text{g}\cdot\text{ml}^{-1}$ | $75\mu\text{M}$ | 20.9pmol | 5.22pmol |
| $100\text{ng}\cdot\text{ml}^{-1}$ | 750nM | 209fmol | 52.2fmol |
| $1\text{ng}\cdot\text{ml}^{-1}$ | 7.5nM | 2.09fmol | 522amol |
| $10\text{pg}\cdot\text{ml}^{-1}$ | 75pM | 20.9amol | 5.22amol |
| Methanol | 0 | 0 | 0 |

hours and the file size around 300MB. Samples were analysed using the same method as that used for the serial dilution of malate: negative ionisation mode, using a 95% MeOH:5% H_2O (v/v) spray, operating at a $1\mu\text{l}\cdot\text{min}^{-1}$ flow rate.

4.2.8 Data processing

Data were processed in HDI, which automatically sets the 100 most abundant peaks and prepares them for display on heat maps, although this value can be adjusted easily. The m/z bins were linked to x-y data, and was plotted on a colour intensity scale at these coordinates. The image of the section (from the pattern file step) was superimposed on this heat map to assist in linking patterns with sample topography. To assist with data and image alignment, the most abundant ion (m/z 255.2) was selected. This showed clear boundaries between the sample and the slide. Using a ubiquitous m/z for alignment meant that any patterns displayed by other m/z could be attributed to features in the sample. 0.4mm^2 regions of interest were drawn onto heat maps and full spectra for these regions exported for detailed analysis in other software. This allows *in silico* dissection of the images, so different regions of the tissue sample can be examined for contrasting metabolic profiles, as seen in chapter 2.

4.3 Results

4.3.1 Phenolics

To explore the potential of the DESI-MS imaging platform, a series of experiments were carried out in a well studied potato system: phenolics accumulation after injury (Burrell 1984). Previous experiments have shown that following injury there is a rapid accumulation of specific phenolic compounds in tuber tissue, such as coumaric acid. This well characterised response was used as a test system for the DESI system - is DESI able to detect a known biochemical response in potato tubers? If so, this would provide a good indication that it would be worth exploring the potential of the system to characterise the spatial distribution of the TCA intermediates identified in previous chapters as being part of the early events of sprouting. Thus, the experimental pipeline established and optimised for the analysis of phenolics in tubers would provide the basis for further analysis focussed on TCA metabolites.

Figure 4.1 on page 108 shows a standard curve for coumaric acid detection on a polysine slide. A slide was spotted with a serial dilution of coumaric acid in methanol, as described in 4.2.3 on page 104 and imaged using DESI in negative mode, with a phenolics-

optimised method. Scans acquired over 5 minute intervals were summed, producing 6 analytical replicates per spot, and the mean ion intensity of the m/z corresponding to coumaric plotted against the molarity of the standard solution. With the exception of the data for the 600nM spot, the standard curve is approximately linear on a \log_{10} scale over the range 6mM-60pM. As the most dilute sample intensity(60pM) was consistently detected at a higher intensity than the control (1-tailed t-test, $p=0.0006$, $t=4.482$, $df=10$), I conclude that it is above the limits of detection for this method.

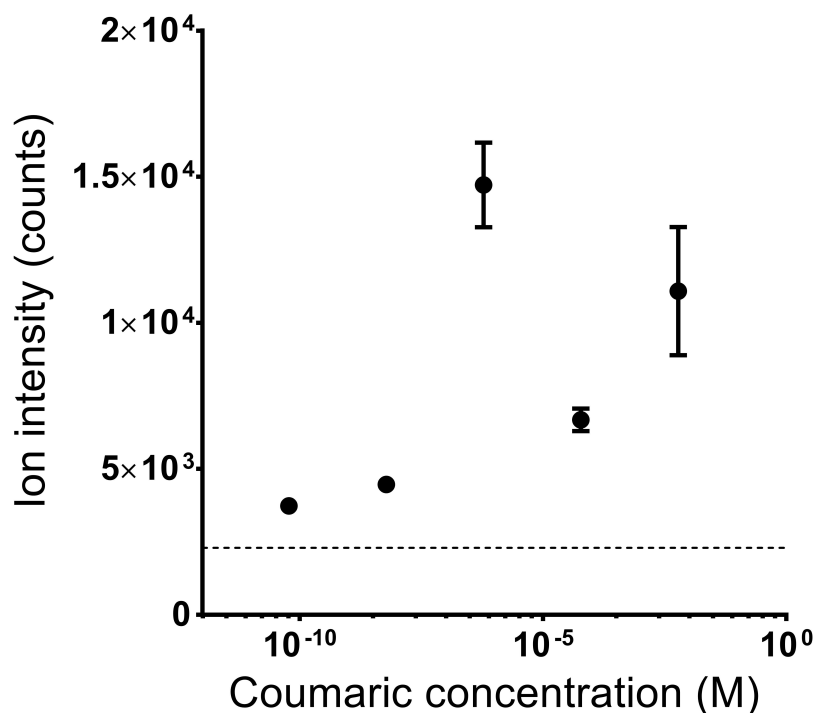


Figure 4.1: The standard curve of coumaric acid detection by the DESI.

Each point represents a different concentration of coumaric acid in methanol, diluted in 100-fold steps. This is represented on a \log_{10} scale. The control (100% methanol) is represented by the dashed line. The confidence interval of this line is too narrow to be presented on this scale. The error bars are standard error of the mean. $n=6$.

Having established that I could reliably detect the coumaric acid standards over a wide range of concentration, I proceeded to investigate whether the same method could detect coumaric acid and related phenolic compounds in tubers and whether an increase in these metabolites was detected after tuber wounding.

Hand section of tubers were either immediately flash-frozen, attached to a glass slide with OCT then freeze dried overnight prior to DESI analysis, or were incubated in phosphate buffer for 24hrs to induce clear wound-induced colouration prior to the same preparation for DESI. Examples of such sections are shown in Figure 4.2A (fresh) and

Figure 4.3A (24 hr post-wounding) on pages 109 and 110 respectively.

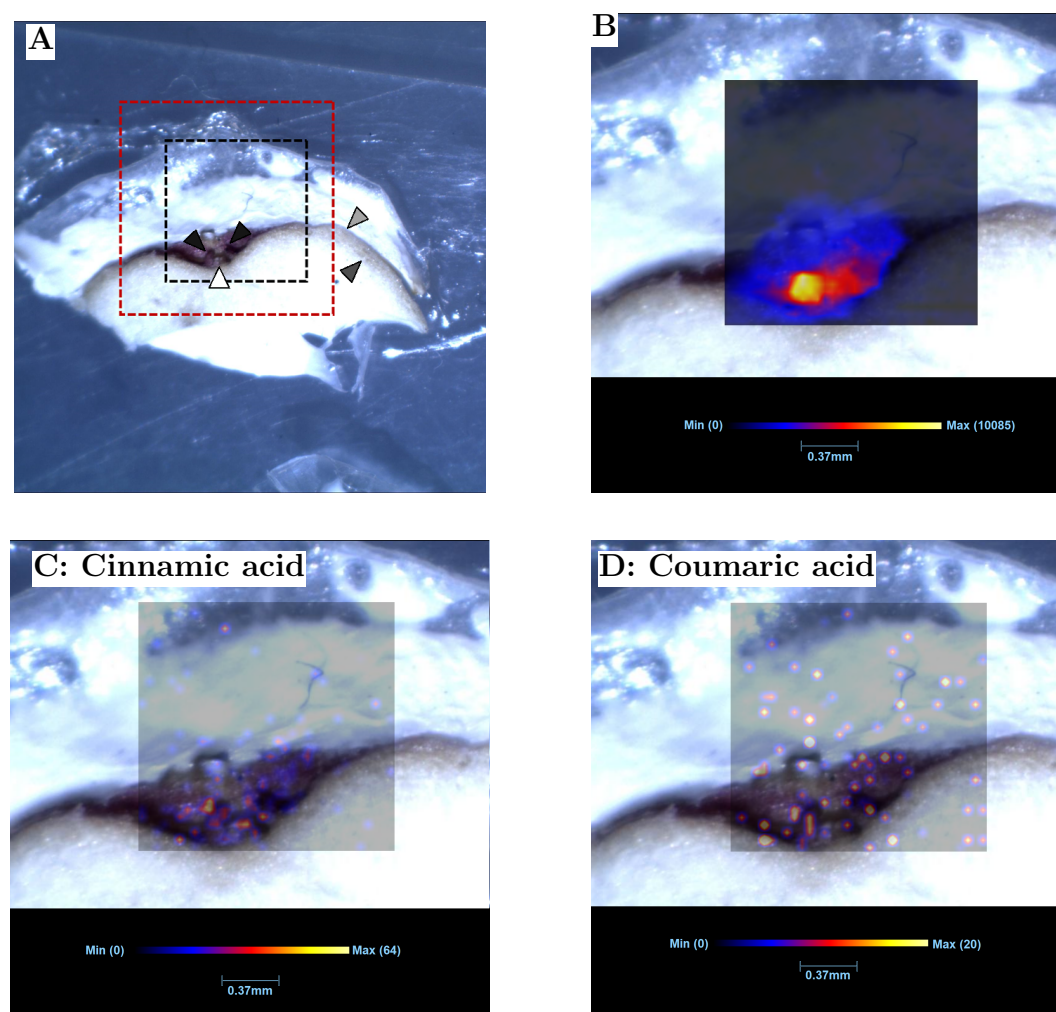


Figure 4.2: Metabolite distribution in a fresh tuber section

The hand section was flash frozen and freeze dried, then analysed by negative mode DESI MSI. A: A 10x magnification stereo microscope image of the tissue section. The box with the black dashed line shows the analysed area, whereas the red dashed line showed the part of the image used as in the data overlay in panels B, C and D. The triangles point to the apical bud (white), leaf bases (black), epidermis (light grey) and cortex (dark grey). B: a heat map showing the distribution of m/z 255.23, the most abundant marker, overlaid on a light microscope image of the tissue section. The maximum intensity on the colour scale is 10085 ion counts. The pixels are smoothed using linear interpolation. C: a heat map showing the distribution of m/z 164.04, putatively identified as cinnamic acid, overlaid on a light microscope image of the tissue section. The maximum intensity on the colour scale is 64 ion counts. The pixels are smoothed using linear interpolation. D: a heat map showing the distribution of m/z 148.05, putatively identified as coumaric acid, overlaid on a light microscope image of the tissue section. The maximum intensity on the colour scale is 20 ion counts. The pixels are smoothed using linear interpolation.

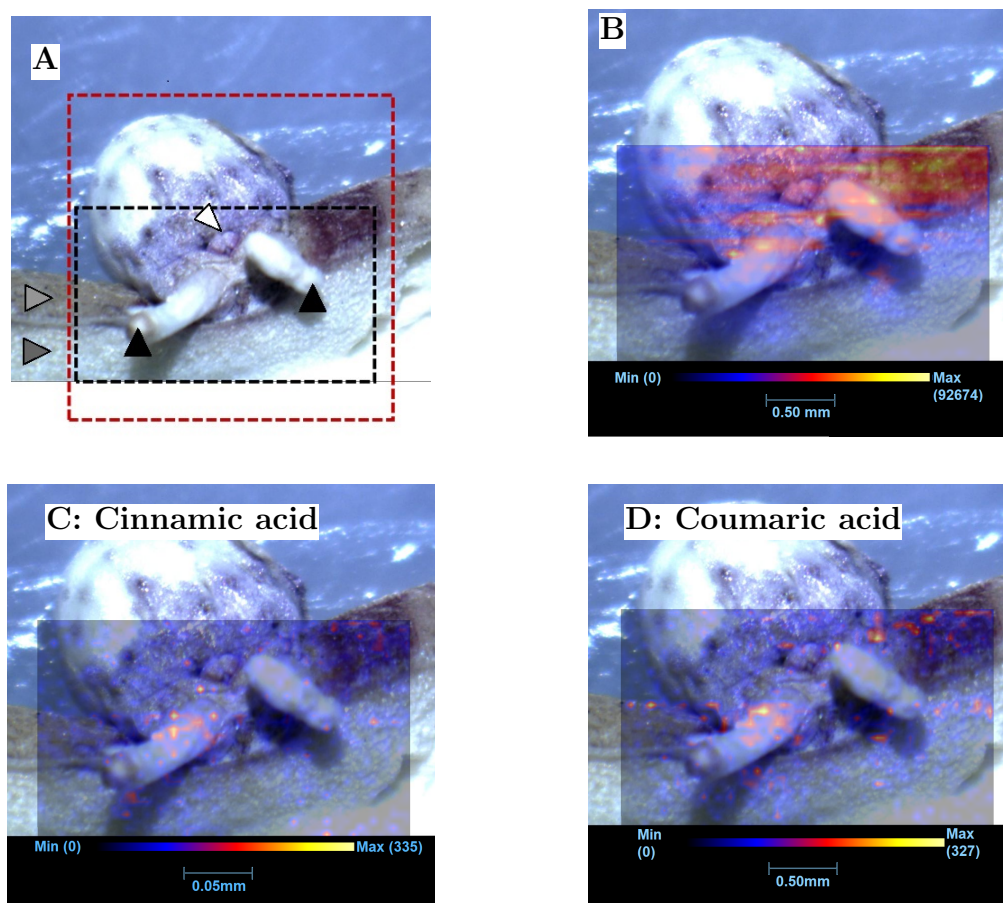


Figure 4.3: Metabolite distribution in a tuber piece, sectioned after 24 hours in pH 5.0 buffer

The hand section was flash frozen and freeze dried, then analysed by negative mode DESI MSI. A: A 10x magnification stereo microscope image of the tissue section. The box with the black dashed line shows the analysed area, whereas the red dashed line showed the part of the image used as in the data overlay in panels C and D. The triangles point to the apical bud (white), growing rootlets (black), epidermis (light grey) and cortex (dark grey). B: a heat map showing the distribution of m/z 255.23, the most abundant marker, overlaid on a light microscope image of the tissue section. The maximum intensity on the colour scale is 92674 ion counts. The pixels are smoothed using linear interpolation. C: a heat map showing the distribution of m/z 164.03, putatively identified as cinnamic acid, overlaid on a light microscope image of the tissue section. The maximum intensity on the colour scale is 335 ion counts. The pixels are smoothed using linear interpolation. D: a heat map showing the distribution of m/z 148.04, putatively identified as coumaric acid, overlaid on a light microscope image of the tissue section. The maximum intensity on the colour scale is 327 ion counts. The pixels are smoothed using linear interpolation.

The metabolic profile of each section was analysed by DESI, in negative mode, using the same parameters as the dilution series described above. Figures 4.2B and 4.3B display heatmaps of the most abundant detected metabolite, m/z 225.23, superimposed on a light microscope image of the fresh tuber hand section (the fresh tuber data are

presented in Figure 4.2, the buffer aged data in Figure 4.3). This metabolite was used to align the MS images and the light microscope images so that other metabolites of interest could be correctly linked to topographical information in the sections. In both fresh and treated tissue, m/z 255.23 was most abundant in the bud region of the analysed tuber sections.

Figures 4.2C and 4.3C show heatmaps of m/z 164.04, which is putatively identified as cinnamic acid on the basis of an earlier test of a standard spotted on a slide. m/z 164.04 is substantially less abundant than m/z 255.23, but is also found in the bud region in both fresh and treated tissue, (with a higher ion count being recorded in the treated tissue). Figure 4.2D 4.3D are heatmaps of m/z 148.05, which is putatively identified as coumaric acid on the basis of an earlier test of a standard spotted on a slide. Again, the coumarate is detected at a higher ion intensity in the treated tissue. The heatmaps are all plotted on individual scales; the maximum ion intensities for the cinnamic and coumaric acid m/z are 4-5 times higher in the treated samples, compared to the fresh tuber tissue. The cinnamic acid and coumaric acid signals are particularly evident in the tuber skin and in the buds.

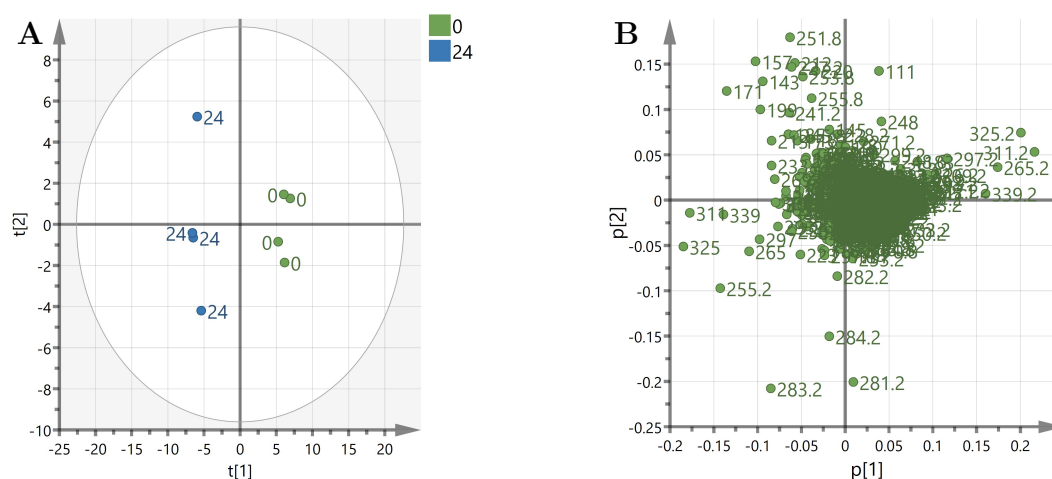


Figure 4.4: PCA analysis comparing regions of interest from the phenolics method DESI images

A PCA of regions of interest from 8 DESI images. Samples were analysed in negative mode with a phenolics-optimised method. $3 \times 0.8 \text{ mm}^2$ regions of interest were created for each image, and the data extracted. Data were simplified by binning to a mass accuracy of $\pm 0.1 \text{ Da}$. A: The PCA score plot from the phenolics image regions of interest. Point label and colour refers to sampling time. Axes are components 1 and 2 of the PCA model. $N=8$. Ellipse = 95% confidence (Hotelling T^2). B: PCA loadings plot from the phenolics image regions of interest. Each point refers to an individual m/z bin, labelled accordingly. Axes are loadings for components 1 and 2 of the PCA model.

3 regions of interest (ROI) were drawn on the images in 4.2, 4.3 and three further

biological replicates for each treatment (selected replicate images are presented in Appendix B). Each ROI was 8 pixels in size ($200\mu\text{m}^2$) and drawn on the bud region. Full spectra (m/z 50-850) for each ROI were extracted and binned. As described in chapter 2, the binning involves collating the 3 ROIs for each tissue sample, using the noise reduction macro to simplify the data. Each ROI is treated as technical replicates, and each processed biological replicate was analysed to produce the PCAs in Figure 4.4 on page 111.

In Figure 4.4A (the PCA scores plot), each point represents the collated data for 3 regions of interest, a process performed for 4 biological replicates for each treatment. There is clear separation along component 1 between the tubers hand sectioned immediately and those aged in Phosphate buffer for 24 hours. The loadings plot, Figure 4.4B can be used to investigate the identity of markers producing this pattern, as was done in Chapter 2. Whilst the putatively identified phenolics compounds are not in evidence in the loadings plot, the most abundant mass, m/z 255.2 is visible in the bottom-left quadrant, close to the component 1 axis.

4.3.2 Malate detection

Having established a reliable protocol for the detection of phenolics in wounded tubers, I worked on developing a detection method for my metabolites of interest from Chapters 2 and 3. This involved optimising the total ion count on a slide spotted with a standard solution of malic acid and a TCA cycle mix. Having optimised the detection of concentrated (7.5mM) malic acid, a dilution series was generated.

Figure 4.5 on page 114 shows a standard curve for malic acid detection on a polysine slide. A slide was spotted with a serial dilution of malic acid in methanol, as described in Table 4.2.6 on page 105 and imaged using DESI in negative mode, with a malate-optimised method. Scans acquired over 10 minute intervals were summed, producing 5 analytical replicates per spot, and the mean ion intensity of the m/z corresponding to malate plotted against the molarity of the standard solution. With the exception of the data for the 75 μ M spot, the standard curve is approximately linear on a \log_{10} scale over the range 7.5mM-75pM. The most dilute sample intensity (75pM) was consistently detected at a higher intensity than the control, but this result was not significant (1-tailed t-test, $p=0.1075$, $t=1.37$, $df=8$), so I conclude that it is at the limits of detection for this method. The next most concentrated sample (7.5nM) was detected at significantly higher levels than the controls (1-tailed t-test, $p=0.0008$, $t=4.636$, $df=8$), so the dilution series appears to have captured the detection method's effective range.

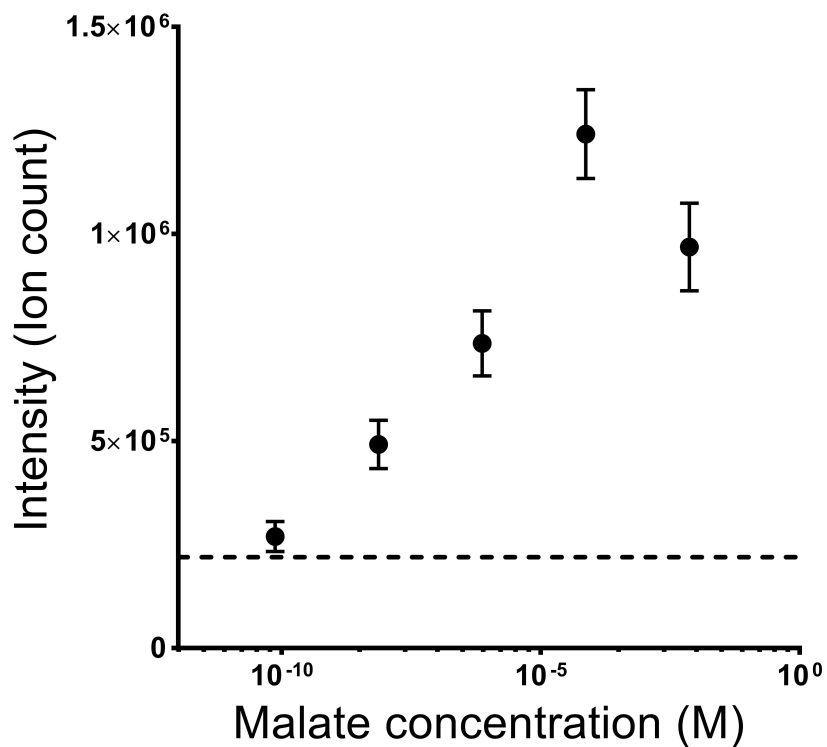


Figure 4.5: The standard curve of malic acid detection by the DESI. Each filled point represents a different concentration of malic acid in methanol, diluted in 100-fold steps. This is represented on a \log_{10} scale. The control (100% methanol) is represented by the dashed line. The confidence interval of this line is too narrow to be presented on this scale. The error bars are standard error of the mean. $n=6$.

4.3.3 The distribution of TCA cycle intermediates in hand sections of tubers

The next 5 Figures (Figures 4.6 to 4.10) refer to an experiment performed on hand sectioned potato tubers, stored for 0 or 6 weeks. The experiment closely resembles the preparation of the phenolics samples above, except that the independent variable is the time tubers spent in storage.

Figure 4.6 on page 116 outlines the preparatory steps undertaken to analyse a fresh hand section (analysed during the week of harvest). Figure 4.6A shows the region analysed by DESI (black box). This region contains an apical bud, hand sectioned longitudinally. The leaf bases are visible at the bottom-middle of the box. There is a colour difference between the cortex and vascular bundle in the tuber. The red box outlines the region used in data overlays in subsequent panels. Figure 4.6B shows the distribution of the abundant marker ion, m/z 255.2. Here it is used to align the data to the image of the sample. There is some detection of the ion outside the tuber region, but there is a clear pattern aligning the peak intensities to anatomical features. Figure 4.6C shows the three regions of interest drawn onto the sample, which are used to produce the data for Figure 4.10, below. These regions correspond to the bud area, as the emphasis in the analysis will be on differences in response to storage in this region.

Figure 4.7 on page 117 shows the distribution of 3 different TCA cycle metabolites: citrate (A), malate (B), fumarate (C) and a composite of all three (D). The detection of $m.z$ 114.9, corresponding to fumarate (Figure 4.7D) was higher than the other two metabolites. By plotting them on individual scales in Figure 4.7D, it is possible to see where they co-occur without being overwhelmed by fumarate's superabundance. Malate (Figure 4.7B) appears to be more abundant in the cortex part of the analysed region, whereas citrate has several hot spots in the bud region. In comparison, fumarate is fairly ubiquitous.

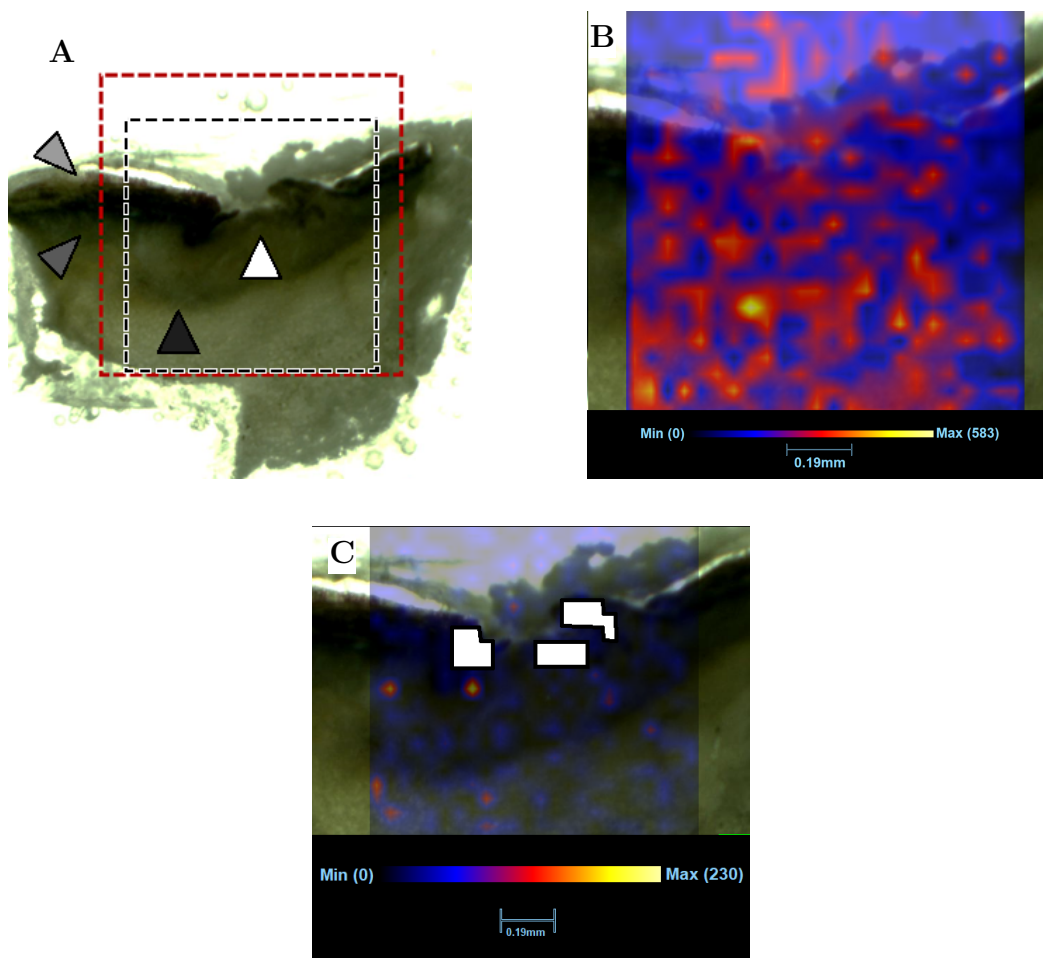


Figure 4.6: Analysis of a fresh tuber hand section

The hand section of tissue was flash frozen, freeze dried and analysed in negative mode DESI MSI. A: A 10x magnification stereo microscope image of the tissue section. The box with the black dashed line shows the analysed area, whereas the red dashed line showed the part of the image used as in the data overlay in panels B, C and Figure 4.7. The triangles point to the apical bud (white), vasculature (black), epidermis (light grey) and cortex (dark grey). B: a heat map showing the distribution of m/z 255.2, the most abundant metabolite, overlaid on a light microscope image of the tissue section. The maximum intensity on the colour scale is 583 ion counts. The pixels are smoothed using linear interpolation. C: a heat map showing the distribution of m/z 255.2, highlighting the regions of interest used in later analysis (see 4.10), overlaid on a light microscope image of the tissue section. The maximum intensity on the colour scale is 230 ion counts. The pixels are smoothed using linear interpolation.

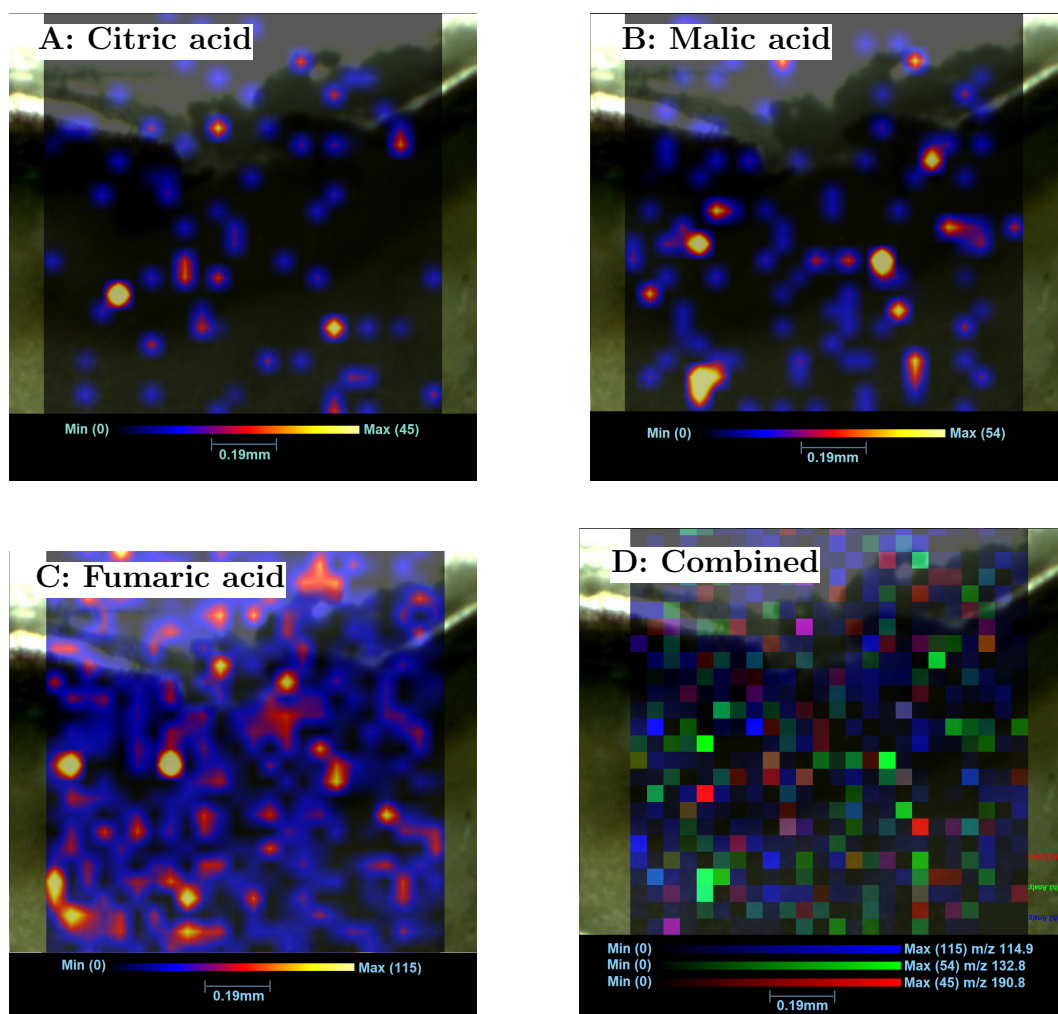


Figure 4.7: Metabolite distribution in a fresh tuber hand section

The hand section of tissue was flash frozen, freeze dried and analysed in negative mode DESI MSI. A: a heat map showing the distribution of m/z 190.9, putatively identified as citric acid, overlaid on a light microscope image of the tissue section. The maximum intensity on the colour scale is 45 ion counts. The pixels are smoothed using linear interpolation. B: a heat map showing the distribution of m/z 133.0, putatively identified as malic acid, overlaid on a light microscope image of the tissue section. The maximum intensity on the colour scale is 54 ion counts. The pixels are smoothed using linear interpolation. C: a heat map showing the distribution of m/z 114.9, putatively identified as fumaric acid, overlaid on a light microscope image of the tissue section. The maximum intensity on the colour scale is 115 ion counts. The pixels are smoothed using linear interpolation. D: a heat map showing the distribution of all three TCA cycle markers, overlaid on a light microscope image of the tissue section. Each moiety is displayed on its own colour intensity scale. The maximum intensity on the fumaric acid colour scale (blue) is 115 ion counts. The maximum intensity on the malic acid colour scale (green) is 54 ion counts. The maximum intensity on the citric acid colour scale (red) is 45 ion counts.

The analysis of the stored counterparts of Figures 4.6 and 4.7 was less successful than the fresh samples, leading to later modifications of this method. Figure 4.8 on

page 119 outlines the preparatory steps undertaken to analyse a hand-section of stored tuber (analysed 6 weeks after harvest). Figure 4.8A shows the region analysed by DESI (black box). This region contains an apical bud, hand sectioned longitudinally. The leaf bases are visible to the left of the box. There is a colour difference between the skin and tuber cortex. The red box outlines the region used in data overlays in subsequent panels. Figure 4.8B shows the distribution of the abundant marker ion, m/z 255.2. Here it is used to align the data to the image of the sample. It is much less abundant than the previous sample: the scale in this image has a maximum of 105 counts, more than 5 times lower than 4.6B. Figure 4.8C shows the three regions of interest drawn onto the sample, which are used to produce the data for the PCA plot in Figure 4.10, below. These regions correspond to the bud area, as the emphasis in the analysis will be on differences in response to storage in this region.

Figure 4.9 on page 120 shows the distribution of 3 different TCA cycle metabolites: citrate (A), malate (B), fumarate (C) and a composite of all three (D). The detection of $m.z$ 114.9, corresponding to fumarate (Figure 4.9D) was higher than the other two metabolites, but all are limited. They are plotted on the same scale in Figure 4.9D; showing that coverage is limited. In spite of the limited detection in this and replicate samples, Figure 4.10 was generated to compare the normalised data from these stored tubers to the samples discussed above (analysed shortly after harvest).

Figure 4.10 on page 121 shows a PCA analysis of the 5 hand sections that were run successfully using the malate detection method. Samples were either fresh samples (analysed on the week of harvest) or Stored samples (analysed 6 weeks after harvest). Each point in the PCA score plot (Figure 4.10A) represents the output of 3 binned regions of interest, all from the same section. Thus, the data processing macro is used to simplify the technical replicates, so the score plot only displays biological replicates. The Fresh samples (analysed on the week of harvest) are aligned along the component 1 axis, whereas the two Stored samples (analysed 6 weeks after harvest) vary along the component 2 axis. The PCA loadings plot (Figure 4.10B) displays the loadings from this principal component analysis. m/z 115, which corresponds to fumarate, is evident and aligns to component 2, which is linked to the difference between fresh and stored tubers. However, the limited detection in some of the samples make interpretations of this analysis limited.

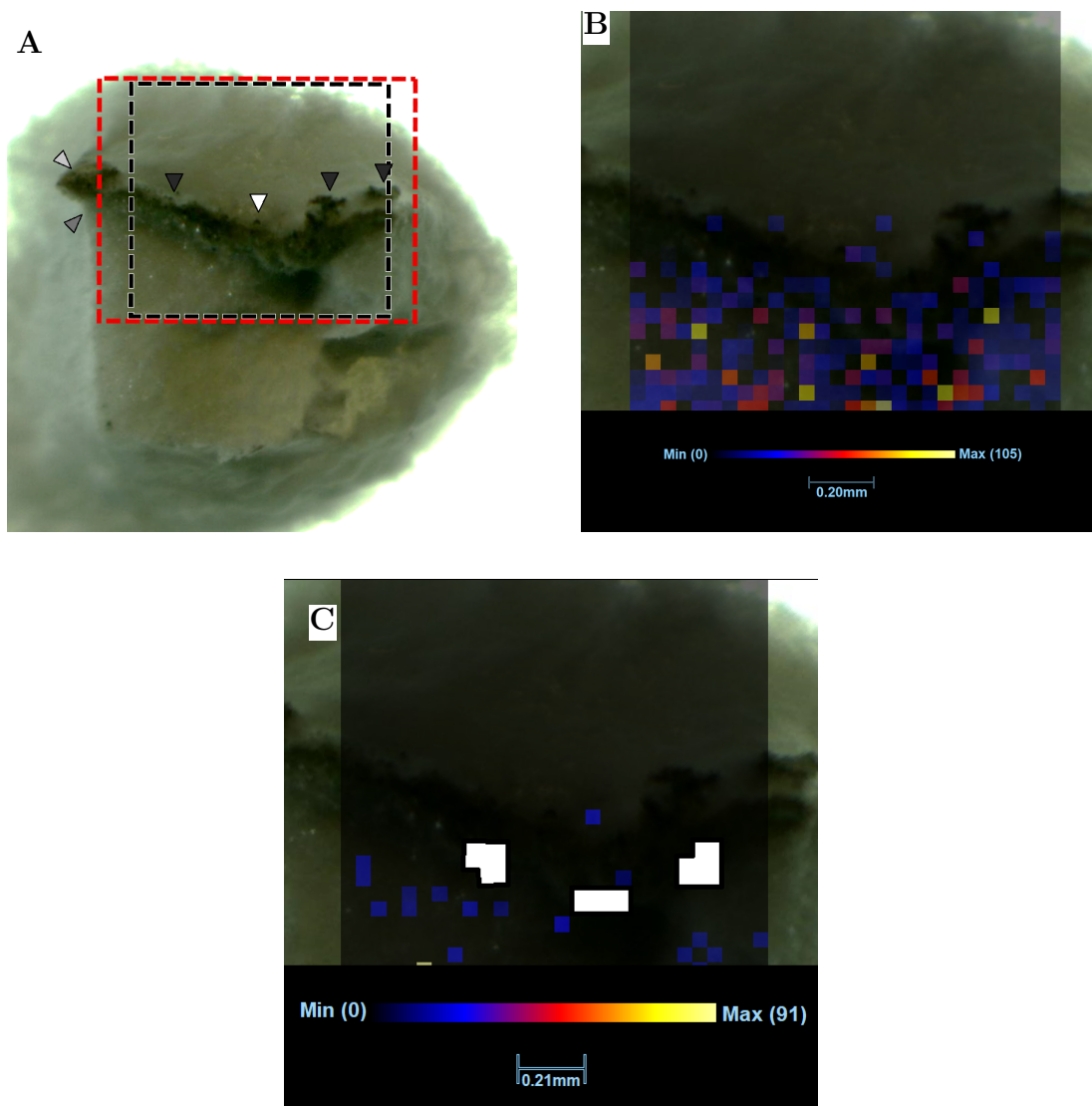


Figure 4.8: Analysis of a stored tuber hand section

The hand section of tissue was flash frozen, freeze dried and analysed in negative mode DESI MSI. A: A 10x magnification stereo microscope image of the tissue section. The box with the black dashed line shows the analysed area, whereas the red dashed line showed the part of the image used as in the data overlay in panels B, C and Figure 4.9. The triangles point to the apical bud (white), additional buds (black), epidermis (light grey) and cortex (dark grey). B: a heat map showing the distribution of m/z 255.2, the most abundant metabolite, overlaid on a light microscope image of the tissue section. The maximum intensity on the colour scale is 105 ion counts. C: a heat map showing the distribution of m/z 255.2, highlighting the regions of interest used in later analysis (see 4.10), overlaid on a light microscope image of the tissue section. The maximum intensity on the colour scale is 15000 ion counts.

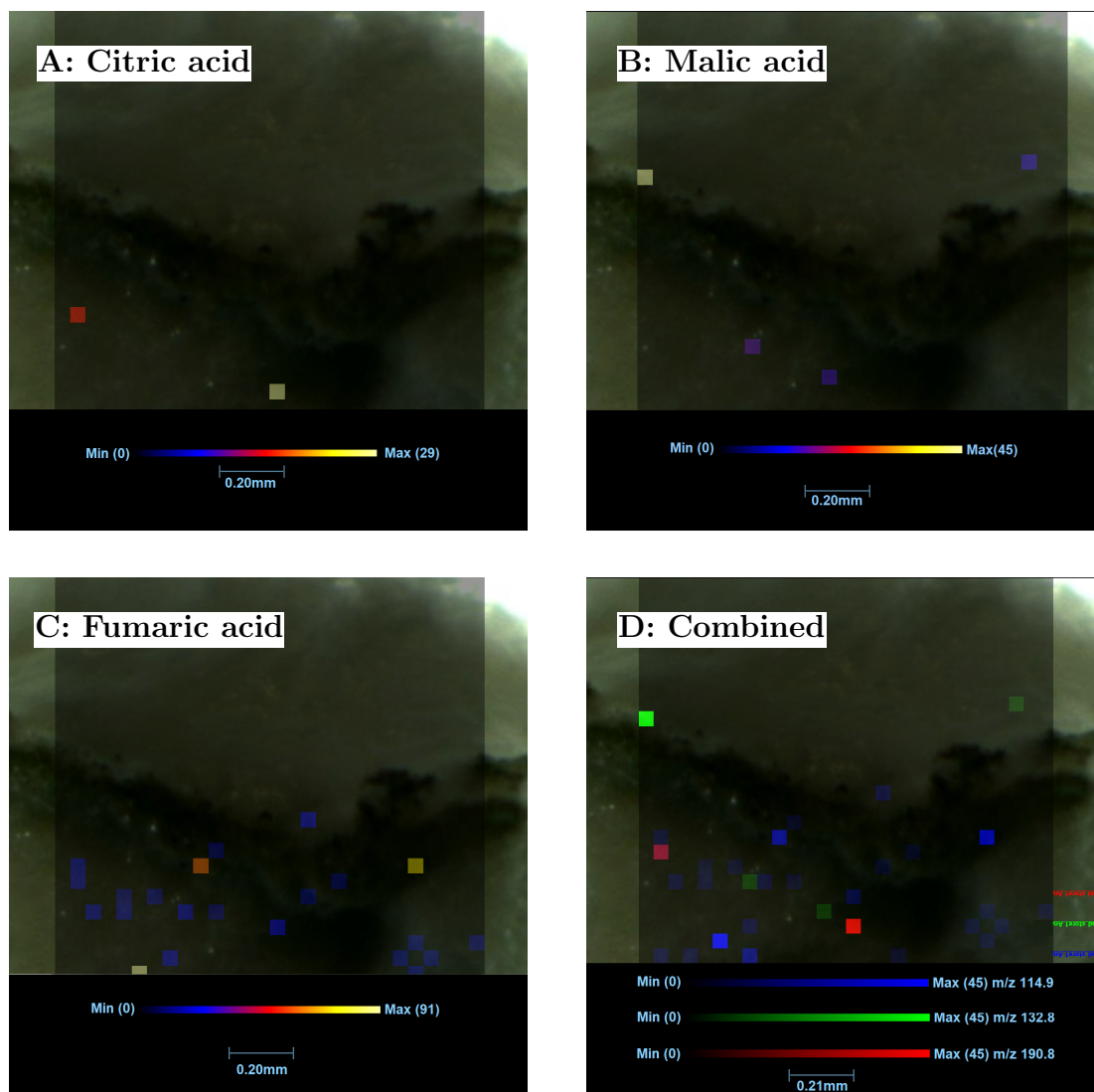


Figure 4.9: Metabolite distribution in a stored tuber hand section

The hand section of tissue was flash frozen, freeze dried and analysed in negative mode DESI MSI. A: a heat map showing the distribution of m/z 190.9, putatively identified as citric acid, overlaid on a light microscope image of the tissue section. The maximum intensity on the colour scale is 29 ion counts. B: a heat map showing the distribution of m/z 132.9, putatively identified as malic acid, overlaid on a light microscope image of the tissue section. The maximum intensity on the colour scale is 45 ion counts. C: a heat map showing the distribution of m/z 114.9, putatively identified as fumaric acid, overlaid on a light microscope image of the tissue section. The maximum intensity on the colour scale is 91 ion counts. D: a heat map showing the distribution of all three TCA cycle markers, overlaid on a light microscope image of the tissue section. Each moiety is displayed on its own colour intensity scale. The maximum intensity on the fumaric acid colour scale (blue) is 45 ion counts. The maximum intensity on the malic acid colour scale (green) is 45 ion counts. The maximum intensity on the citric acid colour scale (red) is 45 ion counts.

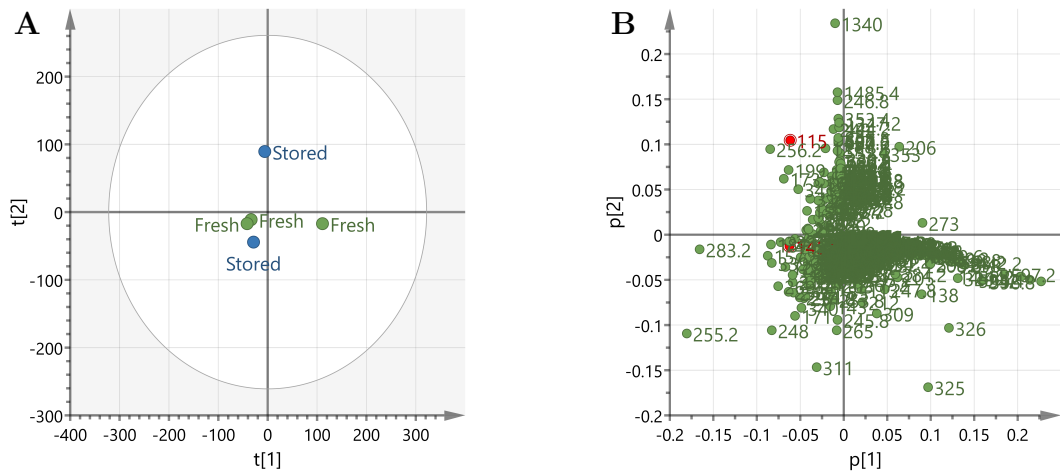


Figure 4.10: PCA analysis comparing regions of interest from the handsection DESI images

A PCA of regions of interest from 8 DESI images. Samples were analysed in negative mode with a TCA-cycle optimised method. $3 \times 0.8 \text{ mm}^2$ regions of interest were created for each image, and the data extracted. Data were simplified by binning to a mass accuracy of $\pm 0.1 \text{ Da}$. A: The PCA score plot from the DESI image regions of interest. Point label and colour refers to sampling time. Axes are components 1 and 2 of the PCA model. $N=8$. Ellipse = 95% confidence (Hotelling T2). B: PCA loadings plot from the DESI image regions of interest. Each point refers to an individual m/z bin, labelled accordingly. Axes are loadings for components 1 and 2 of the PCA model.

4.3.4 The distribution of TCA cycle intermediates in tuber cryosections

The next 5 Figures (Figures 4.11 to 4.15) refer to an experiment performed on potato tubers, cryosectioned after storage for 2 or 8 weeks. The experiment closely resembles the hand sectioned samples above, except that the samples were sectioned to $60 \mu\text{m}$ thickness and were not freeze dried.

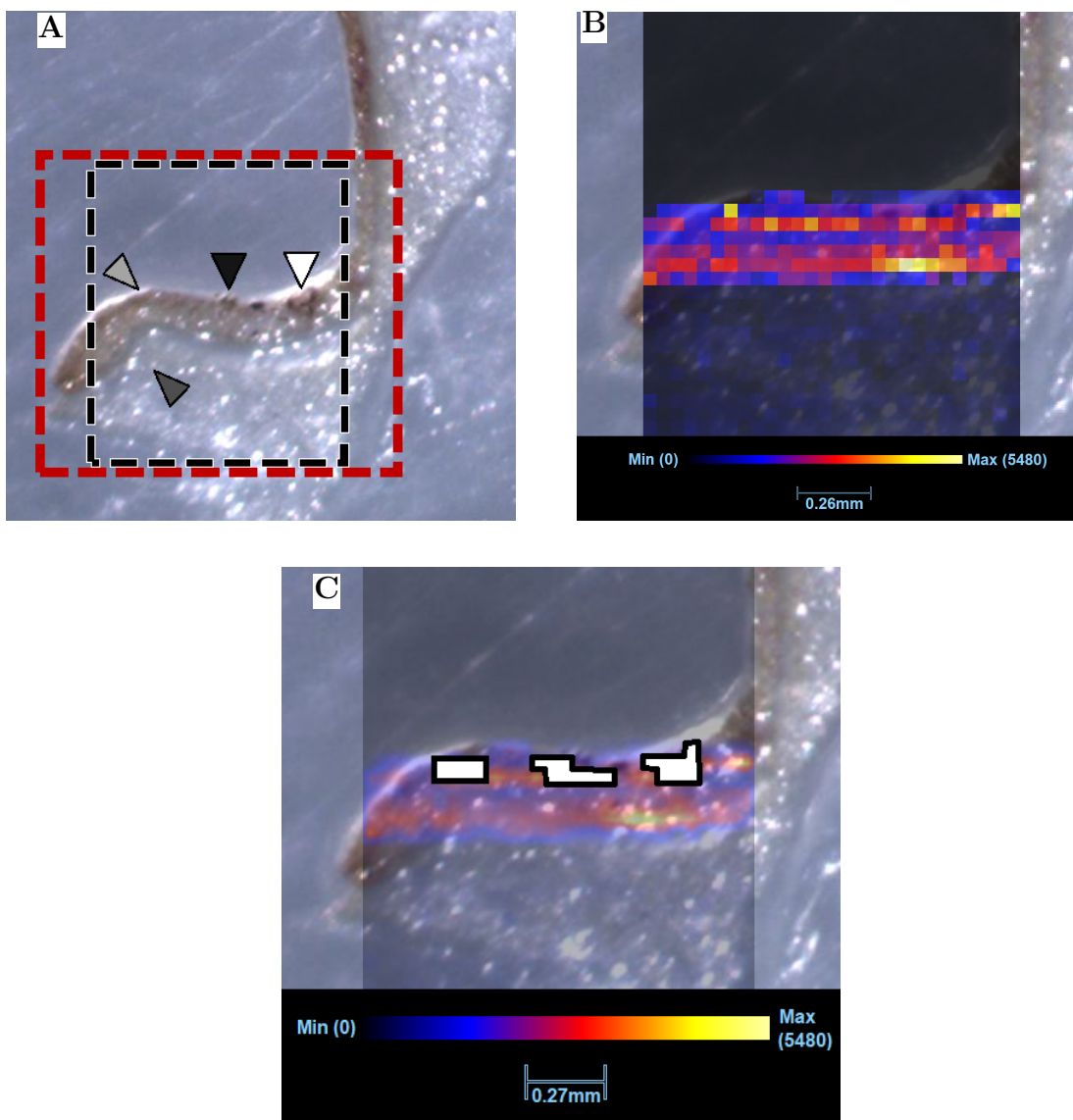


Figure 4.11: Analysis of a fresh tuber cryosection

The cryo section of flash frozen tissue was analysed by negative mode DESI MSI. A: A 10x magnification stereo microscope image of the tissue section. The box with the black dashed line shows the analysed area, whereas the red dashed line showed the part of the image used as in the data overlay in panels B, C and Figure 4.12. The triangles point to the apical bud (white), additional bud (black), epidermis (light grey) and cortex (dark grey). B: a heat map showing the distribution of m/z 255.2, the most abundant metabolite, overlaid on a light microscope image of the tissue section. The maximum intensity on the colour scale is 5480 ion counts. C: a heat map showing the distribution of m/z 255.2, highlighting the regions of interest used in later analysis (see Figure 4.15), overlaid on a light microscope image of the tissue section. The maximum intensity on the colour scale is 5480 ion counts. The pixels are smoothed using linear interpolation.

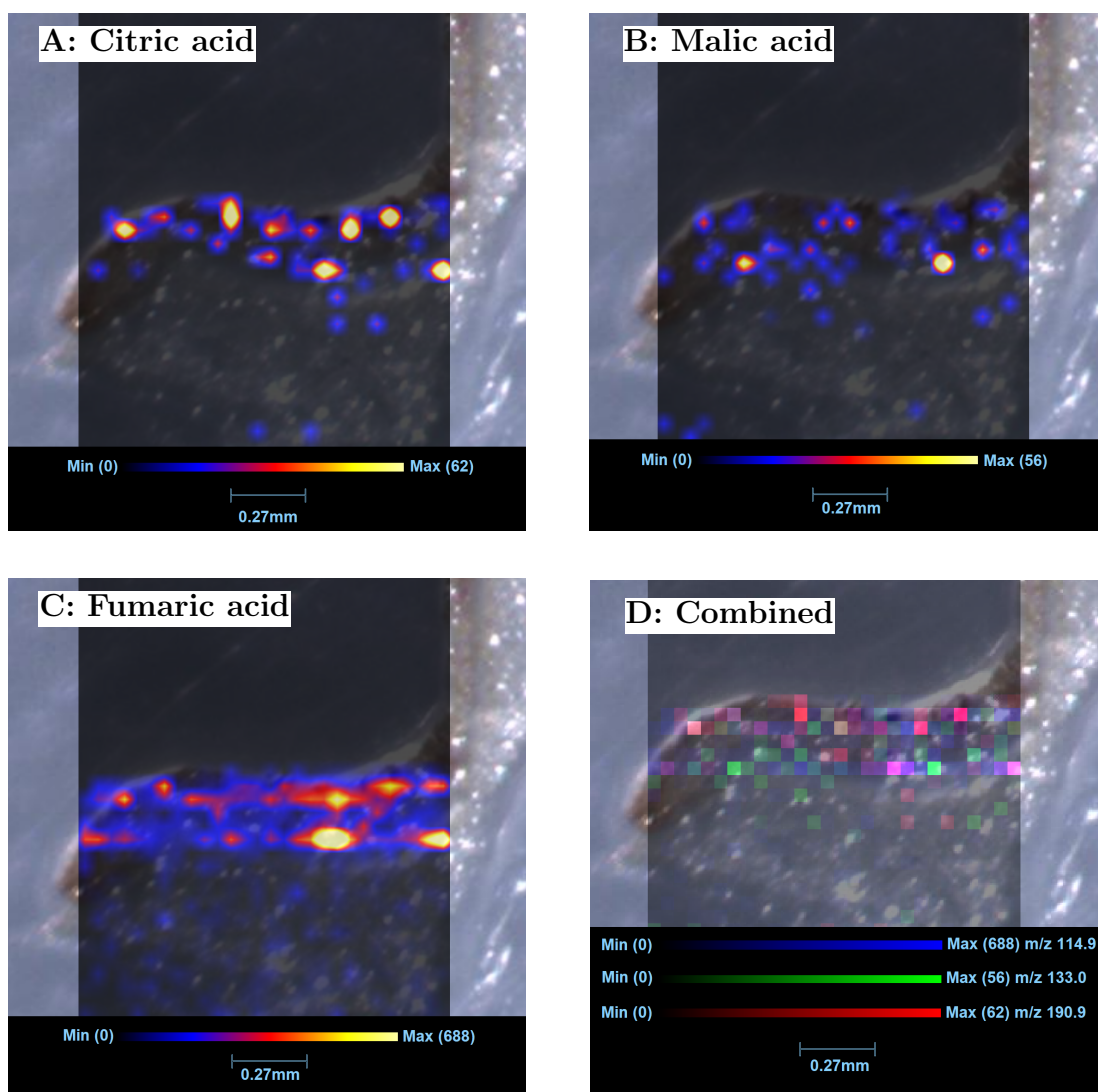


Figure 4.12: Metabolite distribution in a fresh tuber cryosection

The cryo section of flash frozen tissue was analysed by negative mode DESI MSI, building on the data in 122. A: a heat map showing the distribution of m/z 190.9, putatively identified as citric acid, overlaid on a light microscope image of the tissue section. The maximum intensity on the colour scale is 62 ion counts. The pixels are smoothed using linear interpolation. B: a heat map showing the distribution of m/z 133.0, putatively identified as malic acid, overlaid on a light microscope image of the tissue section. The maximum intensity on the colour scale is 56 ion counts. The pixels are smoothed using linear interpolation. C: a heat map showing the distribution of m/z 114.9, putatively identified as fumaric acid, overlaid on a light microscope image of the tissue section. The maximum intensity on the colour scale is 688 ion counts. The pixels are smoothed using linear interpolation. D: a heat map showing the distribution of all three TCA cycle markers, overlaid on a light microscope image of the tissue section. Each moiety is displayed on its own colour intensity scale. The maximum intensity on the fumaric acid colour scale (blue) is 688 ion counts. The maximum intensity on the malic acid colour scale (green) is 56 ion counts. The maximum intensity on the citric acid colour scale (red) is 62 ion counts.

Figure 4.11 on page 122 outlines the preparatory steps undertaken to analyse a cryosection of a fresh tuber (analysed 2 weeks after harvest). Figure 4.11A shows the region analysed by DESI (black box). This region contains an apical bud, hand sectioned longitudinally. The bud is visible in the middle-right of the box. There is a colour difference between the epidermis and the tuber cortex. The red box outlines the region used in data overlays in subsequent panels. Figure 4.11B shows the distribution of the abundant marker ion, m/z 255.2. Here it is used to align the data to the image of the sample. There is a clear pattern aligning the peak intensities to anatomical features. Figure 4.11C shows the three regions of interest drawn onto the sample, which are used to produce the data for Figure 4.15, below. These regions correspond to the bud area, as the emphasis in the analysis will be on differences in response to storage in this region.

Figure 4.12 on page 123 shows the distribution of 3 different TCA cycle metabolites: citrate (A), malate (B), fumarate (C) and a composite of all three (D). The detection of m/z 114.9, corresponding to fumarate (Figure 4.12D) was higher than the other two metabolites. By plotting them on individual scales in Figure 4.12D, it is possible to see where they co-occur without being overwhelmed by fumarate's superabundance. Malate (Figure 4.12B) appears to be more abundant in the cortex part of the analysed region, whereas there are several citrate hot spots in the bud and epidermis region. In comparison, fumarate is fairly ubiquitous.

Figure 4.13 on page 125 outlines the preparatory steps undertaken to analyse a cryosection (analysed 8 weeks after harvest). Figure 4.13A shows the region analysed by DESI (black box). This region contains an apical bud, hand sectioned longitudinally. The leaf bases are visible to the left of the box. There is a colour difference between the epidermis and tuber cortex. The red box outlines the region used in data overlays in subsequent panels. Figure 4.13B shows the distribution of the abundant marker ion, m/z 255.2. Here it is used to align the data to the image of the sample. There is some detection of the ion outside the tuber area, but also a clear correspondence with the bud area. Figure 4.13C shows the three regions of interest drawn onto the sample, which are used to produce the data for the PCA plot in Figure 4.10, below. These regions correspond to the bud area, as the emphasis in the analysis will be on differences in response to storage in this region. It also excludes the high intensity stripe at the bottom of the analysed region (particularly noticeable in 4.13C), which appears to be an experimental artefact, as it doesn't correspond to any anatomical features.

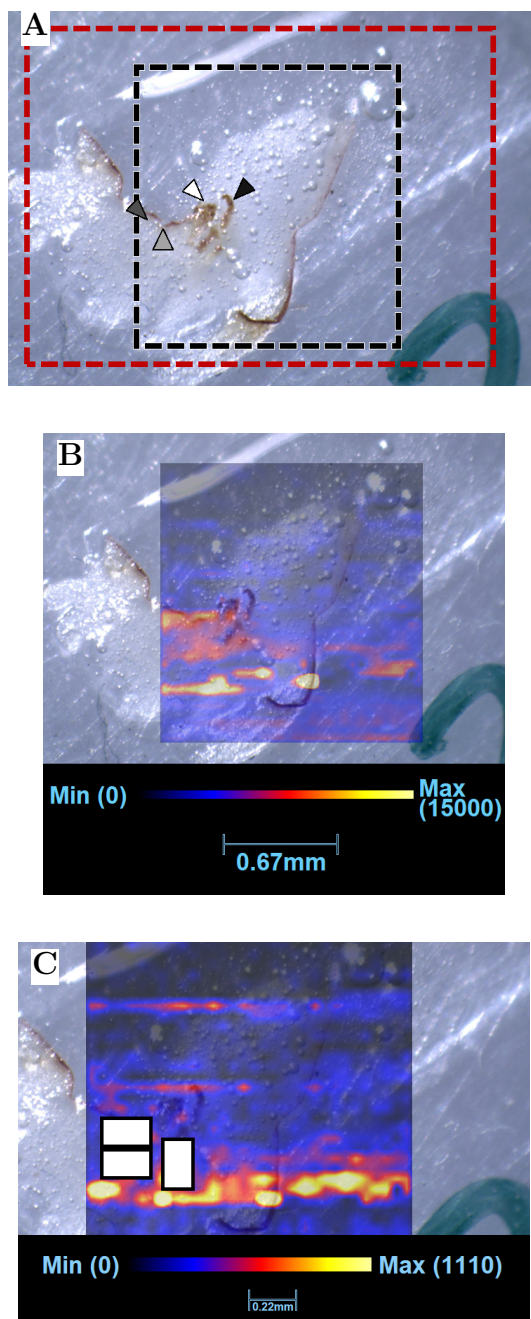


Figure 4.13: Analysis of a stored tuber cryosection

The cryo section of flash frozen tissue was analysed by negative mode DESI MSI. A: A 10x magnification stereo microscope image of the tissue section. The box with the black dashed line shows the analysed area, whereas the red dashed line showed the part of the image used as in the data overlay in panels B, C and Figure 4.14. The triangles point to the apical bud (white), leaf base (black), epidermis (light grey) and cortex (dark grey). B: a heat map showing the distribution of m/z 255.2, the most abundant metabolite, overlaid on a light microscope image of the tissue section. The maximum intensity on the colour scale is 15000 ion counts. The pixels are smoothed using linear interpolation. C: a heat map showing the distribution of m/z 255.2, highlighting the regions of interest used in later analysis (see Figure 4.15), overlaid on a light microscope image of the tissue section. The maximum intensity on the colour scale is 15000 ion counts. The pixels are smoothed using linear interpolation.

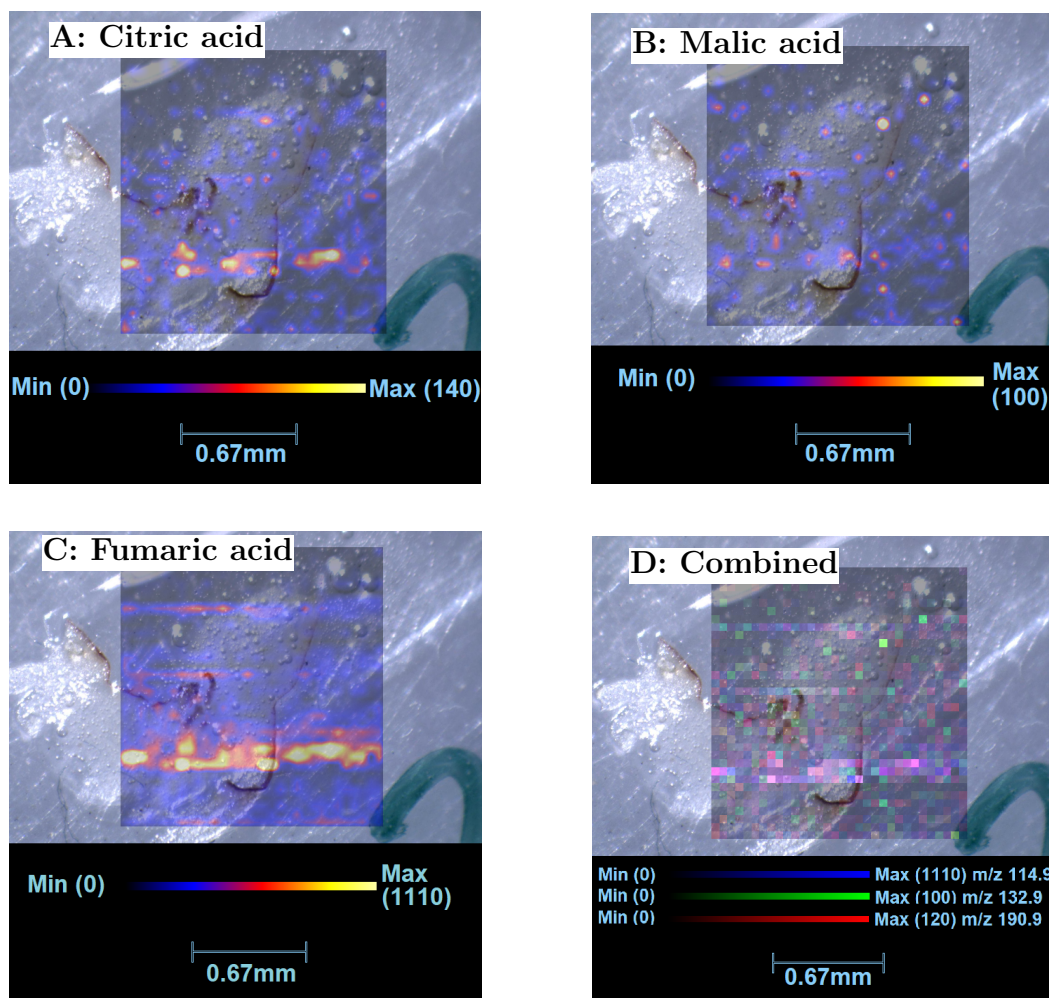


Figure 4.14: Metabolite distribution in a stored tuber cryosection

The cryo section of flash frozen tissue was analysed by negative mode DESI MSI, building on the data in 4.13. A: a heat map showing the distribution of m/z 190.9, putatively identified as citric acid, overlaid on a light microscope image of the tissue section. The maximum intensity on the colour scale is 140 ion counts. The pixels are smoothed using linear interpolation. B: a heat map showing the distribution of m/z 132.9, putatively identified as malic acid, overlaid on a light microscope image of the tissue section. The maximum intensity on the colour scale is 100 ion counts. The pixels are smoothed using linear interpolation. C: a heat map showing the distribution of m/z 114.9, putatively identified as fumaric acid, overlaid on a light microscope image of the tissue section. The maximum intensity on the colour scale is 1110 ion counts. The pixels are smoothed using linear interpolation. D: a heat map showing the distribution of all three TCA cycle markers, overlaid on a light microscope image of the tissue section. Each moiety is displayed on its own colour intensity scale. The maximum intensity on the fumaric acid colour scale (blue) is 1110 ion counts. The maximum intensity on the malic acid colour scale (green) is 100 ion counts. The maximum intensity on the citric acid colour scale (red) is 120 ion counts.

Figure 4.14 on page 126 shows the distribution of 3 different TCA cycle metabolites: citrate (A), malate (B), fumarate (C) and a composite of all three (D). The detection

of m.z 114.9, corresponding to fumarate (Figure 4.14D) was higher than the other two metabolites. The pattern is very similar to that discussed above for 4.12.

In spite of the limited detection in replicate samples, Figure 4.15 was generated to compare the normalised data for fresh and stored tuber samples. Figure 4.15 on page 127 shows a PCA analysis of the 5 cryosections that were run successfully using the malate detection method. Each point in the PCA score plot (Figure 4.15A) represents the output of 3 binned regions of interest, all from the same section. Thus, the data processing macro is used to simplify the technical replicates, so the score plot only displays biological replicates. The Fresh samples (here labelled “NOV” and analysed 2 weeks after harvest) cluster to the left on component 1, whereas the two Stored samples (here labelled “OCT” and analysed 8 weeks after harvest) are to the right of the component 1 axis. The PCA loadings plot (Figure 4.15B) displays the loadings from this principal component analysis. The red highlighted m/z, corresponding to TCA cycle intermediates, are to the left of the component 1 axis, which is linked to the difference between fresh and stored tubers. However, the limited detection in some of the samples has limited the number of replicates, making interpretation of this analysis limited.

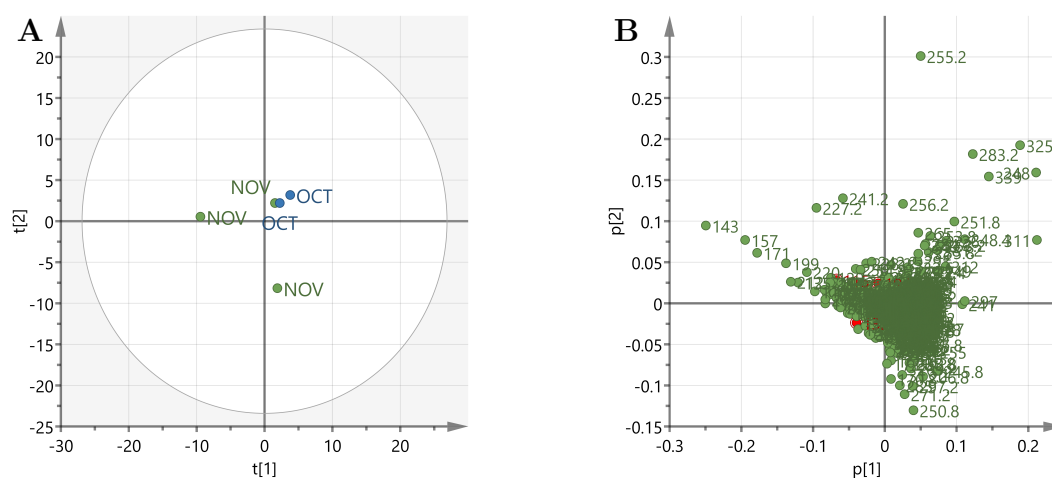


Figure 4.15: PCA analysis comparing regions of interest from the cryosection DESI images

A PCA of regions of interest from 8 DESI images. Samples were analysed in negative mode with a TCA-cycle optimised method. $3 \times 0.8 \text{ mm}^2$ regions of interest were created for each image, and the data extracted. Data were simplified by binning to a mass accuracy of $\pm 0.1 \text{ Da}$. A: The PCA score plot from the DESI image regions of interest. Point label and colour refers to sampling time. Axes are components 1 and 2 of the PCA model. $N=8$. Ellipse = 95% confidence (Hotelling T2). B: PCA loadings plot from the DESI image regions of interest. Each point refers to an individual m/z bin, labelled accordingly. Axes are loadings for components 1 and 2 of the PCA model.

4.3.5 The distribution of TCA cycle intermediates in GA- and control-treated tubers

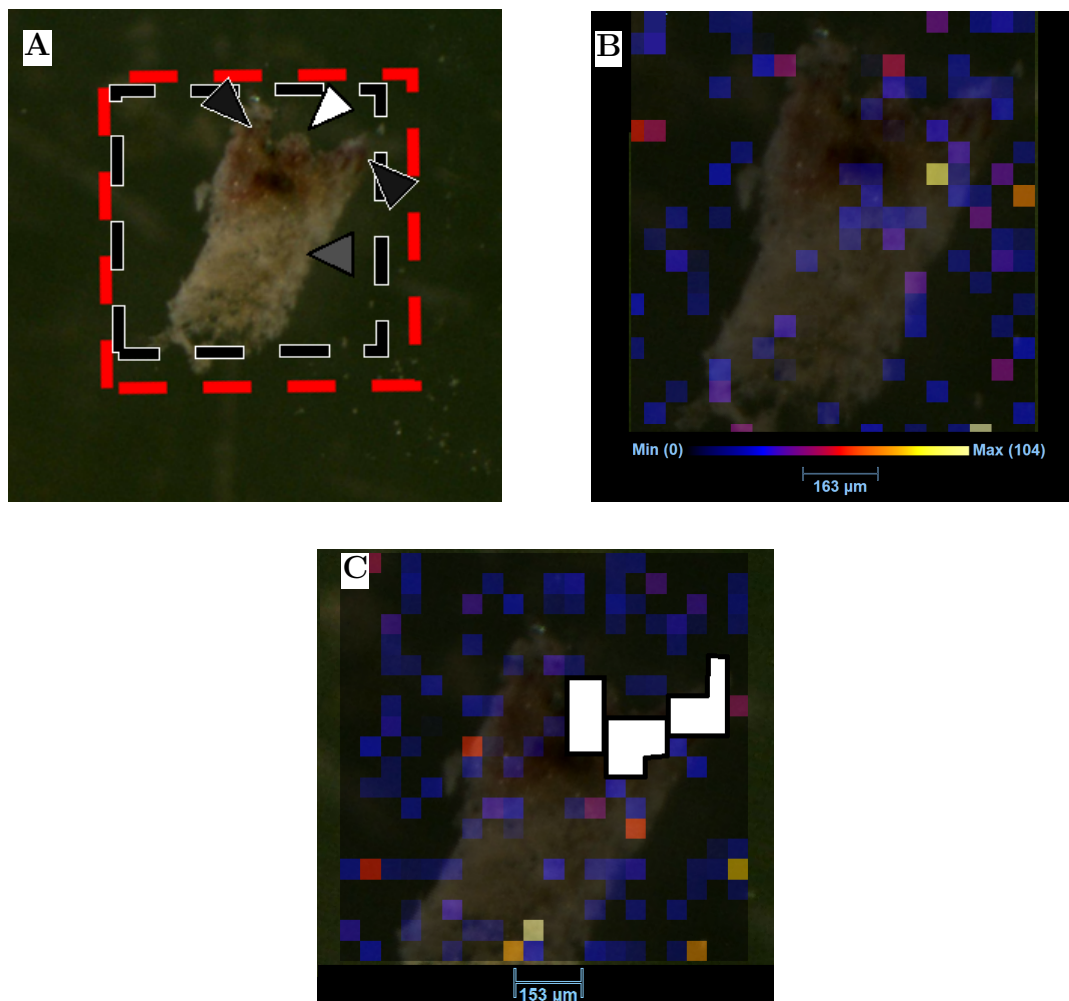


Figure 4.16: Analysis of a tuber cryosection, treated with GA for 72 hours
The cryo section of flash frozen tissue was analysed by negative mode DESI MSI. A: A 10x magnification stereo microscope image of the tissue section. The box with the black dashed line shows the analysed area, whereas the red dashed line showed the part of the image used as in the data overlay in panels B, C and Figure 4.20. The triangles point to the apical bud (white), leaf primordia (black) and cortex (dark grey). B: a heat map showing the distribution of m/z 255.2, the most abundant metabolite, overlaid on a light microscope image of the tissue section. The maximum intensity on the colour scale is 104 ion counts. C: a heat map showing the distribution of m/z 255.2, highlighting the regions of interest used in later analysis (see Figure 4.20), overlaid on a light microscope image of the tissue section. The maximum intensity on the colour scale is 104 ion counts.

The next 5 Figures (Figures 4.16 to 4.20) refer to an experiment performed on potato tubers stored for 8 weeks, treated with GA or water, incubated for 72 hours, then cryosectioned. The experiment closely resembles the experimental design used extensively in chapter 2, except that the samples are $60\mu\text{m}$ sections and a DESI imaging approach was used. Figure 4.16 on page 128 outlines the preparatory steps taken to analyse data for a GA-treated cryosection. Figure 4.16A shows a dissection microscope image of the cryosection. This is quite a small sample, with only the meristem and leaf primordia visible, and several mm of tuber tissue below. The black box illustrates the region analysed by DESI. The red box outlines the region used in data overlays in subsequent panels. Figure 4.16B shows the abundance of the positioning marker ion, m/z 255.2, used to align the data to the sample image. The ion is detected outside the tuber sample, but there are intense peaks corresponding to the leaf primordia and meristem. Figure 4.16C shows the three 0.4mm^2 regions of interest used to extract data for Figure 4.20, below. These areas are drawn over the meristematic tissue and associated organ primordia. Figure 4.17 on page 130 shows the distribution of 3 different TCA cycle metabolites: citrate (A), malate (B), fumarate (C) and a composite of all three (D). These data are derived from the same sample as Figure 4.16. The detection of $m.z$ 114.9, corresponding to fumarate (Figure 4.17D) was higher than the other two metabolites. By plotting them on individual scales in Figure 4.17D, it is possible to see where they co-occur without being overwhelmed by fumarate's abundance. Citrate and malate have intense peaks in the meristem, but were not successfully detected elsewhere (Figure 4.17A and B). Fumarate, in contrast, has a more diffuse distribution (Figure 4.17C).

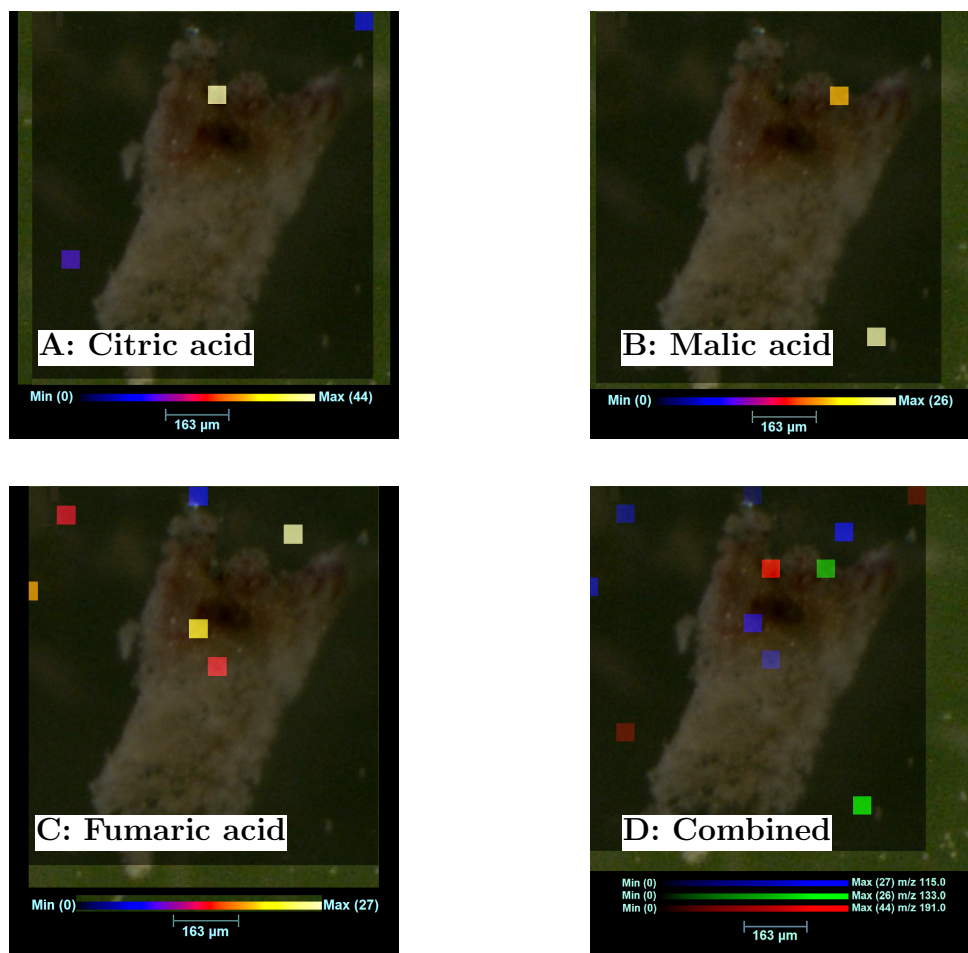


Figure 4.17: Metabolite distribution in a tuber cryosection, treated with GA for 72 hours. The cryo section of flash frozen tissue was analysed by negative mode DESI MSI. A: a heat map showing the distribution of m/z 191.0, putatively identified as citric acid, overlaid on a light microscope image of the tissue section. The maximum intensity on the colour scale is 44 ion counts. B: a heat map showing the distribution of m/z 133.0, putatively identified as malic acid, overlaid on a light microscope image of the tissue section. The maximum intensity on the colour scale is 26 ion counts. C: a heat map showing the distribution of m/z 115.0, putatively identified as fumaric acid, overlaid on a light microscope image of the tissue section. The maximum intensity on the colour scale is 27 ion counts. D: a heat map showing the distribution of all three TCA cycle markers, overlaid on a light microscope image of the tissue section. Each moiety is displayed on its own colour intensity scale. The maximum intensity on the fumaric acid colour scale (blue) is 27 ion counts. The maximum intensity on the malic acid colour scale (green) is 26 ion counts. The maximum intensity on the citric acid colour scale (red) is 44 ion counts.

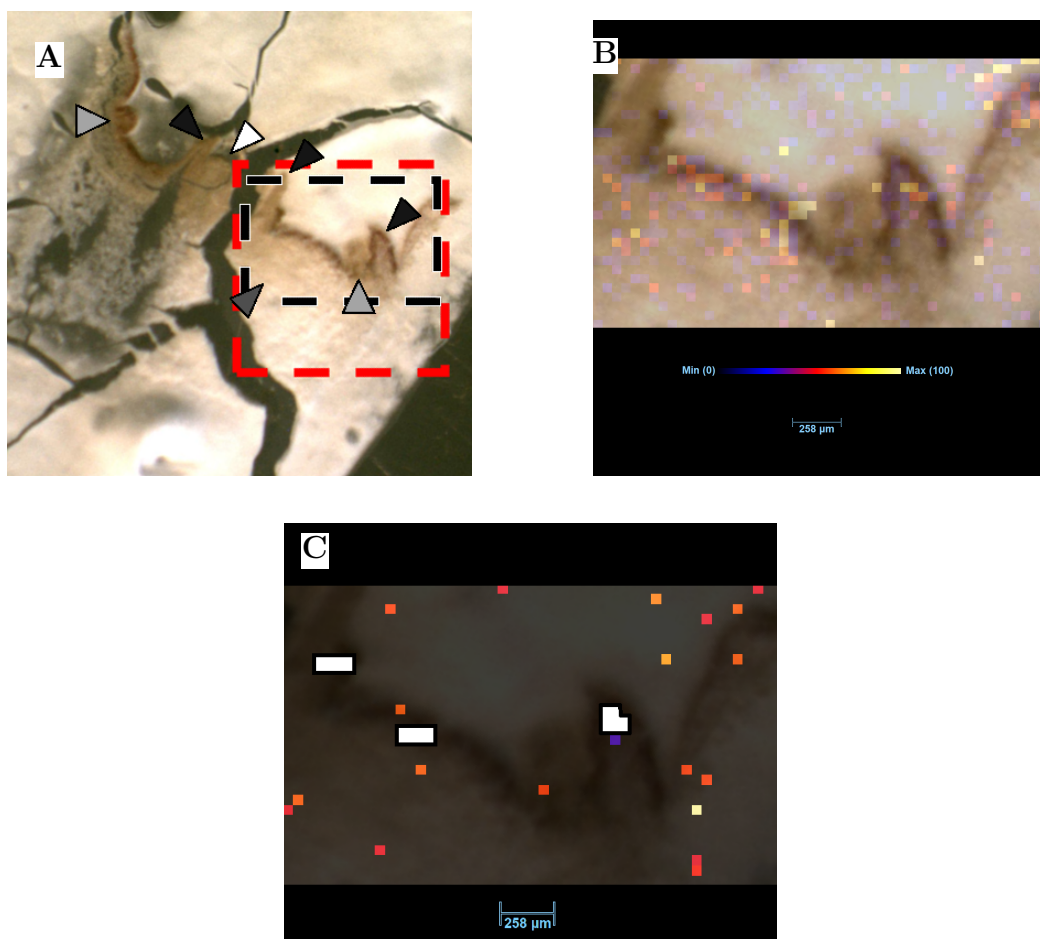


Figure 4.18: Analysis of a tuber cryosection, treated with control (water) for 72 hours. The cryo section of flash frozen tissue was analysed by negative mode DESI MSI. A: A 10x magnification stereo microscope image of the tissue section. The box with the black dashed line shows the analysed area, whereas the red dashed line showed the part of the image used as in the data overlay in panels B, C and Figure 4.20. The triangles point to the apical bud (white), leaf primordia (black), additional buds (light grey) and cortex (dark grey). B: a heat map showing the distribution of m/z 255.2, the most abundant metabolite, overlaid on a light microscope image of the tissue section. The maximum intensity on the colour scale is 100 ion counts. C: a heat map showing the distribution of m/z 255.2, highlighting the regions of interest used in later analysis (see Figure 4.20), overlaid on a light microscope image of the tissue section. The maximum intensity on the colour scale is 100 ion counts.

Figure 4.18 on page 131 shows the same analysis steps as Figure 4.16, but shows a representative control (water-treated) sample cryosection. Figure 4.18A is a dissection microscope image of the cryosection depicted in the subsequent panels. The black box represents the analysed area, whereas the red box shows the image used in subsequent overlays. Due to the damage to the main meristem (top left corner of the red box), the analysis focused on a secondary meristem for this sample. There is a large leaf primordium emerging from it. A similar structure is also visible on the other side of the

section. Figure 4.18B shows the distribution of m/z 255.2. The pattern was used to align the image to the data - there are hotspots on the leaf primordium, along the epidermis and to the top right of the sample. It is worth noting that, whilst the maximum intensity in this image is comparable to Figure 4.16B, there are proportionally more pixels in the red-yellow (intense) part of the colour scale. Figure 4.18C shows the regions of interest used in subsequent analyses. These correspond to the leaf primordium, the base of the main meristem and the epidermal layer between them. The binned version of these data are shown in Figure 4.20, below. Figure 4.19 on page 133 shows the distribution of the 3 different TCA cycle metabolites: citrate (A), malate (B), fumarate (C) and a composite of all three (D). Malate detection was low, limited to 4 individual pixels in the entire sample (Figure 4.19B). In comparison, citrate and fumarate were more diffuse (Figure 4.19A and C).

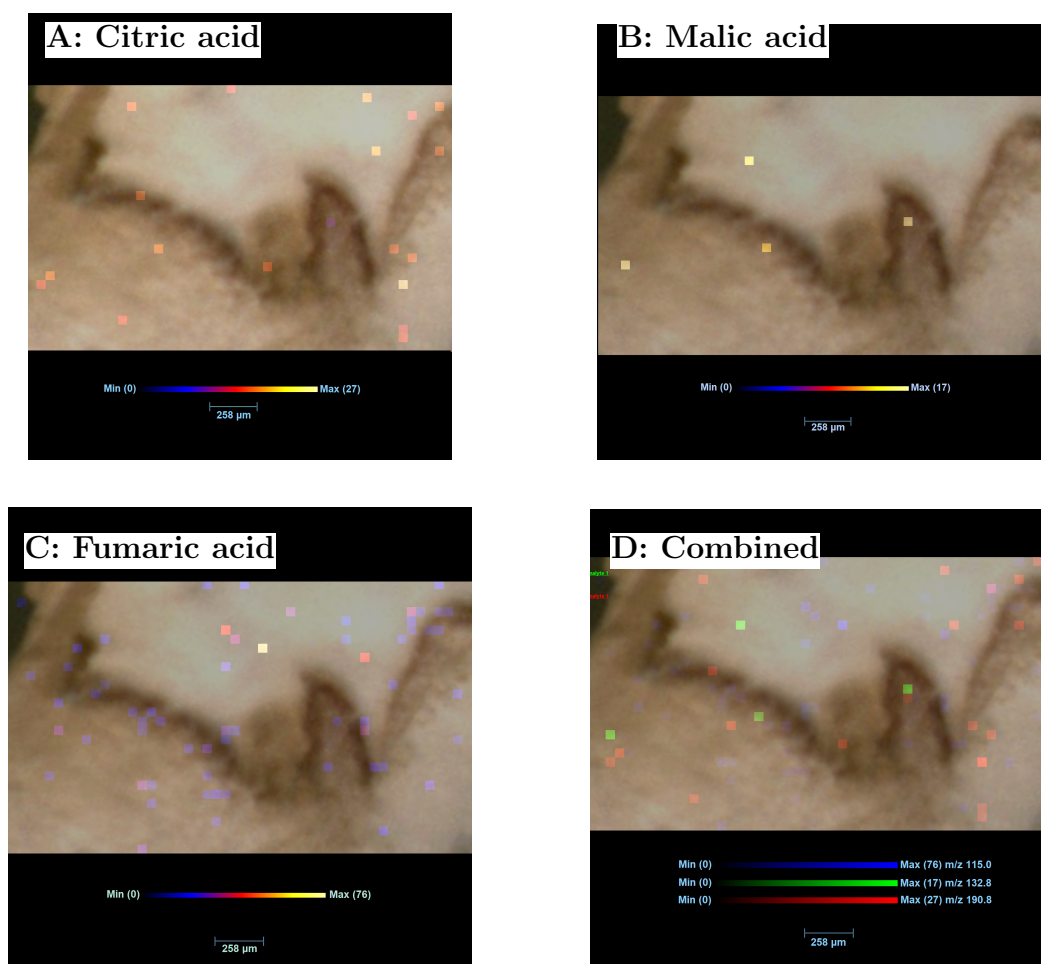


Figure 4.19: Metabolite distribution in a tuber cryosection, treated with control (water) for 72 hours

The cryo section of flash frozen tissue was analysed by negative mode DESI MSI. A: a heat map showing the distribution of m/z 191.0, putatively identified as citric acid, overlaid on a light microscope image of the tissue section. The maximum intensity on the colour scale is 27 ion counts. B: a heat map showing the distribution of m/z 133.0, putatively identified as malic acid, overlaid on a light microscope image of the tissue section. The maximum intensity on the colour scale is 17 ion counts. C: a heat map showing the distribution of m/z 115.0, putatively identified as fumaric acid, overlaid on a light microscope image of the tissue section. The maximum intensity on the colour scale is 76 ion counts. D: a heat map showing the distribution of all three TCA cycle markers, overlaid on a light microscope image of the tissue section. Each moiety is displayed on its own colour intensity scale. The maximum intensity on the fumaric acid colour scale (blue) is 66 ion counts. The maximum intensity on the malic acid colour scale (green) is 17 ion counts. The maximum intensity on the citric acid colour scale (red) is 27 ion counts.

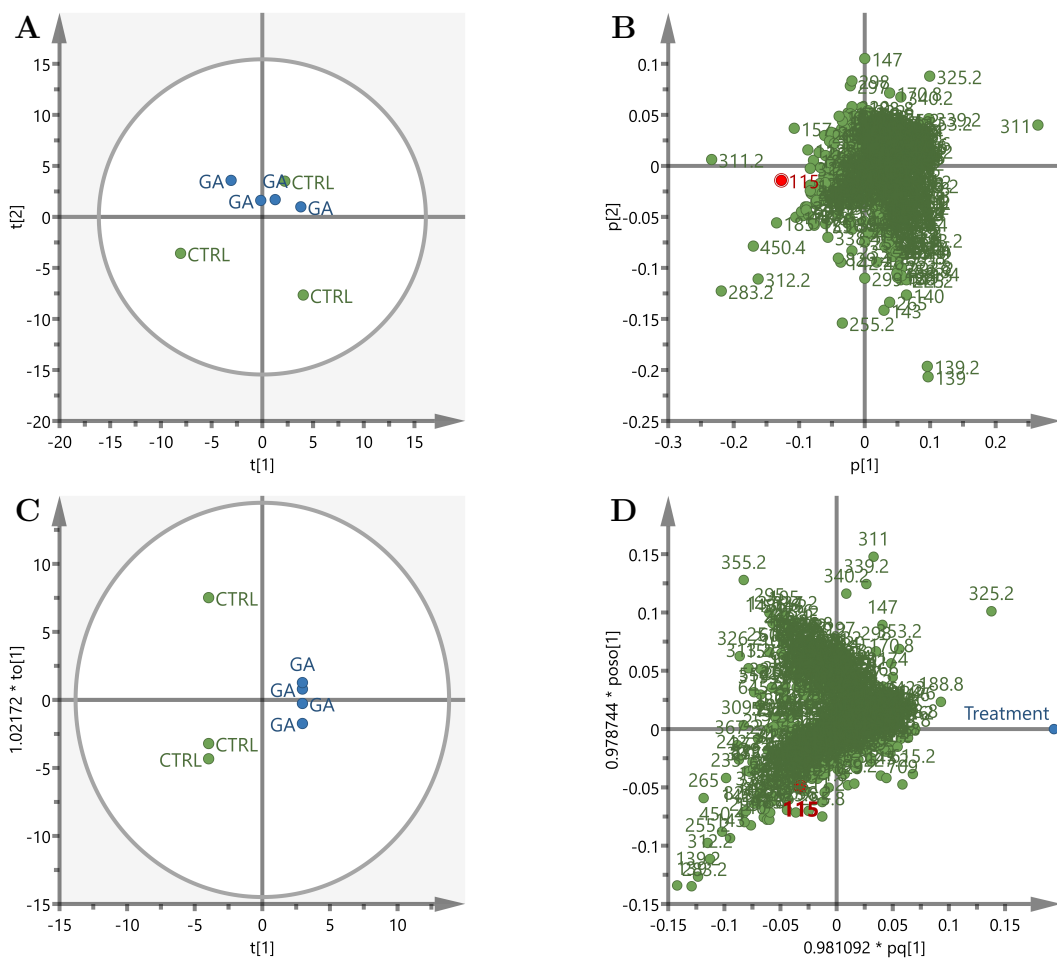


Figure 4.20: Multivariate analyses comparing regions of interest from the GA and control treated tuber DESI images

Multivariate analyses of regions of interest from 7 DESI images. Samples were analysed in negative mode with a TCA-cycle optimised method. $3 \times 0.8 \text{ mm}^2$ regions of interest were created for each image, and the data extracted. Data were simplified by binning to a mass accuracy of $\pm 0.1 \text{ Da}$. A and B are PCA plots, C and D are OPLS plot. A: The PCA score plot from the DESI image regions of interest. Point label and colour refers to treatment. Axes are components 1 and 2 of the PCA model. $N=7$. Ellipse = 95% confidence (Hotelling T2). B: PCA loadings plot from the DESI image regions of interest. Each point refers to an individual m/z bin, labelled accordingly. m/z 115 is highlighted in red. Axes are loadings for components 1 and 2 of the PCA model. C: The OPLS score plot produced by designating treatment as a Y-variable. Point label and colour refers to treatment. Axes are components 1 and 2 of the OPLS model. $N=7$. Ellipse = 95% confidence (Hotelling T2). OPLS loadings plot from the DESI image regions of interest. Each point refers to an individual m/z bin, labelled accordingly. The treatment (Y-variable) is in blue. m/z 115 is highlighted in red. Axes are loadings for components 1 and 2 of the OPLS model.

Data from images shown in Figures 4.16 to 4.19 and replicates were used to generate the multivariate analyses in Figure 4.20 on page 134 (selected replicate images are presented in Appendix B). In total, 7 freeze-dried cryosections were run successfully using the malate-optimised detection method. Figure 4.20A and B show the results of a principal component analysis (PCA) of data extracted from regions of interest of these 7 sections (following the processing protocol used to produce Figures 4.16 and 4.18C). Figure 4.20A shows the score plot: each point represents the output of 3 binned regions of interest in a single section, summarising technical replicates. Thus, each point represents an individual biological replicate. However, even though the GA-treated samples cluster well, the separation is not good enough to confidently distinguish them from controls, although m/z 115 (putative fumarate) is a key discriminant marker. Figure 4.20C and D show the results of an OPLS analysis, separating samples by treatment along component 1 in the score plot (Figure 4.20C). Whilst m/z 115 is not the most discriminant marker, it is at the edge of the loadings plot cluster.

4.3.6 The distribution of TCA cycle intermediates in stored tubers

The next 7 Figures (Figures 4.21 to 4.27) depict DESI-MS images of cryosections from glasshouse grown tubers in a planting series. The samples were stored for 2, 8 or 14 weeks before sampling for imaging (i.e. harvested in January 2019, November 2018 and October 2018 respectively). The samples were analysed using the malate-tuned instrumental parameters, as above. Figure 4.21 on page 136 shows the processing steps associated with preparing these data for analysis and a representative image for the samples harvested in October 2018 (14 weeks before analysis). Figure 4.21A is a dissecting microscope image of the tuber cryosection analysed in subsequent panels. The black box outlines the region sampled by DESI and the red box corresponds to the image overlay. The top right edge of the sample is the epidermis, with a slightly sprouting meristem in the box. Figure 4.21B shows the distribution of m/z 255.2, used to align the sample and data. It is particularly abundant in the meristem and adjacent region. Figure 4.21C shows the 3 regions of interest used to generate Figure 4.27.

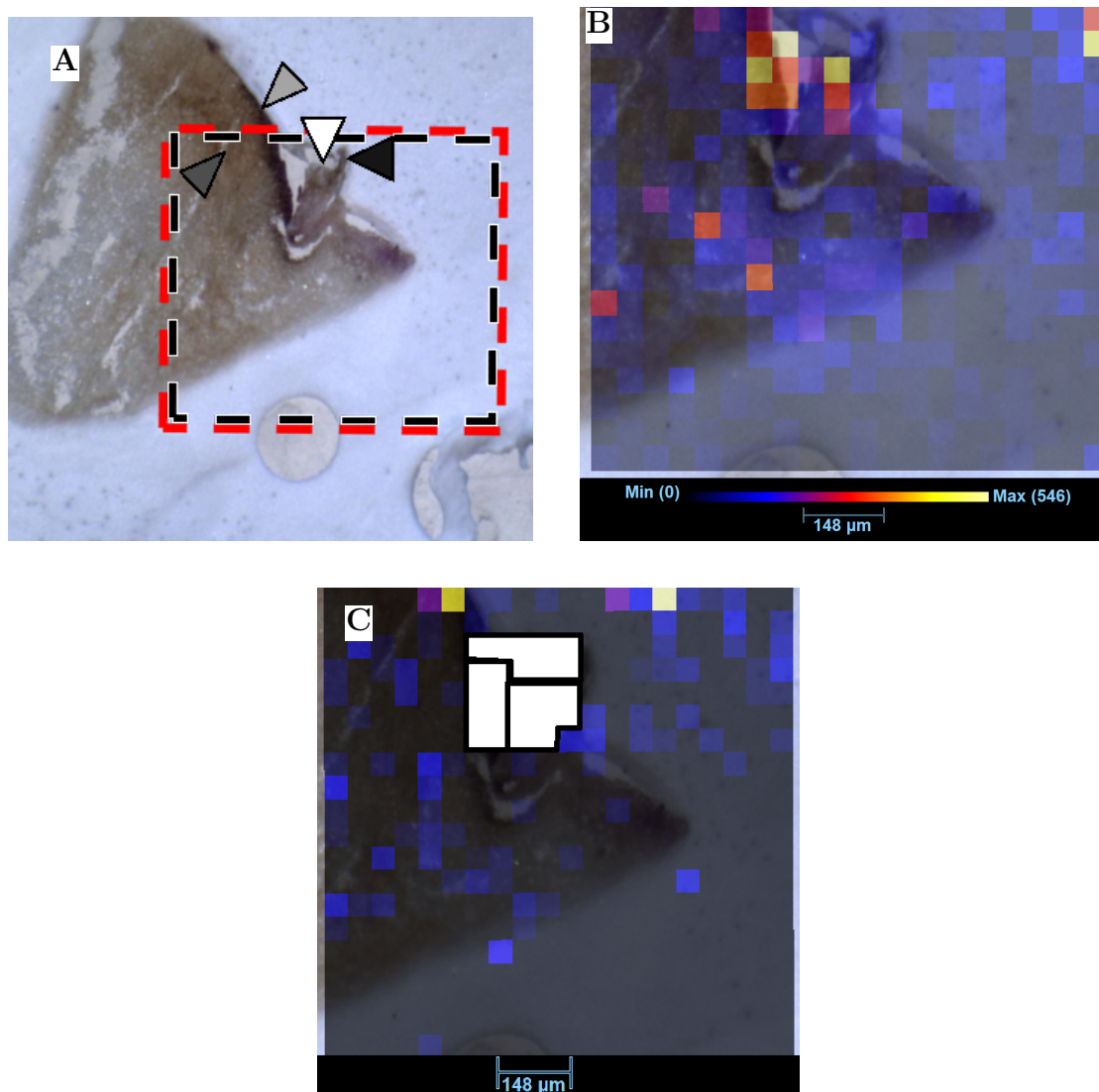


Figure 4.21: Analysis of a tuber cryosection, harvested in october, 14 weeks before analysis

The cryo section of flash frozen tissue was analysed by negative mode DESI MSI. A: A 10x magnification stereo microscope image of the tissue section. The box with the black dashed line shows the analysed area, whereas the red dashed line showed the part of the image used as in the data overlay in panels B, C and Figure 4.27. The triangles point to the apical bud (white), leaf primordia (black), epidermis (light grey) and cortex (dark grey). B: a heat map showing the distribution of m/z 255.2, the most abundant metabolite, overlaid on a light microscope image of the tissue section. The maximum intensity on the colour scale is 546 ion counts. C: a heat map showing the distribution of m/z 114.8, highlighting the regions of interest used in later analysis (see Figure 4.27), overlaid on a light microscope image of the tissue section. The maximum intensity on the colour scale is 150 ion counts.

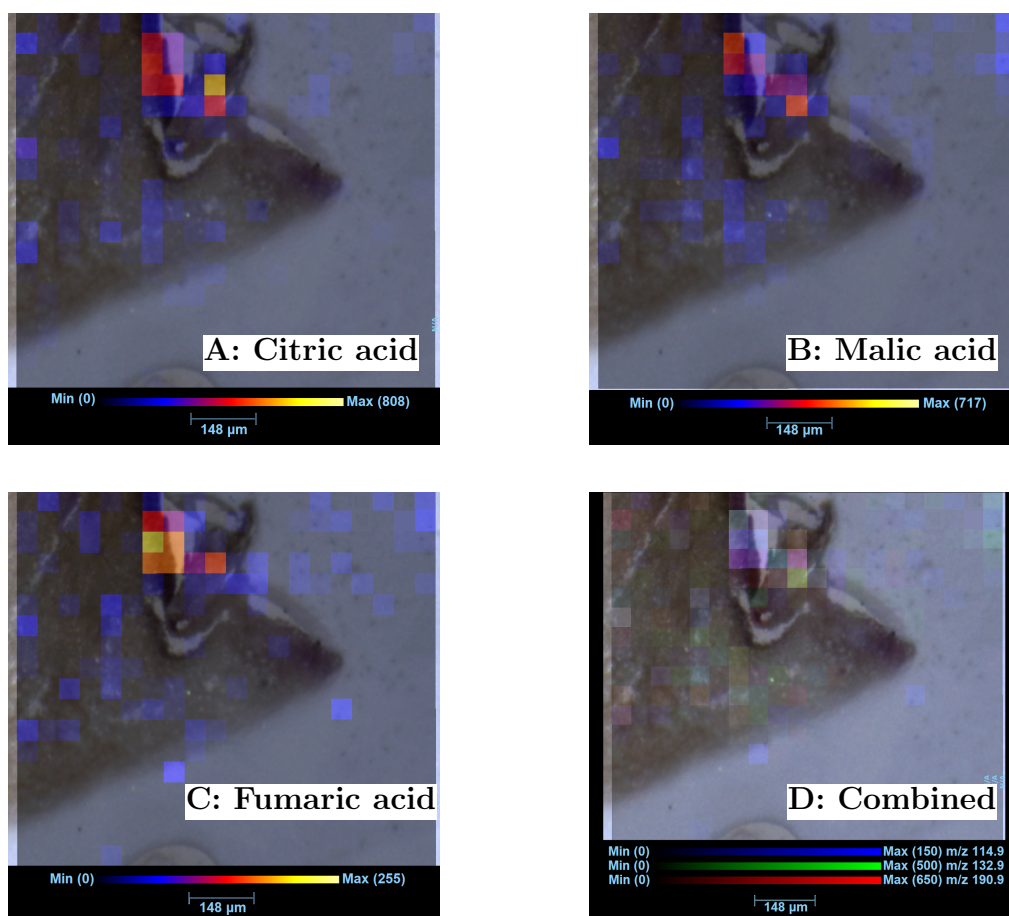


Figure 4.22: Metabolite distribution in a tuber cryosection, harvested in October, 14 weeks before sampling

The cryo section of flash frozen tissue was analysed by negative mode DESI MSI. A: a heat map showing the distribution of m/z 191.0, putatively identified as citric acid, overlaid on a light microscope image of the tissue section. The maximum intensity on the colour scale is 650 ion counts. B: a heat map showing the distribution of m/z 133.0, putatively identified as malic acid, overlaid on a light microscope image of the tissue section. The maximum intensity on the colour scale is 500 ion counts. C: a heat map showing the distribution of m/z 115.0, putatively identified as fumaric acid, overlaid on a light microscope image of the tissue section. The maximum intensity on the colour scale is 150 ion counts. D: a heat map showing the distribution of all three TCA cycle markers, overlaid on a light microscope image of the tissue section. Each moiety is displayed on its own colour intensity scale. The maximum intensity on the fumaric acid colour scale (blue) is 150 ion counts. The maximum intensity on the malic acid colour scale (green) is 500 ion counts. The maximum intensity on the citric acid colour scale (red) is 650 ion counts.

Figure 4.22 on page 137 shows the distribution of 3 different TCA cycle metabolites: citrate (A), malate (B), fumarate (C) and a composite of all three (D). In the case of all 3 metabolites, their detection is highest in the bud area. The maximum detection of fumarate (Figure 4.22C) is 255, about a third of the levels for malate (B - 717)

and citrate (A - 808). Based on the overlay (D), which can normalise these detection differences, there are no particular regions accumulating one metabolite in favour of the rest.

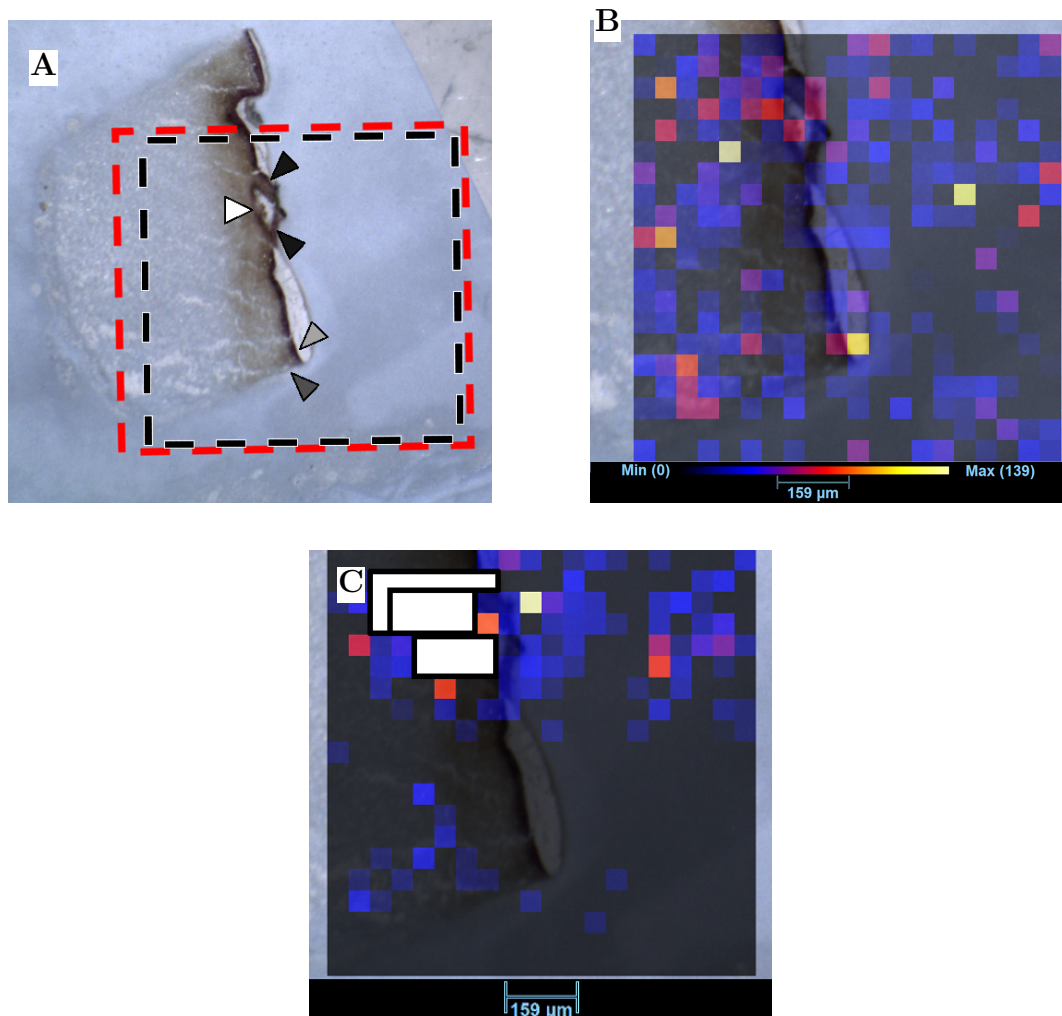


Figure 4.23: Analysis of a tuber cryosection, harvested in November, 8 weeks before sampling.

The cryo section of flash frozen tissue was analysed by negative mode DESI MSI. A: A 10x magnification stereo microscope image of the tissue section. The box with the black dashed line shows the analysed area, whereas the red dashed line showed the part of the image used as in the data overlay in panels B, C and Figure 4.27. The triangles point to the apical bud (white), leaf primordia (black), epidermis (light grey) and cortex (dark grey). B: a heat map showing the distribution of m/z 255.2, the most abundant metabolite, overlaid on a light microscope image of the tissue section. The maximum intensity on the colour scale is 139 ion counts. C: a heat map showing the distribution of m/z 114.9, highlighting the regions of interest used in later analysis (see Figure 4.27), overlaid on a light microscope image of the tissue section. The maximum intensity on the colour scale is 175 ion counts.

Figure 4.23 on page 138 shows the arrangement of a representative sample harvested

in November, 8 weeks before analysis. Figure 4.23A is a dissecting microscope image of the cryosection. The vertical line in the middle of the black box is the epidermis. There are two visible layers in the tuber tissue: the vasculature separates the epidermis and the main cortex. The main bud has 2 leaf bases. The black box outlines the analysed region and the red box is the region used in subsequent data overlays. Figure 4.23B shows a heatmap of m/z 255.2, used to align the data and image. There are hotspots in the meristem region and along the bottom edge of the sample. Figure 4.23C shows the regions of interest used to prepare Figure 4.27; here they correspond to the bud region. Figure 4.24 on page 140 shows the distribution of 3 different TCA cycle metabolites: citrate (A), malate (B), fumarate (C) and a composite of all three (D). The overlay is particularly useful as the maximum detected levels of fumarate (C - 175) are substantially lower than citrate (A - 477) and malate (B - 506) levels. All these metabolites were abundant in the region below the bud, although citrate is the only one detected at high levels in the meristem itself. Figure 4.25 on page 141 shows the processing of representative image from samples harvested in January, 2 weeks before analysis. Figure 4.25A is a dissection microscope image of the cryosection. The red box outlines the picture used in subsequent data overlays, whereas the black box outlines the analysed region. The horizontal line at the bottom of these boxes is the epidermis. There is a recessed bud near the middle, at the edge of the black box. Figure 4.25B shows the distribution of m/z 255.2. This is used to align the data to the picture; there is a hotspot in the meristem region. Figure 4.25C shows the location of regions of interest used to generate data for Figure 4.27.

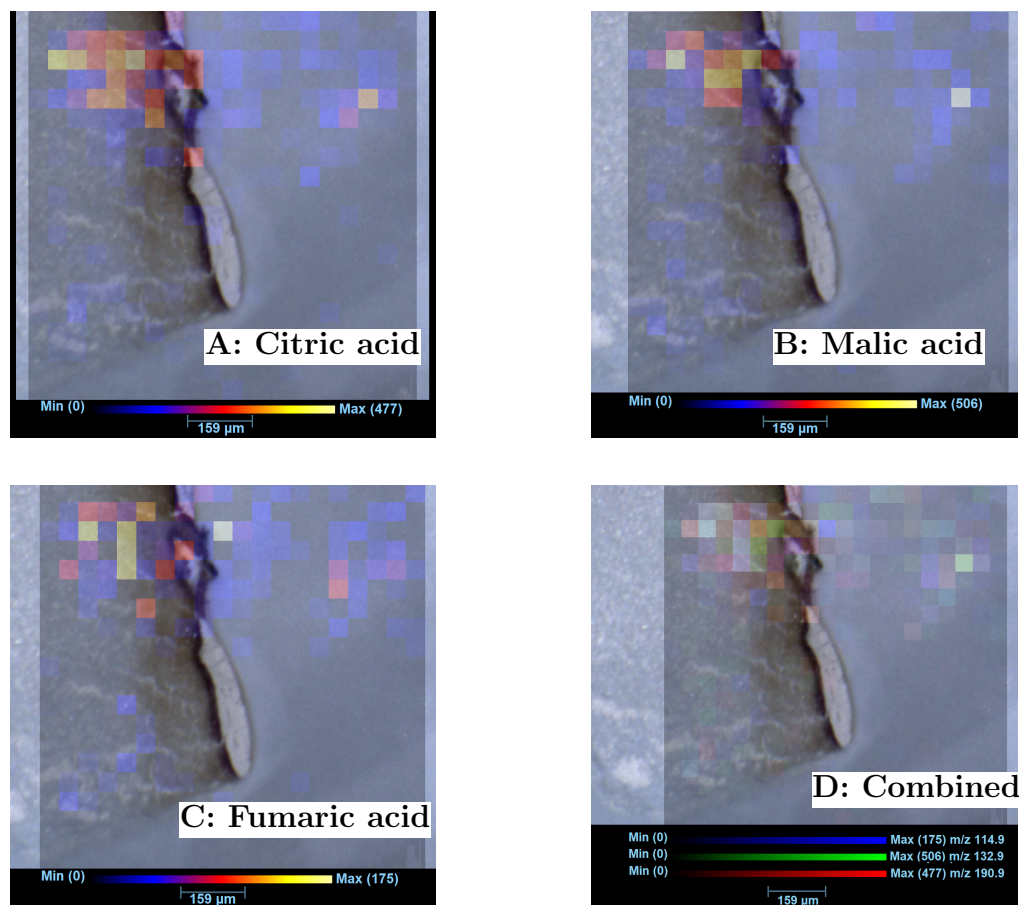


Figure 4.24: Metabolite distribution in a tuber cryosection, harvested in November, 8 weeks before sampling

The cryo section of flash frozen tissue was analysed by negative mode DESI MSI. A: a heat map showing the distribution of m/z 191.0, putatively identified as citric acid, overlaid on a light microscope image of the tissue section. The maximum intensity on the colour scale is 477 ion counts. B: a heat map showing the distribution of m/z 133.0, putatively identified as malic acid, overlaid on a light microscope image of the tissue section. The maximum intensity on the colour scale is 506 ion counts. C: a heat map showing the distribution of m/z 115.0, putatively identified as fumaric acid, overlaid on a light microscope image of the tissue section. The maximum intensity on the colour scale is 175 ion counts. D: a heat map showing the distribution of all three TCA cycle markers, overlaid on a light microscope image of the tissue section. Each moiety is displayed on its own colour intensity scale. The maximum intensity on the fumaric acid colour scale (blue) is 175 ion counts. The maximum intensity on the malic acid colour scale (green) is 506 ion counts. The maximum intensity on the citric acid colour scale (red) is 477 ion counts.

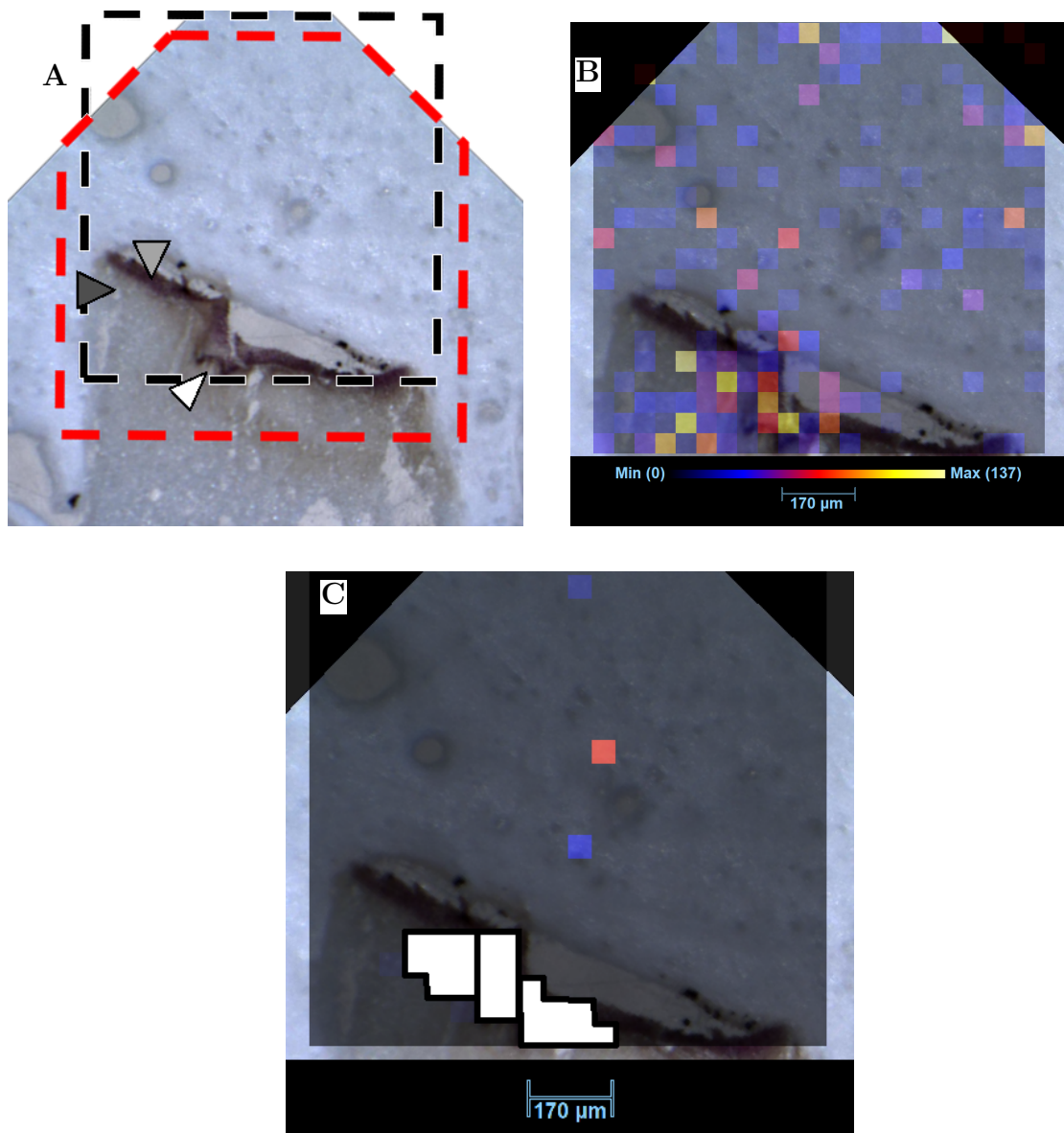


Figure 4.25: Analysis of a tuber cryosection, harvested in January, 2 weeks before analysis. The cryo section of flash frozen tissue was analysed by negative mode DESI MSI. A: A 10x magnification stereo microscope image of the tissue section. The box with the black dashed line shows the analysed area, whereas the red dashed line showed the part of the image used as in the data overlay in panels B, C and Figure 4.27. The triangles point to the apical bud (white), epidermis (light grey) and cortex (dark grey). B: a heat map showing the distribution of m/z 255.2, the most abundant metabolite, overlaid on a light microscope image of the tissue section. The maximum intensity on the colour scale is 137 ion counts. C: a heat map showing the distribution of m/z 114.9, highlighting the regions of interest used in later analysis (see Figure 4.27), overlaid on a light microscope image of the tissue section. The maximum intensity on the colour scale is 150 ion counts.

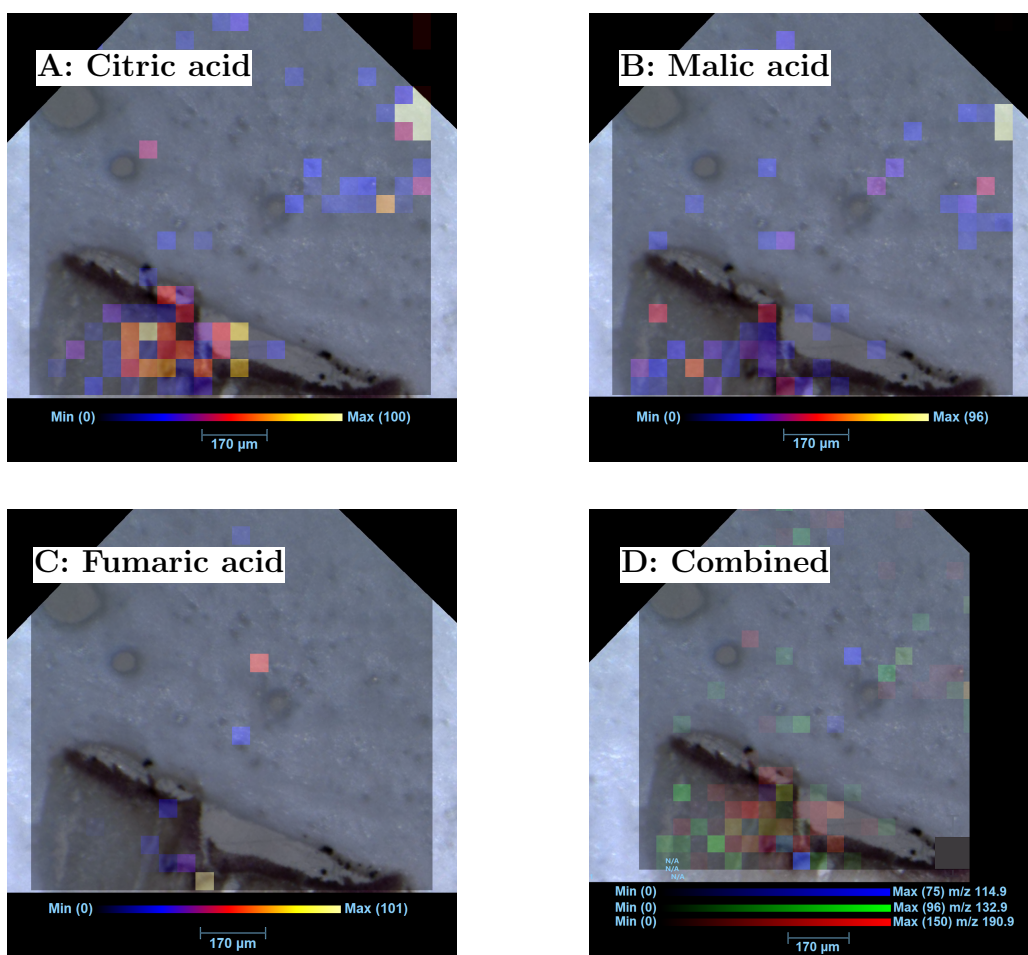


Figure 4.26: Metabolite distribution in a tuber cryosection, harvested in January, 2 weeks before sampling

The cryo section of flash frozen tissue was analysed by negative mode DESI MSI. A: a heat map showing the distribution of m/z 191.0, putatively identified as citric acid, overlaid on a light microscope image of the tissue section. The maximum intensity on the colour scale is 150 ion counts. B: a heat map showing the distribution of m/z 133.0, putatively identified as malic acid, overlaid on a light microscope image of the tissue section. The maximum intensity on the colour scale is 96 ion counts. C: a heat map showing the distribution of m/z 115.0, putatively identified as fumaric acid, overlaid on a light microscope image of the tissue section. The maximum intensity on the colour scale is 75 ion counts. D: a heat map showing the distribution of all three TCA cycle markers, overlaid on a light microscope image of the tissue section. Each moiety is displayed on its own colour intensity scale. The maximum intensity on the fumaric acid colour scale (blue) is 75 ion counts. The maximum intensity on the malic acid colour scale (green) is 96 ion counts. The maximum intensity on the citric acid colour scale (red) is 150 ion counts.

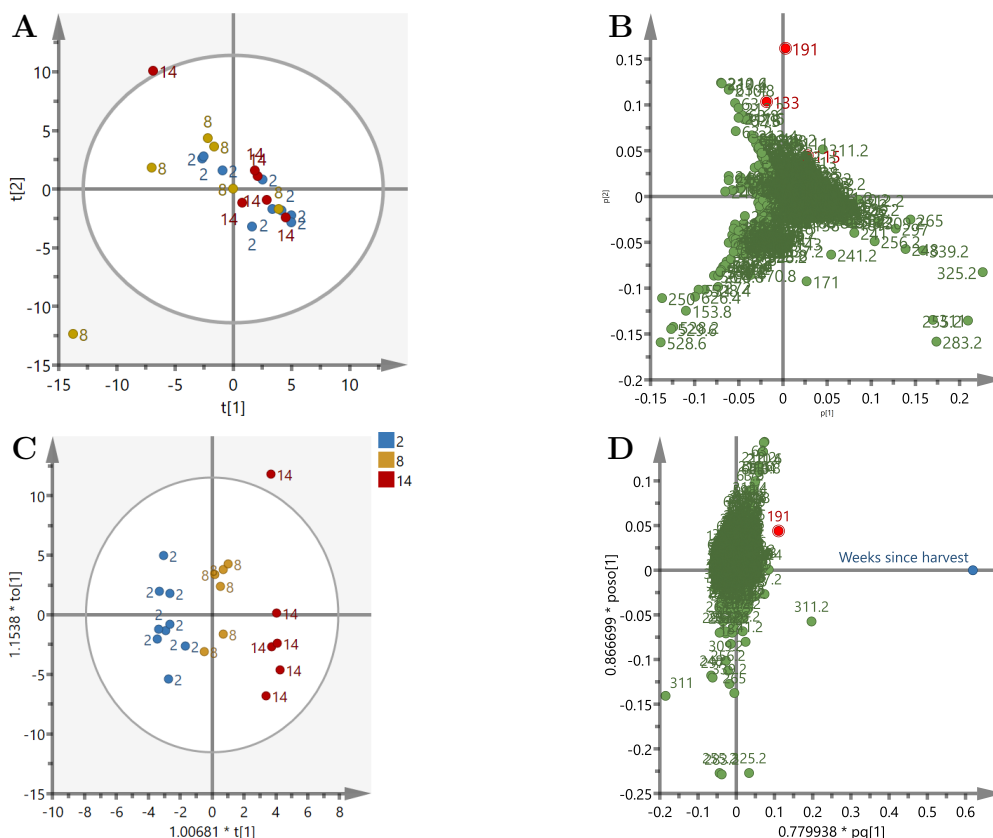


Figure 4.27: Multivariate analyses comparing regions of interest from the glasshouse grown, stored tuber DESI images

Multivariate analyses of regions of interest from 20 DESI images. Samples were analysed in negative mode with a TCA-cycle optimised method. $3 \times 0.8 \text{ mm}^2$ regions of interest were created for each image, and the data extracted. Data were simplified by binning to a mass accuracy of $\pm 0.1 \text{ Da}$. A and B are PCA plots, C and D are OPLS plot. A: The PCA score plot from the DESI image regions of interest. Point label and colour refers to time since harvest (weeks). Axes are components 1 and 2 of the PCA model. $N=20$. Ellipse = 95% confidence (Hotelling T2). B: PCA loadings plot from the DESI image regions of interest. Each point refers to an individual m/z bin, labelled accordingly. m/z 133 and 191 are highlighted in red. Axes are loadings for components 1 and 2 of the PCA model. C: The OPLS score plot with time since harvest as a Y-variable. Point label and colour refers to time since harvest (weeks). Axes are components 1 and 2 of the OPLS model. $N=20$. Ellipse = 95% confidence (Hotelling T2). D: OPLS loadings plot from the DESI image regions of interest. Each point refers to an individual m/z bin, labelled accordingly. The weeks since treatment point (Y-variable) is in blue. m/z 191 is highlighted in red. Axes are loadings for components 1 and 2 of the OPLS model.

Figure 4.26 on page 142 shows the distribution of 3 different TCA cycle metabolites: citrate (A), malate (B), fumarate (C) and a composite of all three (D). the 3 metabolites were detected at comparable maximum levels. However, citrate's hotspot (Figure 4.26A) appears to be larger than malate's (Figure 4.26B) - approximately 20 pixels, compared to 5. The number of pixels containing substantial amounts of fumarate was lower again (Figure 4.26C).

Data from regions of interest for these images (Figures 4.21 to 4.26) and replicates were analysed to produce the multivariate plots in Figure 4.27 on page 143 (selected replicate images are presented in Appendix B). In total, 21 freeze-dried cryosections were analysed successfully using the malate optimised method. There were 6-9 replicates for each timepoint. Figure 4.27 A and B show the results of a principal component analysis (PCA) of data extracted from regions of interest of these 21 sections (following the processing protocol used to produce Figures 4.21, 4.23 and 4.25C). The scores plot in Figure 4.27A shows poor separation between time points: the November samples seem distinct from the others, in spite of being the central time point. m/z 191 (putative citrate), 133 (putative malate) and 115 (putative fumarate) are highlighted in the loadings plot in Figure 4.27B; they remain influential in the distribution of these samples. Figure 4.27C and D show the results of an OPLS analysis, separating samples by number of weeks since harvest along component 1 of the score plot. m/z 191 (putatively citric acid) is a key discriminant marker in this analysis, one of very few clearly separate from the cluster of metabolites in 4.27D.

4.4 Discussion

4.4.1 The detection of phenolic compounds by DESI imaging

Before embarking on the MS imaging aspect of the dormancy project, the power of our DESI platform needed to be investigated in a well established system. Here, I examine DESI-MS-I's ability to detect phenolic compound accumulation in injured tubers. By investigating the established phenomenon of phenolics in tuber tissue, I am able to explore the potential of the DESI system, thus validating any downstream results for TCA markers.

The first step in this DESI validation process was the establishment of a protocol for phenolics detection and an associated standard curve. This involved optimising the instrument parameters on a slide spotted with standard solutions: 6mM coumaric and cinnamic acid, dissolved in MeOH. The coumaric acid was serially diluted in 100-fold steps and imaged using the phenolics protocol in negative mode to produce Figure 4.1

on page 108 - a standard curve for coumaric acid detection on a polysine slide. The concentrations used are listed in Table 4.2.3 on page 104. With the exception of the 600nM sample, the trend is linear on a \log_{10} scale, indicating that there is limited ion suppression and the lowest concentration is above the limits of detection. On this basis, the phenolics detection method was deemed suitable for the analysis of tissue sections.

Representative images from the control and injured tubers are shown in Figures 4.2 and 4.3, on pages 109 and 110. 4 replicate images were analysed for each treatment, and regions of interest were used to create metabolic profiles of key anatomical features for Figure 4.4 on page 111.

Figure 4.2 shows metabolite heat maps for a fresh tuber section, which was flash frozen immediately after sectioning. Figure 4.2B clearly shows the most intense peak is located in the bud area of the sample. The regions of interest were drawn in this area. Figure 4.2C and D show the distribution of (putatively identified) phenolic compounds cinnamic and coumaric acid respectively. Here, the phenolic compounds are also abundant in the bud and on the surface of the tuber.

Figure 4.3 shows metabolite heat maps for a piece of tuber that was aged in Phosphate buffer before hand sectioning. It was flash frozen immediately after sectioning. Figure 4.3B shows the most intense peak, which is not only located in the bud area of the sample, but on the peel. The regions of interest were drawn in the bud rootlet area. Figures 4.3C and D show the distribution of (putatively identified) phenolic compounds cinnamic and coumaric acid respectively. The phenolic compounds are also abundant in the bud and on the surface of the tuber, but more so in the rootlets than the main body of the bud. The colour intensity scale for these phenolics is substantially higher, compared to those in Figure 4.2C and D, whereas Figure 4.2A is comparable to Figure 4.3A, suggesting they are more abundant.

Figure 4.4 collates the metabolic profiles of regions of interest from the phenolics images. Figure 4.4A shows very clear separation of the two groups of samples: $t=0$ hours (control, not treated with buffer) and $t=24$ hours (aged in buffer for 24 hours). This is promising for the potential to perform *in silico* dissection of samples and compare metabolic profiles of different tissue types in a small sample. Figure 4.4B and loadings plots like it could be used to infer metabolic differences, as in Chapter 2.

On the basis of the quality of these data, and the ability to detect the expected changes in metabolism, it was decided to develop a method for the detection of the TCA cycle intermediate, malic acid.

4.4.2 The detection of TCA cycle compounds by DESI imaging

On the strength of the phenolics experiments, a TCA cycle metabolite detection protocol was developed. This entailed using a polysine slide, spotted with concentrated (7.5mM dissolved in MeOH) solutions of malate and citrate. Once the instrument parameters had been optimised on these concentrated solutions, a standard curve was produced (Figure 4.5 on page 114). This standard curve covers a mM-pM range, which represents biologically relevant concentrations. Apart from the 75 μ M sample, they are all linear on a log₁₀ scale, and all but the most dilute sample are significantly different from the controls. This represents a good starting point for the detection of TCA cycle intermediates in biological tissue.

The following figures show the results for representative samples in an imaging experiment, comparing fresh (analysed on the week of harvest Figures 4.6 and 4.7) and stored (analysed 6 weeks after harvest Figures 4.8 and 4.9) potatoes. Figure 4.10 shows the results of a PCA, comparing all the samples successfully run in this experiment.

Figures 4.6 and 4.8 on pages 116 and 119 show the data analysis process. Figures 4.6 and 4.8A show a 10x magnification stereo microscope image of the sample. The black box shows the area chosen for analysis in the HDImage software. The red box represents the area used for image overlays in the 6 subsequent panels for each sample.

Figures 4.6 and 4.8B show the distribution of the most abundant metabolite, m/z 255.2. Once the data have been processed, the heat maps need to be aligned to the analysed regions in the microscope images. By selecting a ubiquitous marker, it is possible to identify the margin of the sample and therefore the bud area. Figures 4.6 and 4.8C show the 3 regions of interest (ROIs) that are drawn onto each sample to produce the data for Figure 4.10. This concept could also be used for other forms of *in silico* dissection, for example normalising bud data against the cortex to identify local changes in metabolite abundance.

Figures 4.7 and 4.9 show TCA cycle data for representative samples in this experiment. Figure 4.7 on page 117 shows the distribution of citrate, malate and fumarate in a representative fresh tuber hand section. Focussing on the composite image (Figure 4.7D), the green (malate) is more abundant in the cortex, whereas fumarate and citrate (co-occur as purple) are more abundant in the bud region of the sample. Unfortunately, none of the stored tuber hand sections ran particularly successfully (with m/z 255.2 counts 5x lower than the fresh sample). The data are presented in Figure 4.9 on page 120, but malate and citrate (4.9B and A) only occur in 6 pixels, hampering data interpretation. This also limits the interpretation of Figure 4.10 on page 121. Not only are there fewer replicates than planned, due to the removal of the worst samples,

views such as Figure 4.9A surely raise some questions on the validity of comparing these data, even when normalised against their individual total ion count. The fact that m/z 115 (fumarate) is clearly discriminant may be more of a reflection on the success of its detection, rather than any functional changes.

Following from this hand sectioning experiment, a similar but more sophisticated sample preparation approach was trialled. These samples were cryosectioned to $60\mu\text{m}$ thickness. The following figures show the results for representative samples in an imaging experiment, comparing fresh (analysed 2 weeks after harvest Figures 4.11 and 4.12) and stored (analysed 8 weeks after harvest Figures 4.13 and 4.14) potatoes. Figure 4.10 shows the results of a PCA, comparing all the samples successfully run in this experiment.

These data are presented using the same layout as above. Again, Figures 4.11 and 4.13 on pages 122 and 125 show the data analysis process. Figures 4.11 and 4.13A show a 10x magnification stereo microscope image of the sections. Here, there is a clear, visible difference between epidermis and cortex tissue. The black box shows the area chosen for analysis in the HDImage software. The red box represents the area used for image overlays in the 6 subsequent panels for each sample.

Figures 4.11 and 4.13B show the distribution of the most abundant metabolite, m/z 255.2. Again, this ubiquitous marker is used for image alignment purposes. Figures 4.11 and 4.13C show the 3 regions of interest (ROIs) that are drawn onto each sample to produce the data for Figure 4.15.

Figures 4.12 and 4.14 show TCA cycle data for representative samples in this experiment. Figure 4.12 on page 123 shows the distribution of citrate, malate and fumarate in a representative fresh tuber hand section. Focussing on the composite image (Figure 4.12D), there appears to be a difference in the distribution of citrate (red) and malate (green); the citrate is on the topmost layer of the epidermis, whereas malate is relatively more abundant at the boundary between the epidermis and the cortex. Fumarate is more abundantly detected in absolute terms, but does not appear to have a major spatial pattern. In Figure 4.14 on page 126, the pattern is somewhat different. Assuming the high intensity patch at the bottom of the analysed area is an experimental artefact, malate (B, green) is relatively more abundant in the bud area. Two malate hotspots are visible in the leaf primordia. In comparison, citrate (A, red) is not particularly intense outside the questionable area. Fumarate (C, blue) has some key peaks at the base of the bud structure.

The data from this experiment were analysed by PCA. these results are presented in Figure 4.15 on page 127. A key advantage of the regions of interest used to generate this figure, is that suspect areas, which resemble analytical defects (for example, the stripe in Figure 4.14), can be excluded from subsequent analysis. Comparing the metabolic

profiles of the 5 successfully analysed samples, there seems to be separation between stored (8 weeks, "OCT") and fresh (2 weeks, "NOV") samples along component 1 (Figure 4.15A). The ubiquitous marker, m/z 255.2, is visible close to the component 2 axis of the loadings plot (Figure 4.15B), suggesting that it is not linked to the observed separation. The TCA cycle markers (in red) are not the clearest loadings, but do appear close to the component 1 axis. The more discriminant metabolites (m/z 143, 157, 171 and 199) are all in a similar mass range to the metabolites of interest discussed so far and may warrant further investigation.

4.4.3 Changes in TCA metabolite distribution with GA treatment

In this experiment, the GA treatment *in vitro* system, used extensively in Chapters 2 and 3, is examined using the DESI imaging platform. The following figures show the results for representative samples in an imaging experiment, comparing GA-treated (flash-frozen and sectioned 72 hours after treatment - Figures 4.16 and 4.17 on pages 128 and 130) and water-treated controls (flash-frozen and sectioned 72 hours after treatment - Figures 4.18 and 4.19 on pages 131 and 133) bud cryosections. Figure 4.20 on page 134 shows the results of a multivariate analysis, comparing all the samples successfully run in this experiment.

The data continue to be presented using the same layout as section 4.4.2, above. Figures 4.17 and 4.19 show the data analysis process. Figures 4.17 and 4.19A show a 10x magnification stereo-microscope image of the sample. The black box shows the area chosen for analysis in the HDI software. The red box represents the area used for image overlays in the 6 subsequent panels for each sample.

Figures 4.17 and 4.19B show the distribution of m/z 255.2, the marker used for image and data alignment. In the case of 4.17B, the ion intensity is quite low, making the interpretation of sample boundaries difficult. Figures 4.17 and 4.19C show the regions of interest used to extract data for the multivariate plots in Figure 4.20.

Figures 4.16 and 4.18 on pages 128 and 131 show the distribution of TCA cycle metabolites for the sections shown in Figures 4.17 and 4.19. Figure 4.16 was treated with GA and incubated for 72 hours, Figure 4.18 was treated in the same way with a water mock.

Focusing in the composite images (Figures 4.16 and 4.18D), the GA-treated sample clearly lacks adequate data coverage. Whilst the TCA cycle markers appear more abundant in the bud region, I am reluctant to infer a pattern based on 10px. Figure 4.18D, on the other hand, has better overall detection. Based on this, I would describe fumarate

as widely distributed, whilst citrate is conspicuously absent from the leaf primordium (black arrow in Figure 4.19A).

The data poverty in Figure 4.16 and some replicates makes the multivariate analysis plots (Figure 4.20) difficult to interpret confidently. The fumarate ion (m/z 115) separates along component 1 of the PCA loadings plot (Figure 4.20B), even though the samples separate approximately by treatment along component 2 of the PCA scores plot (Figure 4.20A). Frankly, this pattern could be caused by a different subset of metabolites being detected in individual sections, rather than a biological mechanism. This was a potentially very interesting experiment to match data from Chapters 2 and 3, but it was not successfully executed here.

4.4.4 Changes in DESI images of glasshouse grown cv. King Edward tuber buds during storage

Figures 4.21 to 4.27 show the results of the most successful and promising DESI imaging experiment I have performed to date. Tubers stored for 2, 8 and 14 weeks were cryosectioned, freeze dried and imaged. These data are presented using the same layout as above, with 2 figures showing a representative sample for each timepoint and a multivariate analysis of all 20 successful samples in Figure 4.27 on page 143.

Figures 4.21, 4.23 and 4.25 on pages 136, 138 and 141 show the data analysis process. Figures 4.21, 4.23 and 4.25A show 10x magnification dissecting microscope images of the cryosections used in subsequent panels. The analysed regions are in black and the data overlay regions are in red. m/z 255.2, the abundant positioning moiety is shown in Figures 4.21, 4.23 and 4.25B. This was used to align sections to DESI data. Figures 4.21, 4.23 and 4.25C shows the regions of interest used to generate data for the multivariate analysis shown in Figure 4.27.

Figures 4.22, 4.24 and 4.26 on pages 137, 140 and 142 show heatmaps of organic acids for each of the sections shown in Figures 4.21, 4.23 and 4.25. The sample in Figure 4.22 was stored for 14 weeks, the one in Figure 4.24 for 8 weeks, and Figure 4.26 for 2 weeks.

Focusing on the composite image (Figure 4.22D) of the longest stored tubers, the three TCA cycle markers all appear more abundant in the sprouting bud. The detected levels of citrate and malate are substantially more intense than fumarate, but the pattern is similar in many ways.

8 weeks after harvest (Figure 4.24), there is a similar pattern. The fumarate, which is less abundant than malate and citrate, seems to be approximately $100\mu\text{m}$ below the bud (Figure 4.24C), compared to citrate (Figure 4.24A) and malate (Figure 4.24B). If reproducible, this would be an interesting observation about the spatial organisation of

the metabolic reconfiguration discussed in this thesis.

The freshly harvested sample, in Figure 4.26, potentially has a similar pattern. Fumarate (Figure 4.26C) is only detected in 8px, but the overall intensity of this sample is substantially lower than Figures 4.22 and 4.24. Malate (Figure 4.26B) and citrate (Figure 4.26A) are displayed on comparable intensity scales. Malate appears to be diffusely distributed in the cortex (20px - 500 μ m), whilst citrate appears to be specifically located in the bud region (intense in 16px - 400 μ m).

Data from this experiment were analysed by PCA and OPLS; the results are shown in Figure 4.27 on page 143. Due to the imperfect separation in the PCA (Figure 4.27A and B), the OPLS is examined in detail. When separated by time since harvest (Figure 4.27C), component 1 of the loadings plot (Figure 4.27D) clearly highlights citrate (m/z191) as a discriminant marker.

With improved lateral resolution (not explored in this chapter) and ion counts of 100-500 per pixel in key markers (as seen in this subsection, above), it would be possible to generate separate regions of interest for different tissue types, such as bud, cortex and vasculature. This would enable a detailed study of the patterns mooted in the discussion of Figure 4.24C and Figure 4.26B (above). This would make it possible to determine if replicate regions of interest cluster by sample or a specific tissue type, and hence identify any bud specific metabolic changes.

4.4.5 Conclusions

The data in this chapter show that DESI is a promising platform for the study of plant metabolic markers. The phenolics section (4.3.1 and 4.4.1) aimed to confirm that data can be produced via DESI imaging of plant sections, i.e. the phenolics study was used as a “training system” for method development. With a few minor modifications of the basic protocol, I was able to detect phenolic compounds in tuber hand sections and detect differences between fresh and buffer-aged samples.

Following on from this basis, I generated a method (optimised on a malate standard solution slide) for the detection of TCA cycle intermediates via DESI. In subsequent analyses I was able to detect TCA cycle intermediates in potato tuber buds. Whilst these images have some limitations, they show promising results for this approach in mass spectrometry imaging.

There is certainly room for improvement of the method in terms of replication and signal intensity. For example, I was unable to reliably produce a large dataset like the one discussed in Figures 4.21-4.27. In that experiment I was able to take 20 replicates from a batch of 24 forward for multivariate analysis. In the GA-treatment data discussed

in 4.3.5, on the other hand, only half the analysed samples are shown, due to very limited signal detection in several samples.

Some of the replication issues are straightforward to solve. For example, there is a visible qualitative difference in the cryosections that ran successfully. With more experience and replicates, these characteristics could be formalised into a specific set of requirements for a DESI-suitable sample. Increasing the consistency in sectioning for DESI would hopefully resolve some of the signal intensity consistency issues identified with the method reported in this chapter.

The spatial resolution used with the DESI method in this chapter is much coarser than that obtainable with MALDI. Here, I consistently used a spatial resolution of $50\mu\text{m}$. Future work exploring the limits of resolution in DESI would definitely be worth exploring, but it is worth noting that MALDI has been used at a spatial resolution of 5- $10\mu\text{m}$ (Horn *et al.* 2012). Whether DESI can achieve this resolution may require technical developments, so at present the limited resolution represents a clear and substantial drawback of my approach in its current state.

Due to the limitations in signal intensity consistency and spatial resolution, I can at present only make limited interpretation of the pattern of TCA metabolites in the region of sprouting tuber buds. Some of the image data are consistent with the results obtained in Chapters 2 and 3 that TCA metabolites accumulate around tubers buds on sprouting. However at present these observation should be treated as indicative only, with more work needed to conclusively show these metabolites specifically accumulate in the bud region of the tuber.

The use of effective *in silico* dissection presents a potentially interesting future approach to metabolomics. As the sophistication of spectrometers coupled to imaging heads approaches parity with those used for liquid sample analysis, such *in silico* dissection may be used more frequently. In this chapter, only buds were examined, but, different regions of interest for different organs could be selected, generating data for multivariate analysis comparing different features on the same section. A similar approach is sometimes used in medical biopsies, which are analysed by mass spectrometry imaging for high throughput detection of malignant areas (Marguilis *et al.* 2018). This suggests that the approach may rapidly become standard, with the data reported here as an exemplar for plant tissue.

Chapter 5

Final discussion

5.1 Overview

This thesis aimed to tackle the agronomically important question of dormancy break in potato tubers, using advanced analytical chemistry techniques. By approaching the system from a developmental biology paradigm and using advanced biochemical and analytical techniques (metabolomics), I aimed to generate novel insights into the process for use by industry, as well as exploring some fascinating fundamental plant biology. The use of metabolomics in biological systems is gaining traction, particularly in animal and medical fields (e.g. Banerjee 2018), as well as in the area of plant science (e.g. Lee *et al.* 2012). Metabolomics represent a snapshot of a sample's phenotype; a particularly valuable characteristic in a dynamic system. Coupling this approach to a mass spectrometry imaging technique allows the biological system to be explored in terms of spatial differences, in addition to changes over time. This is particularly relevant in the context of the plant meristem system as the basis of dormancy, as these intricate structures contain several distinct cell types on a micrometer scale. Unravelling the spatial and temporal patterns of altered biochemistry that accompany and underpin dormancy break will provide insight into both potential molecular markers by which the process can be measured, and identify biochemical targets for future work aimed at developing agrichemicals or storage procedures to ameliorate wastage in the agricultural setting (for review, see Aksenova *et al.* 2013).

5.2 Approach to potato dormancy research

5.2.1 Developmental and metabolic approaches

A major strength of this developmental biology approach is that it bridges a conceptual gap. Research on potatoes has lagged in recent decades, with key aspects of the revolution in molecular biology passing them by (for recent commentary, see Stokstad, 2019). Innovations in genomics and the rate of data production by new sequencing techniques have favoured research into model species with responsive genomes. Whilst this has included closely related species, such as *Solanum lycopersicum* and *Nicotiana tabacum*, the potato has not been a focus of intense research. Potato propagation is largely clonal, making backcrossing and introgression of new genes laborious. Compared to tomato, it also has a longer generation time and requires more space, making it a less natural choice for lab research. Tomato and tobacco are also substantially higher value produce. Furthermore, the potato's commercially important trait, the tuber, is not a shared feature with these relatives, so there is no directly applicable research from other systems. These characteristics of potato mean that it is an ideal candidate for the application of a sophisticated developmental approach to tuber dormancy. This is a feature unique to potato in the economically important Solanaceae (the main other tuber crop is the distantly related the yam, a monocot from a selection of *Dioscorea* species, Burton, 1989).

A fundamental assumption underpinning this thesis is that meristem dynamics are key to potato tuber dormancy. This assumption is validated by the fact that apical dominance is a well characterised trait in tubers (Teper-Bamnlker *et al.* 2012). This has been characterised in studies focusing on hormonal dynamics across the tuber. It is also a long established observation that there is an apex-stolon gradient in reducing sugar availability (Davies 1984), suggesting that this apical dominance trait is associated with local differences in resource utilisation. These factors corroborate the idea that potato dormancy is a system defined by meristem interactions.

In research with an agronomic focus, the major unit of study for potato dormancy still tends to be the tuber, or even at the 1 tonne storage box level. When literature considers the potato tuber as a whole, it limits bud measurements to total length or similar measures. This is in spite of the established observation that tubers contain a reducing sugar concentration gradient, from stolon to apical bud. In contrast, this study focuses on the micrometer scale, emphasising that the meristem is the key functional unit. There have been recent efforts to examine the apical dominance interaction between tuber meristems, which taps into concepts from developmental biology, and the role plant hormones play in this system (Bromley *et al.* 2014). However, the majority of

potato dormancy research still operates with the tuber (or the tuber storage room) as the principal functional unit. By viewing the problem of potato dormancy break as a stem cell dynamic function, I could tap into a large amount of sophisticated molecular and cell biology work, ranging from branching in other plant systems (e.g. Zhang *et al.* 2018) to the Warburg effect in oncogenesis (e.g. Vander Heiden *et al.* 2009).

The importance of meristem activity in potato dormancy break opens a number of interesting opportunities for comparison with related systems. For example, meristem quiescence in tomato axils was examined by a previous graduate student in my research group (Steels 2012). This study yielded a number of interesting insights into the process associated with quiescent meristem reactivation, including the fact that organic acids would be a useful marker to examine. However, potato dormancy has a number of additional characteristics, compared to tomato axils. Whilst the trigger for tomato axil activation tends to involve damage cues and the loss of the apex, potato dormancy break has different drivers. Most notably, the process is linked to the ecological process of dormancy as an overwintering strategy (Burton, 1989). This suggests the existence of in-built timekeeping mechanisms, which are able to distinguish between otherwise similar autumnal and vernal cues. This suggests that it is not only useful and informative to look at potato dormancy break as a meristem quiescence system, but it is also a particularly interesting and distinct plant meristem quiescence system to study.

Another distinguishing feature, compared to tomato axils, that arises from this overwintering function is that the potato tuber meristem is not nutrient limited. The function of the entire tuber's storage reserve is to enable the meristem to survive the winter and produce one growing stem during the next field season. Whilst human selection and the intensity of the environmental stresses associated with the species' Andean natural range may explain the extreme size of this storage reserve, the fact remains that substrate is not a limiting factor for sprouting tubers. The change in resource utilisation by the meristem as it exits dormancy suggests that metabolic strategies may be a key, and previously uncharacterised aspect of potato dormancy break.

Other cell systems certainly adapt their metabolic strategies in response to changing environments. For example, under high nutrient conditions, yeast switch from conventional respiration to aerobic fermentation (Chen *et al.* 2007). There are a range of factors driving this switch. For example, at a high population density, oxygen may become depleted. Furthermore, the reactions associated with anaerobic fermentation only require a functional glycolysis pathway; a newly divided cell does not need to replicate its mitochondria in order to carry out this process. This may give lineages of yeast a competitive advantage in exploiting patches of resources more quickly than those producing a full suite of TCA cycle and ATP synthase electron transport chain proteins.

Metabolic changes during cell proliferation have also been observed in mammalian tumour systems. This has been described as the Warburg effect, also known as aerobic glycolysis. This process is distinct from lactic fermentation, which, in animals, is associated with anoxia or other stressors. The Warburg effect, in contrast, is observed in proliferative cells, even in the presence of oxygen. It has been suggested that this metabolic switch may be a driver for the proliferation (for review, see Garber 2004). As in the yeast systems discussed above, the ability to rapidly process available nutrient sources is a prerequisite for the tumour's increased cell division rate. A key characteristic in the evolution of oncogenic lineages is the ability to rapidly utilise nutrient sources and act as strong sinks, outcompeting other cell lineages, in a similar way to the yeast discussed above (Vander Heiden *et al.* 2009). The Warburg effect does seem to be reflected in my data: in Chapter 3 an asymmetric TCA cycle is detected repeatedly, suggesting a key metabolic dimension to the process.

However, a tumour system represents an aberrant return to proliferation: it drains the organism's resources in an unsustainable way. In contrast, plant meristems, whilst proliferative, are tightly controlled systems, into which nutrients are actively invested. Therefore, mammalian embryogenesis may represent a more comparable, well studied system (for review, see Shyh-Chang *et al.* 2013). In both embryonic stem cells and meristems, proliferation is controlled and most of the daughter cells are funnelled into cell specialisation processes. By comparing the two systems, the key minimum requirements for a cell before its next division can be conceptualised. An extreme example of this basic cell can be seen in human embryology. The 4 divisions between the zygote and the morula stage are known as cleavage, because there is no net growth of the embryo. Even in this scenario, there are essential processes required. The genome needs to be replicated before it next divides, which demands a suite of housekeeping genes, DNA polymerases and histones for chromosome condensation. In addition to this, the enzymes for a functional glycolysis pathway need to be produced. Cleavage also increases the cell surface area/volume ratio, increasing the need for phospholipids. It has been suggested that there is a lag in TCA cycle competence, due to the time taken for mitochondria to replicate and mature in a separate process to cell division (Rahman *et al.* 2013).

Whilst a cleaving morula is an extreme example of cell division with a reduced growth and synthesis cell cycle phase, it can provide insight into the potato sprouting process and the underpinning requirements. In chapter 3, I proposed that some of the TCA fluxes observed are linked to the biosynthesis of amino acids. The process of rapid cell proliferation clearly demands the synthesis of a range of key proteins, in this case, plausibly fed from the starch reserves, via a version of the TCA cycle. Even in the event of mitochondrial immaturity hampering the oxidative phosphorylation part of cell

respiration, some version of the TCA cycle is required to facilitate the conversion of the tuber's nutrient reserves into the macromolecules required for continued proliferative growth.

5.2.2 The TCA cycle and tuber sprouting

The key finding of this thesis is that primary metabolism changes during potato dormancy break in a stereotypic pattern. The data in chapter 2 show that tuber buds at different stages of storage differ; as dormancy weakens, the relative abundance of a small set of metabolic markers varies. The identity of these moieties is explored in Chapter 3, confirming the original hypothesis that specific changes in metabolism are core to this process, linking the concepts from the Warburg effect (above) and more conventional measures of reducing sugar availability. Finally the imaging work in Chapter 4 suggests that these primary metabolism changes are specifically associated with the meristem region. This validates the use of a developmental biology approach with a focus on meristem dynamics. As this work examines potato dormancy break from an unorthodox perspective, it has raised a number of interesting questions to follow.

From a metabolomics point of view, I would be most interested in tracing the fate of sugars being used by a meristem at various stages of dormancy break. This could take the form of a ^{14}C pulse-chase experiment, similar to the original studies used to delineate the TCA cycle. This would help distinguish between large pools of stored metabolites (such as malate in a vacuole) and metabolites actively participating in cell respiration.

A linked future study of interest would be to examine the amino acid dynamics in the tuber. My metabolomic methods were tailored to maximise the detection of organic acid. While there may be amino acid information in the datasets, this may not be comprehensive. For example, phenylalanine is usually analysed in positive ionisation mode, rather than the negative mode used in most of the analyses reported here. It would also be interesting to see if any of the cultivar-specific differences in TCA cycle markers link to the relative abundance of different amino acids. This could have interesting repercussions for low asparagine cultivars that have been developed to minimise acrylamide formation risk (Simplot 2018). For example, these lines may have altered dynamics in the ketoglutarate part of the TCA cycle. It would be interesting to observe the downstream effects of perturbing amino acid dynamics on the TCA cycle and dormancy. This may present interesting data, which might suggest that fluxes can be tipped back into a cycle form (and hence preserve endodormancy) by modifying associated reactions.

The molecular markers discussed in chapters 2 and 3 also provide a framework for comparing tuber responses to any novel dormancy control agents. An ideal candidate

would prolong an endodormancy-like profile, rather than allowing metabolic activation or damage responses to occur. Current approaches are quite simplistic. For example, the major commercial sprout suppression chemical, CIPC, does not prolong true dormancy, but perturbs cell division, thus disrupting sprout growth (Vaughn & Lehnert 1991). Sugar levels can give an indication of the dormancy state of a tuber, but they can be perturbed by a number of factors, such as variety, field conditions and temperature in storage (Herman *et al.* 2016). This means current practice is not a precise predictor of dormancy state, so new metabolite markers identified in this thesis could contribute to improving assessment of procedures.

5.3 DESI as a Mass Spectrometry Imaging platform

Chapter 4 introduces a mass spectrometry imaging platform, Desorption electrospray ionization (DESI), a relatively new modification of the more established Matrix Assisted Laser Desorption Imaging (MALDI). DESI uses a fine spray of solvent to ionise sample sections, mounted on a moving stage, so spectra can be linked to positional information and anatomical features in the original sections, as they are rastered relative to the solvent source.

Mass spectrometry imaging is an increasingly popular method in analysing plant material (for review, see Heyman & Dubery 2015). In the case of my project, it adds an important dimension to the quality of the data. The samples analysed in Chapters 2 and 3 were effectively meristem enriched, rather than a single tissue type. The quality of my dissection was limited by the size of the feature of interest and the importance of avoiding temperature and injury related degradation. The samples largely resembled the section in Figure 4.16A on page 128. Whilst every effort was made to remove the tuber cortex, some was inevitably found in the sample. However, the mass spectrometry imaging approach allows regions of interest to be selected, effectively yielding a detailed *in silico* dissection. This *in silico* dissection also allows control for bud size, which varies substantially during the course of dormancy break. Solvents were scaled to sample mass in the extractions for chapter 2, but this post-processing approach ensures comparable quantities of plant tissue are being discussed. Whilst the production of these mass spectrometry images was a lower throughput approach than the analysis of liquid extracts, I would be more confident in assigning differences identified in the multivariate analysis to the buds in particular when using this region of interest approach.

Imaging also allows the spatial organisation of processes to be examined. The concentration of TCA cycle metabolites in the bud region in Figures 4.22, 4.24 and 4.26 in Chapter 4 emphasises the need to target this part of the tuber when assessing dormancy

break. The process observed clearly involves changes at the bud level, as opposed to a whole tuber process. In the samples harvested at intervals in Figures 4.22, 4.24 and 4.26 on pages 137, 140 and 142, the more freshly harvested samples (short time in storage) show a diffuse pattern of TCA cycle intermediates, particularly of malate, whilst the samples from 14 weeks after harvest (longer time in harvest) show very high levels of these organic acids specifically in the bud.

5.3.1 Comparison with MALDI imaging

This thesis has used a DESI platform for the imaging part of the study. This is closely related to the substantially more established MALDI platform, also available in our mass spectrometry suite. The Waters Synapt G2Si ion mobility spectrometer used for the DESI imaging also has a MALDI ionisation source, meaning both potential experimental approaches share specifications, in terms of sensitivity and mass resolution. I chose to run these experiments using the new DESI, due to the nature of my metabolites of interest and earlier work. The organic acids discussed in Chapter 3 are soluble in methanol based solvents and were detected using electrospray ionisation in Chapter 2. In view of this, the electrospray-based desorption system in the DESI was optimal for subsequent analysis. DESI has been used previously on relevant organic acids in a medical context (Marguilis *et al.* 2018). This was a strength compared to a MALDI approach: the laser-based ionisation approach would have a different selectivity. Assessing the impact of this was beyond the scope of this thesis, but would be an interesting avenue for future work.

There are also practical advantages to consolidating DESI as an alternative to MALDI in mass spectrometry imaging. DESI ionisation takes place at room temperature and ambient atmosphere conditions, making sample introduction and handling substantially easier. Furthermore, DESI is a matrix-free approach. The application of matrix to MALDI samples is a complex process, and involves the introduction of foreign solutes, which need to be taken into account during data analysis.

However, the electrospray ionisation system is a mixed blessing. It was certainly the optimal approach for my metabolites of interest, and it presents the possibility of re-sampling sections repeatedly, which cannot be done in MALDI. However, MALDI has some specific advantages, beyond being a more established system. For example, I used a horizontal resolution of $50\mu\text{m}$, whereas MALDI reports resolutions of $5\text{-}10\mu\text{m}$ (Horn *et al.* 2012). I was reluctant to explore this further, as there was no way of assessing the accuracy of this parameter directly. In contrast, with MALDI, the laser burns a visible scar in the matrix, which can be measured. However, I was not able to generate a similar impression from my DESI spray to confirm the distance between adjacent spray tracks.

Another limitation of DESI is that it is a relatively new technique, certainly in the analysis of plant tissue (Liu *et al.* 2014 have a relevant publication). This was the first large scale study conducted on the DESI in our research group and there are very few published analyses using plant tissue. This means that standard protocols are not fully established and further development of the method to fully establish the reliability of the output data needs to be done. Nevertheless, the initial results reported here are encouraging.

5.3.2 Future imaging work

Data in Chapter 4 demonstrate that the markers identified in Chapter 3 are closely associated with the meristem bud complex. This would not have been possible without using mass spectrometry imaging. Specifically using DESI MS-I has ensured that these imaging data are as comparable as possible to the work underpinning Chapters 2 and 3.

As discussed above, the TCA cycle markers identified have raised a number of interesting questions about amino acid biosynthesis. Future work could include the development of an imaging protocol for the detection of amino acids such as glutamate and aspartate and their precursors since they might represent interesting intermediates in the complex metabolic changes occurring. This could also link into characterising the meristem's utilisation of resources from the main tuber. The importance of storage compound mobilisation in this process suggests that an imaging approach would be optimal in this study to visualise the precise pattern of metabolite in the source tissue (tuber) and sink (bud).

An additional experiment that would be worth performing would be tandem MS (MS/MS) of the cryosections, in order to confirm that the moieties detected at key masses truly correspond to those discussed in chapter 3. This is within the capabilities of the Waters Synapt G2Si ion mobility spectrometer used.

5.4 Final conclusion

In conclusion, this thesis found a previously uncharacterised role for TCA cycle fluxes in potato dormancy break. This links in with some concepts reviewed by Sweetlove *et al.* (2010) and ideas from oncology about the nature of proliferation. The breadth of conditions examined in Chapter 2 (hormone treatment, storage, bud rank and cultivar) and the consistency with which these markers were influential suggests that changes to TCA dynamics are a core part of meristem reactivation in potato dormancy break. The data presented in Chapter 3 raise some interesting questions on what is fundamental

to a cell before division. This links with some of the embryology data discussed above. A fascinating extension of this work would be to track co-occurring changes in amino acid abundance. The final data chapter cements the idea that the meristem is a key unit for dormancy. The TCA cycle intermediates are clearly localised in the bud region, suggesting this is the site of metabolic reconfiguration driving dormancy break.

References

- Aksenova, N. P., Sergeeva, L. I., Konstantinova, T. N., Golyanovskaya, S. A., Koclachevskaya, O. O. & Romanov, G. A. (2013), 'Regulation of potato tuber dormancy and sprouting', *Russian Journal of Plant Physiology* **60**(3), 301–312.
- Banerjee, S. (2018), 'Ambient ionization mass spectrometry imaging for disease diagnosis: Excitements and challenges', *Journal of Biosciences* **43**, 731–738.
- Banerjee, S. & Mazumdar, S. (2012), 'Electrospray ionization mass spectrometry: a technique to access the information beyond the molecular weight if the analyte.', *International Journal of Analytical Chemistry* **2012**, 1–40.
- Bethke, P. C. (2014), 'Ethylene in the atmosphere of commercial potato (*Solanum Tuberosum*) storage bins and potential effects on tuber respiration rate and fried chip color', *American Journal of Potato Research* **91**(6), 688–695.
- Bromley, J. R., Warnes, B. J., Newell, C. A., Thomson, J. C., James, C. M., Turnbull, C. G. & Hanke, D. E. (2014), 'A purine nucleoside phosphorylase in *Solanum tuberosum* l. (potato) with specificity for cytokinins contributes to the duration of tuber endodormancy.', *The Biochemical Journal* **458**(2), 225–237.
- Burrell, M. M. (1984), 'Inhibition of browning, phenoxyacetic acids and phenolic metabolism in potato tuber discs: a model system to study chemicals that control the common scab', *Plant Pathology* **33**, 325–336.
- Burton (1982), *Post-Harvest Physiology of Food Crops.*, Longman.
- Campbell, M. A., Gleichsner, A., Alsbury, R., Horvath, D. & Suttle, J. (2010), 'The sprout inhibitors chlorpropham and 1,4-dimethylnaphthalene elicit different transcriptional profiles and do not suppress growth through a prolongation of the dormant state.', *Plant Molecular Biology* **73**(1-2), 181–189.
- CHEMnetBASE (2015), 'Dictionary of natural products'.
URL: <http://dnp.chemnetbase.com/faces/chemical/ChemicalSearch.xhtml>

- Chen, Z., Odstreil, E. A., Tu, B. P. & McKnight, S. L. (2007), 'Restriction of dna replication of the reductive phase of the metabolic cycle protects genome integrity.', *Science* **316**(5833), 1916–1919.
- Davies (1984), 'Sugar metabolism in stolon tips of potato during early tuberisation.', *Zeitschrift für Pflanzenphysiologie*, **113**(5), 377–381.
- Dodsworth, S. (2009), 'A diverse and intricate signalling network regulates stem cell fate in the shoot apical meristem.', *Developmental Biology* **336**(1), 1–9.
- Eriksson, L., Johansson, E., Kettaneh-Wold, N., J. Trygg, C. W. & Wold, S. (2006), *Multi- and Megavariate Data Analysis*, second edn, Umea: Umetrics.
- FAO stat (2017), 'Official crop statistics'. Online, accessed 2018-09-21.
URL: <http://www.fao.org/faostat/en/#data/QC>
- Fosket, D. E. & Miksche, J. P. (1966), 'A histochemical study of seedling shoot apical meristem of *Pinus lambertiana*.', *American Journal of Botany* **53**(7), 694.
- Friml, J., Wisniewska, J., Benkova, E., Mendgen, K. & Palme, K. (2002), 'Lateral relocation of auxin efflux regulator pin3 mediates tropism in *Arabidopsis*.', *Nature* **415**(6873), 806–809.
- Garber, K. (2004), 'Energy boost: The warburg effect returns in a new theory of cancer', *Journal of the National Cancer Institute* **96**(24), 1805–1806.
- Hartmann, A., Senning, M., Hedden, P., Sonnewald, U. & Sonnewald, S. (2011), 'Reactivation of meristem activity and sprout growth in potato tubers require both cytokinin and gibberellin.', *Plant physiology* **155**(February), 776–796.
- Heltoft, P., Wold, A. & Molteberg, E. L. (2016), 'Effect of ventilation strategy on storage quality indicators of processing potatoes with different maturity levels at harvest', *Postharvest biology and technology* **117**, 21–29.
- Herman, D. J., Knowles, L. O. & Knowles, N. R. (2016), 'Low oxygen storage modulates invertase activity to attenuate cold-induced sweetening and loss of process quality in potato (*Solanum tuberosum* l.)', *Postharvest biology and technology* **121**, 12–117.
- Heyman, H. M. & Dubery, I. A. (2015), 'The potential of mass spectrometry imaging in plant metabolomics: a review.', *Phytochemistry reviews* **15**(2), 297–316.

- Horn, P. J., Korte, A. R., Neogi, P. B., Love, E., Fuchs, J., Strupat, K., Borisjuk, L., Shulaev, V., Lee, Y. J. & Chapman, K. D. (2012), 'Spatial mapping of lipids at cellular resolution in embryos of cotton.', *Plant Cell* **24**(2), 622–636.
- Huang, Z., Tian, S., Ge, X., Zhang, J., Li, S., Li, M., Cheng, J. & Zheng, H. (2014), 'Complexation of chlorpropham with hydroxypropyl- β -cyclodextrin and its application in potato sprout inhibition.', *Carbohydrate Polymers* **107**(July), 241–246.
- Huiling, Z., Juan, H., Jun, L., Conghua, X. & Botao, S. (2014), 'Amylase analysis in potato starch degradation during cold storage and sprouting', *Potato Research* **57**(1), 47–58.
- Janssen, B. J., Drummond, R. S. M. & Snowden, K. C. (2014), 'Regulation of axillary shoot development.', *Current Opinion in Plant Biology* **17**, 28–35.
- Kanehisa, Sato, Kawashima, Furumichi & Tanabe (2018), 'Kyoto encyclopedia of genes and genomes'.
URL: <https://www.kegg.jp/>
- Kerk, N. M. & Feldman, L. J. (1995), 'A biochemical-model for the initiation and maintenance of the quiescent center - implications for organization of root-meristems.', *Development* **121**(9), 2825–2833.
- Kleinkopf, G. E., Oberg, N. A. & Olsen, N. L. (2003), 'Sprout inhibition in storage: Current status, new chemistries and natural compounds', *American Journal of Potato Research* **80**(5), 317–327.
- Lee, Y. J., Perdian, D. C., Song, Z., Yeung, E. S. & Nikolau, B. J. (2012), 'Use of mass spectrometry for imaging metabolites in plants', *Plant Journal* **70**(7), 81–95.
- Li, P. H. (1985), *Potato Physiology*, Academic Press, Inc. Orlando (Florida).
- Liu, B., Zhang, N., Zhao, S. & Wang, D. (2014), 'Proteomic changes during tuber dormancy release process revealed by itraq quantitative proteomics in potato', *Plant Physiology and Biochemistry* **86**(C), 181–190.
- Lu, Z.-H., Donner, E. A., Yada, R. Y. & Liu, Q. (2012), 'Impact of γ -irradiation, cipc treatment, and storage conditions on physicochemical and nutritional properties of potato starches.', *Food Chemistry* **133**(4), 1188–1195.

- Marguilis, K., Chiou, A. S., Aasi, S. Z., Tibshirani, R. J., Tang, J. Y. & Zare, R. N. (2018), ‘Distinguishing malignant from benign microscopic skin lesions using desorption electrospray ionization mass spectrometry imaging’, *Proceedings of the National Academy of Sciences of the United States of America* **115**(25), 6347–6352.
- Mason, M. G., Ross, J. J., Babst, B. A., Wienclaw, B. N. & Beveridge, C. A. (2014), ‘Sugar demand, not auxin, is the initial regulator of apical dominance.’, *Proceedings of the National Academy of Sciences of the United States of America* **111**(16), 6092–6097.
- Matsuura-Endo, C., Ohara-Takafa, A., Chuda, Y., Ono, H., Yada, H., Yoshida, M., Kobayashi, A., Tsuda, S., Takigawa, S., Noda, T., Yamauchi, H. & Mori, M. (2006), ‘Effects of storage temperature on the contents of sugars and free amino acids in tubers from different potato cultivars and acrylamide in chips.’, *Bioscience, Biotechnology, Biochemistry* **70**(5), 1173–1180.
- Mottram, D. S. amnd Wedzicha, B. L. & Dodson, A. T. (2002), ‘Acrylamide is formed in the maillard reaction.’, *Nature* **419**(6906), 448–449.
- Muttucumaru, N., Powers, S. J., Elmore, J. S., Dodson, A., Briddon, A., Mottram, D. S. & Halford, N. (2016), ‘Acrylamide-forming potential of potatoes grown at different locations, and the ratio of free asparagine to reducing sugars at which free asparagine becomes a limiting factor for acrylamide formation.’, *Food Chemistry* **220**(September), 76–86.
- Nakagawa, Y., Nakajima, K. & Suzuki, T. (2004), ‘Chlorpropham induces mitochondrial dysfunction in rat hepatocytes.’, *Toxicology* **200**(2-3), 123–133.
- Öpik, H. & Rolfe, S. (2003), *The Physiology of Flowering Plants.*, 4 edn, Cambridge.
- Orton, F., Rosivatz, E., Scholze, M. & Kortenkamp, A. (2011), ‘Widely used pesticides with previously unknown endocrine activity revealed as *in Vitro* antiandrogens.’, *Environmental Health Perspectives* **119**(6), 794–800.
- Overy, S. A., Walker, H. J., Malone, S., Howard, T. P., Baxter, C. J., Sweetlove, L. J., Hill, S. A. & Quick, W. P. (2005), ‘Application of metabolite profiling to the identification of traits in a population of tomato introgression lines’, *Journal of Experimental Botany* **410**(56), 287–296.
- Passananti, M., Lavorgna, M., Iesce, M. R., DellaGreca, M., Criscuolo, E., Parrella, A., Isidori, M. & Temussi, F. (2014), ‘Chlorpropham and phenisopham: phototransformation and ecotoxicity of carbamates in the aquatic environment’, *Environmental Science - Processes and Impacts* **16**(64), 823–831.

- Paul, V., Ezekiel, R. & Pandey (2016), 'Sprout suppression on potato: need to look beyond cipc for more effective and safer alternatives', *Journal of food Science and Technology* **53**(1), 1–18.
- Peterson, R. L., Barke, r. W. G. & Howarth, M. J. (1985), *Potato Physiology*, Academic Press, Inc. Orlando (Florida), chapter Development and Structure of Tubers, pp. 124–126.
- Potato Genome Sequencing Consortium. (2011), 'Genome sequence and analysis of the tuber crop potato.', *Nature* **475**(7355), 189–195.
- Pptato Pedigree Database (2016), 'Pedigree history'. Online, accessed 2019-06-16.
URL: <https://www.plantbreeding.wur.nl/PotatoPedigree/index.html>
- Rahman, M. M., Rosu, S., Joseph-Strauss, D. & Cohen-Fix, O. (2013), 'Down-regulation of tricarboxylic acid (tca) cycle genes blocks progression through the first mitotic division in *Caenorhabditis elegans* embryos.', *Proceedings of the National Academy of Sciences of the United States of America*. **111**(7), 2602–2607.
- Shyh-Chang, N., Daley, G. Q. & Cantley, L. C. (2013), 'Stem cell metabolism in tissue development and aging.', *Development* **140**(12), 2535–2547.
- Simplot, J. R. (2018), 'Innate potatoes'. Online, accessed 2018-09-21.
URL: <http://www.innatepotatoes.com/newsroom>
- SolCyc (2018), 'Sol genomics network - cellular overview of solanum tuberosum'.
URL: <http://solcyc.solgenomics.net/overviewsWeb/celOv.shtml>
- Steels, C. (2012), The analysis of metabolic change in axillary meristems., PhD thesis, University of Sheffield.
- Sweetlove, L. J., Beard, K. F., Nunes-Nesi, A., Fernie, A. R. & Ratcliffe, R. G. (2010), 'Not just a circle: Flux modes in the plant tca cycle', *Trends in Plant Science* **15**(8), 462–470.
- Tareke, E., Rydberg, P., Karlsson, P. & Eriksson, S. amd Tornqvist, M. (2002), 'Analysis of acrylamide, a carcinogen formed in heated foodstuffs.', *Journal of Agricultural and Food Chemistry* **50**(17), 4998–5006.
- Tata, A., Perez, C. J., Hamid, T. S., Bayfield, M. A. & Ifa, D. R. (2014), 'Analysis of metabolic changes in plant pathosystems by imprint imaging desi-ms', *Journal of The American Society for Mass Spectrometry* **26**(4), 641–648.

- Teper-Bamnolker, P., Buskila, Y., Lopesco, Y., Ben-Dor, S., Saad, I., Holdengreber, V., Belausov, E., Zemach, H., Ori, N., Lers, A. & Eshel, D. (2012), 'Release of apical dominance in potato tuber is accompanied by programmed cell death in the apical bud meristem.', *Plant Physiology* **158**(4), 2053–2067.
- Vander Heiden, M. G., Cantley, L. C. & Thompson, C. B. (2009), 'Understanding the warburg effect: the metabolic requirements of cell proliferation.', *Science* **324**(5930), 1029–1033.
- Vaughn, K. C. & Lehnen, L. P. (1991), 'Mitotic disrupter herbicides.', *Weed Science* **39**(3), 450–457.
- Waldie, T. & Leyser, O. (2018), 'Cytokinin targets auxin transport to promote shoot branching.', *Plant Physiology* **177**(2), 803–818.
- Walker, H. J. (2013), Direct approaches to metabolite profiling by Mass Spectrometry, PhD thesis, University of Sheffield.
- Wang, Q., Kohlen, W., Rossmann, S., Vernoux, T. & Theres, K. (2014), 'Auxin depletion from the leaf axil conditions competence for axillary meristem formation in *Arabidopsis* and tomato.', *The Plant Cell* **26**(5), 2068–2079.
- Zhang, Y., Swart, C., Alseekh, S., Scossa, F., Jiang, L., Obata, T., Graf, A. & Fernie, A. R. (2018), 'The extra-pathway interactome of the tca cycle: Expected and unexpected metabolic interactions', *Plant Physiology* **177**(3), 966–979.

Appendix A

Cultivar pedigree

Figure A.1, on page 168 is a partial pedigree of the 4 tuber cultivars studied throughout this thesis. Single vertical lines indicate progeny produced through open pollination, whereas horizontal bars indicate controlled crosses between cultivars. Where the lines could have been confusing, crossing a number of generations (e.g. Beauty of Hebron x Magnum Bonam and Peterson's Victoria x Herald), I have endeavoured to use double or dashed lines to minimise crossovers and make them distinct. All of this information, including detailed referencing, is now available through the Potato Pedigree Database (Potato Pedigree Database (2016)). The database has been relaunched since I first tried to access it, and now includes very detailed pedigrees of all listed cultivars in a fully searchable form. The original version of Figure A.1 lacked crucial detail, as I was unable to trace the ancestors of Desiree beyond the parental level. The database is fully available in English - before this became available, I found tracing Dutch and German cultivars substantially more challenging than ones of British origin. Interestingly, Russet Burbank and King Edward, which had the most different dormancy habits, were the most closely related. Maris Piper is the result of an introgression from *Solanum andigena*, possibly making it the most genetically distinct of the cultivars studied, in spite of having 4 lines of descent from Peterson's Victoria. With data from Desiree, it becomes clear that it is not particularly distantly related to King Edward and Russet Burbank; it is 3 generations from their common ancestor, Early Rose.

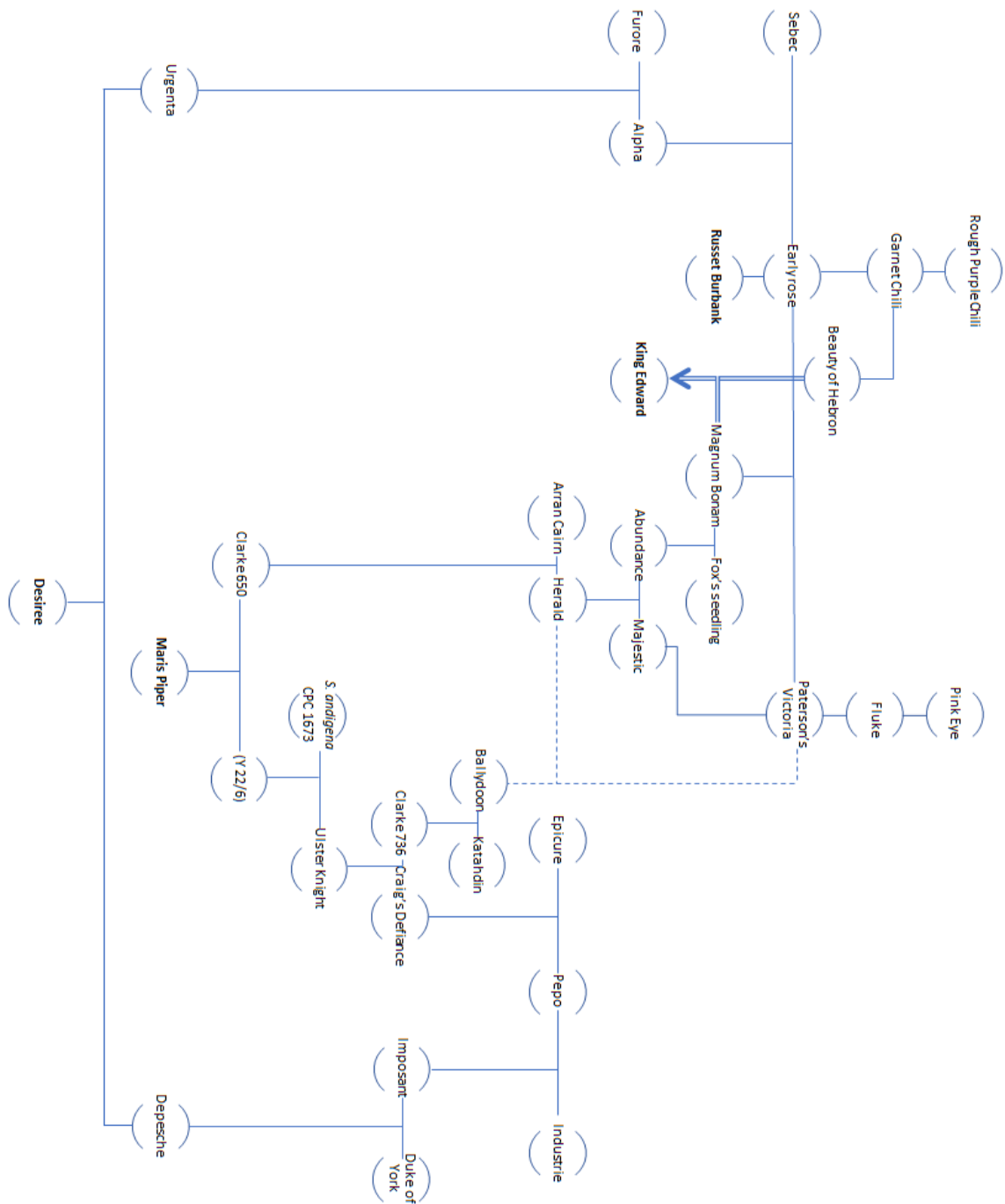


Figure A.1: Partial pedigree of studied cultivars

A partial pedigree of the 4 tuber cultivars studied throughout this thesis (**Russet Burbank**, **Kind Edward**, **Maris Piper**, **Desiree**. In bold). Single vertical lines indicate progeny produced through open pollination, whereas horizontal bars indicate controlled crosses between cultivars. Where the lines could have been confusing, crossing a number of generations (e.g. **Beauty of Hebron** x **Magnum Bonam** and **Peterson's Victoria** x **Herald**), I have endeavoured to use double or dashed lines to minimise crossovers and make them distinct. All of this information, including detailed referencing, is now available through the Potato Pedigree Database (Potato Pedigree Database (2016)).

Appendix B

Replicate DESI images

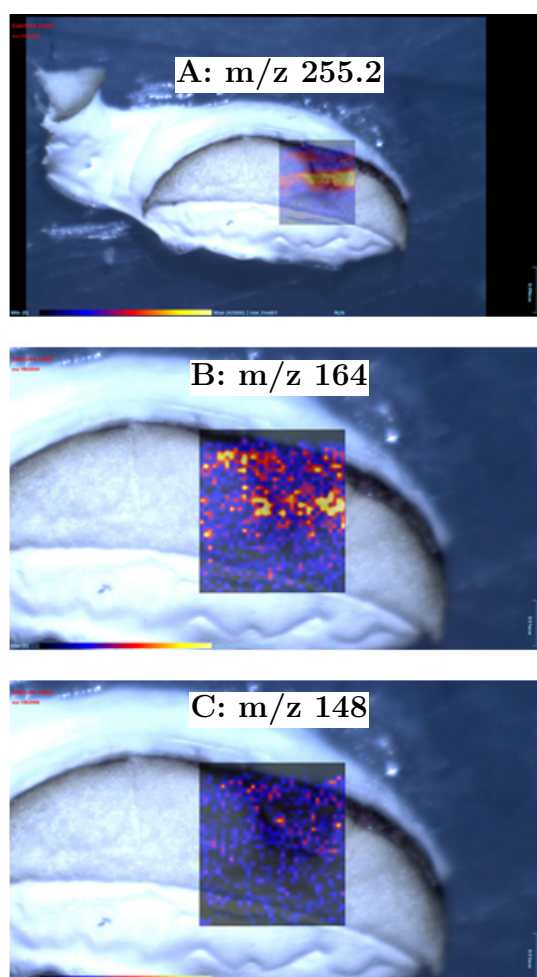


Figure B.1: DESI image of a fresh tuber hand section

The hand section was flash frozen and freeze dried, then analysed by negative mode DESI MSI, using a coumarate-optimised method. A: a heat map showing the distribution of m/z 255.2; B: a heat map showing the distribution of m/z 164; C: a heat map showing the distribution of m/z 148

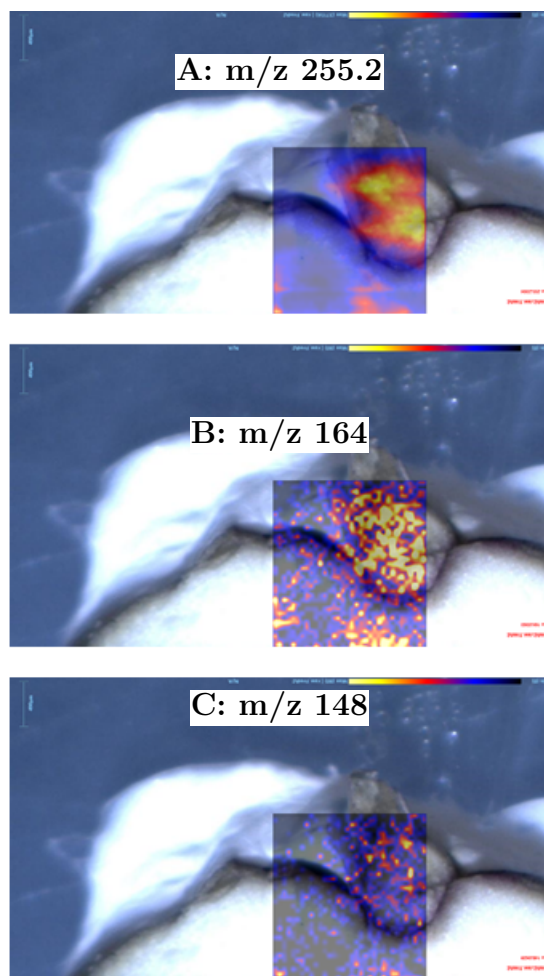


Figure B.2: DESI image of a fresh tuber hand section

The hand section was flash frozen and freeze dried, then analysed by negative mode DESI MSI, using a coumarate-optimised method. A: a heat map showing the distribution of m/z 255.2; B: a heat map showing the distribution of m/z 164; C: a heat map showing the distribution of m/z 148

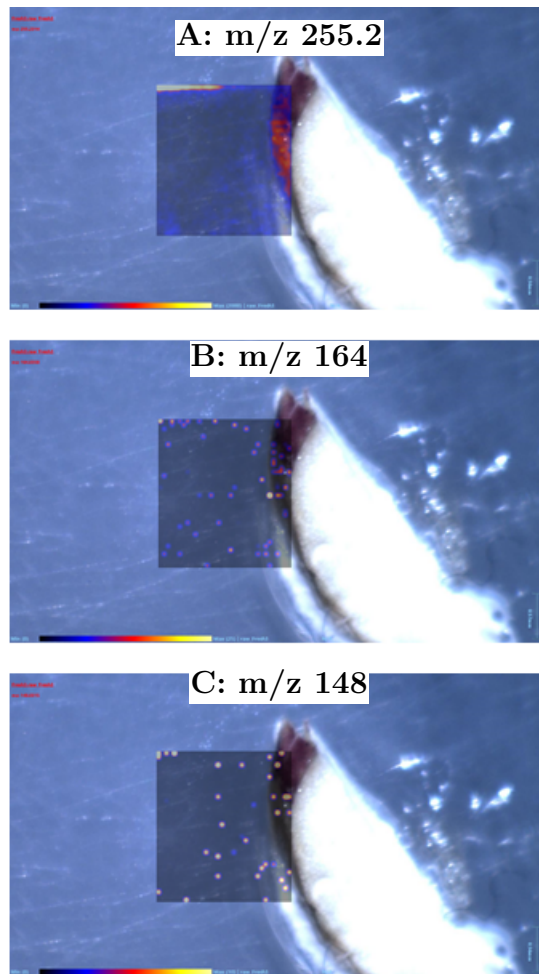
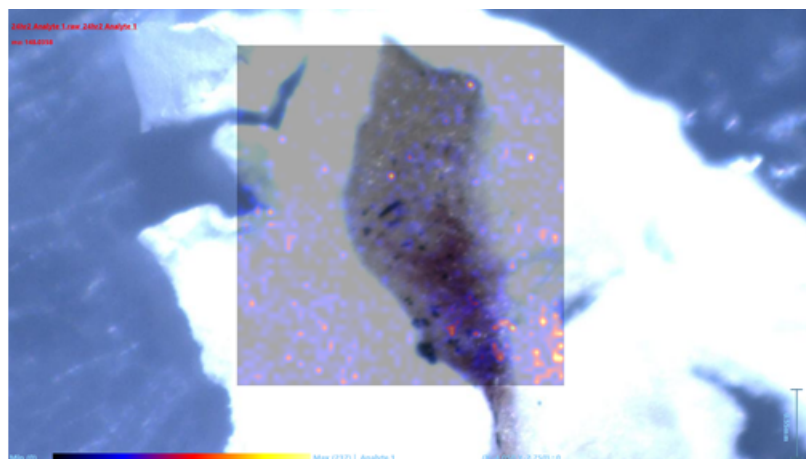


Figure B.3: DESI image of a fresh tuber hand section

The hand section was flash frozen and freeze dried, then analysed by negative mode DESI MSI, using a coumarate-optimised method. A: a heat map showing the distribution of m/z 255.2; B: a heat map showing the distribution of m/z 164; C: a heat map showing the distribution of m/z 148

A: m/z 148



B: m/z 164

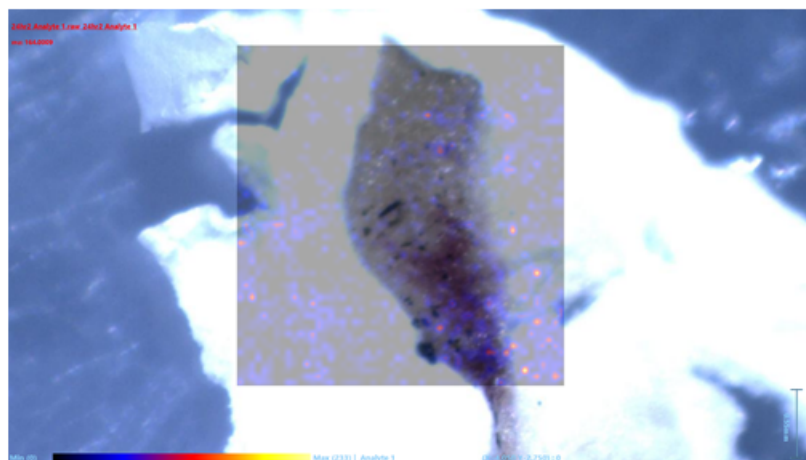


Figure B.4: DESI image - aged in buffer

The hand section was flash frozen and freeze dried, then analysed by negative mode DESI MSI, using a coumarate-optimised method. A: a heat map showing the distribution of m/z 148; B: a heat map showing the distribution of m/z 164

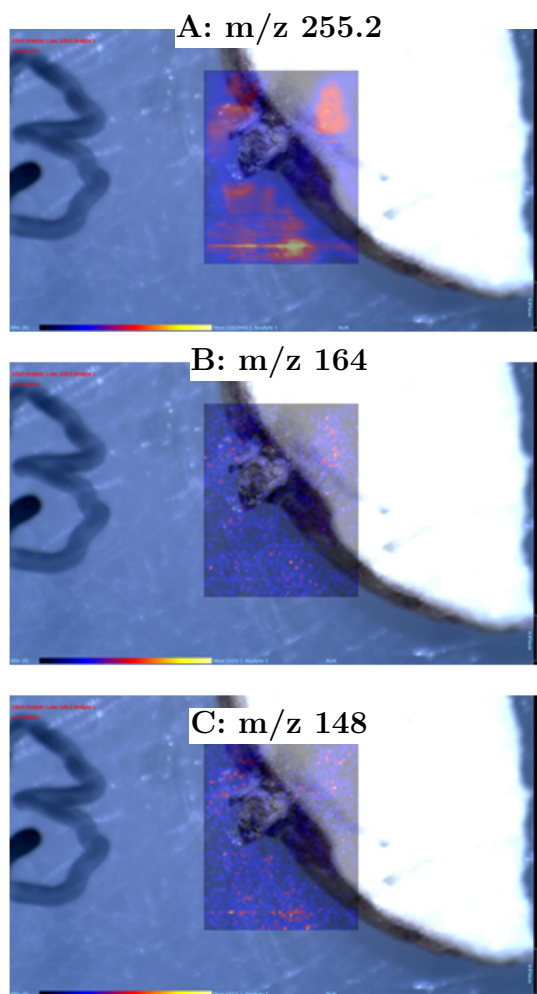


Figure B.5: DESI image - aged in buffer

The hand section was flash frozen and freeze dried, then analysed by negative mode DESI MSI, using a coumarate-optimised method. A: a heat map showing the distribution of m/z 255.2; B: a heat map showing the distribution of m/z 164; C: a heat map showing the distribution of m/z 148

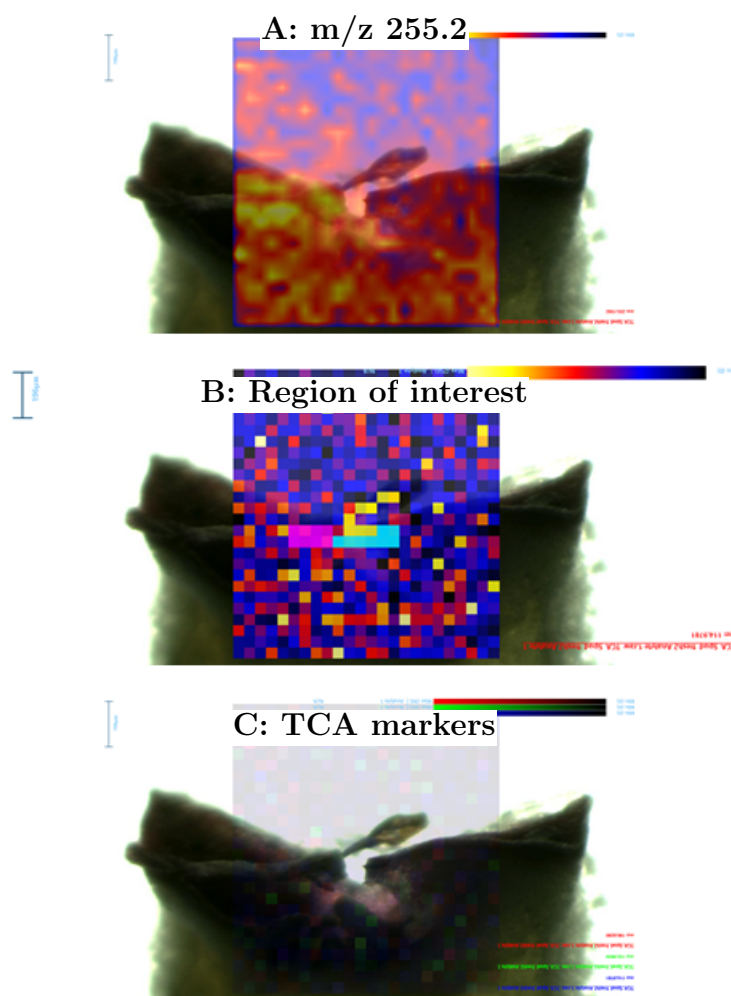


Figure B.6: DESI image of a fresh tuber hand section

The hand section was flash frozen and freeze dried, then analysed by negative mode DESI MSI, using a malate-optimised method. A: a heat map showing the distribution of m/z 255.2; B: Region of interest; C: a heat map showing the distribution of three TCA markers

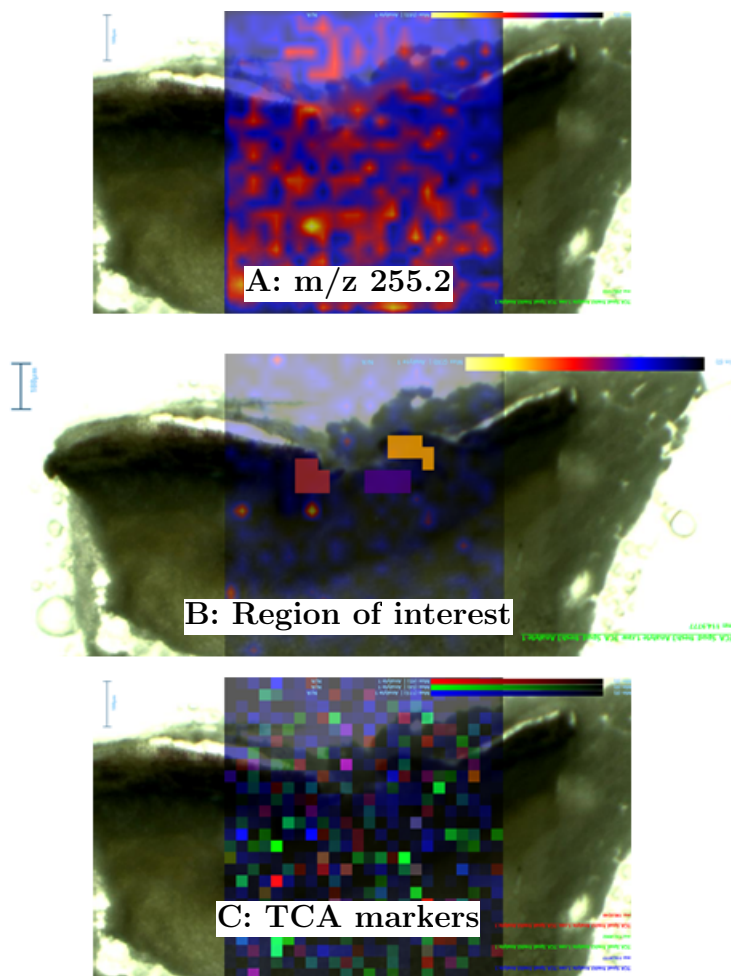


Figure B.7: DESI image of a fresh tuber hand section
The hand section was flash frozen and freeze dried, then analysed by negative mode DESI MSI, using a malate-optimised method. A: a heat map showing the distribution of m/z 255.2; B: Region of interest; C: a heat map showing the distribution of three TCA markers

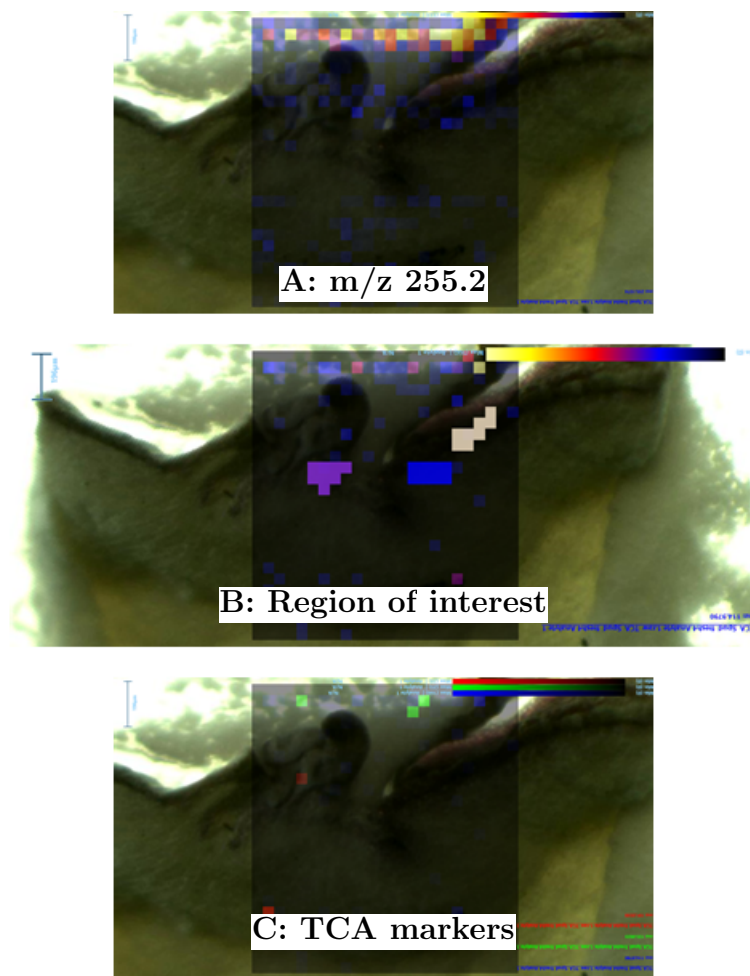


Figure B.8: DESI image of a fresh tuber hand section

The hand section was flash frozen and freeze dried, then analysed by negative mode DESI MSI, using a malate-optimised method. A: a heat map showing the distribution of m/z 255.2; B: Region of interest; C: a heat map showing the distribution of three TCA markers

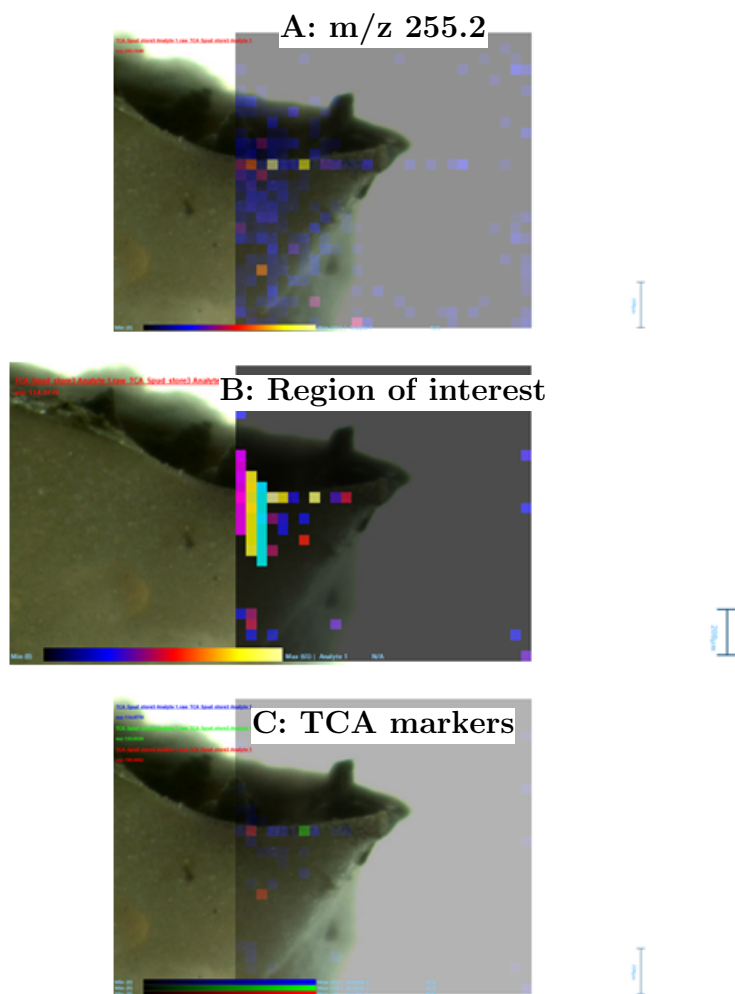


Figure B.9: DESI image - tuber stored for 6 weeks

The hand section was flash frozen and freeze dried, then analysed by negative mode DESI MSI, using a malate-optimised method. A: a heat map showing the distribution of m/z 255.2; B: Region of interest; C: a heat map showing the distribution of three TCA markers

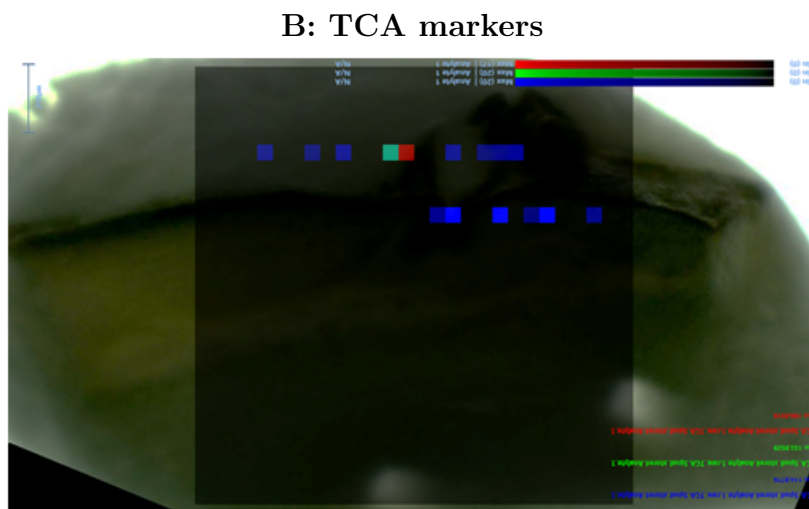
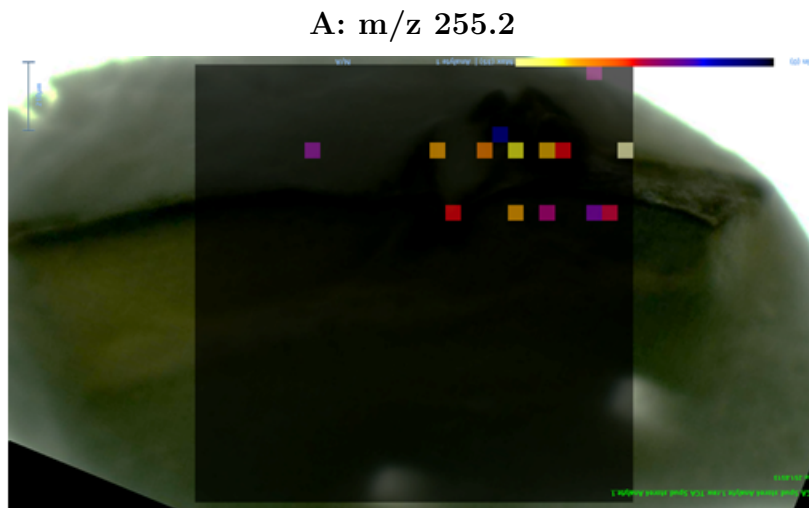


Figure B.10: DESI image - tuber stored for 6 weeks

The hand section was flash frozen and freeze dried, then analysed by negative mode DESI MSI, using a malate-optimised method. A: a heat map showing the distribution of three TCA marker m/z 255.2; B: a heat map showing the distribution of three TCA markers

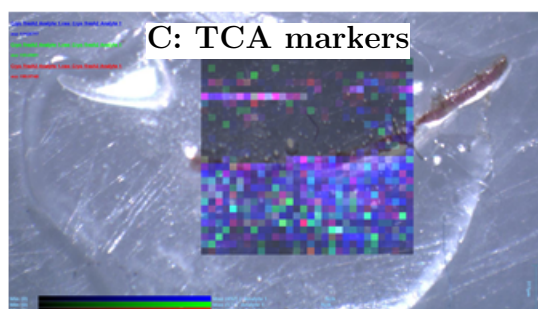
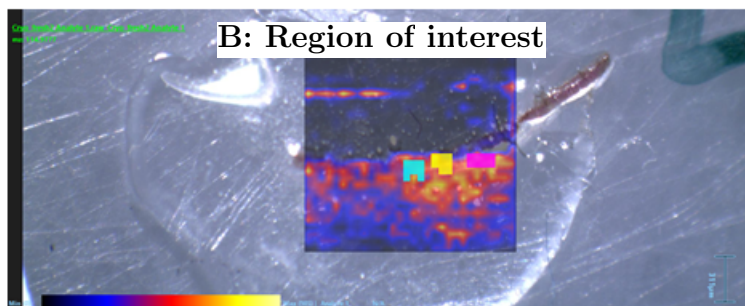
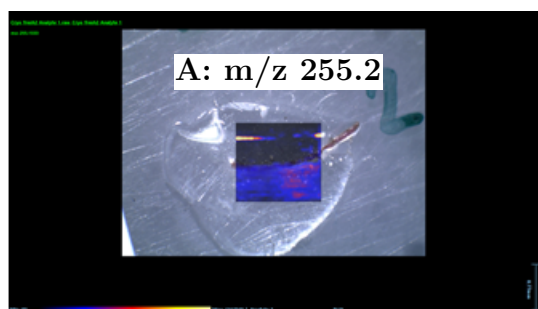


Figure B.11: DESI image of a fresh tuber cryosection
 The cryosection was flash frozen and freeze dried, then analysed by negative mode DESI MSI, using a malate-optimised method. A: a heat map showing the distribution of m/z 255.2; B: Region of interest; C: a heat map showing the distribution of TCA markers

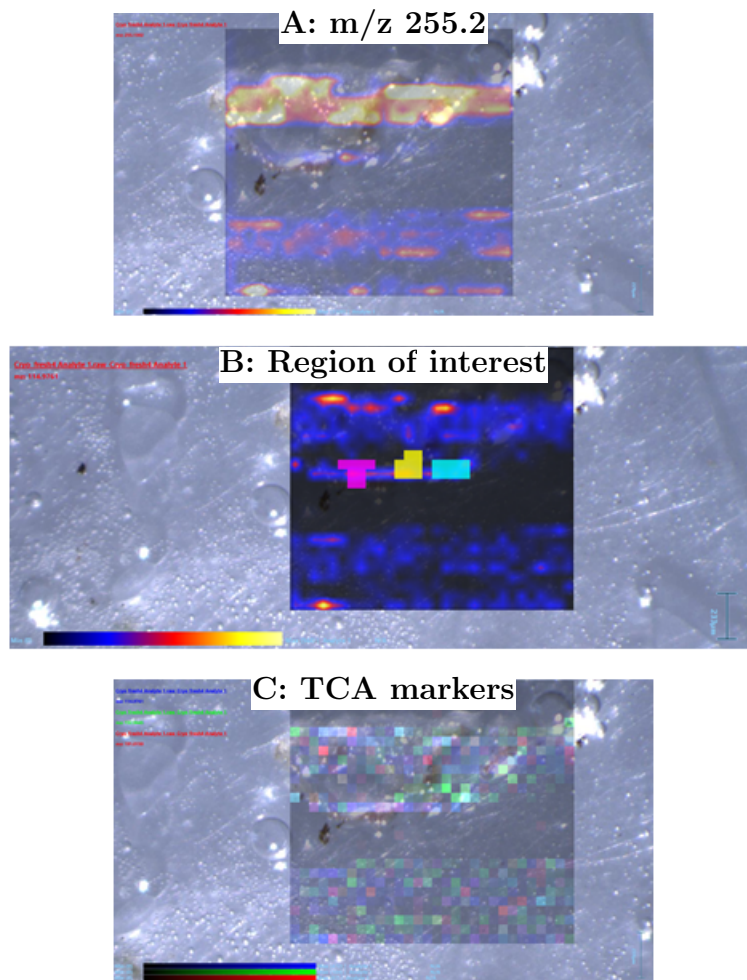
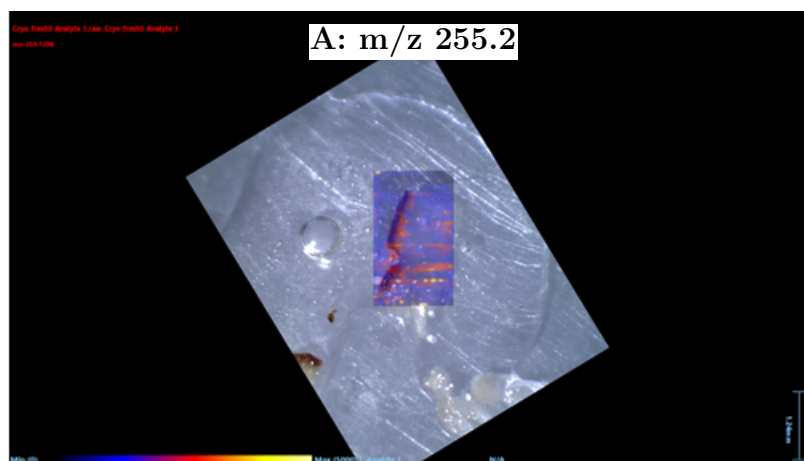


Figure B.12: DESI image of a fresh tuber cryosection

The cryosection was flash frozen and freeze dried, then analysed by negative mode DESI MSI, using a malate-optimised method. A: a heat map showing the distribution of m/z 255.2; B: Region of interest; C: a heat map showing the distribution of three TCA markers



B: TCA markers

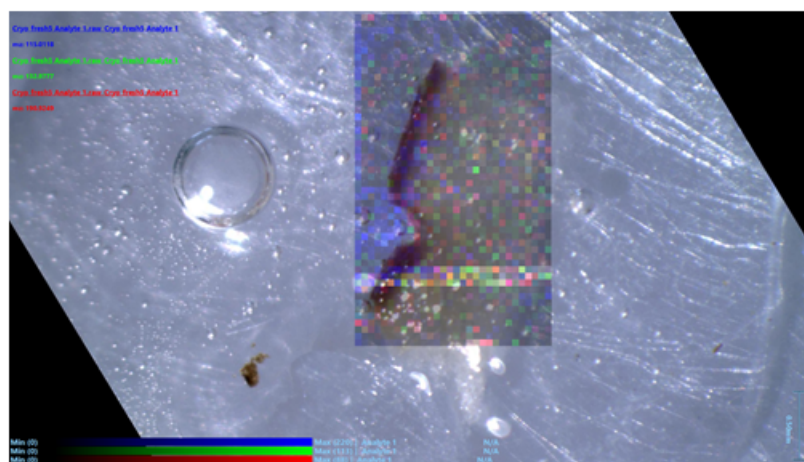


Figure B.13: DESI image of a stored tuber cryosection

The cryosection was flash frozen and freeze dried, then analysed by negative mode DESI MSI, using a malate-optimised method. A: a heat map showing the distribution of m/z 255.2; B: a heat map showing the distribution of three TCA markers